Electronic structure and stability of materials for organic photovoltaic applications

Dissertation
der Mathematisch-Naturwissenschaftlichen Fakultät
der Eberhard Karls Universität Tübingen
zur Erlangung des Grades eines
Doktors der Naturwissenschaften
(Dr. rer. nat.)

vorgelegt von
Aurélien Tournebize
aus Thiers, Frankreich

Tübingen
2015

Gedruckt mit Genehmigung der Mathematisch-Naturwissenschaftlichen Fakultät der Eberhard Karls Universität Tübingen.

Tag der mündlichen Qualifikation:	15.12.2015
Dekan:	Prof. Dr. Wolfgang Rosenstiel
1. Berichterstatter:	Prof. Dr. Thomas Chassé
2. Berichterstatter:	Dr. Agnès Rivaton

Acknowledgements

First, I thank the European Union especially the *Establis* (Ensuring Stability in Organic Solar Cells) project: Marie Curie Initial Training Networks (ITN) – FP7-PEOPLE-ITN-2011-ESTABLIS-290022 for funding. I would like to thank all the members of the *Establis* project especially the coordinator Dr. Roger C. Hiorns and the manager Dr. Mélanie Peudeutour. I consider myself lucky to have been member of this project where I have so much learned. I would like to thank all the partners of *Establis* for the organization of interesting and useful workshops.

I thank Professor Reinhold Fink for accepting to be the president of my jury. I would like to thank Professor Harald Hoppe and Dr. Jörg Ackermann for evaluating my PhD thesis. I also thank Dr. Brigitte Pépin-Donat to have accepted to be member of my jury.

I thank my supervisors Professor Thomas Chassé and Dr. Heiko Peisert for the opportunity of working in the group and their trust. I warmly thank Dr. Agnès Rivaton for her interest, energy and fruitful discussions we had since my first Master internship.

I thank Hilmar Adler, Wolfgang Neu, Elke Nadler and Guillaume Voyard for their precious technical assistances. I thank Professor Christine Taviot-Gueho for XRD experiments, Maxime Defour and Prof. Bruno van Mele for RHC analysis.

I would like to thank all the PhDs and postdocs of *Establis* with whom I traveled all over Europe and spent great moments these last three years: Dr. Stefan Schumann, Dr Graham Morse, Ievgeniia Topolniak, Isabel Fraga, Alberto Gregori, Joanna Kolomanska, Hugo Santos Silva, Hasina Ramanitra, Anna Isakova, Dr. Dargie Deribew, Dr. Simon Dowland, Andreas Distler, Mamadou Seck, Meera Stephen, Safakath Karuthedath and Olena Kozlova. That was a wonderful experience.

I am grateful to my lab- and office- mates in Tübingen: Milutin Ivanovic (Mon petit), Ulf Dettinger (the last VfB Stuttgart fan), Malgorzata Polek (always well organized), Johannes Uihlein (the French artist of Hirschau), Sabine Savu (clairvoyant consulting), Reza Kakavandi (new fan of Lara Fabian), David Balle (lunch time leader), Mathias Glaser and Tanja Wolfer. I thank all of them for the friendly atmosphere, their precious and constant supports.

Je remercie chaleureusement tous les étudiants avec qui j'ai passé de bons moments au sein de l'équipe photochimie de l'institut de chimie de Clermont-Ferrand: Jeff, JuJu, JeaJea, Anne, Guilène (les ex-LPMM), Aurélie Dupuis (mon premier flirt avec l'OPV), Romain Prulho (le taureau maltais), Alexis Colin (le vrai faux Colin), Steeve Collin (le faux vrai Collin), Anthony Perthué (le grand), Camille Rouillon (Mr.), Anthony Chapel (légumophobe), Claire Poncet-Masson (Miss Choco) et Sébastien Berthumeyrie (Jambon d'or).

Merci à Guillaume pour son amitié, vieille de plus de 20 ans.

Merci à ma famille et à Céline.

Scientific articles

Work done during the PhD under submission or in preparation:

[20] The use of HALS in polymer blend for OPV
A. Tournebize, A. Rivaton, H. Peisert, T. Chassé and co-workers.

[19] The role of the electronic transport layers on the stability of OPV devices.
A. Tournebize, H. Peisert, T. Chassé and co-workers.

[18] Energy level alignment between C60 and various electronic transport layers.
A. Tournebize, H. Peisert, T. Chassé and co-workers.

[17] New insights into the delamination mechanism of P3HT:PCBM based solar cells
A. Tournebize, H. Peisert, T. Chassé and co-workers.

[16] Delamination in OPV
A. Gregori, S. Schumann, A. Tournebize, H. Peisert and T. Chassé co-workers.

[15] The role of the chemical structure on the photostability of pi-conjugated polymers, a rule of thumb?
A. Tournebize, I. Fraga, G.E. Morse, A. Rivaton, H. Peisert and T. Chassé, *in preparation.*

[14] Photooxidation of Si-PCPDTBT:PC70BM active layer for organic solar cells applications: a surface and bulk investigation.
A. Tournebize, M. Seck, A. Vincze, A. Rivaton, A. Distler, H-J. Egeelhaf, H. Peisert and T. Chassé, *under submission*

Work done and published during PhD:

[13] The crucial role of confined residual additives on the photostability of P3HT:PCBM active layers.
A. Tournebize, A. Rivaton, H. Peisert and T. Chassé, *J. Phys. Chem. C,* 2015, 119, 9142−9148.

[12] The Effect of Polymer Solubilizing Side-Chains on Solar Cell Stability.
G.E. Morse, A. Tournebize, A. Rivaton, T. Chassé, C. Taviot-Gueho, N. Blouin, O. Lozman and S. Tierney, *Phys. Chem. Chem. Phys.,* 2015,17, 11884-11897.

[11] Is there a photostable conjugated polymer for efficient solar cells?
A. Tournebize, A. Rivaton, J-L. Gardette, C. Taviot-Gueho, D. Bégué, M-A. Arnaud, C. Dagron-Lartigau, H. Medlej, R. Hiorns, S. Beaupré and M. Leclerc, *Polym. Degrad. Stab.*, 2015, 112, 175-184.

[10] A universal route to improving conjugated macromolecule photostability
H. Santos Silva, A. Tournebize, D. Bégué, H. Peisert, T. Chassé, J. -L. Gardette, S. Thérias, A. Rivaton, R. C. Hiorns, *RSC Advances,* 2014, 4, 54919.

[9] Characterization of the degradation process of Si-PCPDTBT:PC70BM (1:2) blend layers deposited on ITO/glass substrate.
M. Seck, A. Vincze, A. Satka, D. Hasko, F. Uherek, A. Tournebize, H. Peisert and T. Chasse, *Sol. Energy Mater. Sol. Cells*, 2014, 132, 210–214.

[8] Molecular orientation in polymer/fullerene blend films and the influence of annealing.
U. Aygül, H. Peisert, D. Batchelor, U. Dettinger, M. Ivanovic, A. Tournebize, S. Mangold, M. Förster, I. Dumsch, S. Kowalski, S. Allard, U. Scherf and T. Chassé, *Sol. Energy Mater. Sol. Cells*, 2014, 128:119–125.

Work done before PhD:

[7] Thermal Stabilisation of Polymer–Fullerene Bulk Heterojunction Morphology for Efficient Photovoltaic Solar Cells.
L. Derue, O. Dautel, A. Tournebize, M. Drees, H. Pan, S. Berthumeyrie, B. Pavageau, E. Cloutet, S. Chambon, L. Hirsch, A. Rivaton, P. Hudhomme, A. Facchetti and G. Wantz, *Adv. Mater*. 2014, 26, 5831–5838.

[6] How Photoinduced Crosslinking Under Operating Conditions Can Reduce PCDTBT-Based Solar Cell Efficiency and then Stabilize It.
A. Tournebize, A. Rivaton, J-L. Gardette, C. Lombard, B. Pépin-Donat, S. Beaupré and M. Leclerc, *Adv. Energy Mater.*, 2014, 4, 10.

[5] Photostability of organic materials used in polymer solar cells.
A. Rivaton, A. Tournebize, J. Gaume, P-O. Bussière, J-L. Gardette and S. Therias, *Polym. Int.*, 2014, 63, 8, 1335–1345.

[4] New insights into the mechanisms of photodegradation / stabilization of P3HT:PCBM active layers using poly(3-hexyl-d13-thiophene).
A. Tournebize, P-O. Bussière, A. Rivaton, J-L. Gardette, Kion Norrman, Frederik C. Krebs, H. Medlej, R. Hiorns and C. Dagron-Lartigau, *Chem. Mater*., 2013, 25(22), 4522-4528.

[3] Impact of UV-visible light on the morphological and photochemical behavior of a low-bandgap poly(2,7-carbazole) derivative for use in high-performance solar cells.
A. Tournebize, P-W-W. Chung, P-O Bussière, A. Rivaton, J-L. Gardette, S. Beaupré and M. Leclerc, *Adv. Energy Mater*., 2013, 3, 4, 478–487.

[2] Why do chemical sensors for explosives detection lose their fluorescence under UV-visible exposure?
A. Tournebize, P-W-W. Chung, S. Thérias, P-O. Bussière, A. Rivaton, T. Caron, F. Serein-Spiraud, J-P. Lère-Porte, P. Montméat, and J-L. Gardette, *Polym. Degrad. Stab.*, 2012, 97, 8, 1355–1365.

[1] Morphology and photochemical stability of P3HT:PCBM active layers of organic solar cells.
A. Dupuis, A. Tournebize, P.-O. Bussiere, A. Rivaton, J.-L. Gardette, *Eur. Phys. J. Appl. Phys*., 2011, 56, 34104.

[Patent] AFM coupled in situ irradiation, P-O. Bussière, S. Therias, J-L. Gardette, A. Tournebize, S. Berthumeyrie.

Scientific contributions

The present PhD work: “Electronic structure and stability of polymer blend materials for organic photovoltaic application” belongs to the *Establis* (Ensuring Stability in Organic Solar Cells) project: **Marie Curie Initial Training Networks (ITN) – FP7-PEOPLE-ITN-2011-ESTABLIS-290022.**

The project gathers 11 partners (academic and industries, **Figure 0.1**) across the Europe, 50 researchers including 12 PhDs and 4 post-docs.

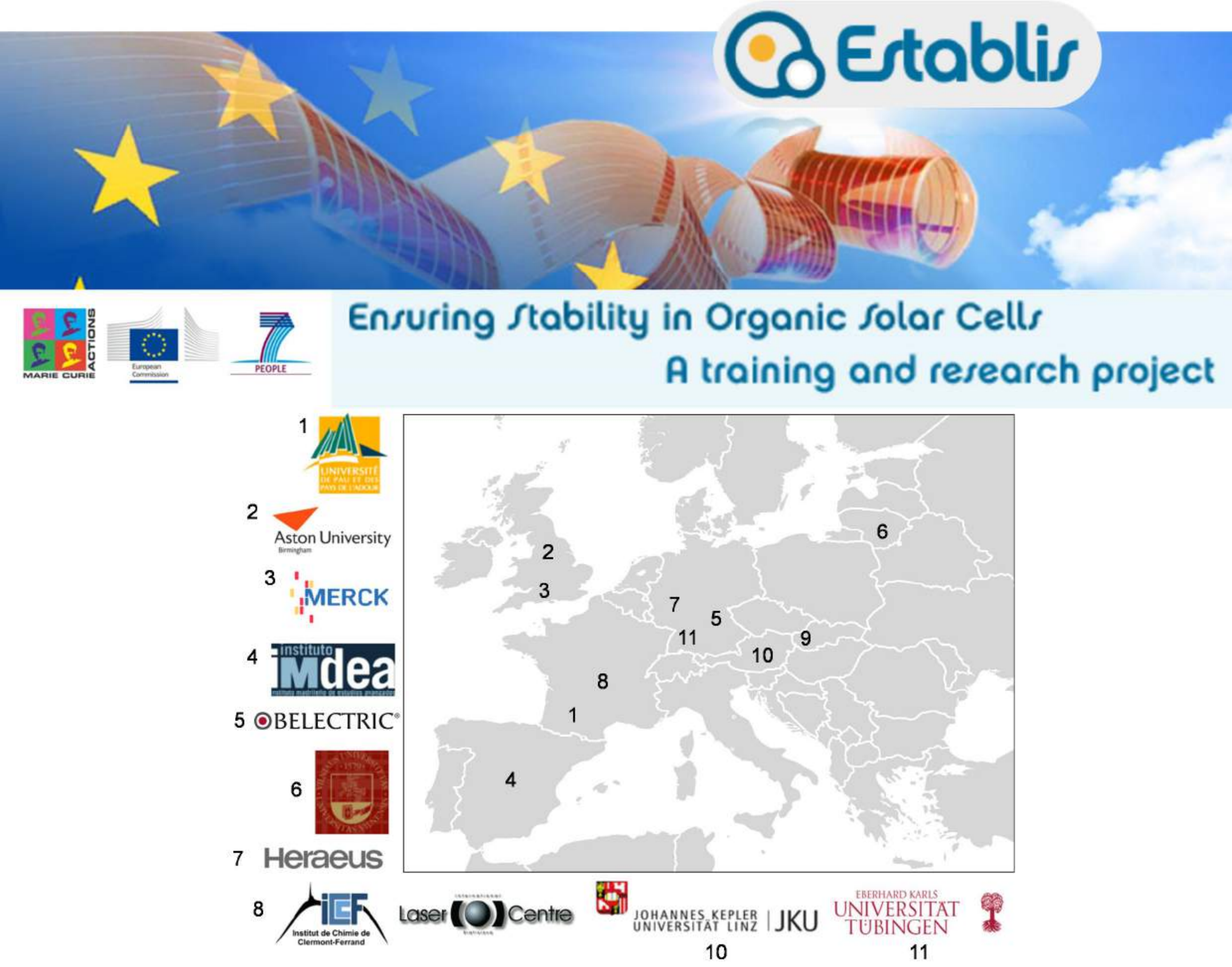

Figure 0.1 - All the *Establis* partners

The present manuscript is the result of intense scientific collaborations within the *Establis* project. Thus, exchange of materials, devices and discussions were constant along these past three years. For clarifying who did what in each part of the manuscript, please refer to the *"Scientific contribution"* sections which are located in the introduction of each part. The name and ESR/ER number of each partner will be specified for each contribution according to the **Table 0-1**. You can refer to the PhD thesis of all ESRs student.

N°	Name	Partner	Investigation
ESR1	Hugo Santos Silva	1	Synthesis and modelling of polyfullerenes
ESR2	Alberto Gregori	1	Synthesis and rheological characterisation of (co)polymers for organic solar cells
ESR3	Meera Stephen	6	Design and fabrication organic bulk heterojunction solar cells for charge carrier transport and recombination measurements
ESR4	Safakath Karuthedath	4	Reversible and irreversible oxygen effects on the exciton dynamics in photovoltaic devices: a time domain study
ESR5	Olena Kozlova	10	Organic bulk heterojunction solar cells for charge carrier transport and recombination measurements
ESR6	Anna Isakova	2	Synthesis of ligands and polymers for application in organic solar cells
ESR7	Joanna Kolomanska	2	Synthesis of polymers and copolymers for application in organic solar cells
ESR8	Isabel Fraga	8	Photochemical behaviour of new organic materials for OSCs
ESR9	Ievgeniia Topolniak	8	Development of photosable nanocomposites barrier layers
ESR10	Aurélien Tournebize	11	Electronic structure and stability of polymer blend materials for OPV
ESR11	Mamadou Seck	9	Combining surface and vertical profile studies of organic materials in solar cells
ESR12	Hasina Ramanitra	1	Synthesis of polyfullerenes
ER1	Dr. Dargie Deribew	5	Effect of degradation on charge carrier dynamics
ER2	Dr. Simon Dowland	5	Identification of Achilles' Heels of Organic Bulk Heterojunction Solar Cells
ER3	Dr. Graham Morse	3	Design, synthesis and characterization of higher stability donor polymers for bulk heterojunction solar cells
ER4	Dr. Stefan Schumann	7	Tailoring PEDOT-dispersions towards their use in organic solar cells

Table 0.1 - List of PhD (ESR) and post-docs (ER) involved in *Establis*.

Table of content

General introduction..1

Chapter 1 - OPV, overview and stability 7

1.1. The conventional photovoltaic 9

1.1.1. A brief history 9
1.1.2. General description of a silicon solar cell.. 10
1.1.3. Efficiency racing 11
1.1.4. Limits of the conventional PV 13

1.2. The emergence of a new class of PV 14

1.2.1. Organic photovoltaic: new properties, new applications 14
1.2.2. Electronic structure and properties of organic materials for OPV.......... 15
1.2.3. General device structure, principle and electrical characteristics 17
1.2.4. OPV development, history and main breakthroughs............................. 20
1.2.5. What OPV needs to face now: efficiency, cost and lifetime 25

1.3. Stability in OPV.. 28

1.3.1. General aspects 28
1.3.2. Stability related to the donor material: the pi-conjugated polymer.......... 28
1.3.3. Variables influencing the pi-conjugated polymer degradation, how to compare 31
1.3.4. Stability related to the acceptor material and the donor-acceptor blend film 33
1.3.5. Stability and interfaces 35

1.4. Summary and motivation 36

Chapter 2 – Stability of polymer blends materials 39

2.1. Introduction to Chapter 2 41

2.2. Relationship between the side chain structure and polymer photo-stability 42

2.2.1. Introduction 42
2.2.2. Experimental 44
2.2.3. Results 45

2.2.4. Discussion 53

2.2.5. Conclusion 56

2.3. Relationship between the side chain structure and BHJ thermal stability 57

2.3.1. Introduction 57

2.3.2. Experimental 59

2.3.3. Results and discussion 60

2.3.4. Conclusion 70

2.4. Relationship between the side chain structure and device lifetime. 71

2.4.1. Introduction 71

2.4.2. Experimental 71

2.4.3. Results 74

2.4.4. Discussion 85

2.4.5. Conclusion 87

2.5. Summary of Chapter 2 89

Chapter 3 –The role of the “third component” on polymer blend stability 91

3.1. Introduction to Chapter 3 93

3.2. The crucial role of confined residual additives on the photostability of polymer blends 94

3.2.1. Introduction 94

3.2.2. Experimental 95

3.2.3. Results and discussion 96

3.2.4. Conclusion 106

3.3. The use of HALS (Hindered Amine Light Stabilizers) in polymer blend films 107

3.3.1. Introduction 107

3.3.2. Experimental 108

3.3.3. Results and discussion 109

3.3.4. Conclusion 115

3.4. The use of a poly-fullerene as BHJ thermal stabilizer 116

3.4.1. Introduction 116

3.4.2. Experimental 117

3.4.3. Results and discussion.. 119

3.4.4. Conclusion 125

3.5. Summary of Chapter 3 126

Chapter 4 – Identification of the mechanical breaking point in pristine and aged OSCs 127

4.1. Introduction to Chapter 4 129

4.2. Identification of the mechanical breaking point in pristine OSCs. 131

4.2.1. Introduction 131

4.2.2. Experimental 132

4.2.3. Results and discussion.. 134

4.2.4. Conclusion 149

4.3. Identification of the mechanical breaking point in aged OSCs... 150

4.3.1. Introduction 150

4.3.2. Experimental 151

4.3.3. Results and discussion.. 152

4.3.4. Conclusion 158

4.4. Summary of Chapter 4 159

Chapter 5 – Electronic structure (ES), energy level alignments (ELA) and interactions between the active layer (AL) and the electron transporting layer (ETL)...161

5.1. Introduction to Chapter 5 163

5.1.1. Models 163
5.1.2. OPV devices, active layer (AL) / electron transporting layer (ETL) interface 165
5.2. ES and ELA between C60 and various ETL. 167
5.2.1. Introduction 167
5.2.2. Experimental 167
5.2.3. Results and discussion 169
5.2.4. Conclusion 183
5.3. Influence of ETL on device stability 185
5.3.1. Introduction 185
5.3.2. Experimental 185
5.3.3. Results 186
5.3.4. Discussion 197
5.3.5. Conclusion 197
5.4. Summary of Chapter 5 198

General conclusion 199

Bibliography 203

Appendix 213

General introduction

The present work takes place within the context of the development of renewable energies in our society. The need of energies has always been a major issue for the humanity and is nowadays in the center of all interests. Since always, energy transitions transform societies.[1-3]

Energy transitions, key periods in the history.

In the modern history of Europe, the first energy transition was the substitution of wood by coal marking the beginning of the industrial revolution (16-18th century). The transition from hand production methods to machine methods was accompanied by a change of the energetic resources. The industrial revolution transformed deeply the society and politic within nations and between nations.[1] The second energy transition was the shift to oil fuel and gas. At the beginning of the 20th century, coal was still the most used mineral resource but the development of the automobile boosted the use of fuel. Again, the energy shift was accompanied by important and rapid technological developments and by deep changes in societies. The search of energy resources was controlled much more by geopolitics than by the probability of discovery.[1] Technological development and the search of new type of energy sources played crucial roles during wars especially the Second World War where the use of nuclear weapons by the United States marked its end. After that, the Atomic Energy Act of 1946 made the atomic energy an absolute monopoly of the federal government of the United States. Important restrictions were made in order to not divulgate information concerning the nuclear energy. The atomic energy played an important role also during the Cold War. Latter, all restrictions were revised before utilities could own or build nuclear power stations. The second part of the 20th century was marked by the real emergence of the ecological thought. For the first time, it was recognized by the scientific community that the use of energy resources can impact drastically our environment. The intergovernmental panel on climate change (IPCC) was created in 1988 under the auspice of the United Nations. The IPCC provides scientific information related to the impacts of human induced climate change[4] and shared in 2007 the Nobel Peace Prize. The use of coal and fossil fuels induces the release of many gas contributing to the global warming of the planet. At this regard, the nuclear energy appears to be better, but other crucial problems regarding the security and the storage/recycling of nuclear wastes for the long term remain unsolved. The temperature increase of oceans and atmosphere impacts the climate and therefore all the living ecosystems of the planet. Nowadays, we are in the middle of a very important and complex energetic transition. Indeed, the energy transition has to consider many aspects which are economy, geopolitics and ecology.

Which energy resource should we use?

By definition, the shift to renewable energies is the only solution for a long term development. **Figure 0.3,** extracted from the website of Perez et al.[5] summarizes the different energy resources available on our planet. All the finite resources are by definition not interesting for a long term development. Currently, the most used resources are the finite resources such as: petroleum, natural gas, Uranium and coal. **Figure 0.3** very clearly shows that the solar resource has by far the best potential for the production of a clean energy. The solar resource has many and huge advantages. The sun provides a free, none finite energy which is available wherever we are on the planet (even if the energy is not perfectly well distributed). Since always, the solar energy was used for his natural heating property. The Roman bathhouses (1-4th centuries BC) had large south facing "window" to let the sun warm the edifice and latter Justinian (6th century

BC) initiated the “sun rights” to ensure individual access to the sun. Nowadays, for the modern use, the solar energy has to be converted into electricity.

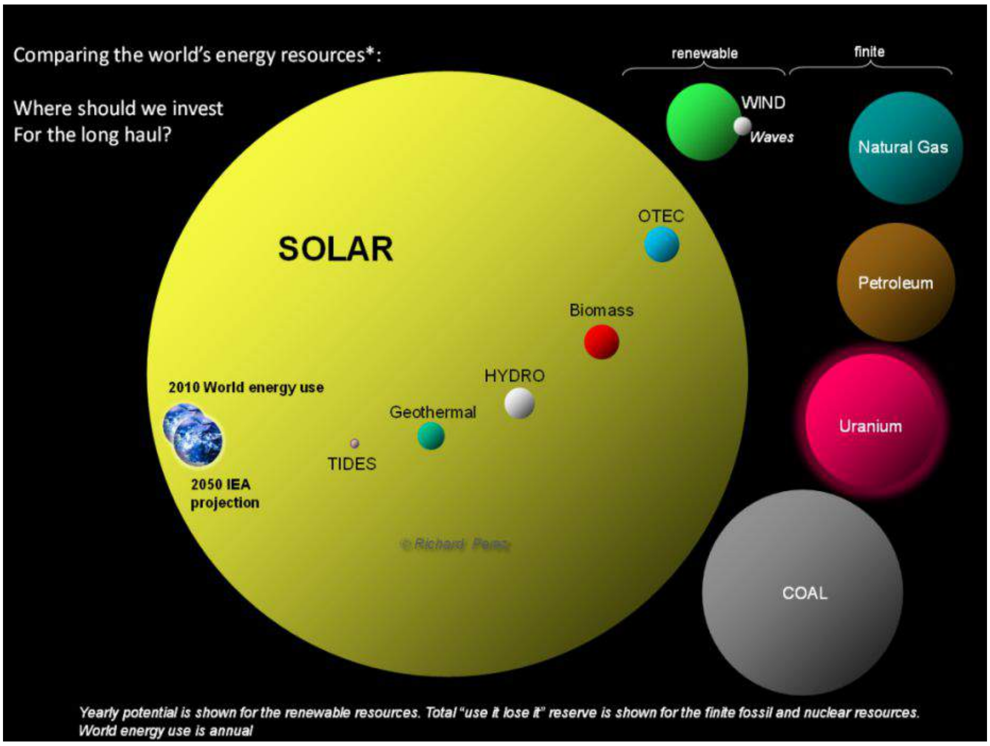

Figure 0.3 - Scheme of World’s energy resources extracted from Perez et al.[5]

The idea of a system able to convert the light into electricity has been made possible after several scientific discoveries along the 19th and 20th centuries. The photovoltaic (PV) technology is officially born in 1954 and has been developed and improved until nowadays.

Figure 0.4 - How can we convert the solar energy in electricity?

New types of photovoltaic devices with new properties recently emerged such as the organic photovoltaic (OPV). Based on organic materials such as conjugated small molecules or polymers, the devices are ultra-thin, flexible, colorful, transparent and tunable. The organic materials can be formulated into inks and the devices can be therefore printed with a potential low cost production. Since two decades, OPV is the object of intense investigations for optimizing device performance and more recently device lifetime. While the device performance of OPV devices was significantly enhanced, the main weak point concerns the stability. Because the materials used in OPV are organic, the device exhibits performance loss when exposed to outdoor conditions meaning light combined with ambient air and humidity. This makes the study of the OPV stability very challenging and also absolutely necessary for the success of the technology.

The present manuscript has the main goal to contribute to the understanding of the various degradation processes in order to propose solutions allowing the fabrication of OPV devices with longer lifetimes. The understanding of degradation mechanisms and the proposal of stabilization strategies in OPV require knowledge in various fields and investigations at different scales.

The present manuscript is divided in five chapters:

- Chapter 1 provides general information on OPV. A brief history, general structures and characteristics of OPV devices are reported. Then, a state of art concerning the stability in OPV is presented. We will show that the degradation of the devices performance has several origins and that many factors come into play.
- Chapter 2 is dedicated to the stability of a series of polymer blend materials which constitute the active layer of OPV devices. Firstly, the photo-stability of series of low band gap polymers (and blends) is reported. The impact of the chemical structure and physical properties of the polymers on their respective photo-stabilities is discussed. Secondly, the thermal behavior of the same series of conjugated polymers is investigated. Attempts to make some link with the thermal stability of the polymer blends (phase separation of the donor/acceptor materials) are proposed. Finally, the stability of encapsulated devices based on the polymer series is studied and the role of the polymer is discussed.
- Chapter 3 concerns the role of a “third component” on the polymer blend stability. The first part deals with the crucial role of confined residual additives on the photo-stability of polymer blend materials. The use of HALS (Hindered Amine Light Stabilizers) additives in polymer blend films for OPV is the topic of the second part. Finally, the last part focuses on the use of a polyfullerene as a morphological stabilizer for polymer blends.
- Chapter 4 is devoted to the interface between the active layer and the hole transporting layer. This interface is known to constitute a weak point in terms of adhesion, and consequently the devices performances can suffer from delamination. The first part of this chapter concerns the understanding of the delamination process in pristine devices. Two strategies are tested for improving the adhesion between the two layers. The second part is focused on the delamination mechanism when the devices are submitted to artificial ageing.
- Chapter 5 is dedicated to the interface between the active layer and the electron transporting layer. This chapter is divided into two parts with the study of energy level alignments between C60 and various electron transporting layers in a first part. The second part is devoted to the evolution of the interactions between the two layers when exposed to light and thermal stress.

Except for Chapter 1, all Chapters are based on the same structure: *introduction, experimental, results and discussion* and *conclusion.*

An appendix is given at the end of the manuscript with additional information concerning the experimental techniques and also supporting results concerning the Chapter 2, 3, 4 and 5.

The present work is the result of a collaborative work within the *Establis* project. In each general introduction, a "*scientific contribution"* paragraph summarizes the different contributions of the different partners of the *Establis* project.

Chapter 1

OPV, overview and stability

1.1. The conventional photovoltaic

The conversion of sunlight into electricity, in other words the emerging of Photovoltaic (PV) systems, has been possible by several discoveries along the end of the 19th and 20th centuries. This first section concerns the historical development of the PV technology.

1.1.1. A brief history

The French scientist Alexandre Edmond Becquerel observed in 1839 for the first time the photoelectric effect.[6,7] He observed that an electrolytic cell can generate more electricity when exposed to light. In 1876, William Grylls Adams and Richard Evans Day demonstrated that light can be changed into electricity from a solid metal (selenium), and the first cell was fabricated by C. E. Fritts and the results were published in 1886.[8] The photoelectric effect was theoretically explained by Albert Einstein in his paper published in 1905.[9] The possible conversion of light into electricity was demonstrated for several solids such as cadmium sulfide, copper/copper oxides and silicon.

The first light sensitive devices were patented in 1941 by R. S. Ohl.[10] The Photovoltaic (PV) technology was officially born in 1954 in the United States with the development of silicon solar cells in the Bell labs by Daryl Chapin, Calvin Fuller, and Gerald Pearson. [11] They improved the efficiencies from 4% up to 11%. The PV was boosted by the space race in the 50s and 60s. All the satellites were using PV as it is the only source of energy available and the cost was not the most important criterion for aero spatial applications.

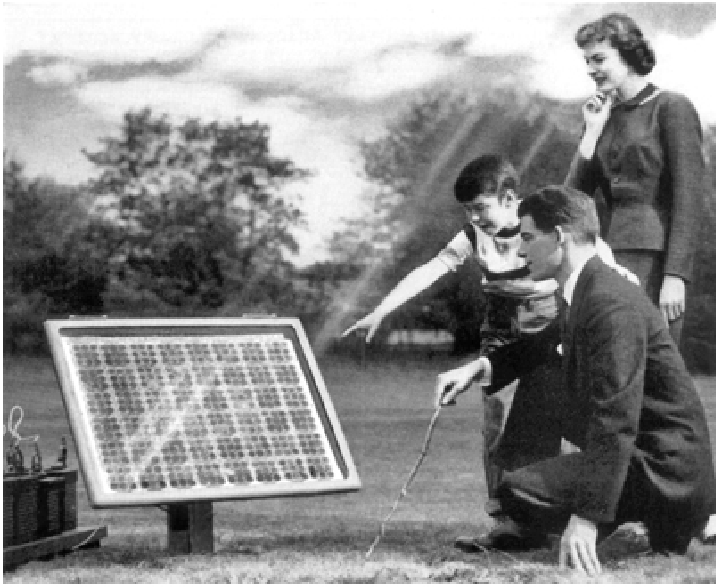

Figure 1.1 - Publicity of Bell Lab in 1954. Extracted from http://www.computerhistory.org

However, the use of PV cells on earth is problematic as the cost is one of the most important criteria. In the 70s, Dr. Elliot Berman, with financial help from Exxon Corporation, designed a significantly less costly solar cell by using a poorer grade of silicon and packaging the cells with cheaper materials. Thus, the price downs from $100/watt to $20/watt thus starting the competitiveness of the PV the technology on the market. PV appeared in our environment such as the insertion of solar modules in the Railway in Georgia (1974) or the production of electricity in rural areas in Australia (70s). Many groups all over the world developed and optimized the PV technology mainly based on silicon.

1.1.2. General description of a silicon solar cell

Silicon which constitutes most of the current photovoltaic cells is a semi-conductor material. **Figure 1.2** shows the main elements which constitute most of the semi-conductor materials. A semi-conductor can be made from a single element such as silicon or a composite such as GaAs, CdTe or Si_xGe_{1-x} for example. The conductivity of a material can be described by the band theory as shown in **Figure 1.2**. Each material has a valence band (VB) where the electrons are located and a conduction band (CB) which is unoccupied by electrons. In the case of a metal, the VB and CB bands are overlapping and the electrons can move from the VB to the CB very easily. For an insulator, the two bands are separated by a big energetic gap and the electrons cannot go to the CB. A semi-conductor has also a gap but energetically less important than insulators. Thus, the energy needed for an electron to move from the VB to the CB (Eg, gap energy) can be overcome by an incoming source of energy, sunlight in the case of photovoltaic.

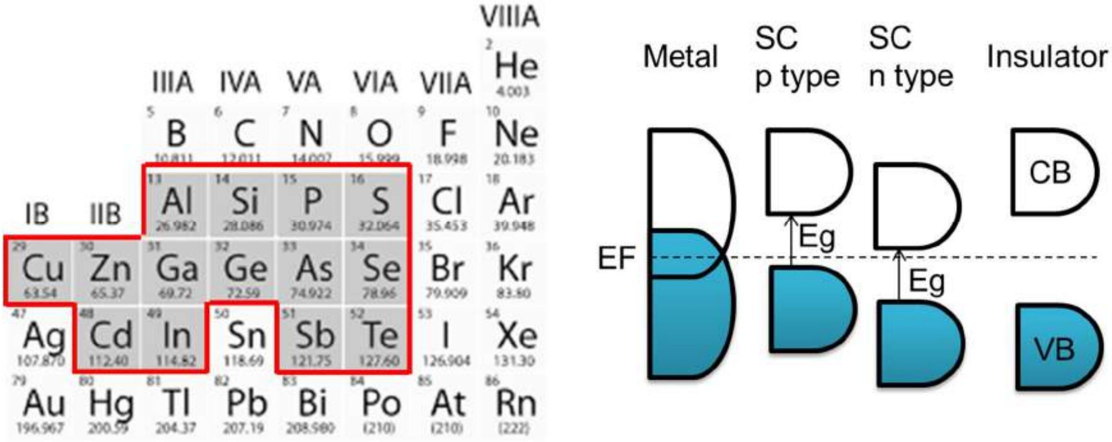

Figure 1.2 - On the left side, part of the periodic table focusing on the main elements (red) which constitute most of the semi-conductors materials. On the right side, representation of the band theory which explains the conductivity or none conductivity of materials.

Thus, a semi-conductor with an appropriate gap like silicon in contact with metal electrodes and exposed to sunlight can produce electricity. A brief description of a silicon solar cell is presented in **Figure 1.3**. The silicon substrate is usually covered by n-type silicon leading to the formation of a P/N junction. Excitons or electron/hole pairs are formed after light absorption in the p- or n-type silicon. Then, the excitons diffuse to the P/N junction and charges are separated thanks to the energetic difference before reaching their respective electrodes.

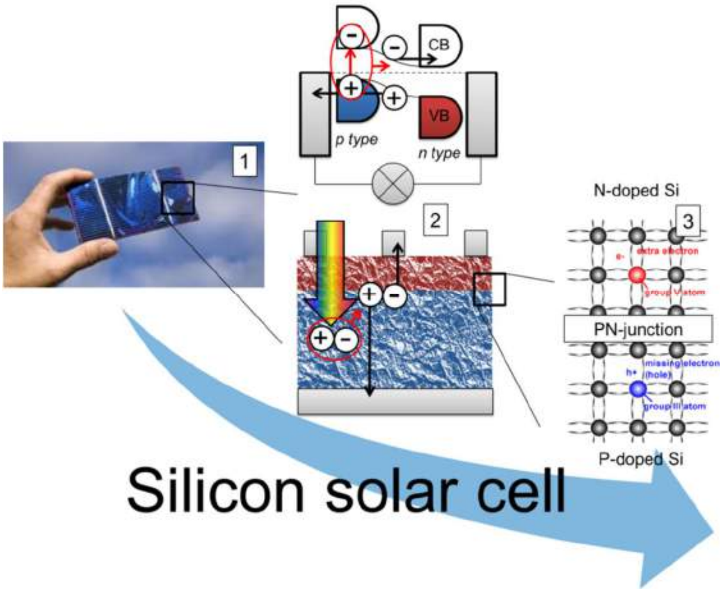

Figure 1.3 - Multiscale description of a silicon solar cell. Photograph of a Si solar cell (1), cross section and energetic levels (2) and atomic lattice close to the P/N junction (3).

The band gap of the silicon depends on the natural and intrinsic quality of the extracted silicon. Thus, in order to optimize the bang gap, doping processes are used. Elements belonging to the column III (**Figure 1.2**) have one electron missing compared to silicon (IV column) and are added to the Si matrix in order to make p-doped materials. For n-doped materials, elements of the V column are added.

1.1.3. Efficiency racing

Figure 1.4 shows the development of the solar cells from the 70s until the last update in 2015 by the National Renewable Energies Laboratory (NREL). The best efficiencies obtained for various types of solar cells are thus reported in **Figure 1.4**. We can observe the evolution of the conventional solar cells made from silicon but we can observe that many other types of solar cells were developed in parallel. **Figure 1.4** ranks the solar cells in four groups: Multi-junction Cells, Crystalline Si Cells, Thin Film Technology and Emerging PV. The three first types of cells can be grouped together as “conventional cells” as these cells are based on at least one solid semi-conductor (silicon, cadmium, copper, indium, gallium or selenium mainly). Two main ways were investigated for increasing the device efficiency of these “conventional cells”. These two ways are related to the two axis of the solar spectrum. (**Figure 1.5**)

The X axis corresponds to the wavelength (nm) or energy (eV) of the photons. More photons from the solar spectrum can be absorbed and more energy we can expect to extract.

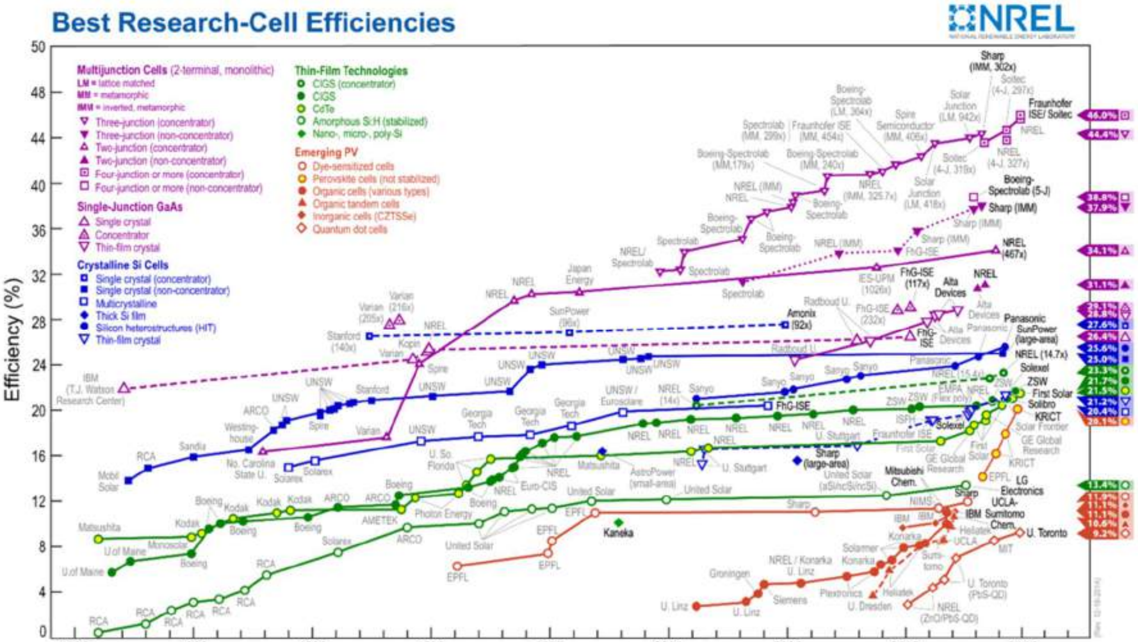

Figure 1.4 - Latest update (2015) of the best research-cell efficiencies from the National Renewable Energies Laboratory (NREL).

The semi-conductors used for conventional cells are a solid metal with a well-defined gap corresponding to the energy difference between his valence band (VB) and his conduction band (CB). (**Figure 1.2**) This gap defines the energy needed for allowing the electrons of the VB to reach the CB. This energy is provided by the incoming light. Therefore the gap of a semi-conductor for PV applications must be in the range of the energy of the photons received by the material. The point is that the sunlight spectrum is very broad. (**Figure 1.5**)

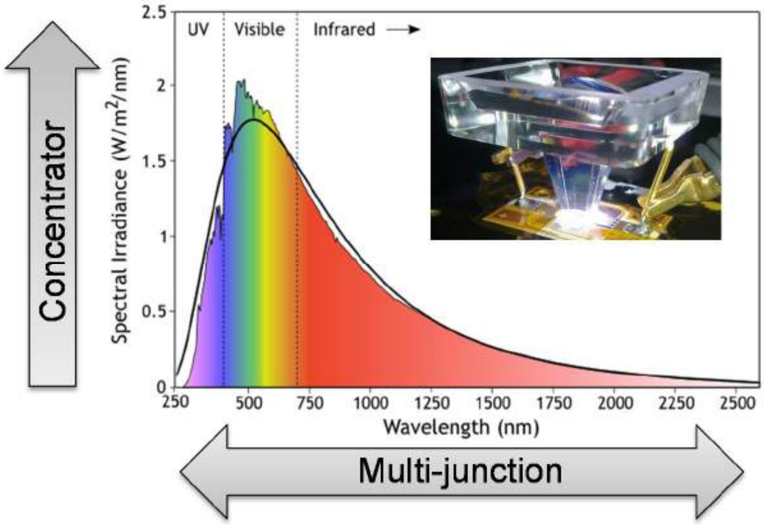

Figure 1.5 - Solar spectrum and Photograph of a multi-junction cell under a thousand of suns. Adapted from: http://publiclab.org and http://www.nanowerk.com

Therefore, a single junction cell catches only a small part of the emitted photons. A straightforward idea is to stack several materials with different gaps thus matching the global solar spectrum. The obtained cell is called a multi-junction cell.

The Y axis of the solar spectrum (**Figure 1.5**) is the intensity of photons. The intensity can be considerably increased by using a concentrator. The light is focused by different mirrors and is concentrated on the cell. Thus, some solar cells can work under an equivalent of several hundreds of suns. The current world record of solar cell efficiency (46%, Dec. 2014) has been obtained by Soitec and CEA-Leti, France, together with the Fraunhofer Institute for Solar Energy Systems ISE, Germany. The solar cell was based on four junctions absorbing the photons from 300 until 1750 nm under 508 suns.

1.1.4. Limits of the conventional PV

Currently, conventional PV panels in the market have efficiencies of about 15-18% with a performance guarantee of 20-25 years. The PV development pushed the scientific community to understand the limits of the solar cells efficiency. Different models, theoretical or semi-empirical were thus developed just after the publication of Chapin and coworkers in 1954. Two years after, J. J. Loferski et al. published a theoretical work on the prediction of the efficiency related to the gap of the semi-conductor.[12] In 1961, W. Shockley and H. Quisser published the “Detailed Balance Limit of Efficiency of p-n Junction Solar Cells”.[13] Most of the models, even recent, are inspired by this latter work. For a single junction, the maximum efficiency was calculated to be 33.7%. In 1980, A. De Vos calculated a maximum efficiency of 86.8% for an infinite number of junctions.[14]

Efficiency is not the only parameter which is relevant for the PV technology. The industrial fabrication of conventional PV modules requires the use of high purity silicon leading to the use of various not environmentally friendly chemicals and low yield processes.[15]

The adaptability and design of solar panels are more and more important criteria for the urban environment. Although the conventional silicon PV is nowadays popular on the market, the design of the panels is limited and the current panels look similar than the first created in 1954. The conventional panels are rigid and need to be oriented in a specific manner (45° oriented South-Est). Thus, the supports in the urban environment must be designed in consequence.

That’s why solar cells based on different materials with new design and properties were developed in parallel and have really emerged recently.

1.2. The emergence of a new class of PV

1.2.1. Organic photovoltaic: new properties, new applications

Figure 1.4 showed the emergence of new types of solar cells such like organic solar cells (OSCs). The difference is that the semi-conductors used are organic materials. The use of organic materials allows the fabrication of solar cells with new properties such as transparency, low weight and flexibility. The OPV modules are easily tunable (device geometry, color, size …) and therefore can be integrated in a large type of supports (**Figure 1.6**). The OPV module can be now adapted to the support which is the opposite for conventional PV modules.

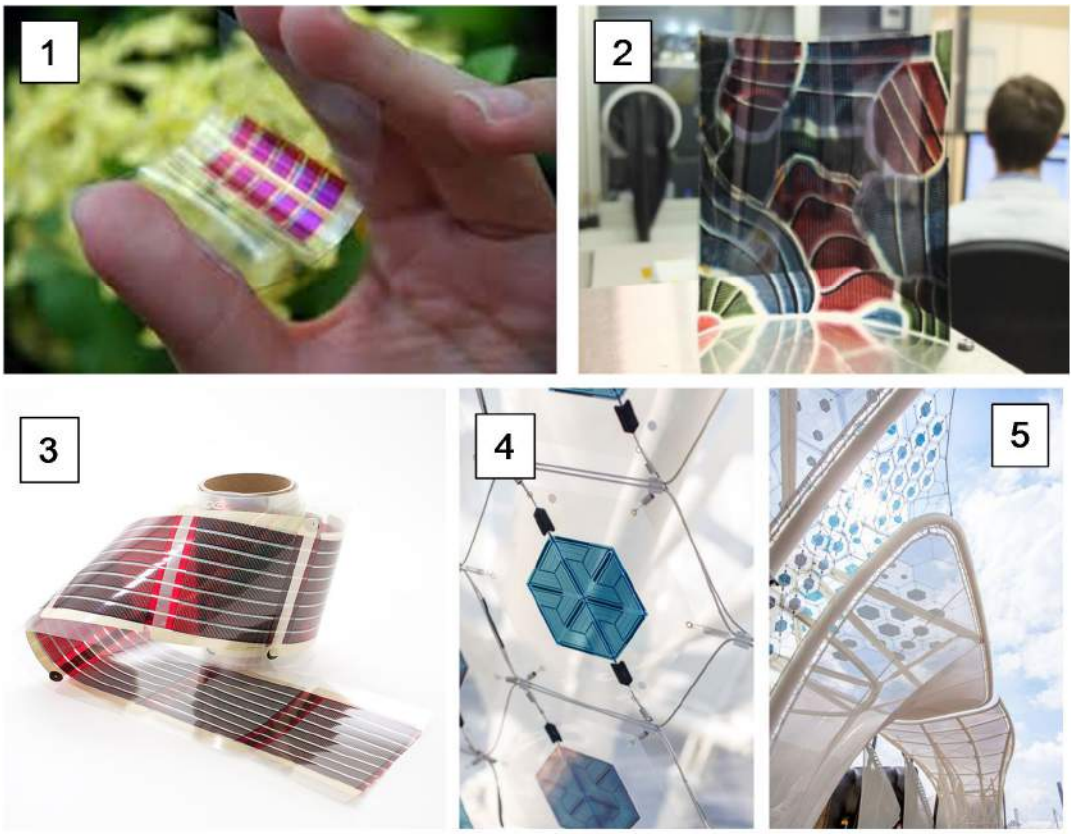

Figure 1.6 - Photographs of a standard OSC (1, extracted from http://www.ecofriend.com), the first polychrome solar module (2, extracted from http://www.energyharvestingjournal.com) made by Disasolar Compagny, modules from OPV infinity (3, extracted from http://infinitypv.com) and the blue flexible solar cells of Belectric compagny used for the Universal exposition in Milan 2015. (4 and 5, extracted from http://www.solarte.de)

Organic materials for solar cells applications absorb efficiently the incident light resulting in a very thin layer of active materials (~100 nm). Two of the main advantages are that the organic material can be casted on flexible substrates and the amount of material needed is reduced. The performance of OPV devices is less dependent of the intensity and the angle of the incident light compared to conventional PV systems. Additionally, OPV devices have an opposite behavior compared to conventional devices when exposed to temperature. Once exposed to sunlight, the temperature of devices can significantly increase, which has a negative impact on the performances of silicon solar cells while the performances of OPV systems are preserved or even slightly improved. One of the greatest advantages of OPV is that organic materials can be dissolved and formulated in inks and are therefore compatible with printing technologies thus giving the opportunity to produce devices with a potential low production cost.

1.2.2. Electronic structure and properties of organic materials for OPV

In this section, the origin of electronic properties of organic materials for OPV is reported. In the case of conventional solar cells based on crystalline semiconductors such as silicon, the solid is based on a 3D crystal lattices and all individual HOMOs and LUMOs interact strongly thus forming a valence and conduction bands respectively. In the case of organic molecules, the interactions between HOMOs and LUMOs are too weak to form valence and conduction bands. Thus, the electronic properties of semi-conducting organic materials can be described by the molecular orbitals theory. Let consider organic material family like polymers. Standard polyolefins such as polyethylene are based on carbon in the sp^3 configuration. (**Figure 1.7**) In this case, the valence of carbon is saturated thus forming two C-C sigma bonds and two C-H sigma bonds. Although saturated polymers are widely used for many applications, they are insulators and therefore not relevant for OPV applications.

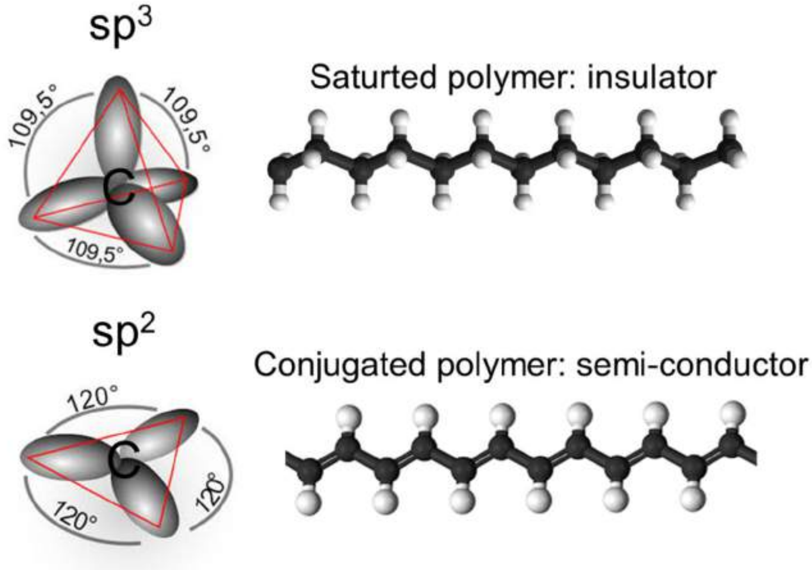

Figure 1.7 - Hydrides orbital in sp^2 or sp^3 configurations giving polyethylene (insulator) or polyacetylene (semi-conductor) respectively.

When carbons are in sp^2 configuration, 2 sigma bonds with carbon atoms and one with an hydrogen atom are formed. Therefore, one electron located on p_z orbital remains and can form a π bond with the neighboring carbon. A closer look at a C=C bond, as shown in **Figure 1.8**, reveals that the pi level is energetically isolated from the sigma level and is partially shared with the neighboring atom. For this reason, polymers or molecules based on sp^2 carbons have unique electronic properties.

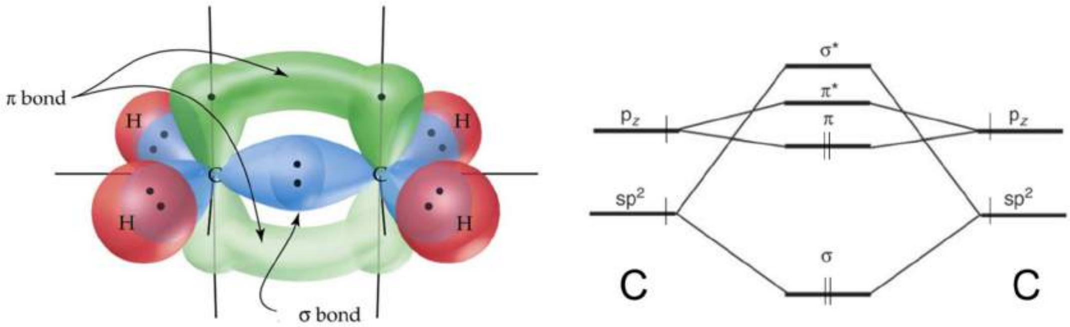

Figure 1.8 - Representation of orbitals in ethylene molecule associated to their energetic levels.

According to **Figure 1.8**, electrons can be promoted from the π level which is the Highest Occupied Molecular Orbital (HOMO) to the π* level which is the Lowest Unoccupied Molecular Orbitals (LUMO). The electronic π-π * transition in unsaturated polymers does not lead to bond breaking. Indeed, the sigma-sigma bonds are still intact and maintain the polymer structure. For the ethylene molecule, the π-π * transition is the most probable electronic transition and an energy of 173 kcal/mol (7.5 eV) is required meaning an incoming light with a wavelength of 165 nm. This transition is by definition impossible when sunlight is considered as incoming source of energy. Indeed, the solar spectrum starts at ~ 300 nm meaning 4.1 eV. In other words, the ethylene molecule is not able to absorb the photons of sunlight. By increasing the π conjugated system, the electrons can be delocalized through the polymer chain thus decreasing the π- π* energy transition. Thus, the HOMO and LUMO levels are modified resulting in a reduction of the gap. (**Figure 1.9**)

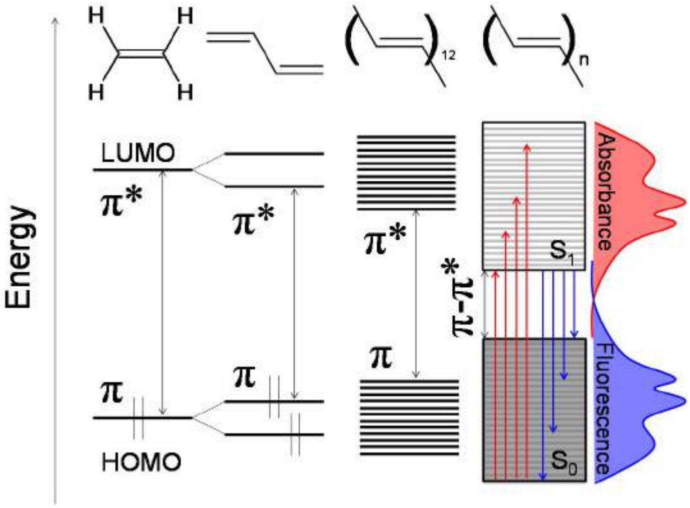

Figure 1.9 - HOMO and LUMO levels from the (ethylene) molecule to the (polyacethylene) polymer. The red arrows show possible electronic transitions (S_0-S_1) which define the absorbance of the material. The blue arrows are radiative transitions (S_1-S_0) called fluorescence.

Exposed to sunlight, electrons of the organic material from the singlet ground state (S_0) can be promoted to the singlet excited state (S_1). Different transitions are possible (S_0-S_1) defining the absorbance spectra of the material. Once excited, the electrons can reach the lowest level of S_1 by non-radiative relaxation (vibrational relaxation). Then, radiative transitions from the excited singlet state to the ground states are possible and correspond to the fluorescence spectrum of the material. Thus, π conjugated molecules and polymers can absorb photons in the sunlight domain which is the first requirement for materials used for photovoltaic applications. Other properties are required for having a good candidate for OPV applications such as, conductivity, energetic levels, morphology, charges mobility etc…

1.2.3. General device structure, principle and electrical characteristics

The general structure of an OSC is shown in **Figure 1.10**. Usually, a substrate (glass or plastic) is covered by a thin layer of conductive and transparent material like Indium thin oxide (ITO) which is the first electrode and a thin layer of organic semi-conductors is coated on top of it. The organic layer is also called the active layer as it is the layer in which the PV conversion takes place. The second electrode, such as aluminum (Al), is then evaporated.

The general principle of light conversion in OSCs is described in **Figure 1.10**. The light coming from the sun passes through the transparent electrode (ITO) and is absorbed by the organic material. The electrons are excited from the occupied (HOMO) to the unoccupied (LUMO) orbitals. Thus, electron/hole pairs (excitons) are created and need to be separated from the exciton state, and can lastly migrate in the device to reach finally their respective electrodes.

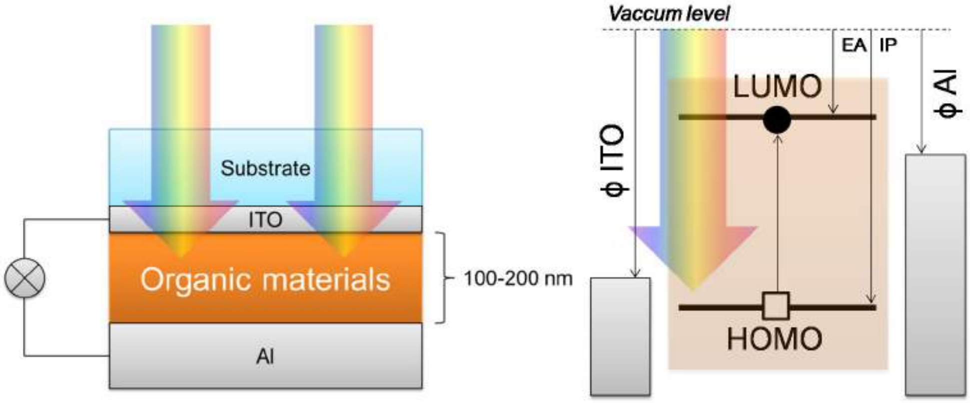

Figure 1.10 – A basic structure of an OSC (left) associated to the energetic levels of the different materials (right).

As previously mentioned, the first requirement of the organic material is to absorb the incident light. Once excited, the electrons can relax via fluorescence which is an undesired process for the light conversion. Indeed, electron must be transferred to the electrodes. That's why the materials (organic or electrodes) must have appropriate energetic levels depending on their electronic structures. The organic semi-conductor used has HOMO and LUMO levels while the electrodes are defined by their work function (WF). The WF is the energy between the vacuum

(E_{VAC}) and the Fermi level (E_F) and is a fundamental electronic characteristic of a metal or semiconductor. Thus, materials having a low WF are good materials for collecting electrons (or good barriers for holes extraction) and high WF corresponds to good materials for collecting holes (or good barriers for electrons extraction). Regarding the organic material, the energy between the LUMO and E_{VAC} is the electronic affinity (EA) and the ionization potential (IP) is the energy required for removing one electron and corresponds to the energy between the HOMO and E_{VAC}. Thus, an OSC is based on materials with appropriate energetic levels allowing charge transfers. Once the electron/hole pairs formed after light absorption, the electrons and holes have to be collected to their respective electrodes. For that, the WF of the electrode collecting the electrons must be low (close to the EA of the organic semiconductor) and the one colleting the holes must be high (close to the IP of the organic semiconductor) in order to match the HOMO and LUMO levels of the organic material respectively. **Figure 1.10** shows the energetic levels of the different materials of an OSC.

Once good materials selected, OSCs are tested and electrical parameters are obtained. The main electrical characteristics of an OSC are represented in **Figure 1.11**.

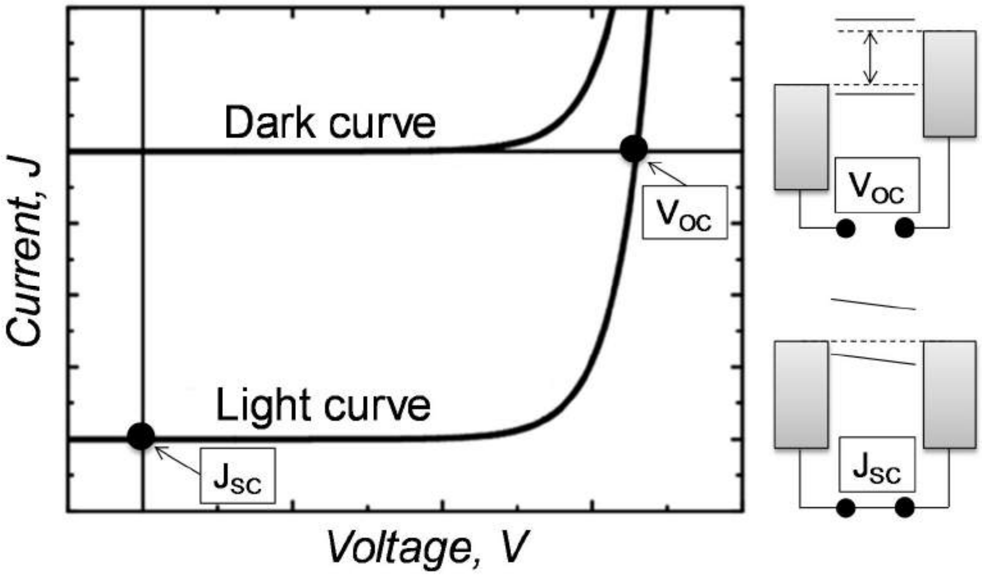

Figure 1.11 - Typical J(V) curve and main electrical characteristics of an OSC.

The dark curve contains information on the serial and shunt resistances and diode ideality of the device. Once illuminated, three main values can be extracted in order to calculate the device efficiency.

The short circuit current (J_{SC}) is the maximum current that can run through the cell when the cell is short circuited (V= 0V). The short-circuit current is due to the generation and collection of light-generated carriers from the organic layer.

The open circuit voltage (V_{OC}) is the maximum voltage difference attainable between the two electrodes when the current is zero. The V_{OC} corresponds to the amount of forward bias on the solar cell due to the bias of the solar cell junction with the light-generated current.

The fill factor (FF) corresponds to the available power at the maximum power point divided by the V_{OC} and J_{SC}. A solar cell can be considered as a particular type of diode. Ideally, a perfect solar cell corresponds to the curve 1 in **Figure 1.12** and can be described by the equation (1). In reality, solar cells have defects which can be considered by adding resistances in the circuit model (**Figure 1.12**). Parallel resistance (R_P) can model manufacturing defects or others which can lead to additional and undesired pathway of the current. Thus, higher is the R_P, better are the cell performances. The series resistance (R_s) corresponds to intern defects of the cell or wires. In this case, lower is the R_S, better is the cell efficiency. In realistic cases, R_P is < ∞ and $R_S > 0$. The FF is directly affected by the values of R_S and R_P of the cell. **Figure 1.12** shows the J(V) curves as function of R_S and R_P. Increasing R_P and decreasing R_s lead to a higher FF, thus resulting in greater efficiency. Thus, the generated current can be expressed by the equation (2) considering R_S and R_P.

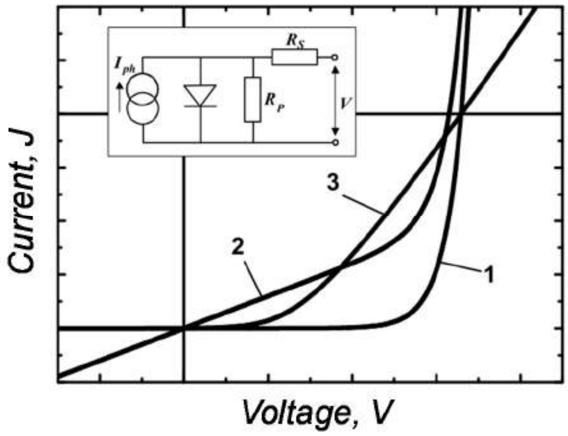

$$J = J_S \left[\exp\left(\frac{eU}{kT}\right) - 1 \right] - J_{ph} \quad \textbf{(1)}$$

$$J = J_S \left[\exp\left(\frac{e(U - R_S J)}{kT}\right) - 1 \right] + \frac{U - R_S J}{R_P} - J_{ph} \quad \textbf{(2)}$$

Figure 1.12 - J(V) curves associated to the electric circuit model. The curve 1 corresponds to a cell with a $R_P = \infty$ and $R_S = 0$ (ideal), curve 2 to $R_P = 30\Omega$ and $R_S = 0$ and curve 3 to $R_P = \infty$ and $R_S = 8\Omega$. Equation for an ideal solar cells (1) and adapted when the parallel and series resistances (R_P and R_S) are considered (2). J is the current, J_S is the saturation current, *e* is the elementary charge, U is the voltage, k the Boltzmann constant, T the temperature and J_{PH} is the photo current density.

Finally, the power conversion efficiency (PCE) is the most used value to compare solar cells. The PCE is defined as the ratio between the power obtained (P_{out}) on the incident power (P_{in}). P_{out} depends on the three main values previously described: V_{OC}, J_{SC} and FF.

$$P_{out} = V_{OC} x J_{SC} x FF$$

$$PCE = P_{out}/P_{in} = (V_{OC} x J_{SC} x FF)/P_{in}$$

The PCE depends of the incident light. Therefore, the conditions of measurement need to be controlled and specified. The common light emission standard used is the AM1.5 conditions. (Air Mass 1.5) It corresponds to 1000 W/m² (in UV-vis-IR domains) and is the same amount as what receives a sample on a tilted surface (37°) with a zenith angle of 48°.

The external quantum efficiency (EQE) includes the effect of optical losses such as transmission and reflection. However, it is often useful to look at the quantum efficiency of the light left after the reflected and transmitted light has been lost. Internal quantum efficiency (IQE) refers to the efficiency with photons that are not reflected or transmitted out of the cell and can therefore generate collectable carriers. By measuring the reflection and transmission of a device, the EQE curve can be corrected to obtain the IQE curve.

1.2.4. OPV development, history and main breakthroughs

OPV has emerged relatively recently (in terms of research and development and industrial applications) but the first tests of solar cells based on organic materials are not new. A part of the coming information have been extracted from the article of H. Spanggaard and F.C. Krebs where the history and the development of the OPV is reported.[16]

- *Discovery of photoconductive organic materials*

The development of OPV corresponds to the discovery of organic materials from which charges can be generated when exposed to light and then extracted. In other words, photoconductive materials are required. Photoconductivity in organic compound such as Anthracene was reported for the first time by Pochettino in 1906 and then Volmer in 1913.[17,18] Later during the 50s and 60s, a semi-conductor behavior was observed for several organic compounds such as methylene blue or phtalocyanine molecules. One of the first photo-conducting polymers used was polyvinylcarbazole (PVK) in the 50s. This latter was used by Hoegel et al. as an electophotographic agent and a report was published in 1958.[16] In the 70s, several polymers such as poly(sulfur nitride) and polyacetylene were studied and used as conducting materials when doped. In 1977, H. Shirakawa, MacDiarmid and A. J. Heeger published a paper on the synthesis of halogen derivatives of polyacetylene.[19] They received the Nobel Prize in 2000 for their work on conducting polymers which marked the real interest of the scientific community. Glenis et al. was one of the first groups to report the use of several types of polythiophenes.[20] By analogy to inorganic semiconductors, these organic semiconductors were first used in OSC devices as a single layer of organic semiconductors. The device performances were below 0.1 %.

- *Interface donor/acceptor*

The first and major breakthrough was patented by Tang et al. in 1979 and published latter in 1986.[21] This group obtained an efficiency of 1% with a bilayer solar cell. The interface between two semi-conductors leads to the formation of local fields at the interface, thus facilitating the dissociation of excitons. The importance of the donor/acceptor interface was thus born. At the same time, a class of organic materials was discovered and intensively investigated. This class is based on fullerene (C60) which has been firstly discovered by Kroto et al in 1985.[22] Considerable interests for C60 and particularly to its electronic properties in the solid state (high electron affinity, relative transparence in thin film and its good conductance) pushed C60 and fullerene to be a standard material for organic electronic applications. One of the first OSCs based on a polymer as donor and C60 as acceptor has been reported by Sariciftci et al. in 1993.[23] They demonstrated by photoexciton spectroscopy, time resolved photoluminescence and electron spin resonance measurements the existence of electrons transfer between the donor polymer and the acceptor C60. Moriata et al. worked on poly(3-alkylthiophene)/C60 based solar cells and published the same year.[24] Halls et al. investigated polyphenylvinylene/C60 based solar cells and published in 1996.[25] From models, they extracted a diffusion length of the exciton of 6-8 nm in the solid state. From these previous studies, it becomes clear that the interface between donor and acceptor helps the charges dissociation and strategies to maximize donor/acceptor interfaces, ideally in the exciton length range appeared and that the thickness of most organic materials should be in the range of 100-200 nm to get the optimal light absorption/charges extraction ratio.

- *The Bulk Heterojunction (BHJ)*

The second important breakthrough was the concept of dispersed heterojunction or bulk heterojunction (BHJ). The idea is to multiply the interface between donor and acceptor by mixing the two materials in a single layer thus maximizing the zone where excitons can be separated into free charges. (Red area in **Figure 1.13**)

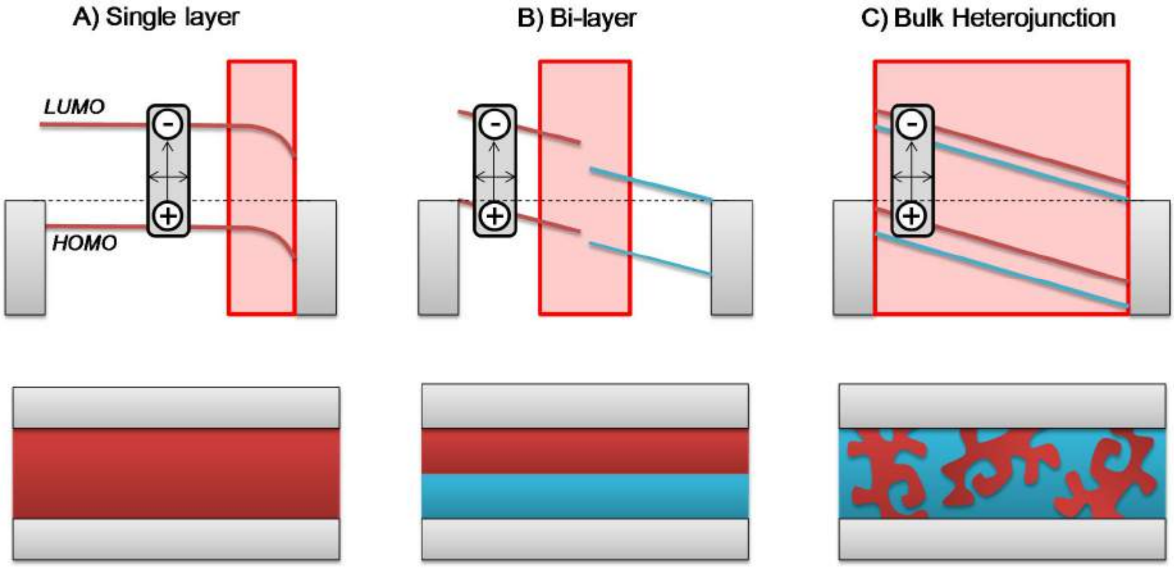

Figure 1.13 - Illustration of the energy levels in the case of a single organic layer (a), bi-layer donor/acceptor (b) and BHJ configurations (c). The red zone represents the depletion where the exciton can be separated by the difference of energy levels.

Thus, by optimizing the donor and acceptor domains at the nanoscale, close to the exciton length diffusion, significant improvement can be expected. However, the concept is restricted by the intrinsic poor solubility of the C60 in the usual solvent used for solubilizing the donor material. Thus, in 1994, the first dispersed polymer heterojunction solar cell was fabricated by Yu et al.[26] with a poly[2-methoxy-5-(2'-ethyl-hexyloxyj-1,4-phenylene vinylene] MEH:PPV/C60 (10:1 weight ratio). The solubility issue was solved by Hummelen et al. in 1995.[26] A series of C60 derivatives was synthetized with a high solubility in many solvents of interest. Thus, films with ratio of 80% C60 derivatives can be reached and devices in the range 2-3% of efficiencies started to be fabricated.

- *Toward the best BHJ morphology*

In the 90s, OSCs based on polymers (PSCs) appeared to have a real interest for the scientific community. PSCs of 2-3 % can be attained when the donor and acceptor materials form a single layer called active layer. The morphology of the polymer blend layer became a major topic for increasing the device performances. Theoretical calculations/models propose the Colum like morphology with the width close to the excition diffusion length (5-10 nm) as the ideal morphology. (**Figure 1.14**)[27]

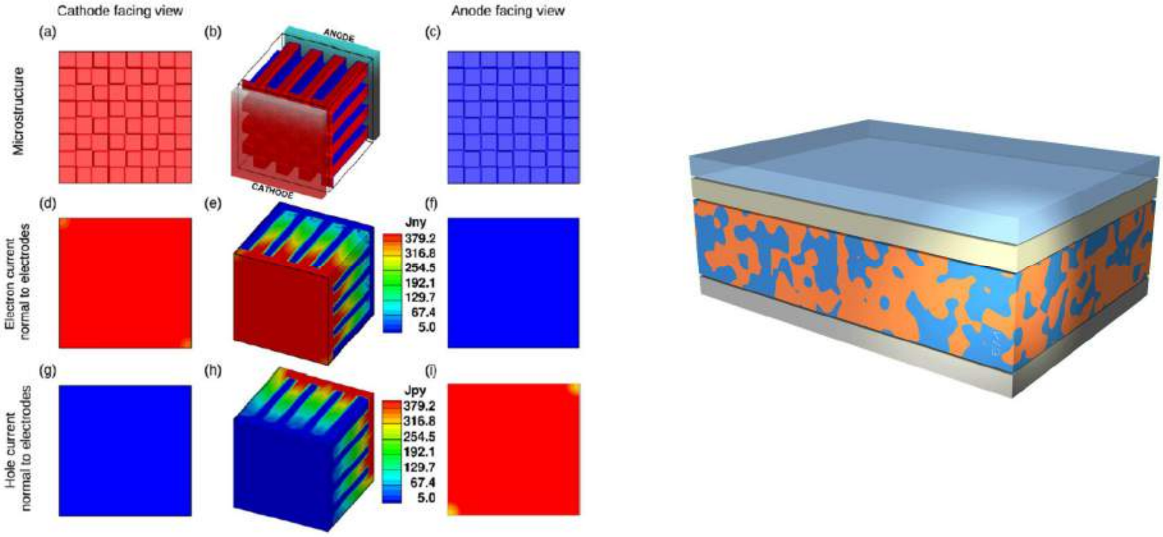

Figure 1.14 - Ideal BHJ morphology extracted from Kodali et al.[27] (left) and a realistic picture of a BHJ (right). Extracted from http://www.nanochemistry.it

In this ideal morphology, the size of each column has to be in the range of the exciton diffusion length (5-10 nm). The percolation pathway is necessary to extract the charges to the respective electrodes. Experimentally, this morphology is difficult to obtain especially when the process of film processing has to be as cheap as possible in order to be economically competitive. **Figure 1.14** shows a more realistic BHJ morphology obtained after casting materials from solution. Many groups work on the morphological aspects of polymer blend films in order to find solutions easily adaptable and with a potential low cost for controlling and improving the BHJ morphology. In practical, the BHJ morphology depends on many parameters that we can rank in three categories: formulation, processing and post-treatments.

The formulation step consists of selecting materials and solvents. Their intrinsic properties such as the chemical structure[28-32], physico-chemical properties[33-35] of the donor and acceptor materials as well as boiling point (Bp) of the solvents dictate the BHJ morphology of the dried film. Bartelet et al.[35] observed that higher the molecular weight is (In the case of the poly(di(2-ethylhexyloxy)benzo[1,2-b:4,5-b′]dithiophene-co-octylthieno[3,4-c]pyrrole-4,6-dione), so called PBDTTPD) higher the device performance is. Urien et al.[36] observed that region-regular P3HT gives better performances than region-random version. The self-assembly and crystallinity of the polymer blend packing is important for efficient charge transport. By changing one carbon atom for a Si atom, the polymer crystallinity was increased leading to a better charge extraction.[37] Many groups investigated the side chain variation of the polymer on the blend morphology and device performance. In this regard, a review of Mei et al.[28] has been published in 2013. The chemical structure of the fullerene derivatives especially regarding the adducts on the C60 has been also investigated and a review by Li et al.[38] has been published in 2013. The selection of the solvent(s) is also very important. By choosing several solvents in a controlled way, the BHJ morphology can be tuned and significantly improved [34,35,39-41]. Lee et al.[42] proposed criteria for the successful use additives. According to the authors, the additive must have a higher boiling point (Bp) than the host solvent and a selective solubility with the polymer or the fullerene derivative. Thus, the device performance can be significantly improved by adding 2-3 % of additive (in volume). Additives were then widely used for many polymer blend films and became an easy and efficient way to boost the device performances. However, side effects were later observed when additives are used.[40]

Regarding the processing step, the blade casting technique is considered as the most representative technique (lab scale) of the roll to roll technique (industrial scale).[43] Spin coating is a well-known technique used in many labs. Dip and drop coating can be also used even if the deposition of the thin film is less controlled. Spray and evaporation (in vacuum) are two techniques used for small molecules or metals.[44] By changing different parameters of any techniques, the morphology of the BHJ is impacted.[45]

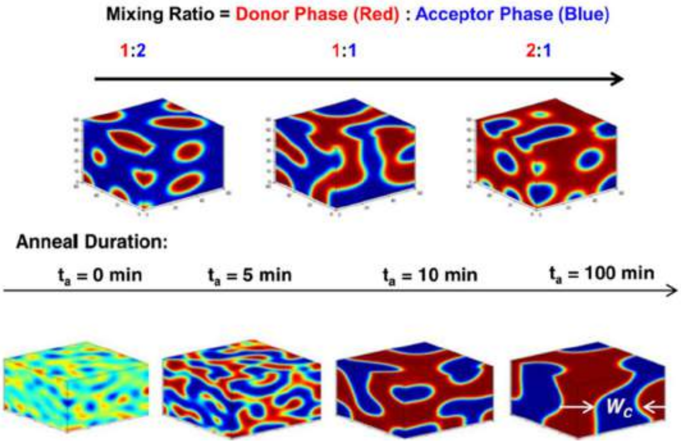

Figure 1.15 - Influence of donor/acceptor ratio and thermal annealing on the phase separation in a BHJ. Extracted from Ray et al. [46]

Concerning the post treatments, thermal annealing (in inert atmosphere in order to avoid oxidation) is the most used post-treatment process due to its simplicity. By far, the most famous polymer blend investigated was the P3HT:$PC_{60}BM$ blend.[47] Many groups worked on this active layer and optimized the formulation, processing and treatments. Different temperatures or time frames of annealing were investigated by different groups.[48-50] It has been demonstrated that in P3HT:$PC_{60}BM$ blend, $PC_{60}BM$ is thermodynamically sensitive and can diffuse in the solid film thus creating a phase separation. In general, a short thermal treatment (10 min / 120°C) increases significantly the device performance.[50] Solvent annealing is also a way to modify the BHJ morphology and can potentially improve the device performance.[51] The casted film is stored in a room with a controlled atmosphere saturated in the desired solvent.

- *New type of pi-conjugated polymers: the low band gaps (LBG)*

Besides the morphology, donor polymers such as MDMO:PPV or P3HT had a major issue which is sunlight absorption. Indeed, these polymers absorb only a small part of the incoming light. In the first decade of 2000, the appearance of new polymers allowed a broader absorption up to the infrared region. The group of M. Leclerc is one of the first to have synthesized “low band gap” (LBG) polymers. The structure of these polymers consists of a succession of donor/acceptor parts thus decreasing the global optical gap of the polymer. Thus, many groups in the world synthesized LBG polymers with various donor/acceptors combinations. In this new jungle of LBG polymers, PCDTBT, PCPDTBT and PBDTTPD were the most used and investigated. By using LGB polymers, the device performances have been substantially enhanced.

- *Interlayers*

The charge transfer at the interfaces is fundamental in OPV. The general structure of an OSC consists of an active layer inserted between two electrodes. When the energy levels are not optimal, energetic barriers are formed at the interfaces (electron and hole extraction interfaces). Thus, it has been demonstrated than the use of interlayers between the active layer and electrodes can significantly improve charges extraction (reduction of the energetic barriers).[52] A hole transport layer HTL (or electron blocking layer EBL) and an electron transport layer ETL (or hole blocking layer HBL) are two additional layers which constitute standard OSCs. More generally, these additional layers are also called anode buffer layer (ABL) and cathode buffer layer (CBL) and can be used for both OSC architecture. (**Figure 1.16**)

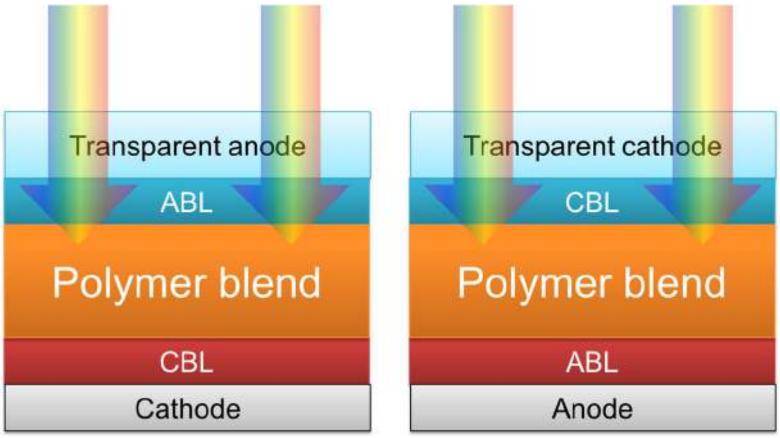

Figure 1.16 - ABL and CBL for normal and inverted OSCs.

Most of the HTL are organic and PEDOT:PSS is by far the most use in organic electronics.[53] The layer consists of a mixture of two polymers; the poly(3,4-ethylenedioxythiophene) (PEDOT) and the sulfonated polystyrene (PSS). This latter is an anionic polymer (balanced by sodium) and make the mixture water soluble. PEDOT:PSS films have good forming property and optical transparency (in the sunlight range). For inverted structures, the deposition of PEDOT:PSS (water based) on polymer:fullerne (hydrophobic) was problematic, due to the high surface tension. The problem was rapidly solved by changing the surfactant in the liquid. The high work function of PEDOT:PSS is ideal for holes transport and electrons blocking. Its polymeric nature makes the layer robust to mechanical deformation. Many scientific groups and industries studied the PEDOT:PSS in order to improve its conductivity, adhesion, process. Other HTL are used especially oxides such as MoO_3, V_2O_5 and other materials.

Due to its low work function and high electron mobility, ZnO is one of the most used ETL in inverted devices. ZnO films can be obtained from a precursor solution or nanoparticles from water or alcohol solutions. The conductance and electronic properties of ZnO strongly depends on the cleaning/post-treatment process or storage conditions.[54] Recently, aliphatic polymers were used as surface modifier of electrodes.[55,56] The most famous is probably the polyethylenimine (PEI). An ultrathin layer of PEI (4-6 nm) can significantly decrease the work function of a large number of electrodes. Thus, ITO modified by PEI can be use instead of ZnO. Zhou et al.[55] demonstrated the universal ability of aliphatic amine to produce low cost, environmental friendly and air stable low work function electrodes. Other ETL were studied such as TiOx, LiF or CsF.

- *OPV development, summary*

Even if the field is still under progress, tremendous efforts have been done in order to understand the complex mechanisms in OPV. **Figure 1.17** summarizes the main steps of the photo-conversion in OPV devices according to the main discoveries previously mentioned. The current device performance record is 11.1 %. (**Figure 1.14**)

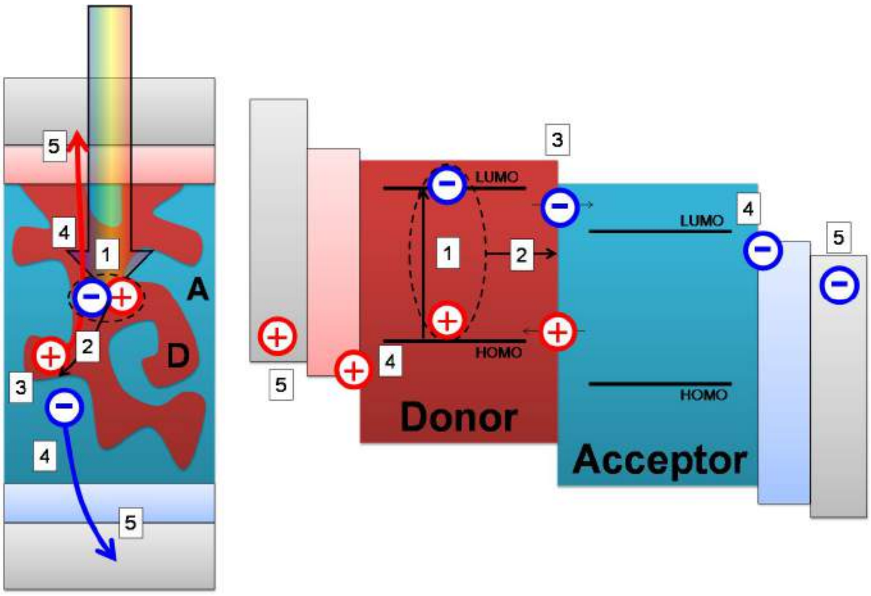

Figure 1.17 Full description of OSC principles: (1) formation of excitons by light absorption (2) exciton diffusion to the donor/acceptor interface (3) charges dissociation (4) charges migration thanks to the percolation pathway (5) charges collection.

1.2.5. What OPV needs to face now: efficiency, cost and lifetime

A schematic triangle was proposed by C.J. Brabec[57] pointing out the three criteria that OPV needs to fulfill to become a successful industrial technology: cost, efficiency and lifetime. **Figure 1.18** illustrates the general aspect of the conventional PV (SiPV) compared to the OPV technology according to the three criteria previously mentioned. SiPV is a mature technology with efficient and robust cells. Indeed, SiPV devices exhibit very little degradation of performance in the time. Although the silicon is relatively abundant, it initial purity significantly varies, and purification steps can be required impacting directly the final cost of the PV modules. Therefore, the rarefaction of good quality silicon will have a negative impact on the final production cost due to purification or doping processes. Additionally, some industrial steps are not environmentally friendly.

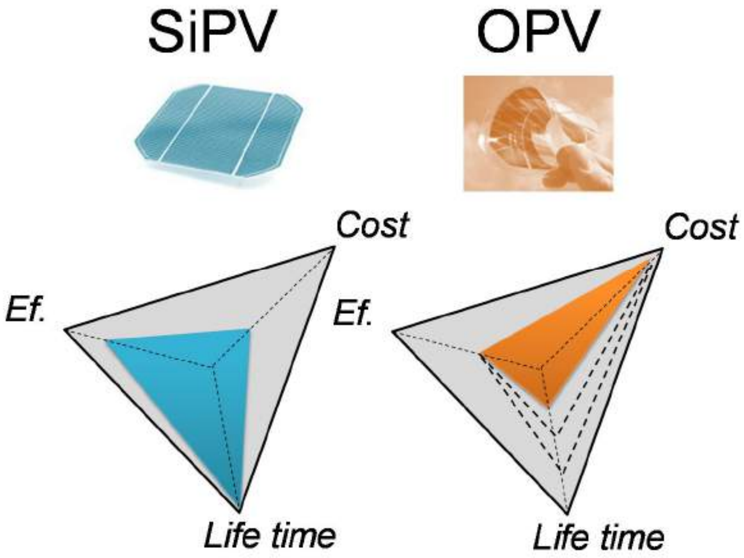

Figure 1.18 - Overview of SiPV and OPV in terms of efficiency, cost and lifetime.

The cost is the (potential) very good side of OPV as the amount of materials used is very low, and the devices printable making OPV a cheap industrial technology. According to some economical models[58], the part of the energy in the global Grow Domestic Product (GDP) is around 10% in USA and represents 15US$/GJ. This represents for a solar convertor of 15%, a total cost of 54 $/m² to manufacture. With the printing process, OPV has the potential to reach this value. It is important to remind that the three criteria cost, efficiency and lifetime cannot be separated from each other. Let consider a module of 15% which has a certain area. For producing the same amount of electrical power, a module of 10% has to have a higher surface meaning additional cost for the installation. (if we consider the same installation cost for both modules). Therefore, we need to have efficient modules in order to make the installation and the total cost of the technology attractive. The 15% performance is a target that many models consider as a minimum in order to make profits.[58] The current efficiency record for OSCs is 11.1% and was obtained with a tandem polymer based solar cell. Several models were proposed to estimate the maximum efficiency which can be obtained for OSCs, single BHJ.[59] The Schockley-Queisser limit model has been adapted for OPV by T. Kirchartz et al.[60] in 2009. They found a theoretical efficiency maximum of 23% for a polymer:fullerene based solar cell. These authors concluded that several reasons can explain the gap between theoretical and experiment results: The energy difference between the exciton and the charge transfer state at the interface with the acceptor, the optical losses, inefficient collection of exciton generated, high probability of non-radiative recombination and low charge mobilities.[59] The target of 15% efficiency seems to be very difficult to be obtained with a single junction. However, **Figure 1.19** shows that the targeted efficiency can be more easily attained by tandem solar cells.

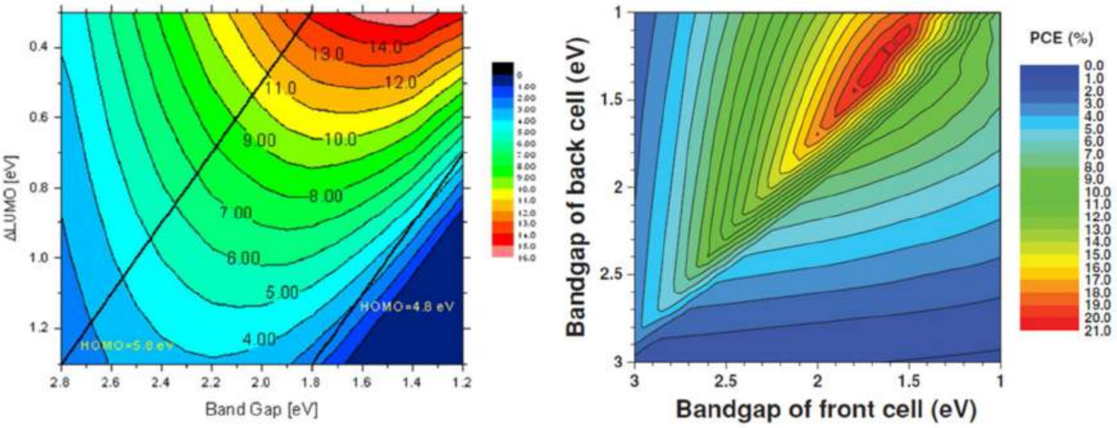

Figure 1.19 - On the left, theoretical efficiency for a single junction OSCs using $PC_{60}BM$ (LUMO 4.3 eV) , EQE of 80% and FF of 75% from Scharber et al.[59] On the right, theoretical efficiency for tandem OSCs for the same EQE/FF from Li et al.[61]

15% efficient device is interesting only if it remains stable in the time. Indeed, the cost-efficiency of a device strongly depends on the lifetime of the device.[62] According to the model proposed by McFarland[58], a solar convertor of 15% efficiency must cost up to 54\$/m² in order to fit with the cost of electricity (based on the price of electricity of 15US\$/GJ in USA in 2012). Let's consider an OPV system of 15% and 1 m² producing electricity from AM1.5 conditions (1000W) and produced with 54\$. The power electricity obtained is thus 150Wp which leads to a final price of 0.36US\$/Wp. With additional assumptions (Dennler et al.[62] and McFarland et al. [58]) the lifetime of a 15% device giving electricity 0.36US\$/Wp has to be close to 25 years in order to generate profits. Of course, it is difficult to estimate a minimum of lifetime as many assumptions are made and models are most of the time compared to silicon solar systems for roof applications. The cost also depends of the targeted application. It makes sense that the required lifetime of an OPV module inserted in the façade of a building has to be significantly longer than for nomad applications. **Figure 1.20** shows that stability was not the main interest of the scientific community in the past, but has recently grown. It is absolutely essential to get stable devices for a promising industrial future. This is not an option, this is a requirement. The coming section will focus on the stability in OPV.

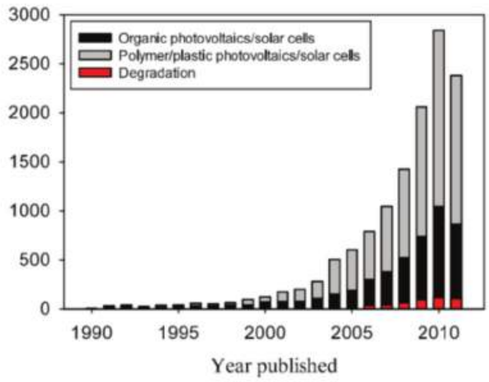

Figure 1.20 - Extracted from the review of F.C. Krebs et al.[63]

1.3. Stability in OPV

1.3.1. General aspects

The stability in OPV can be seen from different point of views. The interesting property is of course the power conversion efficiency (PCE). But it is very complex and difficult to know why or what is responsible of the drop of the performances. The starting point is probably to summarize the different components of an OSC and to which degradation triggers cells are exposed under operating conditions.

We have seen that OSCs are made from various type of materials: organic materials (active layer and buffer layers), inorganic materials and/or metals (electrodes and buffer layers) superposed in 5/6 thin layers. Under operating conditions, that is to say the outside environment, light, temperature, oxygen and humidity are the main actors which can play a role in the degradation of the device performances. Exposed to ambient air conditions, device lifetime is question of few hours. A first strategy is to avoid undesired agents which are responsible for the rapid degradation. That's why OSCs are encapsulated in a transparent packaging. Thus, diffusion of atmospheric oxygen and humidity can be avoided resulting in significant improvement of the device lifetime.[64] A clear dependence of the OSC architecture on the stability was observed. The standard structure has a low work function back electrode (usually aluminum or calcium) having the tendency to be poorly resistant to oxidation. In the inverted version, the back electrode (usually silver) is much more stable especially upon oxidation. Thus, inverted structure is a simple and efficient way to significantly increase the device lifetime.[63] Nevertheless, the lifetime depends on the barrier efficiency of the packaging which is directly linked to the cost of the material and therefore to the global cost of the device. Currently, it seems difficult to combine ultra-barrier and flexible packaging with low-cost. Additionally, from the synthesis to the industrial production, it is difficult to avoid any contact between the materials and the oxygen/humidity. Even minimized, the concentration of oxygen in the materials is enough to initiate degradation. As a conclusion, it is essential to focus on the packaging especially for having the best barrier/cost ratio, but also to investigate the stability of the materials which constitute OSCs exposed to ambient conditions. Stability in OPV is a major issue and very complex topic compared to conventional PV. Indeed, the organic materials are by nature sensitive to the operating conditions making the stability in OPV a very challenging topic.

1.3.2. Stability related to the donor material: pi-conjugated polymer

The photodegradation of the organic materials which compose the active layer is one of the main issues. By photodegradation, we can note that reversible and irreversible processes can occur.[65] The oxygen can interact with the conjugated polymer thus forming a charge transfer complex which was found to be fully reversible when the material is annealed. We are going to focus only on the irreversible degradation of organic materials meaning when new covalent chemical bonds are formed (i.e. modification of the chemical structure). Once exposed to light and oxygen, photochemical reactions can occur and influence the device performance. The photooxidation of individual donor polymers has been intensively studied in the past. Several mechanisms of degradation were proposed: radical mechanisms, superoxide formation and intervention of singlet oxygen.

- *The radical mechanism*

The radical mechanism of photo/thermooxidation of polymers is commonly described as a mechanism in three steps: initiation, propagation and termination (**Figure 1.21**).

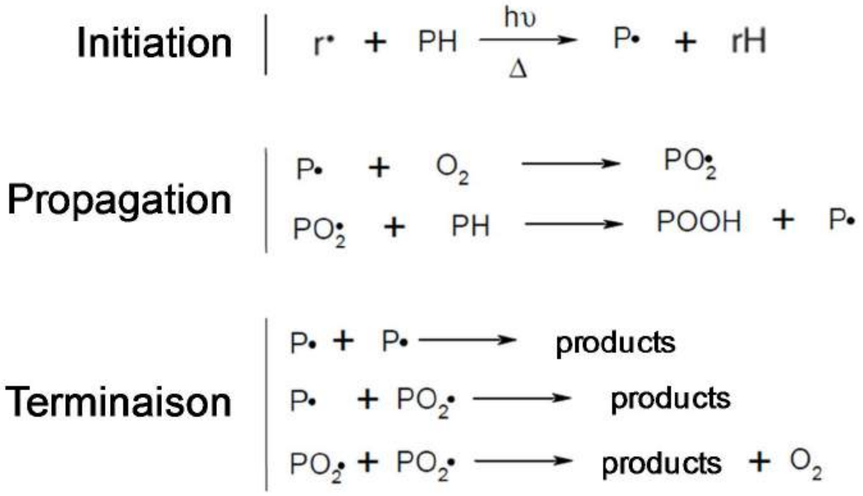

Figure 1.21 - Chain radical mechanism of oxidation for a polymer P.

The initiation step consists of abstraction of labile hydrogen atoms by free radicals (residues synthesis catalysis or defects, or from the polymer itself). Hydroperoxides then formed (primary oxidation products) can be thermally or photochemically decomposed leading to at the end of the chain oxidation process the formation of stable photoproducts such as carbonyl derivatives. This degradation process is the mechanism by which most of polymers (conjugated or not) degrade.[66-68] The first conjugated polymers for PSCs application i.e. polyphenylenevinylene (PPV) and poly[2-methoxy-5-(30,70-dimethyloctyloxy)-1,4-phenylenevinylene] (MDMO–PPV) were investigated by Chambon et al.[69,70] Infrared spectroscopy was used as a technique to follow the evolution of the chemical structure of the polymer film upon degradation. The photodegradation in air leads to the disappearance of the initial structure concomitant with the formation of photoproducts (identified/attributed by chemical treatments). Preferential degradation of the vinylene moieties were observed for both PPV and MDMO:PPV and a mechanism of degradation was proposed involving radical chain reactions from the ground state. (**Figure 1.22**)

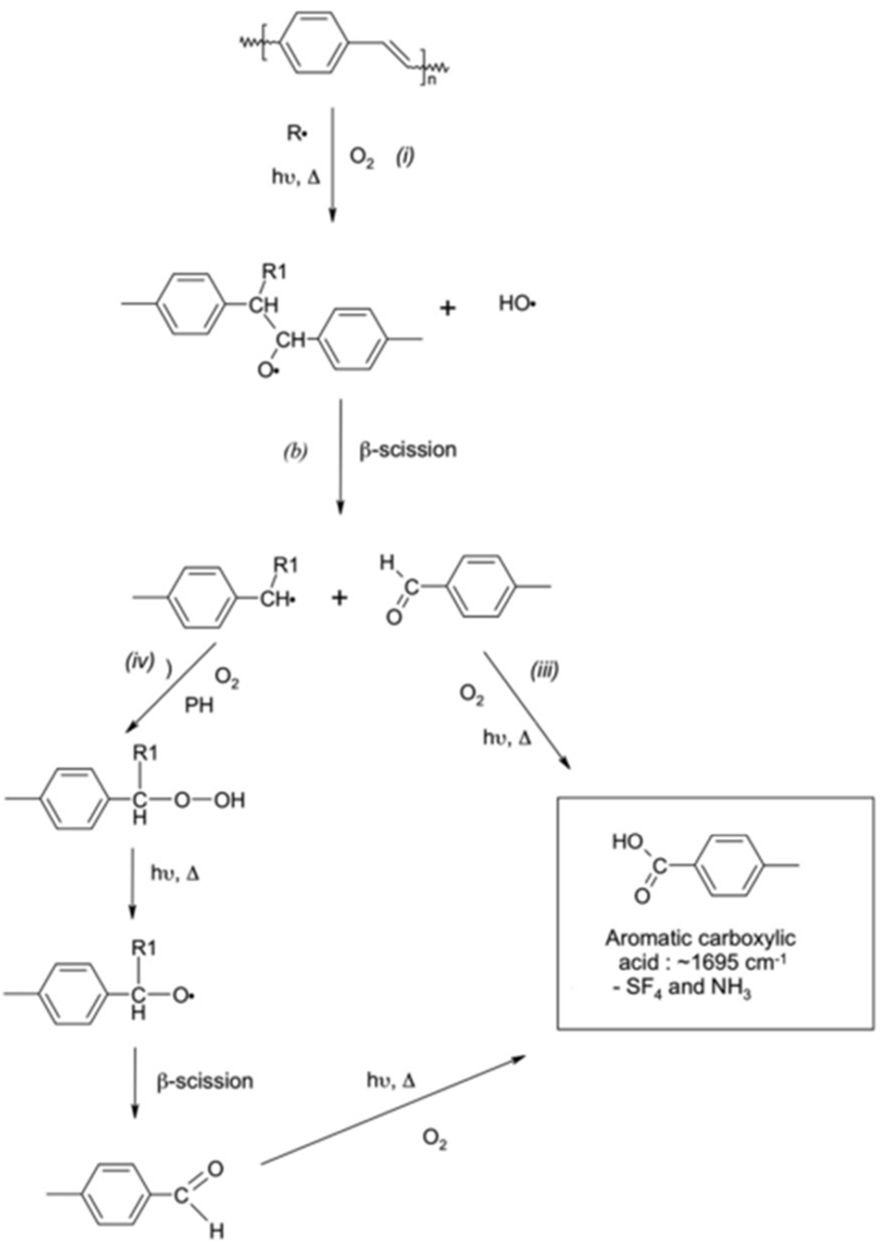

Figure 1.22 - Proposed mechanism of formation of the main photoproducts by Chambon et al.[70]

The stability of PPV and MDMO:PPV polymers were both relatively low and the complete disappearance of the polymer absorption was question of minutes when exposed to light and air. Then, poly(3-hexylthiophene) (P3HT) was the donor polymer at the center of most of scientific studies. The stability of P3HT was found to be significantly higher than that of PPV or MDMO:PPV.[71] This was attributed to the poor resistance of exocyclic double bounds of PPV and MDMO:PPV polymers. Although, the structure of P3HT was shown to be more stable than that of MDMO-PPV, the weak point of the structure was attributed to the side chain and especially to the labile hydrogen on the carbon atom in alpha position to the pi-conjugated system considered as the first site of the chain radical oxidation mechanism. The combination of spectroscopic techniques (IR and XPS) as well as chemical treatments allowed the following of the evolution of the chemical structure and a mechanism of photooxidation and thermooxidation has been proposed.[72,73] Hintz et al.[74,75] studied different environmental factors such as the light intensity, oxygen pressure or wavelength dependence. The photochemical and morphological behavior of low bang gap polymers such like the poly[9-(1-octylnonyl)-9H-carbazole-2,7-diyl-2,5-thiophenediyl-2,1,3-benzothiadiazole-4,7-diyl-2,5-thiophenediyl] (PCDTBT) or the poly[(4,4′-bis(2-ethylhexyl)dithieno[3,2-b:2′,3′-d]silole)-2,6-diyl-alt-(4,7-bis(2-thienyl)-2,1,3-benzothiadiazole)-5,5′-diyl] (Si-PCPDTBT) have been recently investigated.[76,77]

- *Intervention of singlet oxygen*

The involvement of singlet oxygen in the photodegradation mechanism of conjugated polymer is the object of controversy in the literature. The formation of singlet oxygen in presence of pi-conjugated polymers was well observed in the literature but the direct participation of the so-formed $^1O_2$ in the polymer photooxidation mechanism remains controversial. The production of singlet oxygen necessitates some conditions. After excitation $S_0 \rightarrow S_1$ and intersystem crossing $S_1 \rightarrow T_1$, the triplet state must be higher in terms of energy to expect a transfer of energy with the ground state of oxygen. Additionally, the lifetime of the triplet state of the conjugated polymer and then the formed singlet oxygen need to be long enough to expect a reaction. In the case of P3HT, the quantum yield of triplet formation was found to be very low thus making the formation of singlet oxygen very unlikely. However, Abdou et al. proposed the formation of singlet oxygen via the dissociation of an excited state charge transfer complex.[78,79] They discussed about the role of singlet oxygen in the mechanism of P3HT photodegradation. Manceau et al.[80] observed no involvement of singlet oxygen in the mechanism of degradation of P3HT.

1.3.3. Variables influencing the pi-conjugated polymer degradation, how to compare

The mechanism of degradation of individual polymers is important but it is also important to know why a polymer is more or less stable than another one. The question is now, how to compare different polymers? The UV-vis absorbance is usually the property which is followed during aging, as the first property of the pi-conjugated polymer is to absorb the incoming light. Thus, the intrinsic stability of pi-conjugated polymer can be defined as the rate of absorbance losses versus time of exposure. The direct comparison of absorbance losses for comparing the polymer stability is possible but important factors and precautions need to be considered. First, concerning the polymer film itself, Tromholt et al.[81] investigated the thickness/absorbance dependence on the intrinsic polymer stability. Thus, can be compared, polymers with similar pristine absorbance (considering similar extinction coefficient between polymers). Then, once polymer films prepared in order to have a fair comparison, the next point is about the conditions of degradation. It is important to compare the polymer stability in controlled conditions. ISOS protocols are available in the literature.[82]

- *Influence of the chemical structure*

Manceau et al.[71] screened the photostability in air of a large type of polymers based on different chemical structures. (**Figure 1.23**) These authors confirmed the poor stability of exocyclic double bounds of PPV/MDMO:PPV polymers and the better stability of chemical units without side chains. The results are in line with the studies of the Rivaton group: the proposed mechanism of polymer degradation is based on the radical chain degradation starting by the abstraction of labile hydrogens from the side chain. Although essential for the polymer solubility and processing, the side chains appear to be the weak point in terms of photostability. However, it seems not reasonable to consider the chemical structure as the only parameter impacting the polymer stability.

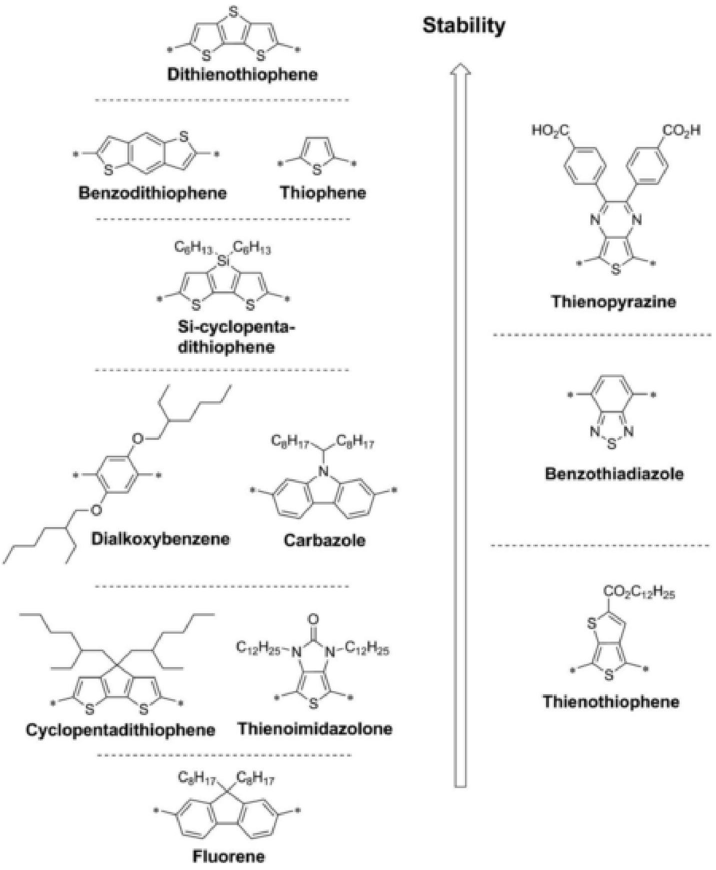

Figure 1.23 - Proposed order of photostability for various chemical structures (donor and acceptor units on the left side and right sides respectively) by Manceau et al.[71]

- *Influence of the physical properties*

Different photo-stabilities were found for two P3HT of different regioregularity.[74,83] The regiorandom one was more unstable than the regioregular one indicating that the polymer organization/packing and especially crystallinity has an importance on the polymer stability. The well-ordered or crystalline domains are more resistant to the oxygen diffusion.[83]

- *Influence of the process and morphology*

Thin films of PBDTTPD from the same polymer batch but processed differently can exhibit different photostabilities due to a change of the polymer packing and crystallinity.[84] By increasing the temperature when the polymer is in solution, the polymer pi-pi stacking is suppressed and therefore less stable is the PBDTTPD film when exposed to light and oxygen.

- *Influence of the synthesis and batch variation*

Kong et al. observed that in the case of PCDTBT, the device performance and lifetime (light and oxygen exposure) can be significantly improved by selecting only the longest polymer chains.[85] Indeed, they observed that the shortest polymer chains were rich in impurities/defects and act as charge traps which decreases the device performance but also the lifetime. These impurities and traps are probably source of radicals which can participate to the polymer degradation. McGehee et al. also observed for PBDTTPD based devices that polymer impurities are linked to the device performance and stability.[86]

1.3.4. Stability related to the acceptor material and the donor-acceptor blend film

As all organic materials, $PC_{60}BM$ suffers from chemical changes when exposed to light and oxygen. Taliani et al.[87] proposed a mechanism of C60 photooxidation. C60 is also known to be a radical scavenger and radicals can be directly trapped by the C60 moieties.[88] Reese et al.[89] observed that the oxidation of $PC_{60}BM$ leads to a shift of the LUMO level thus acting as electron traps.

When $PC_{60}BM$ is mixed with a conjugated polymer, it forms a polymer blend which is the active layer of OSCs. In a polymer blend film, $PC_{60}BM$ stabilizes most of the donor polymers. Enhanced stability was observed for MDMO:PPV, P3HT, PCDTBT, Si-PCPDTBT and probably many others polymers. Different possible mechanism can explain this stabilization: UV filter effect, excited state quenching and radical scavenging. Distler et al.[90] demonstrated that the filter effect is not the main mechanism responsible of the stabilization of P3HT by $PC_{60}BM$. Chambon et al.[88] shown that $PC_{60}BM$ stabilizes MDMO:PPV in the same manner in thermooxidation (compared to photooxidation). Thus, they concluded that the main mechanism of stabilization of the MDMO:PPV by $PC_{60}BM$ is likely the scavenging effect (no light-induced effects). Although $PC_{60}BM$ stabilizes most of the polymers, the factor of stabilization varies meaning that quenching and scavenging effects which are two mechanisms which require close proximity between polymer and fullerene depend most likely on the degree of phase separation in the film. Distler et al. found that for PCPDTBT, $PC_{60}BM$ decreases the stability of the polymer and when the polymer/fullerene phase are more separated, the effect of $PC_{60}BM$ is almost suppressed.[90] In some cases, $PC_{60}BM$ increases the degradation rate of the polymer. This was observed for PCPDTBT and PTB7 polymers.[90,91] For PCPDTBT, the triplet population increases when blended with $PC_{60}BM$.[90] The increase of the triplet state may initiate the degradation via singlet oxygen thus accelerating the degradation of the polymer.

- *Thermal stability of the polymer blend film*

The nano domains of $PC_{60}BM$ in the BHJ film tend to grow versus time with respect of the Ostwald ripening.[92,93] This effect is accelerated when the polymer blend film is heated. The optimal morphology is therefore not thermally stable and larger domains lead to increase the amount of exciton recombination. Recently, a review was published regarding the important impact of the polymer glass transition (Tg) on the polymer blend stability.[94] Intermolecular crosslinking is a straightforward way to freeze the BHJ blend thus avoiding molecular diffusion.

However, the reaction has to be controlled in order to avoid side effects which can affect the device performance. A first approach is the use of a modified polymer with specific ending groups attached on the side chain. Miyanishi et al. synthetized a crosslinkable P3HT with vinylene group attached on the side chain.[95] They observed a clear decrease of the $PC_{60}BM$ crystallization. Frechet et al.[96] used a P3HT-based copolymer and a low band gap copolymer bearing a bromide atom at the end of the lateral chain for cross-linking upon UV irradiation with efficient stabilization of the BHJ morphology. Crosslinkable groups were also attached on the acceptor material. Azide groups were used for crosslinking the fullerene. Finally, the use of small additives as crosslinkers was investigated. Derue et al.[97] demonstrated the selective reaction of the azide groups of a small molecule used as additive on the C60 moieties and efficient stabilization of the BHJ blend with no side effects on the device performance was observed. Finally a review regarding crosslinking in BHJ blend was recently published by Wantz et al.[93] They summarized the different approaches investigated in the past and concluded that the acceptor-acceptor crosslinking seems to be the most efficient strategy to stabilize polymer blend BHJ.

1.3.5. Stability and interfaces

As previously mentioned, additional thin interlayers are inserted between electrodes and the active layer in order to favor charges transfer and extraction. Thus, a standard OSC (normal or inverted structure) consists of a minimum of 5 layers and 4 interfaces. Additionally, the chemical nature of the layers is different, metallic for the electrodes, organic for the active layer and organic or inorganic for the buffer layers. Thus, many reactions/interactions, physical or chemical, can occur during the OSC fabrication and can evolve drastically upon operating conditions. So, the insertion of buffer layers has an impact not only on the initial performance but also on the device stability.

Regarding the ETL, several groups observed a clear role on the device stability. Kanai et al[98] observed a specific degradation of the organic materials of the active layer and ITO. By inserting a thin layer of MoO_3, this latter degradation has been avoided.[98] Wang et al.[99] observed an enhancement of the stability (storage in ambient air) when a CrO_x layer was evaporated between the aluminum electrode and the active layer. Li et al.[100] observed a stabilization of the P3HT:$PC_{60}BM$ layer versus photooxidation when a TiOx layer is deposited on the top (ETL in normal structure). Thus, it was suggested that TiOx layer tends to increase the lifetime of the device against UV and oxygen exposure. ZnO is one of the most used ETL in inverted devices but can also be used in normal structures. Ferreira et al.[101] observed a higher air stability of devices when a ZnO layer is inserted between aluminum and P3HT:$PC_{60}BM$ layer.

Concerning the HTL, the PEDOT:PSS is by far the most used organic material for organic electronic applications. The PEDOT:PSS consists of a mixture of two polymers, PEDOT and PSS ionic polymer water soluble. Formulation, additives and surfactant varies depending of the use of the layer. In an inverted structure, PEDOT:PSS in aqueous solution is deposited on the top of polymer blend layer which is hydrophobic. Thus, formulation of PEDOT:PSS was modified in order to have a good affinity with the active layer to optimize the process. However, the interface between PEDOT:PSS and active layer is still one issue. Dupont et al.[102,103] investigated the mechanical behavior of modules made by roll to roll process. Adhesion tests revealed that the weakest interface was the one between PEDOT:PSS and P3HT:$PC_{60}BM$. In another paper, they found that the interface with MoO_3 (instead of PEDOT:PSS) was even worse. They discussed on the role of the device geometry on the strength of the PEDOT:PSS/P3HT interface. They explained this role by the vertical phase separation of the PEDOT:PSS and P3HT:$PC_{60}BM$ during film formation. Thus, in a normal geometry, the PSS (ionic polymer) chains interfere with P3HT creating a dipole $P3HT^+/PSS^-$ making the interface stronger. In the inverted structure, P3HT is in contact with PEDOT and no interface dipole is formed.

1.4. Summary and motivation

The first part of this chapter 1 was about the development of the conventional PV which has been intensively investigated and became a mature technology. However, the conventional PV technology has some limits which reduce possibilities for more applications.

With the development of conjugated organic molecules and polymers, the OPV became a possible alternative and complementary technology to the conventional PV. The flexibility, transparency, potential low cost fabrication of the modules combined to the infinite possibilities of device design make the OPV very attractive. For some economical models, OPV is the only PV technology which has the potential to generate profits. However, the technology needs additional efforts from the scientific and engineering community to be a successful industrial technology.

One of the most challenging aspects is, the lifetime of the OSCs. We have reported in the last section of this first chapter that the stability in OPV is a very complex topic which needs indispensable scientific knowledge of different disciplines, photochemistry, physics and chemistry. Although, important efforts were recently done by the scientific community, degradation and stabilization of OSCs require additional investigations.

The present manuscript has the main objective to provide more understanding regarding the stability in OPV in various aspects:

We have reported that the chemical structure of the pi-conjugated polymers have a direct influence on material and therefore device stability. In particular, the side chains of pi-conjugated polymers although necessary for the good solution processing, play a key role in the polymer stability. (1.3.3) The aim of the Chapter 2 is to provide a better understanding of the role of the side chain structure of a series of low band gap polymers on stability at different levels: intrinsic photostabiliy of polymers in air (**2.2**), polymer blend thermal stability (**2.3**) and encapsulated device stability (**2.4**).

We have reported (1.2.4) that additives can be used to improve the BHJ morphology and enhance device performance. However, the most used additives have high boiling point and a part remains trapped in the thin film. The use of photo-stabilizers additives in OPV was poorly investigated. We have reported also that small molecules can be used as a thermal BHJ stabilizer. (1.3.4) The aim of the Chapter 3 is to understand the role of various “third components” on polymer blend stability. In a first part, the influence of residual additives used as BHJ optimizer on polymer blend photostability has been investigated (**3.2**). The use of Hindered Amine Light Stabilizers (HALS) molecules was studied for improving the polymer blend photostability in air (**3.3**). Finally, the insertion of a poly-fullerene (**3.4)** was tested as additive for improving the BHJ thermal stability.

Delamination is a known issue for OPV but remains relatively weakly investigated. It is known that in inverted device configuration the interface between PEDOT:PSS and the P3HT is the limiting interface in terms of adhesion. (1.3.5) The objective of the Chapter 4 is to give new insights into device delamination by identifying as precisely as possible the breaking points in inverted fresh (**4.2**) and aged devices (**4.3**). Strategies were proposed and tested for strengthening the layers adhesion.

The energy level alignment (ELA) between each layers are of main interest for optimizing device performance. (1.2.4) In inverted device configuration different materials can be used as electron transport layers (ETL) but little is known about ELA with the acceptor material and their influence of device stability. The Chapter 5 has the goal to investigate the ELA between various ETLs such as ITO, ITO/PEI, ZnO and ZnO/interlayers. The influence of ETLs on device photo and thermal stability was studied.

Chapter 2

Stability of polymer blend materials

2.1. Introduction to Chapter 2

The polymer blend materials constitute the active layer of a polymer solar cell (PSC). This layer consists of a mixture of a p-type polymer and an n-type material. The selection of the p-type polymer has a tremendous importance on the solar cell performance. Indeed, the three first steps of the solar conversion - which are i) light absorption ii) exciton dissociation (interface with the n-type material) and iii) holes transport to the interface with the hole transporting layer (HTL) directly depend on the choice of the p-type polymer. The chemical structure of a p-type polymer contains two different main parts: the pi-conjugated backbone and the side chains. The design of both backbone and side chain has been widely studied the last decade in order to get improvement regarding the device performance.[28-30,104] However, less is known concerning the impact of the p-type polymer structure on the photo- or thermal stability of the polymer blend films.

In this chapter, we focus on the stability of a series of low band gap (LBG) polymers with systematic side chain variation.

The first part of Chapter 2 addresses the relationship between side chain structure and polymer photostability (**2.1**). When exposed to the combination of light and oxygen, we show that the chemical nature of the side chain plays an important role on the photostability, but that additional parameters come into play. The study is then extended to the polymer blend (with $PC_{60}BM$, the acceptor material) films.

In a second part, the relationship between side chain structure and BHJ thermal stability is explored. We show how the side chain of the donor polymer impacts the thermal properties of the polymer and blend firstly, and the phase separation (polymer:fullerene) in the blend films secondly.

The final part is devoted to the relationship between side chain structure and device lifetime. Inverted devices (ITO/ZnO/LBG:$PC_{60}BM$/PEDOT:PSS/Ag) based on the polymer series were fabricated and encapsulated. Exposed to light, the lifetime of encapsulated devices is confronted to the photochemical and morphological behavior of the LBG:$PC_{60}BM$ layers.

Scientific contribution

The present work is the result of a collaborative work within the *Establis* project. The synthesis of the low band gap polymer series and the fabrication of OSC devices have been performed by Dr. Graham E. Morse (Merck Company). The experimental results regarding the relationship between the side chain structure and polymer photo-stability is supported by theoretical calculations done by Hugo Santos Sylva (ESR1).[105] The comparison of pi-conjugated polymers was extended with variation of the backbone structure was done Isabel Fraga Dominguez (ESR8). The Rapid Heat Cool Calorimetry (RHC) measurements were done by Maxime Defour, supervised by Prof. Bruno van Mele from the FYSC (Physical Chemistry and Polymer Science) research group.

2.2. Relationship between the side chain structure and polymer photo-stability

2.2.1. Introduction

In this part, we focus on the photo-stability in air of p-type polymers. The photostability of individual materials, especially the one of the most used pi-conjugated donor polymers for OPV application, has been investigated in the past: MDMO:PPV[69,106], P3HT[72,74], PCDTBT[76], PBDTTPD[84] and Si-PCPDTBT[77,107]. For each of these polymers, the side chain was evidenced to be the weak point in terms of photostability, responsible for the first step of the chain radical oxidation mechanism which provokes the degradation of the polymer. (**Figure 1.21**) The same conclusion regarding the effect of the side chain on the stability was proposed by Krebs et al.[63] However, the polymer side chains are necessary to render conjugated polymer soluble in organic solvents, for film processing and BHJ morphology optimization. In this regard, the Krebs group investigated the use of thermo cleavable side chains.[108] Thus, polymer films (with the side chains) can be prepared and a post-thermal treatment eliminates the side chains thus increasing the polymer photostability in the device. However, the device performances based on these polymers are fairly poor. Manceau et al.[71] tried to find direct correlation between polymer structure and photostability. However, it is important to remind that the photostability of polymers depends not only on the chemical structure but also depends on various parameters such as the morphology, impurities / defects / residues from synthesis and physico-chemical properties. (See 1.3.3)

In the present work, a series of low band gap polymers was designed with side chain variation on the same skeleton. The selected pi-conjugated backbone is a combination of benzodithiophene (BDT) and diketopyrrolopyrrole (DPP) units. (**Figure 2.1**) The side chain variation is also represented.

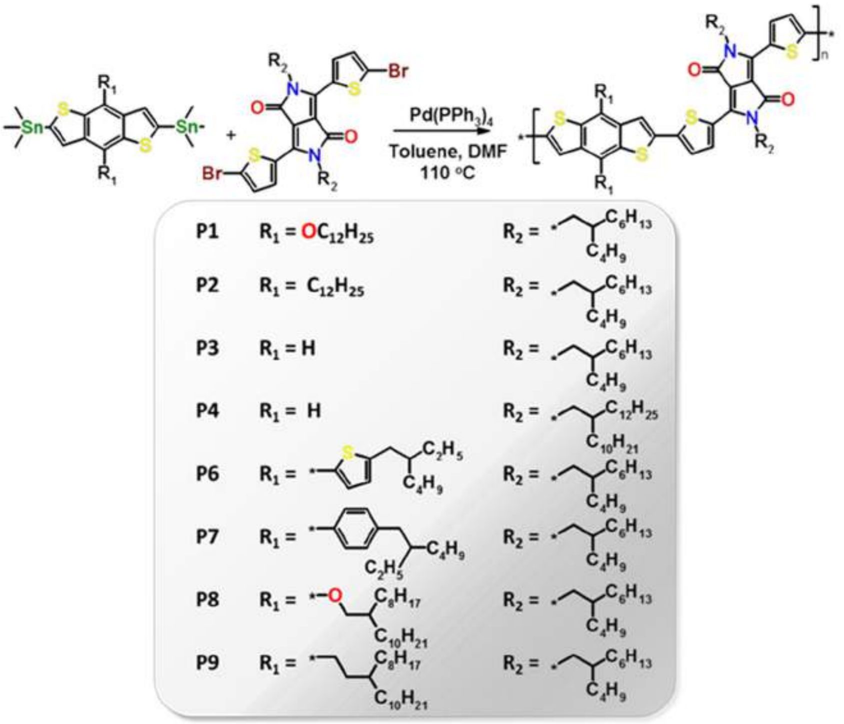

Figure 2.1 - Variation of side chains on R_1 and R_2 positions. R_2 remains constant except for P4 where the side chain has been extended for increasing the solubility. On R_1, no side chain (-H group, with $-C_2(C_4/C_6)$ and $-C_2(C_{10}/C_8)$ version), alkyl (-R linear and branched version), alkoxy (-OR linear and branched version) and aromatic (-ArR, thiophene and phenyl version) are attached.

Thus, the photostability of eight low band gap polymers (P1, P2, P3, P4, P6, P7, P8 and P9) was investigated with four types of chemical structures: no side chain (-H group, P3/P4), alkyl (-R group, P2/P9), alkoxy (-OR group, P1/P8) and aromatic (-ArR group, P6/P7). For the –H group, P4 has a longer R_2 side chain for increasing the polymer solubility. The –R and –OR group are composed of a linear and branched side chain version. Finally, the –ArR group is based on a thiophene and phenyl side chain. The polymer films were processed in order to be comparable and submitted to the same condition of degradation.[81] (See experimental part) Then, the role of the side chain structure on the intrinsic stability of the polymers was studied. As various other parameters are susceptible to impact the polymer stability, we also considered the pristine morphology and physical property (Mn, Mw, PDI) of the LBG polymers.

2.2.2. Experimental

Please, refer to the appendix (A1) for additional details on the experimental techniques.

- *Polymer synthesis*

The polymer series was synthesized and provided by Dr. Graham E. Morse (Merck) and the details are available in a paper recently published.[109]

- *Film processing and photostability evaluation*

All polymers were solubilized in orthodichlorobenzene (10 mg/ml) at 80°C. Thin films were obtained by spin casting the solution on glass and KBr substrates. The films were selected in order to have similar and comparable UV-vis absorbance. This is important as the thickness/absorbance influence the polymer stability.[81] The polymer films were exposed to the same condition of degradation, in ambient air (30−35% humidity) in a SUNTEST device (from Atlas) equipped with a xenon lamp. The light intensity was 750 W m^{-2} in the 300− 800 nm domain, and the temperature of the samples was ca. 42 °C.

- *Spectroscopy analysis*

IR spectra were recorded in transmission with a Nicolet 760-FTIR spectrophotometer working with OMNIC software. Spectra were obtained using 32 scan summations and a 4 cm^{-1} resolution. Changes in UV−vis spectra were followed with a Shimadzu UV-2101PC spectrophotometer equipped with an integrating sphere.

- *Morphological characterization*

X-ray diffraction analyses were made using a PANalytical X'Pert Pro diffractometer equipped with a X'Celerator detector and a Cu anticathode (Ka1/Ka2). The instrument was used in the θ-θ reflection mode, fitted with a nickel filter, 0.04 rad Soller slits, 5mm mask, 1/160° fixed divergence slit, and 1/32° fixed antiscatter slit. XRD data were measured over a range of 1e40° (2θ) with a step size of 0.0167° and a total counting time of about 3 h.

A Nanoscope IIIa atomic force microscope (AFM) from Veeco Instruments was used for surface topography measurement.

2.2.3 Results

- *Pristine characterization*

The typical absorbance spectrum (300-1000 nm) of one of the polymer series is shown in **Figure 2.2**. All the spectra of the series are available in Appendix (A2.1). The absorbance spectra consist of a maximum in the border UV/vis region (400 nm) and two main maximums in the visible region (690 and 760 nm).

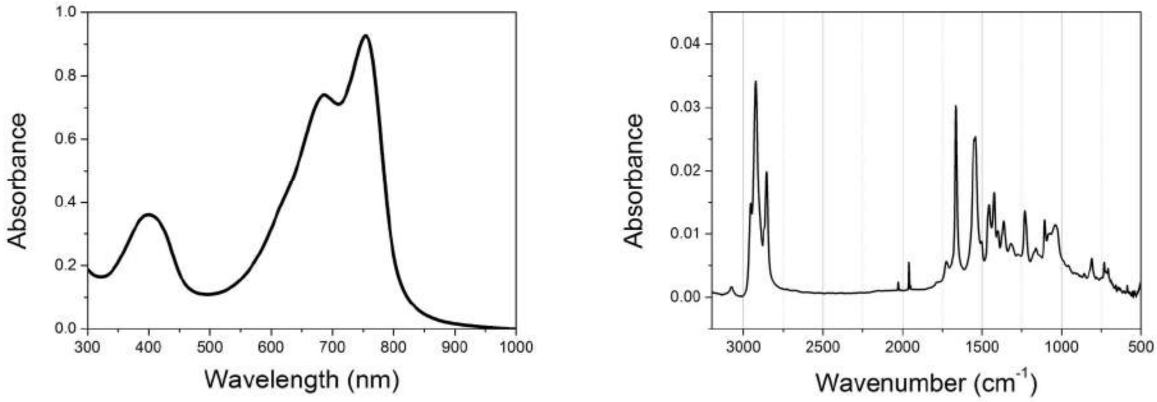

Figure 2.2 - Typical UV-vis (left) and IR spectra (right) of a LBG polymer. (P1 on KBr substrate in this case)

The IR spectra of the pristine polymer films are very similar as the entire backbone remains constant. A typical spectrum is shown in **Figure 2.2**. All spectra of the series are available in Appendix (A2.1). The attribution of the main IR bands can be done by using database literature[110,111] and comparing the spectra of all the materials. The attribution is summarized in **Table 2.1**.

The vibrational modes corresponding to the side chains are located in the 3100-2850 cm^{-1} (C-H stretching) and 1350-1100 cm^{-1} (C-H bending) regions. The C=O stretching of the DPP unit is assigned to the strong vibration at 1664 cm^{-1}. In the case of an amide group where the nitrogen is included in a ring, the C=O vibration appears as a doublet.[110,111] The double bands are visible in our case at 1727 and 1664 cm^{-1}. The pi-conjugated system can be directly linked to the bands at 1552 and 1542 cm^{-1} which are attributed to aromatic C=C stretching. Comparison between polymers within the series can help to determine some attributions. For example, by comparing P1 and P2 spectra, only two bands observed in the IR spectrum of P1 (1362 and 1036 cm^{-1}) are not present in the case of P2 and can therefore be attributed to the C-O stretching modes. In order to check if the synthetized polymers have the expected structure, we have calculated the ratio between the band at 2924 cm^{-1} (C-H stretching) and the one at 1542 cm^{-1} (C=C ring). The ratio makes our results independent of the film thickness and should reflect the amount of C-H bonds related to the alkyl side chain (IR in transmission). Except a deviation for P9, the C-H/C=C ratios are in good agreement with the number of carbons expected from the chemical structure (**Figure 2.3**).

Vibrational mode (cm^{-1})	**Attribution**
3076	C-H stretching
2955	C-H stretching
2924*	C-H stretching
2854	C-H stretching
1727	C=O stretching
1664	C=O stretching
1552	C=C ring
1542*	C=C ring
1459	CH_2 scissoring
1427	CH_2 in plane deformation
1362	C-O stretching sym
1320	CH sym deformation
1228	C-H bending
1162	C-H bending
1105	C-H bending
1036	C-O stretching asym
808	CH out of plan
732	CH out of plan

Table 2.1 - Attribution of the main modes of a thin film of P1. The modes at 2924 and 1542 cm-^{4} were used to monitor degradation kinetics.

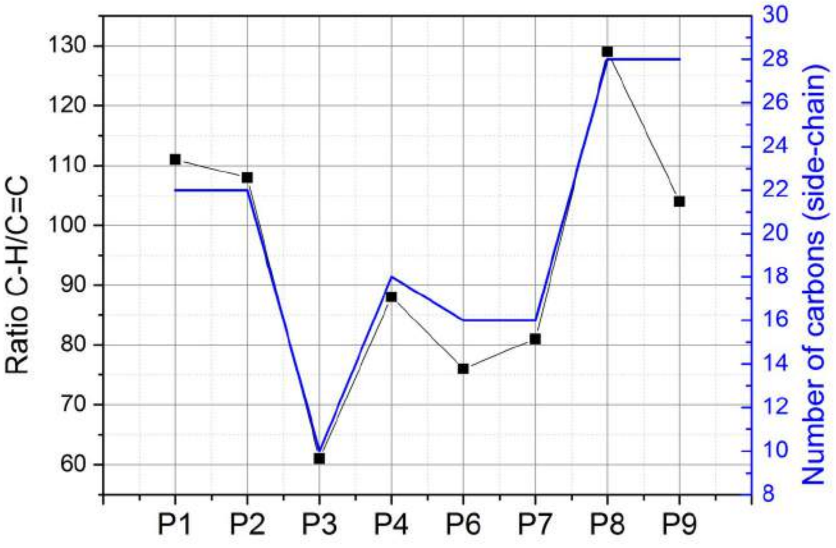

Figure 2.3 - C-H (area 3000-2755 cm^{-1}) / C=C (intensity at 1540 cm^{-1}) ratio obtained from IR spectra: experimental value (black), theoretical number of carbons of the side-chains (blue).

The pristine characterization is essential for the study of polymer photostability as it the identification of the most relevant datas. Besides the UV-vis absorbance, we have used the C=C mode at 1542 cm^{-1} to monitor the degradation of the conjugated system and the C-H stretching at 2924 cm^{-1} to monitor the degradation of the side chain.

- *Polymers photostability evaluation*

Figure 2.4 shows the procedure used to evaluate the photostability of the polymer series, using P2 as an example. All the spectra for all the polymers are available in Appendix (A2.4).

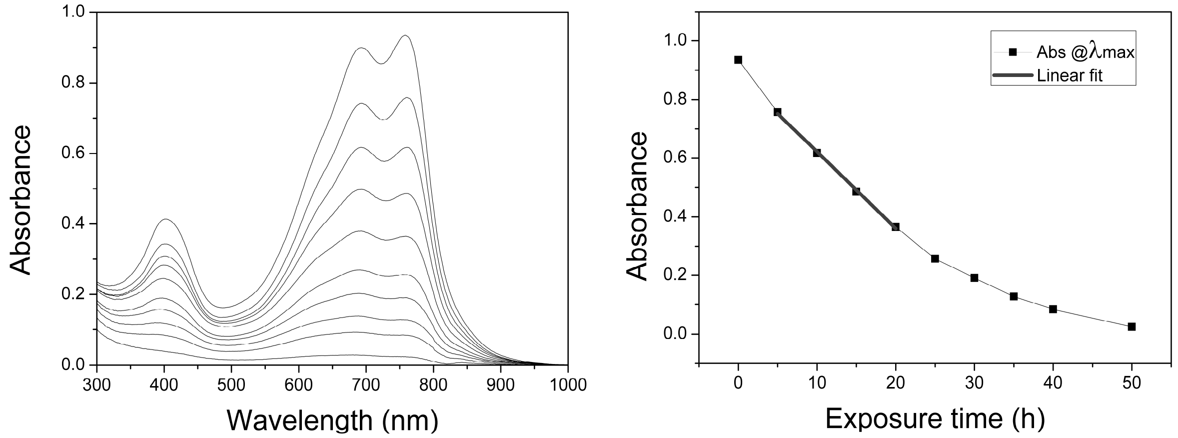

Figure 2.4 - Evolution of the UV-vis (300-1000 nm) absorbance along the exposure time (left). The photodegradation rate corresponds to the slope of the linear fit of the kinetic (right). Here are shown data obtained for P2 as an example.

As expected, the absorbance of all polymers decreases versus exposure time. This effect is irreversible and is a consequence of the evolution of the chemical structure of the polymers when exposed to the combination of light and oxygen. The evolution of the chemical structure was investigated by IR spectroscopy and all the individual spectra are available in Appendix (A2.3). Thus, for all the series, the concomitant decrease of the pristine structure and appearance of photooxidized structure (C=O envelope in the region 1900-1650 cm^{-1} and large bands at about 3200 cm^{-1} for the –OH function) was observed. (**Figure 2.5** and Appendix, A2.3)

Figure 2.5 shows the example of P7. P7 was chosen as it is the most unstable polymer and the complete degradation process is rapidly obtained. Thus, we can observe the concomitant decrease of the C-H and C=C bands intensity and increase of C=O bands in the 0-30h irradiation period. Then, C=O function reaches a plateau and C-H and C=C group have almost vanished (**Figure 2.5**, T>30h) corresponding to a loss of 94% of the absorbance. We can note the emergence of two bands after 50h of irradiation at 1108 and 616 cm^{-1}. These two bands can be attributed to the formation of sulfinate esters and were also observed to be formed for various thiophene based pi-conjugated polymers such as P3HT[72] or PCDTBT[76]. These authors observed the emergence sulfinate esters at the end of the photooxidation process indicating the high degree of polymer degradation as it corresponds to ring opening. The same behavior was observed for all the polymers suggesting comparable mechanisms, but differences in photodegradation kinetics were observed.

The photodegradation rate was extracted for all polymers as the slope of the linear fit of the UV-vis loss along the degradation time. (**Figure 2.4**, right) **Table 2.2** summarizes the measured degradation rates for all the polymer series.

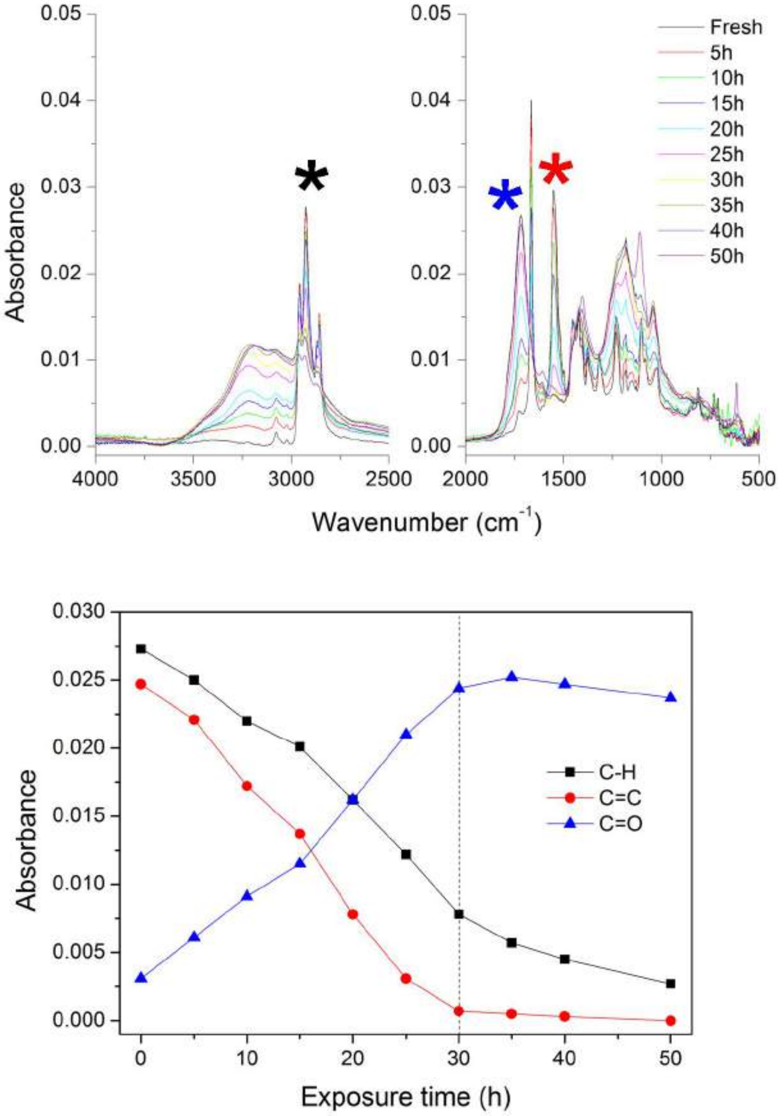

Figure 2.5 - Typical evolution of the chemical structure observed in the polymer series (here is the example of P7) with the decrease of the C-H (2924 cm^{-1}, **black**), C=C (1542 cm^{-1}, **red**) and increase of C=O (1718 cm^{-1}, **blue**) on the top. Kinetic of the C-H (2924 cm^{-1}, **black**), C=C (1542 cm^{-1}, **red**) and C=O (1718 cm^{-1}, **blue**) is shown on the bottom.

	P1	**P2**	**P3**	**P4**	**P6**	**P7**	**P8**	**P9**
R_1	$-OC_{12}$	$-C_{12}$	-H	-H	$-ThC_2(C_2/C_4)$	$-PhC_2(C_2/C_4)$	$-OC_2(C_8/C_{10})$	$-C_3(C_8/C_{10})$
R_2	$-C_2(C_4/C_6)$	$-C_2(C_4/C_6)$	$-C_2(C_4/C_6)$	$-C_2(C_{10}/C_8)$	$-C_2(C_4/C_6)$	$-C_2(C_4/C_6)$	$-C_2(C_4/C_6)$	$-C_2(C_4/C_6)$
Rate	11.7	26.1	2.8	7.3	41.8	41.9	2.4	10.0
Std.dev.	0.6	0.6	0.5	0.5	2.3	1.2	0.5	0.7
Rank	5	6	2	3	7	8	1	4

Table 2.2 - Photodegradation rates obtained from the UV-vis decay of the polymer series. The rank is from the most stable (1) to the less stable (8) polymer.

The polymers can be ranked from the most to the less stable as following: P8~P3>P4>P9>P1>P2>P6~P7. The next sections will concern the role of various factors which could (or not) explain this rank of polymer photostability.

- *The role of the side chain structure*

We first tried to correlate the photostability ranking with the structure of the side chains. **Figure 2.6** shows that the polymers without side-chain on the donor BDT unit (P3 and P4) are relatively more resistant than the other polymers.

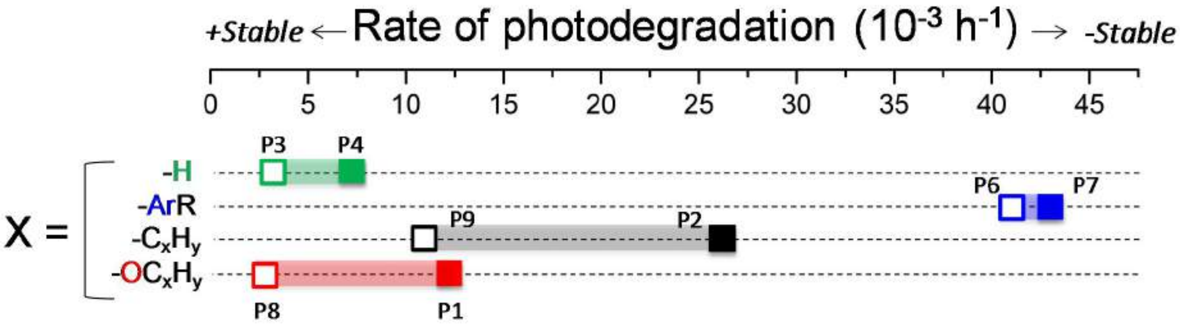

Figure 2.6 - Photodegradation rates associated to the corresponding structure of the side chain. In the –H group, P4 has longer side-chains (on R_2) than P3, P9 and P8 are the branched version of the –R and –OR groups respectively while P2 and P1 are the linear versions. P6 is the thiophene based side-chain and P7 is the phenyl version.

The most unstable polymers are P6 and P7 and correspond to the polymer with an aromatic group –ArR (with Ar = thiophene or phenyl) attached to the pi-conjugated backbone. Polymers with alkyl side-chains (P9 and P2) are globally less stable than the alkoxy version (P8 and P1), whether the chain is linear or branched. In –R and –OR groups, the branched side-chain is more stable than the linear version. Thus, at this step, taking only into account the chemical structure of the side chain, the polymers can be ranked from the most to the less stable as following: -H > -OR > -R > -ArR. The results are discussed in the coming discussion part (2.2.4).

- *The role of the morphology*

AFM and XRD analysis were performed on the pristine P1, P2, P4 and P6 polymers (one of each group: -OR, -R, -H and –ArR respectively). **Figure 2.7** shows the XRD patterns and data are compared to P3HT which is known to be a well ordered polymer in thin films. Unlike P3HT, the investigated series has no diffraction peaks. Only P4 exhibits a small peak at 4.2° (21.2A) corresponding to the interchain distance.

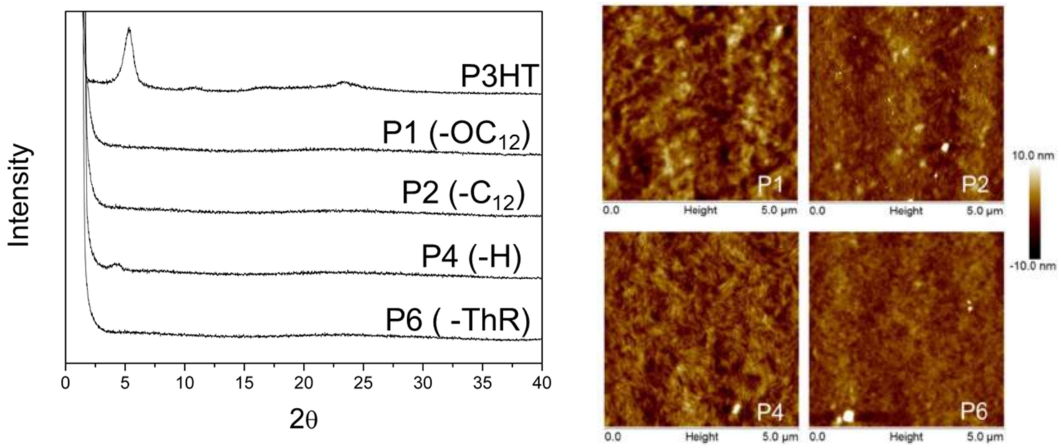

Figure 2.7 - XRD pattern (left) and AFM images (right) of P1, P2, P4 and P6.

AFM images show relative smooth and comparable surfaces for P1, P2, P4 and P6 with a rout mean square (RMS) of 2.2, 1.7, 1.8 and 1.6 nm respectively. We can note that a “grain-like” structure is visible for all the polymers to a greater or lesser extent. From these results, no significant morphological difference can be evidenced between the different side-chain groups.

- *The role of the polymer physical properties*

Polymers are usually characterized by their molecular number (Mn) or weight (Mw) and polydispersity index (PDI). Here, the properties of the polymers (Mn, Mw and PDI) are facing their respective photostability. (**Table 2.3**)

	P1	**P2**	**P3**	**P4**	**P6**	**P7**	**P8**	**P9**
Mn	40	93	*	32	130	*	25	82
Mw	130	320	*	72	730	*	55	190
PDI	3.4	3.5	*	2.2	5.5	*	2.2	2.3
Rate	11.7	26.1	2.8	7.3	41.8	41.9	2.4	10.0
Rank	5	6	2	3	7	8	1	4

Table 2.3 - Polymer properties Mn, Mw and PDI associated to their respective photodegradation rates. P3 and P7 were not soluble enough to perform GPC measurements.

The PDI is usually an indicator which reflects the electronic quality of conjugated polymers. [85] **Figure 2.8** shows a clear trend between PDI and photostability. Higher the PDI is and less stable the polymer is.

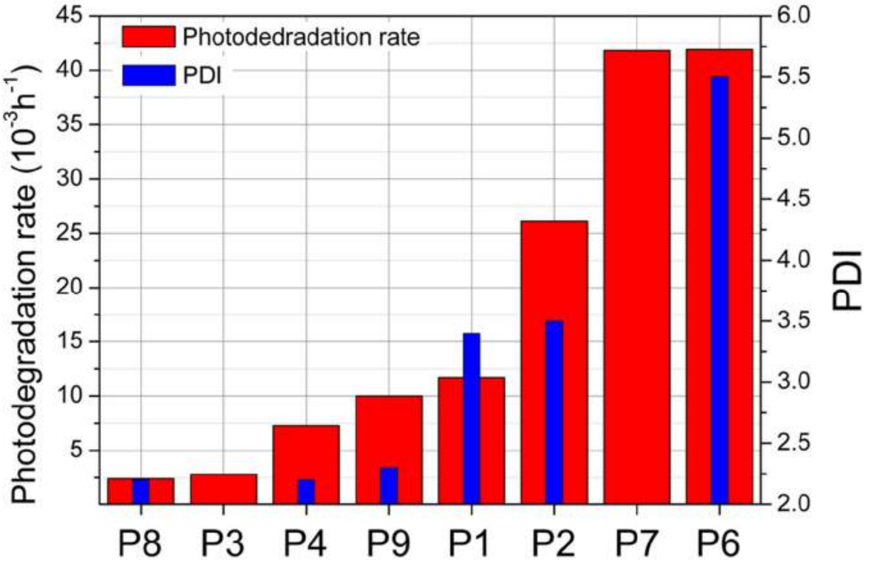

Figure 2.8 - Photodegradation rate of the polymers associated with their respective polydispersity index (PDI).

- *Effect of $PC_{60}BM$*

Then, the photodegradation study was extended to polymer blend films. For this investigation, we selected only one polymer of each type of side-chains: P1 (-OR), P2 (-R), P4 (-H) and P6 (-ArR). $PC_{60}BM$ was chosen as the acceptor for all polymer blend films and was added in 1:2 weight ratio (polymer:$PC_{60}BM$). Again, for a fair comparison, films were deposited in order to get similar initial absorbance (individual UV-vis and IR spectra are available in Appendix A2.2 and A2.5). The blend films were submitted to the same degradation conditions as those of the neat polymer films. Photodegradation rates were extracted using the same procedure as previously reported in **Figure 2.2**. **Figure 2.9** shows the effect of $PC_{60}BM$ on the polymer series.

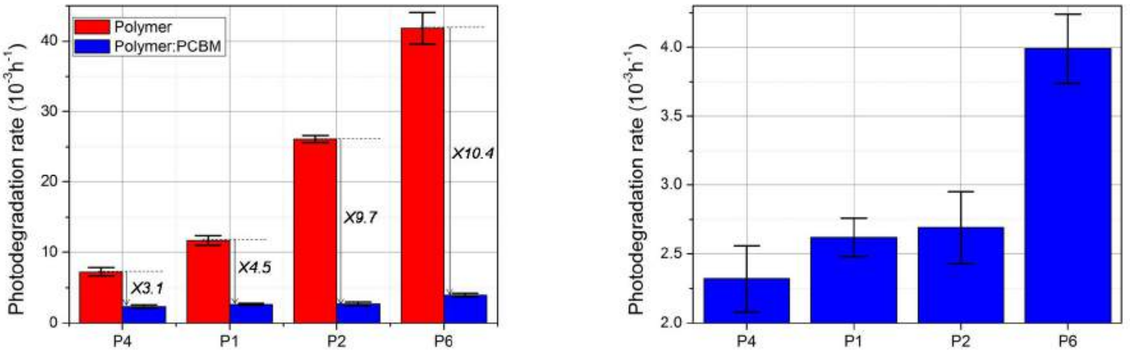

Figure 2.9 – Effect of $PC_{60}BM$ on the polymer photodegradation rates (left). Zoom on the polymer:$PC_{60}BM$ area (right).

$PC_{60}BM$ clearly stabilizes all the polymers. Although, the rank of stability remains unchanged (P4>P1>P2>P6 w/wo $PC_{60}BM$) the factor of stabilization significantly fluctuates. Indeed, the factor of stabilization was found to be 3.1, 4.5, 9.7 and 10.4 for P4, P1, P2 and P6 respectively. Interestingly, the factors are proportional to the intrinsic stability of the polymer. More unstable is the neat polymer, more effective is the $PC_{60}BM$ stabilization.

	P1	**P2**	**P4**	**P6**
Rate	11.7	26.1	7.3	41.8
Rank	2	3	1	4
Stab. fact. $PC_{60}BM$	4.5	9.7	3.1	10.4

Table 2.4 - Polymer photodegradation rates associated to the stabilizing factor provided by $PC_{60}BM$.

As the polymers and $PC_{60}BM$ absorb at different regions, we can compare the photodegradation rates of the polymers and $PC_{60}BM$. The two regions are shown in **Figure 2.10** (right) and the photodegradation rates were extracted as previously reported in **Figure 2.2** for both materials. The obtained photodegradation rates are reported in **Figure 2.10** (left). In the four cases, $PC_{60}BM$ degrades faster than the polymer. However, the degradation of $PC_{60}BM$ (evolution of the band at 334 nm) is not significantly different within the various blends, the difference being in the range of the error bars except for P6 where $PC_{60}BM$ degraded faster.

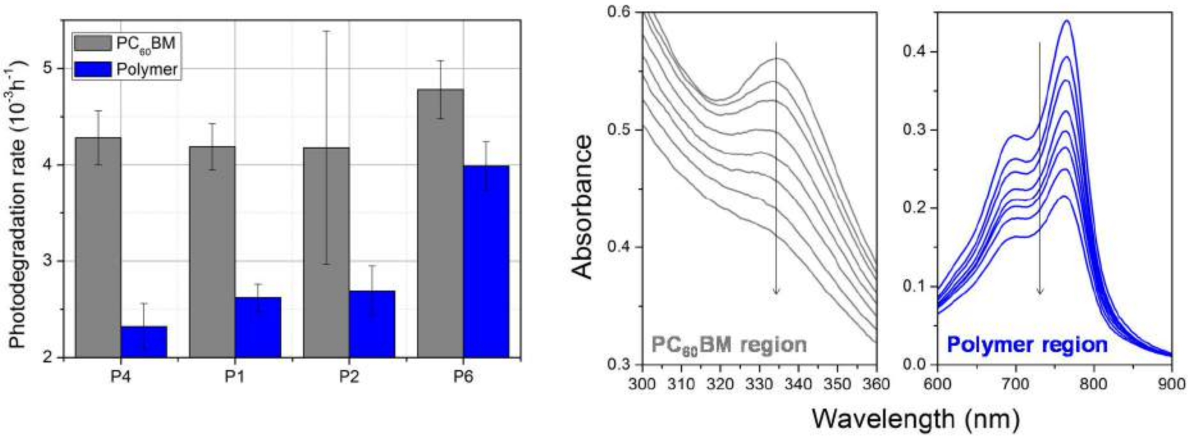

Figure 2.10 - Polymer (blue) and $PC_{60}BM$ (grey) photodegradation rates in the blend films (left) obtained from the decrease of the UV-vis spectra (left).

2.2.4. Discussion

From the results reported in the morphology section, it is obvious that the investigated polymers are amorphous with no well-organized structure, and are relatively similar whatever the side chain structure is. As described in the introduction section (1.3.3), it is known that the polymer order, and especially crystallinity, influences and enhances the polymer photostability.[112] In the investigated polymer series, we can exclude the morphology as the main parameter influencing the polymer stability.

On the opposite, from the results reported in the chemical structure of the side chain section, the nature of the side chain has an important influence on the polymer stability. The polymers without side chains P3 and P4 (-H) are the most stable. These results are in line with previous studies of the Rivaton group who pointed the side chain as the weak point of conjugated polymers in terms of photooxidative stability.[66,72,76] By suppressing the side chain (R_1), the polymer stability can be significantly increased. However, the suppression or restriction of the side-chain attached to the polymer results in a lower solubility which is a key point to optimize the BHJ morphology. Krebs et al. investigated the stability of conjugated polymers with thermo-cleavable side chains.[108] Although the polymer stability was improved, the device performances were quite low and the lifetime of the corresponding devices was not evaluated to our knowledge. Therefore, the suppression of the side-chain does not seem to be a viable strategy, and therefore the search of resistant side-chains appears to be essential. Our results show that the alkoxy side-chains render polymers more stable compared to alkyl side-chains. In order to find the underlying explanation, it is necessary to remind the basics of the chain radical oxidation mechanism of polymers. The mechanism has been described in details in a recent review of Rivaton et al.[66] The initiation step starts with the abstraction of the labile hydrogen atoms of the polymer. Then, the degradation process propagates by rapid reaction with oxygen. The impact of heteroatoms and especially the oxygen located between the conjugated skeleton and the side chain on the lability of hydrogen atoms has been recently investigated by Santos Silva et al.[105] The bond dissociation energy (BDE) has been calculated for various types of polymer structures. The calculations show that an oxygen atom in alpha position of the conjugated system stabilizes the polymer against radical attacks. This is due to the fact that for a fully carbonated side chain, the radical formed after hydrogen abstraction on the CH_2 group in alpha position is stabilized by the electronic delocalization of the complete pi-conjugated system. When an oxygen atom is inserted between the pi-conjugated system and the first CH_2 group of the side chain, the radical formed is not stabilized because the oxygen atom cuts the electronic communication with the conjugated system. Oppositely, we recall that the insertion of oxygen atoms in other positions of the side chain has a negative impact on the polymer stability (See Santos Silva et al.[105] for more details). In the present case, results obtained with the investigated series of polymer confirm the results obtained by Santos Silva et al. Indeed, the alkoxyl versions P1 (-OR linear) and P8 (-OR branched) are more stable than P2 (-R linear) and P9 (-R branched) respectively. At this step, we can explain why the polymer P3 and P4 (-H) are relatively stable and why the alkoxy side-chains are more resistant than the alkyl version. However, by only considering only the chemical structure of the side chain, we are not able to explain the reason why the –ArR group is less stable than the -R version and why the branched version are more stable than linear one.

From the polymer physical properties section, we have evidenced a clear impact of the PDI on the polymer stability. It is commonly accepted that a high Mw and narrow PDI result in a high electronic quality of the polymer.[85] Kong et al. recently observed that traps are located in the shortest fraction of the PCDTBT chain distribution.[85] These authors selectively extracted the high Mn fraction and fabricated devices based on that fraction. They observed better performances and more resistant devices against photooxidation due to the suppression of defects and traps located preferentially in the short polymer chains. Our present observation supports the idea that traps /residues /defects which constitute initial sources of radicals are probably more abundant when the PDI is high. Thus, as suggested by results reported in **Figure 2.6**, the PDI of the polymer in the studied series seems be a main factor which can influence the polymer stability. Looking in more details, the variation of PDI alone cannot however fully explain the differences in polymer stability. Indeed, when we compare P1 (-OR linear) and P2 (-R linear), the PDI is similar but a significant difference of stability was measured. The same comment is valid for P8 (-OR branched), P4 (-H) and P9 (-R branched).

Finally, we have shown in the chemical structure of the side chain and polymer physical properties sections that clear trends could be evidenced but that individual sections independently of one other cannot fully explain the variations in polymer stability. In the chemical structure of the side chain section, the difference of stability between linear and branched side chain was not fully explained as well as the difference between –R and –ArR groups. In the polymer physical properties section the difference between P1 (-OR linear) and P2 (-R linear) as well as the one between P8 (-OR branched), P4 (-H) and P9 (-R branched) cannot be explained by the variation of PDI. Thus, we have tried to combine these two factors, chemical structure and PDI. **Figure 2.11** shows the photostability of the different polymers associated to their respective PDI and side chain structure. We still observe the general trend dictated by the PDI. The section *i* corresponds to the –ArR (P6) polymer which is the most unstable polymer. We are now able to explain its poor resistance by the high lability of the hydrogen atom on the CH_2 in alpha position to the thiophene group (as for alkyl group) firstly and by its relative high PDI (unlike alkyl group) secondly. Section *ii* compares P1 (-OR linear) and P2 (-R linear). Both polymers are more stable than P6 probably due to their lower PDI. However, the PDI, very similar for both materials, cannot explain the difference of stability between the two polymers. But the difference of stability is fully supported by the discussion in the chemical structure of the side chain section which explains the higher resistance of the alkoxy side chain compared to the alkyl version. The same reasoning can be applied for section *iii*. P8 (-OR branched), P4 (-H) and P9 (-R branched) are globally more stable due to their relative low PDI and the difference of stability between these three polymers is mainly related to the difference in their side chain structure.

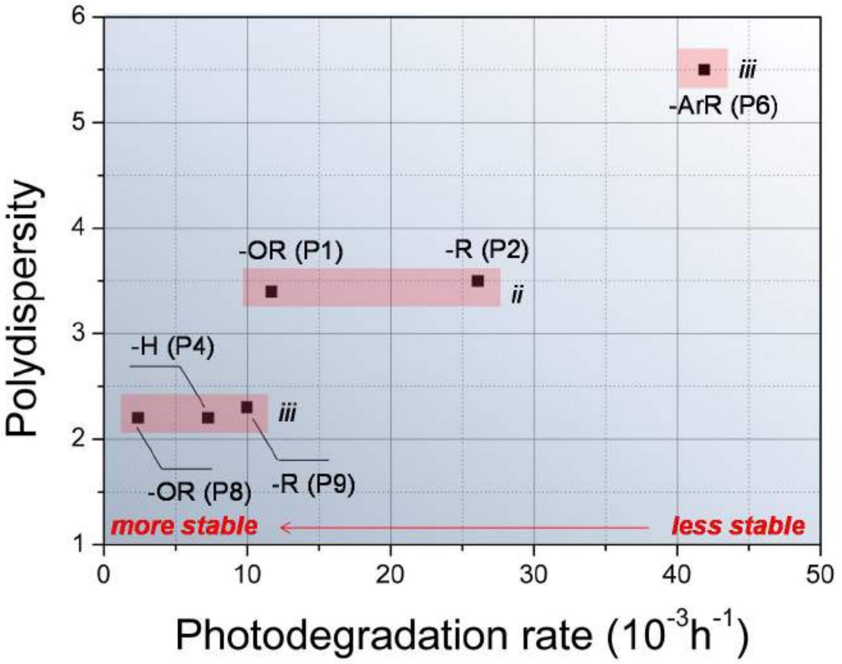

Figure 2.11 - Photodegradation rate versus PDI and associated to the side-chain structure.

Finally, in the effect of $PC_{60}BM$ section, we have shown that the fullerene derivative stabilized all the polymer series, stabilization effect usually observed for most of the conjugated polymers. The excited state quenching effect and the radical scavenger property of $PC_{60}BM$ are the two main properties responsible for the polymer stabilization.[88,90] However, our results show that the stabilization factor depends on the polymer and more interestingly on its intrinsic stabilities. Our results reveal that more unstable a polymer is, and more $PC_{60}BM$ stabilizes it in the blend. This can be a first explanation for the difference in the stabilization effect of $PC_{60}BM$. The mechanism of $PC_{60}BM$ stabilization requires a close proximity between $PC_{60}BM$ and the polymer. Therefore, a second possible explanation for the difference in the stabilizing effect provided by $PC_{60}BM$ could be related to its repartition, more or less homogeneous, within the polymeric matrix. Besides, it is interesting to note that $PC_{60}BM$ has a comparable stability when mixed with P4 (-H), P1 (-OR linear) and P2 (-R linear). (**Figure 2.11**) But $PC_{60}BM$ is slightly more unstable when mixed with P6 (-ArR), the most unstable polymer. Therefore, we could explain this by the fact that $PC_{60}BM$ intrinsically suffers from photooxidative degradation as any organic compound and is more affected when mixed with P6.

2.2.5. Conclusion

The evaluation and comparison of polymers in terms of photostability is complex and depends on many parameters. In the present work, we have compared the photostability of a series of polymer with the same backbone structure, with similar pristine morphology, processed in the same way and submitted to the same degradation conditions. We showed that the photostability of the investigated polymer series is dictated by two main factors, the chemical structure of the side-chain and the polydispersity (PDI) of the polymer. The nature of side-chain is related to the lability of the hydrogen atoms it contains versus radical attack. The PDI may be related to the amount of initial defects or impurities which can play an important role on the polymer photostability.

Thus, our results suggest that alkoxy side-chains are promising candidate for soluble and photo-resistant pi-conjugated polymers due to the protecting effect of the oxygen atom. Additionally, a low PDI appear to be a favorable factor regarding the polymer photostability as it probably corresponds to a low amount of defects/traps potentially source of fragile site versus the photooxidative process. Our results show that the stability of a polymer is dictated by its synthesis: the selection of the side chain structure and the control of the synthesis (influencing PDI) are crucial parameters.

2.3. Relationship between the side chain structure and BHJ thermal stability

2.3.1. Introduction

The bulk hetero-Junction (BHJ) morphology is one of the key parameters which impacts the device performance. The initial BHJ morphology is not thermally stable and phase separation occurs resulting in a drop of the device performances[93] (See 1.3.4 section). The phase separation is due to the diffusion of $PC_{60}BM$ molecules through the polymeric matrix. The difference of side-chain structure of the polymer can influence the diffusion of $PC_{60}BM$ molecules and therefore the thermal stability of the polymer blend. The side chain brings some sterical disorder which can restrict the $PC_{60}BM$ diffusion. Polymers are by nature not well ordered materials even if some polymers (conjugated or not) can crystallize.[94,113] Nevertheless, most of the pi-conjugated are amorphous but local organizations are possible. In order to get equilibrium conformation, structural conformation must take place and are thermally activated.[94] When a certain temperature is achieved, the polymer chains have enough energy to change their conformations. This temperature is called glass transition (Tg) and is an important characteristic of a polymer. Indeed, a polymer which has a Tg below the room temperature is in a rubbery state and has mechanical properties different to those having a Tg higher than the room temperature and which is therefore in a glassy state at room temperature. The concept of Tg has important impact for plastics in general, but also for pi-conjugated polymers. It is important to note that the creation of a binary system by the insertion of molecules such as $PC_{60}BM$ impacts the polymer chain assembly and therefore the Tg of a polymer blend is different than the neat polymer. According to several studies, P3HT has a Tg of about 12-14°C (may fluctuate with the method used or the polymer physical properties) and the P3HT:$PC_{60}BM$ (1:1) has a Tg about 40-50°C.[49,94,114] The Tg of the blend should be seen as a limiting temperature which should not be reached during the device fabrication.[94] Indeed, the diffusion of $PC_{60}BM$ through the polymer is facilitated when the Tg of the blend is reached resulting in agglomeration of $PC_{60}BM$ and a drop of the device performance.[94,115] The diffusion of $PC_{60}BM$ molecules is therefore more difficult in a frozen (glassy) matrix (below Tg). However, due to the fragile equilibrium of the polymer blend nanostructure, a sub-glass transition annealing can be in some cases enough to reorganize the BHJ and optimize the device performance.[116] It is known that change in the chemical structure of a polymer can have drastic influence of its Tg.[94] Thus, it has been observed that the Tg for MDMO-PPV and P3HT increases gradually when the side chain is shortened.[94] In general, the more complex and encumbered is the chemical structure of a polymer, more it is difficult to change chain conformation, and higher the Tg is.

Here, we investigate the role of the side chain structure of the donor pi-conjugated polymer on the thermal stability of Bulk heterojunction (BHJ) polymer blend films. As it was mentioned in the first part of the chapter, our series of low band gap polymers have different side chain structures and physical properties such has molecular number/weight (Mn/Mw) which can impact the Tg. We have selected P1 (-OR), P2 (-R), P4 (-H) and P6 (-ArR) polymers as they are based on different side chain structures and physical properties. (**Figure 2.12** and **Table 2.5**) In a first step, thin polymer films were fabricated and submitted to heating/cooling steps in a home-made chamber adapted to performing Raman spectroscopy in order to measure their respective Tg

(See Appendix A1 for details). Previous studies demonstrated that Raman spectroscopy is a powerful tool for investigating the glass transition (Tg) of polymer thin film.[117,118] The detection of Tg is based on the fact that the relaxation of polymer chains is accompanied by a change in the vibration modes observable by Raman spectroscopy. Thus, Liem et al. measured the Tg of polystyrene and conjugated polymers thin films.[117,118] In polymer thin film, the Tg depends on the film thickness and the interaction between the polymer chains with the upper (if confined) and lower (substrate) surfaces.[119] Thus, the mobility of the polymer chains can varies depending if the chains are in the bulk or at the interfaces resulting in an "interface Tg" and a "bulk Tg" .[119] Therefore, in our study we compare polymer thin film in the same way: comparable thickness and no upper confinement. UV-vis and AFM analysis were carried out before and after the heating/cooling steps in order to provide more information on the polymer reorganization. Then, the same experiments were performed for the polymer blend films (polymer:$PC_{60}BM$ 1:2).

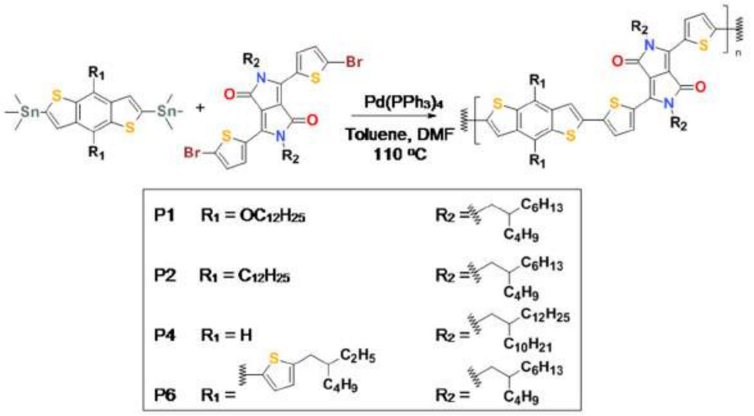

Figure 2.12 – Chemical structure and physical properties of P1, P2, P4 and P6.

	P1	P2	P4	P6
Mn/Mw	40/130	93/320	32/72	130/730
PDI	3.4	3.5	2.2	5.5

Table 2.5 - Physical properties of P1, P2, P4 and P6.

2.3.2. Experimental

Please, refer to the appendix (A1) for additional details on the experimental techniques.

- *Annealing setup (See Appendix A1 for details)*

The polymer blends were deposited on glass substrates and inserted on a heatable boron nitride plate in the home made chamber adapted for performing Raman spectroscopy. The temperature ramp was 1.5°C/min for heating and 4°C for cooling and Raman spectra were recorded along the heating/cooling steps between the room temperature up to 150°C. UV-vis and AFM analysis were performed before and after the heating/cooling steps.

- *Raman spectroscopy*

The acquisition parameters as well as the stability of the polymers upon Raman beam were checked out. The time of exposure was 15 seconds for 4 cycles per acquisition. The laser is an Argon beam (532 nm) and the incident power was lowered thanks to a filter. In inert atmosphere, the investigated polymers were stable enough for performing analysis thus excluding any degradation from the laser.

- *Rapid Heat Cool Calorimetry (RHC) (Maxime Defour, Physical Chemistry and Polymer Science)*

The RHC curves were obtained from the second heating at 500 K/min after cooling at 20° K/min. The slow cooling was used to allow potential crystallization whereas the fast heating was used to increase sensitivity and avoid reorganization of the morphology during the heating segment. Each experiment was done under inert atmosphere (helium) in aluminium crucibles.

- *UV-vis spectroscopy*

UV/VIS spectra were recorded in transmission mode using a homemade set up containing fiber optic, spectrometers from ocean optics (Maya2000) and a combination of deuterium and halogen lamps as light sources.

- *AFM*

A Nanoscope IIIa atomic force microscope (AFM) from Veeco Instruments was used for surface topography measurements. Images were obtained using the repulsive mode in intermittent contact, more commonly called the "tapping" mode. The RMS (root mean square) represents the standard deviation of the Z-axis values of a given surface.

- *Optical microscopy*

Film morphology was observed by an optical microscope (OLYMPUS, BH) equipped with a CCD camera.

2.3.3. Results and discussion

- *Thermal transitions of the pi-conjugated polymers series.*

We first focused on neat polymers to look at the impact of the side chain on the thermal behavior of polymers. Thin films (~150 nm) of P1, P2, P4 and P6 were prepared and placed in the home made chamber under inert atmosphere (See Appendix for details). **Figure 2.13** shows the evolution of the absorbance before-after the heating/cooling step (RT→150°C at 1.5°C/min and 150°C → RT at 4°C/min).

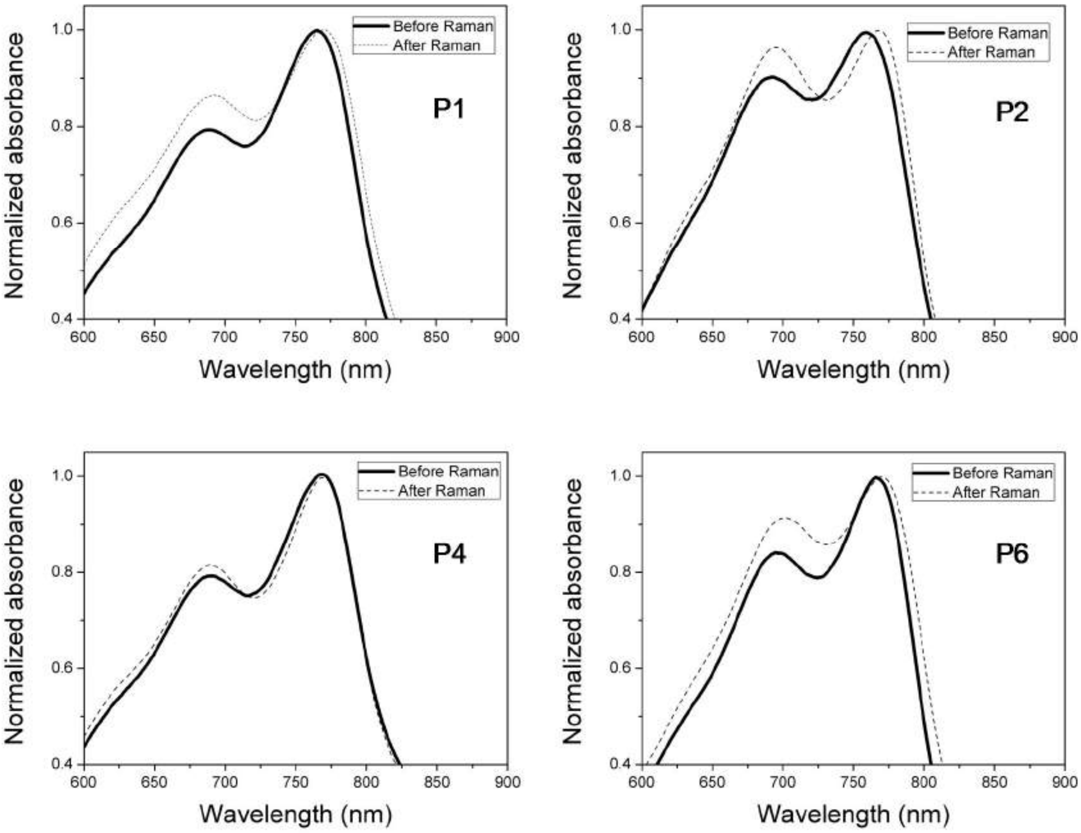

Figure 2.13 - Impact of the annealing step (RT→150°C at 1.5°C/min and 150°C → RT at 4°C/min) on the absorbance of P1 (-OR), P2 (-R), P4 (-H) and P6 (-ThR).

The UV-vis absorbance for the polymer series consists of two maxima in the visible domain. Spectra reported in **Fig. 2.13** show that the annealing step has an influence on the relative intensity of these two maxima, and that this effect is less pronounced for P4. Additionally, a batochromic shift, more or less important depending on the polymer can be observed (**Table 2.6**).

	P1	P2	P4	P6
Before	765 nm / 1.62 eV	759 eV / 1.63 eV	769 eV / 1.61 eV	766 nm / 1.62 eV
After	772 nm /1.61 eV	769 eV / 1.61 eV	769 eV / 1.61 eV	770 ev / 1.61 eV

Table 2.6 - Position of the main maximum before and after the annealing step (RT→150°C at 1.5°C/min and 150°C → RT at 4°C/min).

These changes in the UV-vis spectra suggest potential structural reorganization of the polymer chains during the annealing treatment. **Figure 2.14** shows the evolution of the morphology of the surface of these samples evidenced by AFM.

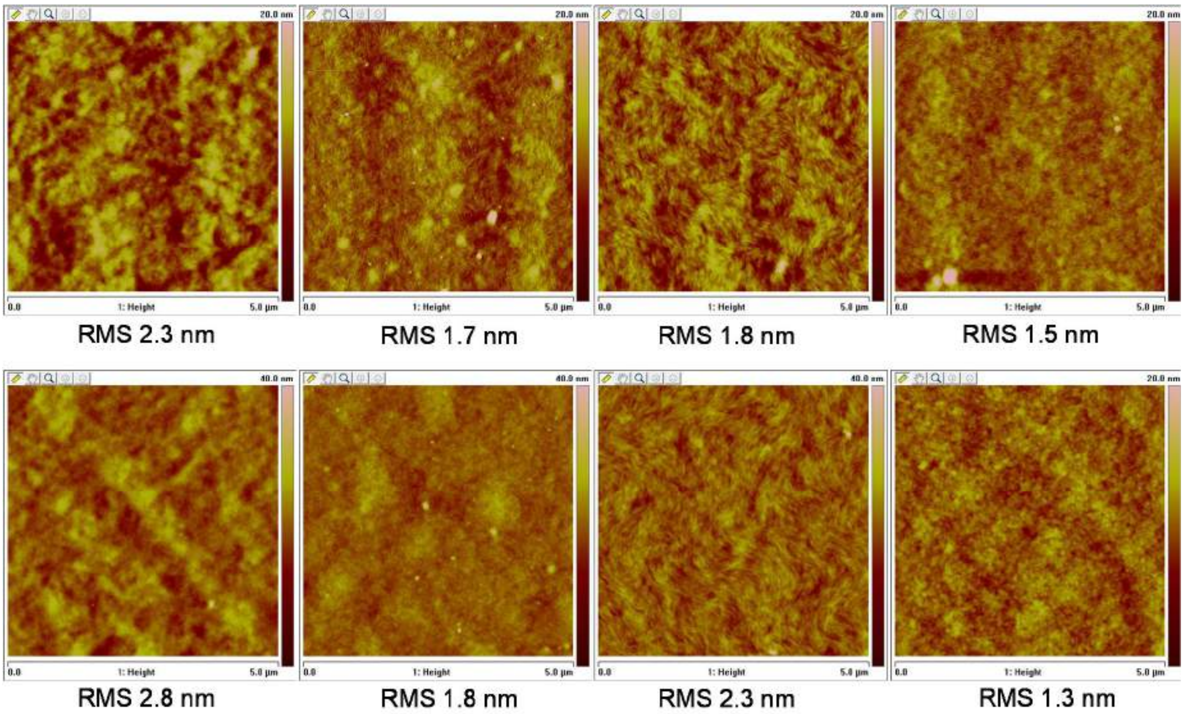

Figure 2.14 - AFM images of P1, P2, P4 and P6 (from the left to the right) before (top row) and after annealing (bottom row) RT→150°C at 1.5°C/min and 150°C → RT at 4°C/min.

AFM images first show that the surface morphologies of the four pristine polymers (before annealing treatment) are relatively similar with comparable surface roughness. The chemical structure of the side chain as well as the distribution of the macromolecular chains can influence the morphology of conjugated polymers.[94] [28] These latter data are reported in **Table 2.5**. However P4 shows a more specific morphology like hair/wave structure which could be explained by the fact that P4 is the polymer of the series without side chain on the BDT unit and has the lowest molecular weight of the series. Nevertheless, for all polymers, no significant differences can be observed before and after the annealing step. It means that the polymer reorganizations observed with UV-vis spectroscopy occur at lower scale than AFM or are located deeper in the bulk. The temperature maximum (150°C) is maybe also not high enough for significant morphological changes.

Raman spectra were recorded along the annealing treatment (RT→150°C at 1.5°C/min and 150°C → RT at 4°C/min). It is noteworthy the polymers are excited at 532 nm to get the Raman spectra, correspond to a weak absorption area. (none-resonance mode) **Figure 2.15** shows the main vibrational modes (1200-1600 cm^{-1}) of P1 (-OR) recorded at room and higher temperatures. Four main peaks are observed at 1332 (peak 1), 1390 (peak 2), 1442 (peak 3) and 1473 cm^{-1} (peak 4), and are attributed to the pi-conjugated system. (See Appendix A2.6 for pristine Raman spectra of P1, P2, P4 and P6) These peaks are observed for all polymers of the series. However, a detailed attribution was not performed. All the peaks decrease in the same manner. **Figure 2.16** shows the evolution of the intensity of the peak 4 (the most intense) versus temperature during the first heating step, cooling step and second heating step for P1, P2, P4 and P6. We can observe that all spectra evolve in the same way. Spectra does not change significantly until a certain temperature which is about 43, 44, 46 and 46°C for P1, P2, P4 and P6 respectively. Beyond this temperature we can observe a clear drop of the intensity of the peak as well as the one of the complete spectrum (See Appendix A2.7). We can realize that during the following cooling the pristine spectra are restored, thus indicating that the transformation was reversible and that the polymers were not degraded during the thermal treatments (inert atmosphere). The next heating step shows that the process is reproducible even if the temperatures where the drop occurs are higher than those of the first heating step. These experiments suggest that the drop of Raman intensity is a thermal assisted phenomenon, is reversible and reproducible. Surprisingly, we do not observe significant differences in our polymer series. The difference of side chains and molecular weight should theoretically influence the Tg.[94]

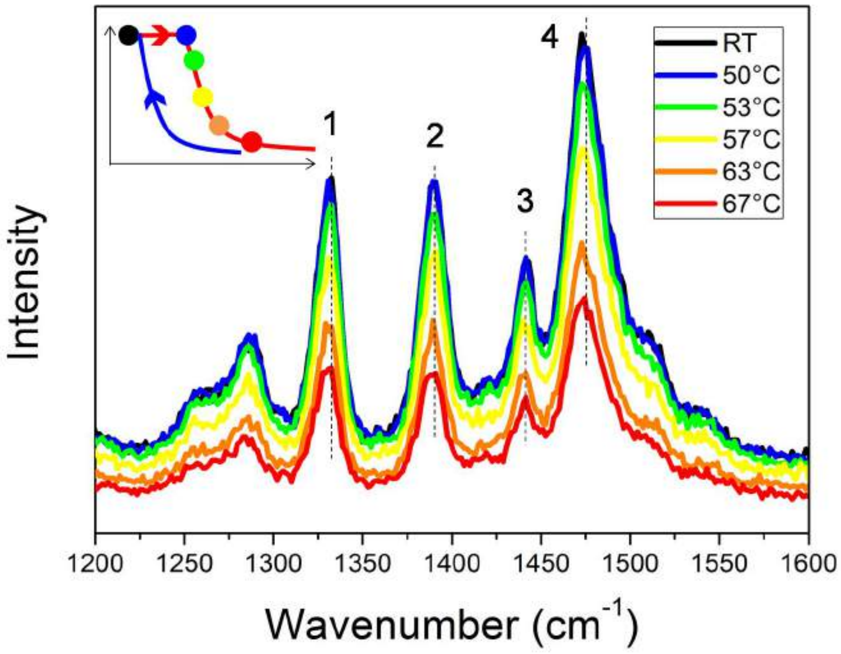

Figure 2.15 - Raman spectra of P1 recorded at room temperature (black) and different temperatures in inert atmosphere. (RT→150°C at 1.5°C/min and 150°C → RT at 4°C/min). The

insert show the intensity of peak 4 (as **Figure 2.17**) versus temperature (heating in red and cooling in blue).

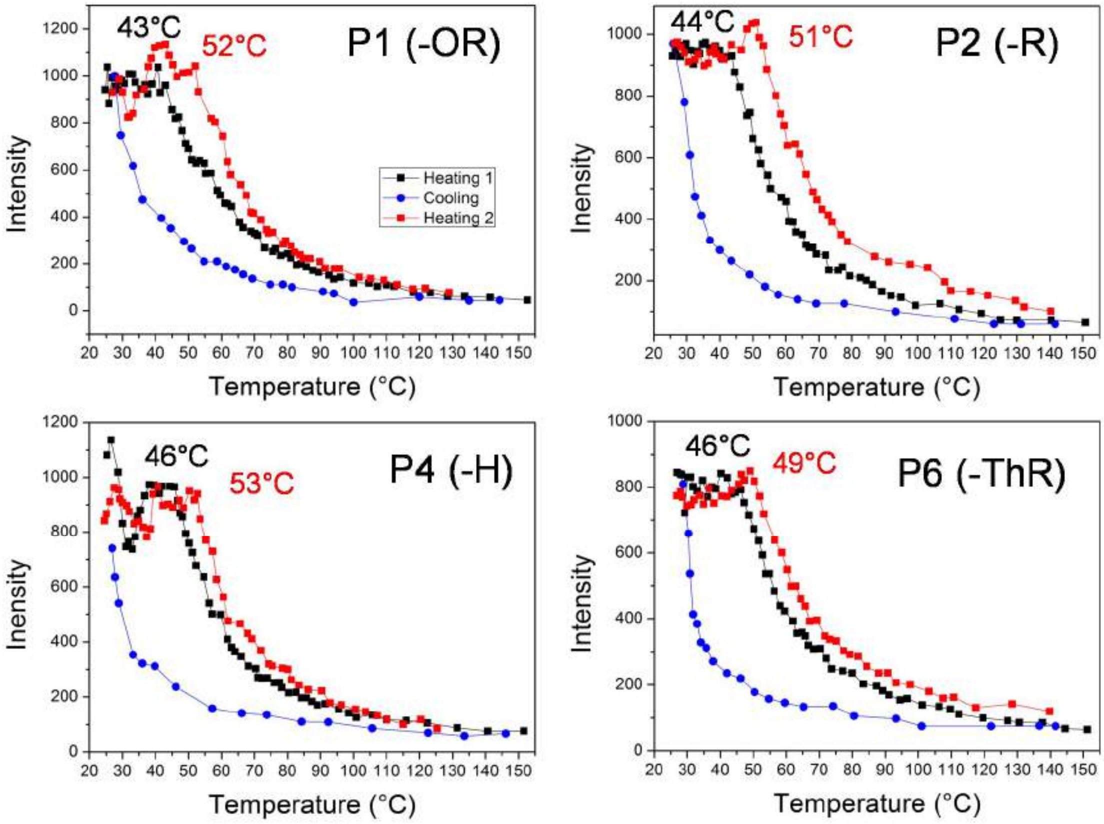

Figure 2.16 - Evolution of the intensity of the peak 4 versus temperature for P1, P2, P4 and P6. (RT→150°C at 1.5°C/min and 150°C → RT at 4°C/min).

The temperatures at which the drop of Raman intensity occurs seems relatively low to be a Tg at least of low ban gap polymers.[94] Indeed, Tg of LBG polymers are mostly higher than 100°C.[94,120] Therefore, we decided to measure the thermal transitions of our polymer series using Rapid Heat Cool Calorimetry (RHC). The high ramp of temperature (500K/min) makes the technique highly sensitive especially for measuring the Tg (See experiment section for more information). **Figure 2.17** shows the RHC curves obtained for P1 (-OR), P2 (-R), P4 (-H) and P6 (-ThR).

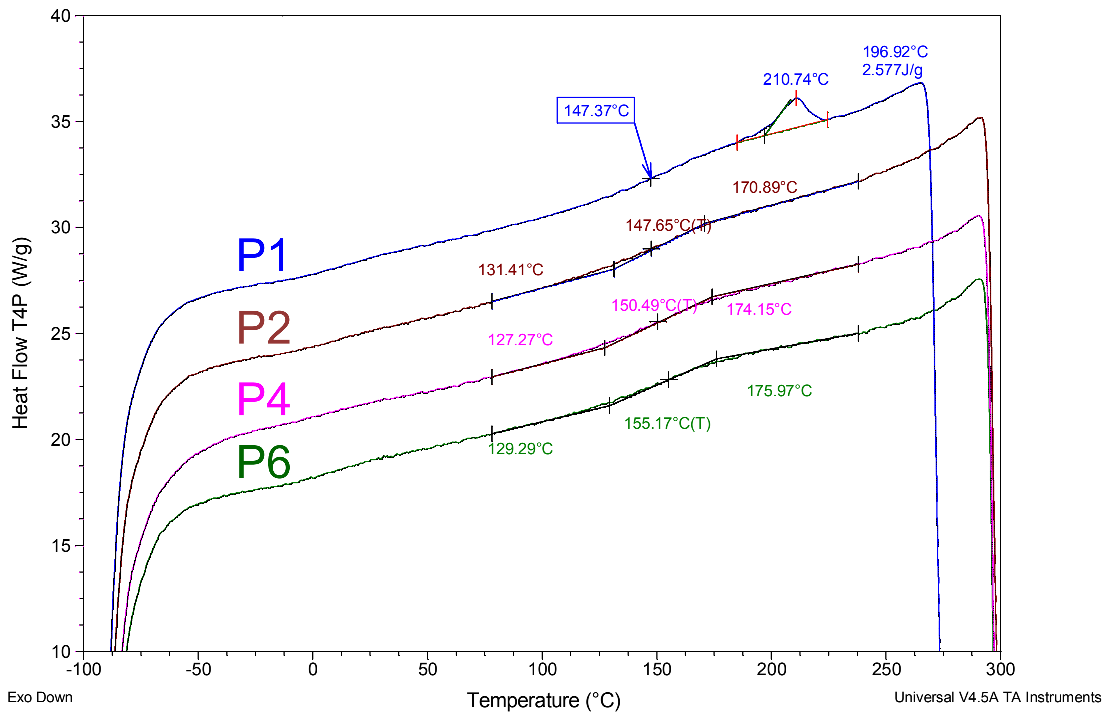

Figure 2.17 - RHC results obtained for P1 (-OR), P2 (-R), P4 (-H) and P6 (-ThR). The curves correspond to the second heating (500 K/min) after cooling at 20 K/min.

From RHC measurements, the Tg was determined to be 147.4, 147.7, 150.5 and 155.2 °C for P1 (-OR), P2 (-R), P4 (-H) and P6 (-ThR) respectively. It is important to note that the polymer powder was analyzed in the case of RHC measurements and not as thin films. We can note that P1 (-OR side chain) is the only polymer (in powder) with a semi-crystalline behavior. We observe a variation of 7°C in the series. For P3HT, it has been demonstrated that the Tg of the polymer decreases progressively when the side chain is extended.[94] In our case, P4 (no side chain on BDT) has a lower Tg (-5°C) than P6 (branched thiophene based side chain). On the other hand, the Tg of a polymer usually increases when the molecular weight increases. However, it has been shown that after a certain value, the increase of Mn has no significant impact on the Tg of the polymer.[94] Therefore, by comparing P4 (no side chain, low Mn) and P6 (side chain, high Mn) the influence of Mn is maybe counter balanced by the effect of side chain, thus resulting in a small variation of Tgs. In our series, the change is side chain on the BDT unit only and molecular weight seem to have relative small impact on the Tgs.

Compared to the Raman datas, the values obtained by RHC are largely higher. One hypothesis is that the low temperatures obtained from the Raman spectra could correspond to sub-transitions. It is important to remind that RHC measurements were done on polymer powder while films were prepared for Raman measurements. Chloroform was used for processing pi-conjugated polymer thin films and the fact that the temperatures are close one from each other could be in line with migration of residual and trapped solvents. The temperatures measured with Raman are close to the boiling point of the chloroform (60°C). The fact that higher temperatures were obtained for the second heating could support the fact that trapped solvent plasticized the polymer before the solvent migration. However, the temperatures obtained during the second heating (supposed to be without residual solvents) are still far from the RHC values. Another hypothesis is that sub-transitions might be possible only when the polymers are prepared as thin films.

- *Thermal stability of the polymer blends*

In a second step, the four polymers were blended with $PC_{60}BM$ (1:2) and submitted to the same heating/cooling steps (RT→150°C at 1.5°C/min and 150°C → RT at 4°C/min) followed by the same set of experiments. Unlike the neat polymers, there is a visual difference after the heating/cooling. The films appear to be quite more opaque, especially in the case of P4. **Figure 2.18** shows the UV-Visible spectra of the four polymer blends before and after heating/cooling. Focusing on P1 and P2 blends, the thermal treatment provokes a change in the baseline suggesting physical change within the thin film such as reflection and/or scattering a part of the incident light which is consistent with the formation of $PC_{60}BM$ agglomerates. This effect is much more pronounced for P4 while it is not visible for P6.

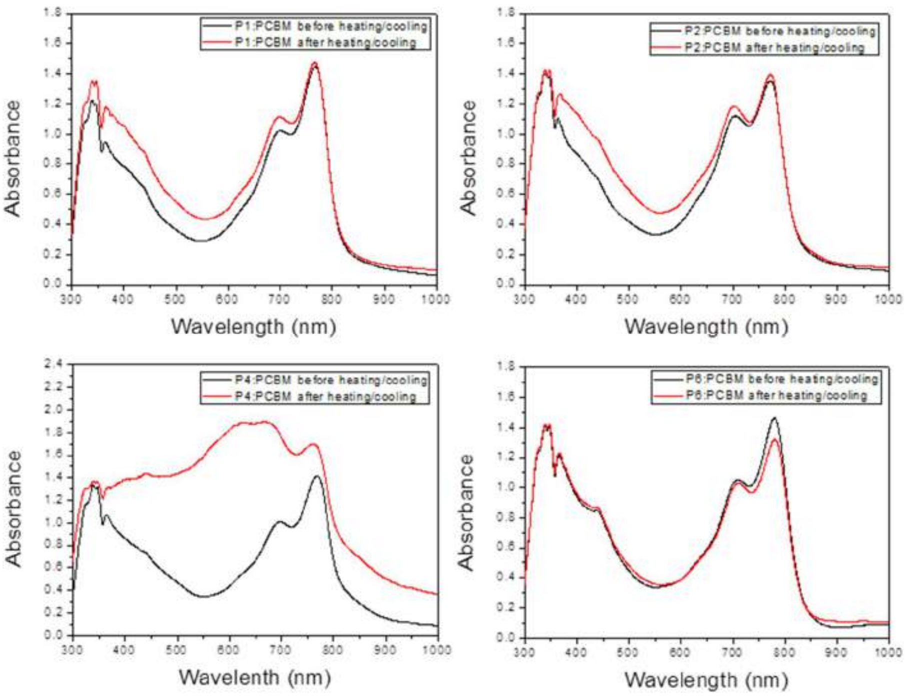

Figure 2.18 - Effect of the heating/cooling (RT→150°C at 1.5°C/min and 150°C → RT at 4°C/min) on the UV-Visible spectra of P1(-OR), P2 (-R), P4 (-H) and P6 (-ThR) blended with $PC_{60}BM$. (1:2)

Optical microscopy images (**Figure 2.19**) confirm the crystallization of $PC_{60}BM$ in the case of P1, P2 and even more pronounced for P4. Image in the middle is located on a specific area where the $PC_{60}BM$ agglomeration was partially present. The image on the right corresponds to an area with high amount of $PC_{60}BM$ agglomerates.

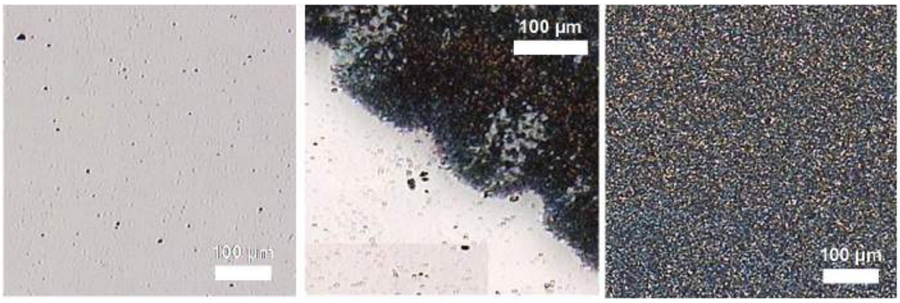

Figure 2.19 - Optical microscopy images of P4:PC$_{60}$BM (1:2) before (left) and after the heating/cooling (middle and right).

We also performed AFM analysis in order to probe the surface morphology at a smaller scale. **Figure 2.2,** shows all the images recorded before and after heating/cooling for the different polymer blends. Regarding P1 and P2 blend films, we clearly observe that the pristine surfaces are smooth (RMS 1.6 nm for 5x5 µm images). After the heating/cooling treatment, the surfaces become very rough due to the formation of PC$_{60}$BM agglomerates. After the same heating/cooling on polymers alone (**Figure 2.14**), AFM images did not reveal significant differences. Therefore the clear change of morphology observed for the blends can be attributed to the diffusion of PC$_{60}$BM and formation of agglomerates. A more detailed analysis reveals that after heating/cooling, the surface of P1 looks less structured than the one of P2 where clear shapes can be observed. PC$_{60}$BM agglomerates are ~1 µm size and cover completely the surface. In the case of P4, we can observe before heating/cooling some spots at large scale probably due to none dissolved PC$_{60}$BM. After heating/cooling, we can observe the formation of agglomerates of PC$_{60}$BM as for P1 and P2 but they are larger. For P6, we can observe the formation of flower like structures after heating/cooling but the roughness is quite less important than the one of P1, P2 and especially P4. AFM images are in line with data obtained thanks to UV-vis analysis. Indeed, the important change in UV-vis spectrum in the case of P4 can be attributed to the important phase separation with the formation of large PC$_{60}$BM agglomerates observed by AFM and optical microscopy which provokes light scattering. For P6, the degree of phase separation is less important resulting in a small evolution of the UV-Visible spectra and a moderate modification of the surface morphology. P1 and P2 blends have an intermediate between P4 and P6, with a modification of the UV-visible spectra also explained by PC$_{60}$BM agglomerates.

The heating/cooling induces drastic modification of the polymer blend morphology. The final temperature is close to the measured Tg of the neat polymer series (not the Tg of blends). From UV-vis and AFM datas, we can rank the polymer blends as function of their thermal stability (phase separation due to PC$_{60}$BM diffusion) from the most resistant to the most unstable: P6<P1~P2<P4. Clear difference of phase separation rates were observed while the Tgs are relatively close. The rank thermal stability does not follow the Tg ranking. In our series, the Tg seems not to be the main parameter which can influence the thermal stability of the polymer blends. However, we can try to find an explanation based on the potential role of the side chain and the physical properties of the polymers regarding the thermal stability of the polymer blends.

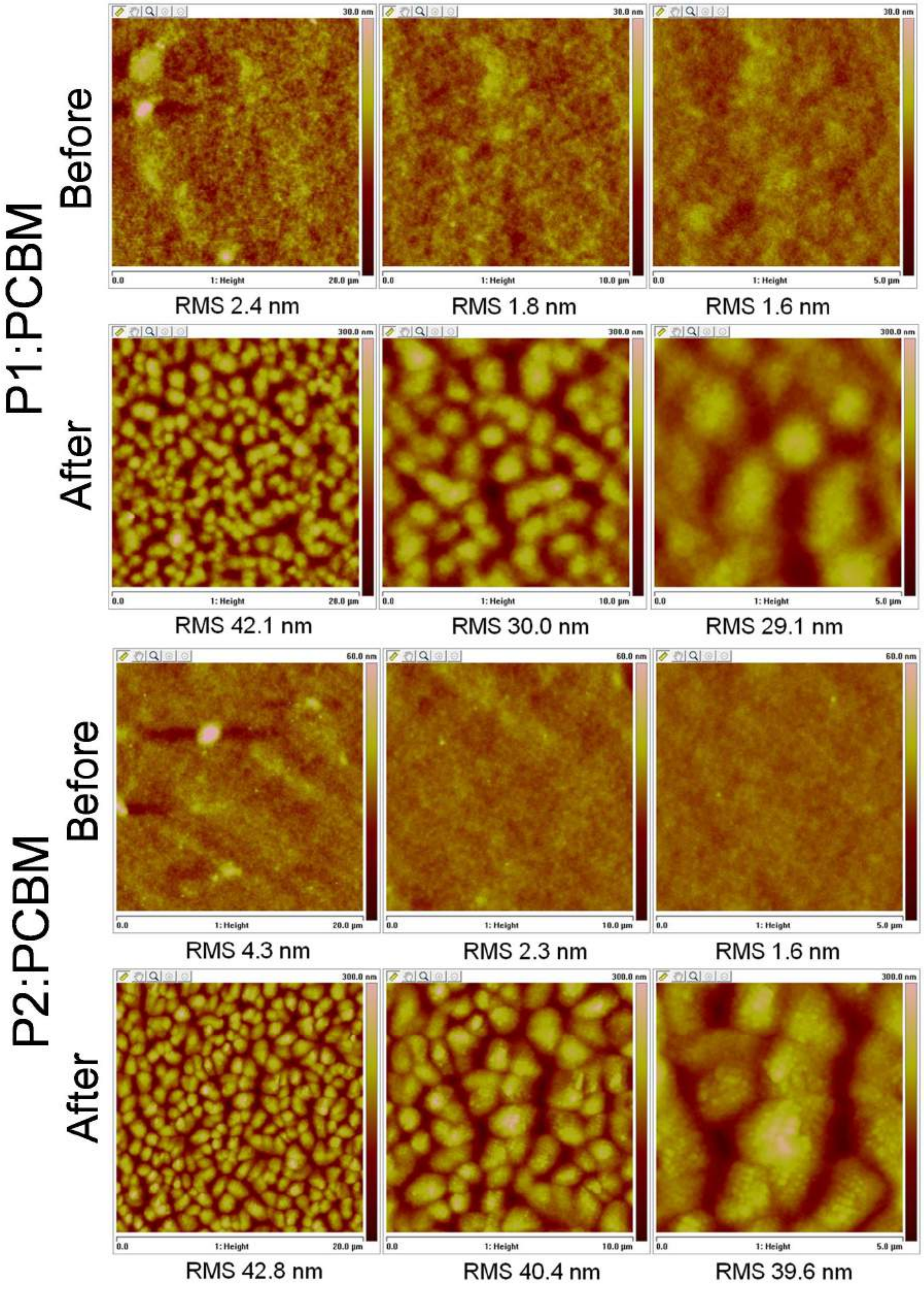
P1:PCBM
Before
30.0 nm
0.0
1: Height
20.0 µm
10.0 µm
5.0 µm
RMS 2.4 nm
RMS 1.8 nm
RMS 1.6 nm
After
300.0 nm
RMS 42.1 nm
RMS 30.0 nm
RMS 29.1 nm
P2:PCBM
Before
60.0 nm
RMS 4.3 nm
RMS 2.3 nm
RMS 1.6 nm
After
300.0 nm
RMS 42.8 nm
RMS 40.4 nm
RMS 39.6 nm

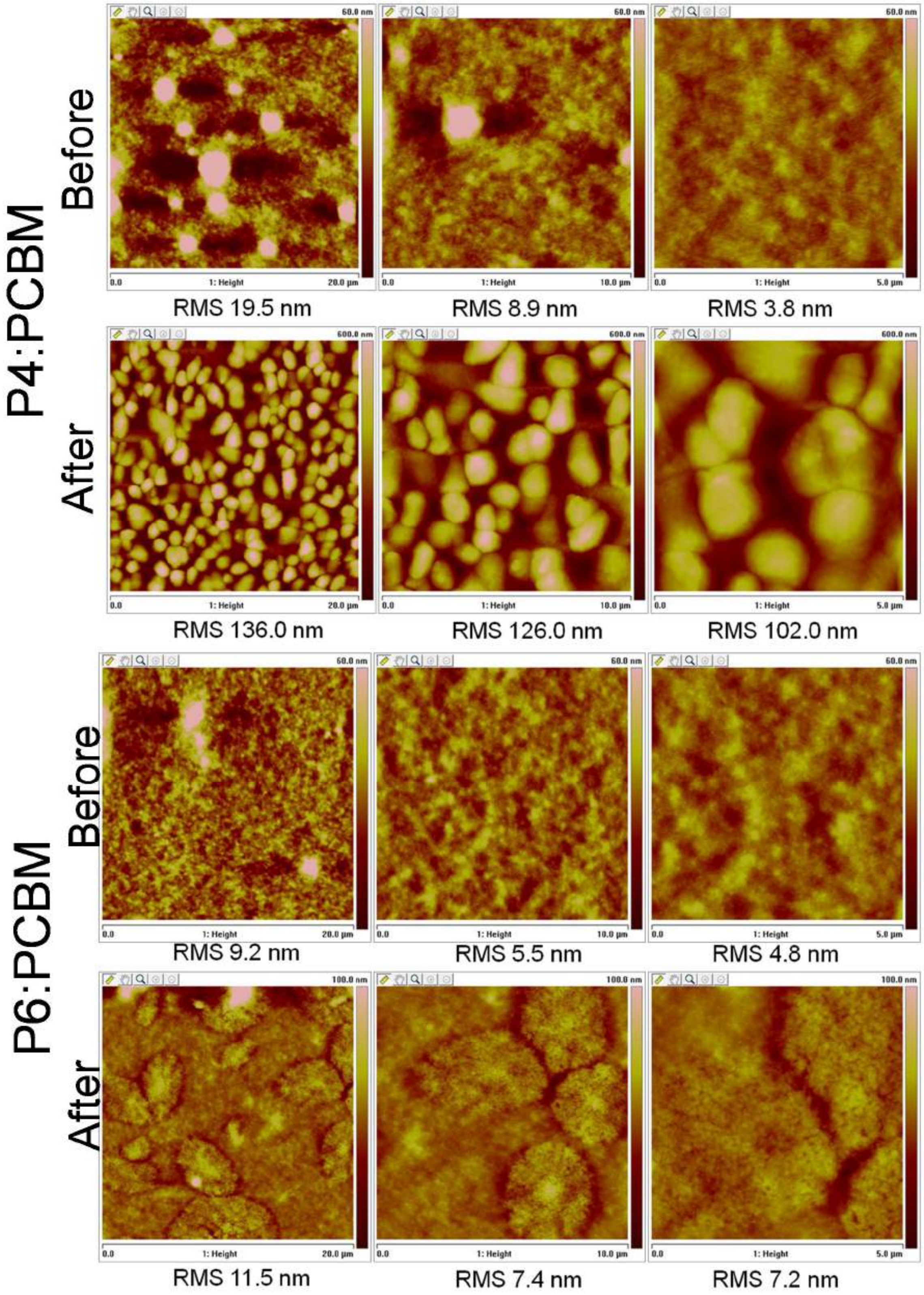

Figure 2.20 - AFM images of P1, P2, P4 and P6 blend films before (top row) and after annealing treatment (bottom row) at different scales. (RT→150°C→RT with a ramp of 1.5°C/min).

P4 blend is the less thermally stable, and P4 is the polymer without side chain on the BDT unit and has the lowest Mn of the series. Thus, the lack of side chain could induce free space facilitating $PC_{60}BM$ diffusion. The other polymers have relative long side chains which could reduce the $PC_{60}Bm$ diffusion. The high Mn of P6 may favor the thermal stability of the BHJ.

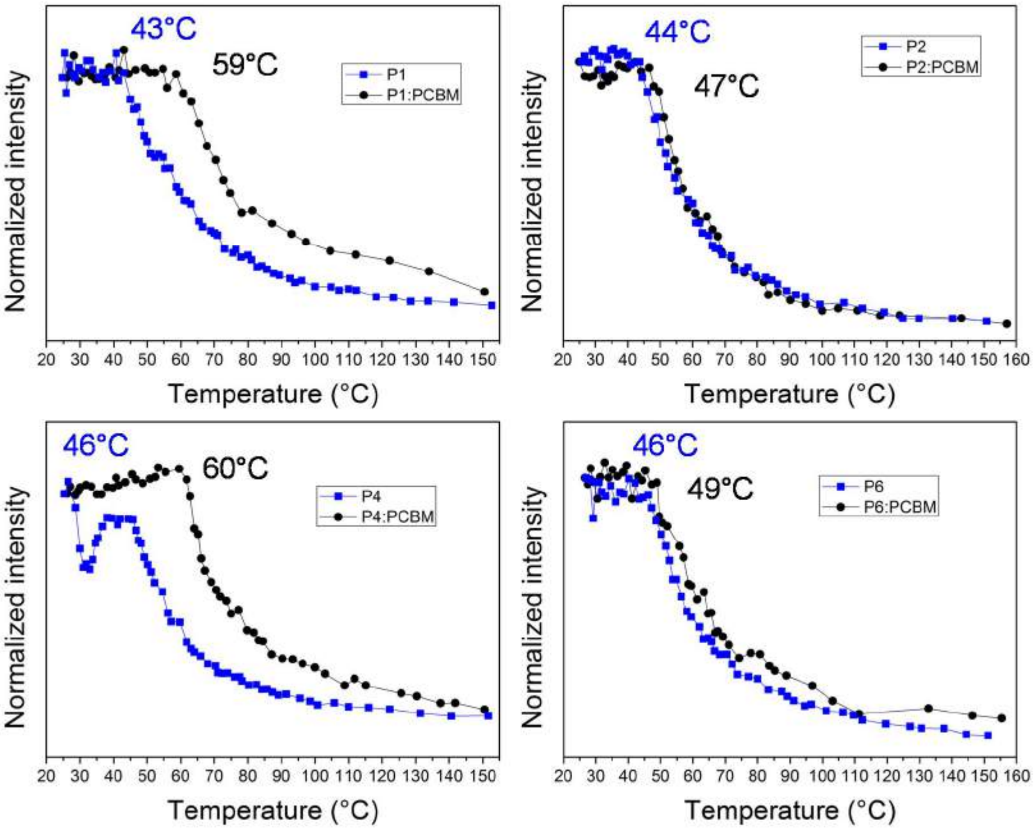

Figure 2.21 - Evolution of the intensity of the peak 4 (Raman) versus temperature for P1, P2, P4 and P6 (blue) and their blend versions (1:2 with $PC_{60}BM$). (RT→150°C at 1.5°C/min and 150°C → RT at 4°C/min).

By using Raman in the same manner as it was done for the neat polymer films, the measurements was performed for the blend films (1:2 polymer:$PC_{60}BM$ ratio). **Figure 2.21** shows that when blended the temperatures where the drops occur are shifter to higher temperatures: +16°C, +3°C, +14°C and +3°C for P1, P2, P4 and P6 respectively. These results may suggest that the insertion of $PC_{60}BM$ may influence the possible sub-transition temperatures especially in the case of P1 and P6.

2.3.4. Conclusion

In this part, we have investigated the role of the polymer side chain on the thermal stability of the polymer:$PC_{60}BM$ blend films. We have observed the Tg of the polymer series do not change significantly. However, the stability of the polymer blends, in other word the capability of the $PC_{60}BM$ molecules to diffuse and to agglomerate depends of the polymeric matrix. Therefore, the Tg is in our series cannot be considered as the main parameter influencing the polymer blend stability. By using Raman spectroscopy, we possibly found sub-transitions in the polymer and blends series which could explain that the annealing at sub-Tg temperature can be enough to modify the BHJ morphology and device performance.[116] The difference of thermal stability could be explained by the influence of the presence or not of side chain and physical properties such as the molecular weight on the $PC_{60}BM$ diffusion through the polymeric matrix.

2.4. Relationship between the side chain structure and device stability

2.4.1. Introduction

Herein we report on the impact of a wide variety of side-chains on a donor-acceptor polymer system in order to specifically investigate the role of solubilizing side-chains on PSC (polymer solar cell) stability. In this study, the investigation will focus on commonly used monomers for the development of polymers for PSC. In recent years, polymer solar cells (PSC) containing benzodithiophene (BDT) as a donor and diketopyrrolopyrrole (DPP) as an acceptor have gained in popularity and demonstrated power conversion efficiencies greater than 6%.[121,122] As a model system, benzodithiophene (BDT) with different side-chains are synthesized and co-polymerized with diketopyrrolopyrrole (DPP) forming four low bandgap poly-BDT-*alt*-DPP (PBDTDPP) polymers. The polymer blends are subsequently characterized optimized in inverted PSC devices and their stability assessed under AM1.5 irradiation in absence of oxygen and thermal treatment (50°C). A detailed investigation of the polymer blend ageing during AM1.5 exposure thanks to the combination of XRD, AFM, UV-Vis and IR analysis allowed to propose an hypothesis on their degradation mechanism, and subsequently to suggest routes to increase PSCs operational stability.

2.4.2. Experimental

Please, refer to the appendix (A1) for additional details on the experimental techniques.

- *Polymer synthesis, physical properties of the polymers and of their blends with* $PC_{60}BM$

The synthesis of the investigated polymers has been recently published by Morse et al.[109] The chemical structures were already shown in **Figure 2.12**.

Polymer blends films have a green color, and they strongly absorb in the 600-800 nm with a lambda max of 766, 769, 767 and 777 nm for P1, P2, P4 and P6 respectively (**Figure 2.24**). Their absorption onsets are between 800 nm and 900 nm which correlate to an optical band gap of 1.5 eV (**Table 2.7**). The frontier orbital energy levels of the pure polymer films were measured by solution cyclic voltammetry. Across the range of polymer side-chains only minimal differences in IP and EA energy levels were observed. The frontier energy levels were measured to be between -5.3 eV to -5.4 eV for their IP, and -3.8 eV to -3.9 eV for their EA and these data are within the ±0.1 eV experimental error associated with solution cyclic voltammetry (**Table 2.7**). The hole mobilities of the polymers were measured in top gate organic transistors. Each of the polymers displayed similar transistor hole mobilities, roughly 0.02 $cm^2\ V^{-1}\ s^{-1}$. Overall, the properties of the four studied polymers are similar in optical absorption, frontier energy levels and hole mobility (**Table 2.7**).

Polymer	Mn [kg mol^{-1}] [a]	Mw [kg mol^{-1}] [a]	PDI [a]	IP (eV) [c]	EA (eV) [c]	Optical gap (eV)	μ_h [cm^2 V^{-1} s^{-1}] [b]
P1	40	130	3.4	-5.3	-3.8	1.5	0.024
P2	93	320	3.5	-5.3	-3.8	1.5	0.023
P4	32	72	2.2	-5.4	-3.9	1.5	0.026
P6	130	730	5.5	-5.4	-3.9	1.5	0.024

Table 2.7 - Physical properties of polymers P1, P2, P4 and P6. [a] Measured at 140 ˚C in 1,2,4-trichlorobenzene. [b] Saturated hole mobility measured in top gate OTFT deposited from DCB and annealed at 100°C. [c] Approximated by cyclic voltammetry.

- *Device fabrication, Inverted Architecture*

The zinc oxide transport layer was formed by spin-coating a solution of zinc acetate dihydrate (Aldrich) in DMSO at 160 g L^{-1} at 4000 rpm for 10 seconds followed by a 5 minutes thermal anneal process at 300 ˚C.[123] The active layer was deposited by blade coating inside a glovebox. On top of the active layer 0.9 mL of PEDOT:PSS Clevios HTL Solar SCA 246-9 (Heraeus) was spread and uniformly coated by spin-coating at 1100 rpm for 130 seconds without an annealing step. The silver top electrode was applied by vacuum deposition at 2×10^{-6} mbar at 1-5 Å/s.

- *Device fabrication, Standard Architecture*

1 mL of PEDOT:PSS Clevios AI 4083 was spread and uniformly coated by spin-coating at 1000 rpm for 20 seconds and then 4000 rpm for 120 seconds onto a UV ozone treated ITO substrate. The substrate was then heated to 120 °C in a glovebox for 30 minutes. The active layer was deposited by blade coating inside a glovebox. The top electrode comprising 20 nm of calcium and 100 nm of aluminum was applied by vacuum deposition at 2×10^{-6} mbar and 1-5 Å/s.

- *Encapsulation and measurement*

The devices were subsequently encapsulated with a top glass cover slide containing a 120 µm cavity in the center of the slide. The outer edge of the cover slide was sealed using UV curing epoxy. The devices were exposed to AM1.5 in a Newport 94082A Solar Simulator and data was collected using a Keithley (2400) connected through a Keithley (2750) switch system. Thermal heating of the devices was performed on a hotplate. Thermal measurements of the illumination area were measured using a mercury thermometer recording a temperature of 37 ˚C. The encapsulated devices surfaces reached elevated temperature of 45±1 ˚C during illumination measured by a RS 1327K infrared thermometer fitted with a thermocouple. The temperature of the internal cavity was measured using the infrared thermometer to be 47±2 ˚C however the measurement may not be accurate due to the reflective nature of the silver/glass surfaces and should be considered a minimum temperature. Thermal experiments were performed at a hotplate set-point of 105 ˚C. The surface temperature was measured to be 50±4 ˚C at the center of each of the devices throughout the experiment.

- *Transistor mobility and cyclic voltammetry*

Mobility measurements of the polymers were measured in top-gate organic transistor architecture. The polymers were dissolved at 7 mg mL^{-1} in 1,2-dichlorobenzene (DCB) and cast hot at 100 ˚C by spincoating for 15 seconds at 500 rpm and 120 seconds at 1200 rpm. The films were then subsequently annealed at 100 ˚C for 3 minutes and their saturated hole mobilities were measured. Cyclic voltammograms were recorded using a Princeton Applied Research VersaSTAT 4 potentiostat. Films of the polymers were cast from a concentrated chloroform solution onto a platinum wire working electrode. Voltammograms were recorded in an anhydrous acetonitrile solution containing 0.1 M NBu_4^+ BF_4^- electrolyte with a platinum wire counter electrode and 0.1 M Ag/$AgNO_3$ in acetonitrile reference electrode. The solutions were purged with N_2 gas and referenced to an external ferrocene solution which was also used to calculate the ionization potential (IP) and electron affinity (EA) positions ($E_{orbital} = -(E_{onset} + 5.1)$ eV).[124] Gel permeation chromatrography (GPC) was performed with an Agilent Technologies PL-GPC 220 eluted at 1mL/min with 140 ˚C HPLC grade 1,2,4-trichlorobenzene (Aldrich) through a PLgel 10 µm Mixed-B (300×7.5 mm) GPC column. The polymers were analysed with a refractive index detector calibrated with narrow polystyrene standards. Samples were prepared at a concentration of 1 mg mL^{-1} and filtered at 140 ˚C prior to analysis.

- *UV-Vis, AFM, FTIR analysis. Light soaking conditions*

Films of P1, P2, P4 and P6 blends were cast from solution (5:1 chloroform (CF):DCB formulation (see Table 2)). The films were deposited on glass substrates in order to perform UV-visible spectroscopy, AFM and XRD measurements and on KBr substrates for FTIR spectroscopy. Furthermore, the KBr substrates are particularly interesting to investigate the UV range (200-300 nm) which is the region of $PC_{60}BM$ absorption. The samples were encapsulated in tubes sealed under vacuum (10^{-6} mbar) in order to eliminate the presence of oxygen. The films were exposed to light (simulated solar irradiation, Xe lamp, 750 Wm^{-2} [300-800 nm], ~45°C) and this degradation was monitored by UV-Vis and IR spectroscopy. In order to make sure that the vacuum has no impact on the samples, all of them were preliminary sealed and stored for 24 hours in the dark. The UV-visible and IR spectra were recorded before and after encapsulation and we have observed no change in the full spectra for all polymer blends. Infrared spectra were recorded in transmission with a Nicolet 760-FTIR spectrophotometer working with OMNIC software. Spectra were obtained using 32 scan summations and a 4 cm^{-1} resolution. Changes in UV-Vis spectra were followed with a Shimadzu UV-2101PC spectrophotometer equipped with an integrating sphere.

- *X-ray diffraction*

X-ray diffraction analyses were made using a PANalytical X′Pert Pro diffractometer equipped with a X′Celerator detector and a Cu anticathode (Kα1/Kα2). The instrument was used in the θ−θ reflection mode, fitted with a nickel filter, 0.04 rad Soller slits, 5 mm mask, 1/16° fixed divergence slit, and 1/32° fixed antiscatter slit. XRD data were measured over a range of 1−40° (2θ) with a step size of 0.0167° and a total counting time of about 3 h.

2.4.3. Results

- *Optimized OPV devices*

OPV devices based on the four polymers blended with $PC_{60}BM$ were fabricated in order to investigate their stability. A conventional inverted OPV architecture was used for the devices due to its improved stability reported in literature - ITO/ZnO/Active layer/PEDOT:PSS/Ag(100nm) (**Figure 2.22**).[125]

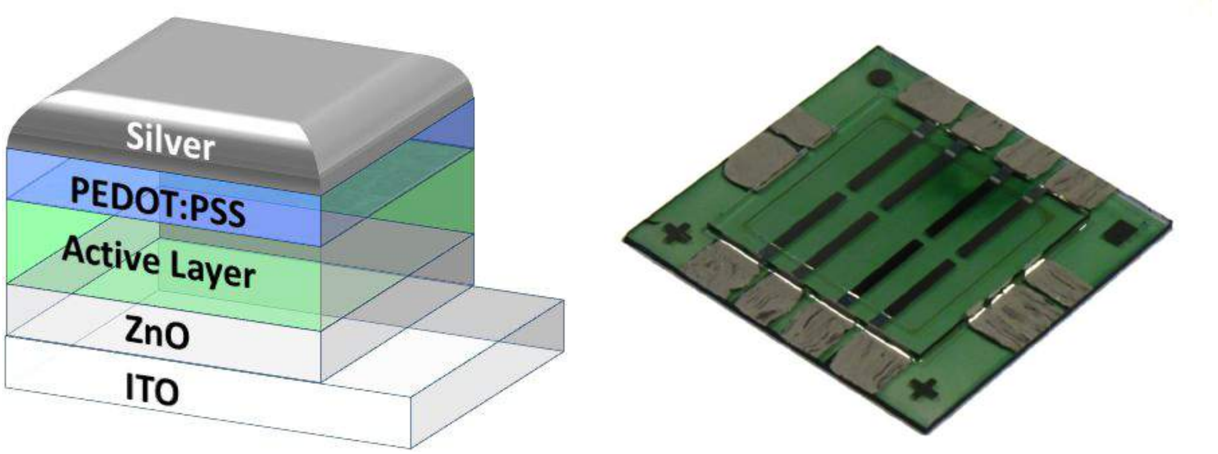

Figure 2.22 - Inverted device architecture (left) and image of final encapsulated device (right).

Each material was optimized by ink formulation, varying solvent selection and concentration. Preliminary screening was performed in orthodiclorobenzene (oDCB), chloroform (CF), and a ratio of CF:oDCB. A doctor blade was used to deposit the active layer with a coating speed of 30 mm s^{-1} and a blade gap of 0.1 mm. Coatings of P1 and P2 in neat oDCB contained fine undissolved particulate due to the low solubility of the P1 and P2. Coatings obtained from CF were better due to higher solubility, but device performance was generally poor, likely caused by inadequate phase separation. A mixture of CF:oDCB, inspired by the work of Janssen,[126] was found to be an ideal solvent/non-solvent mixture resulting in 2-5 minute drying times and sufficient phase separation. A solvent ratio of CF:oDCB was optimized for P1 at a 5:1 ratio for P1:$PC_{60}BM$ 1:2 blends. This same solvent formulation was used across the series of polymers to negate the effect of solvents on active layer degradation. Short circuit current of the devices was optimized by varying concentration in the formulation. The optimal concentrations for P1, P2, P4 and P6 were found to be 12, 10, 20, and 15 mg mL^{-1} respectively. Once optimized, power conversion efficiencies for the series were all above 2.5% reaching over 5% in the case of P1 (**Table 2.7**, **Figure 2.23**). These results are well in line with other reports of PBDT-co-DPP polymers in the literature.[122,127,128] Similar results were obtained when these formulations were tested in a standard device architecture, ITO/PEDOT:PSS/Active layer/Ca(30 nm)/Al(100 nm) (**Table 2.7**), albeit with slightly lower performance.

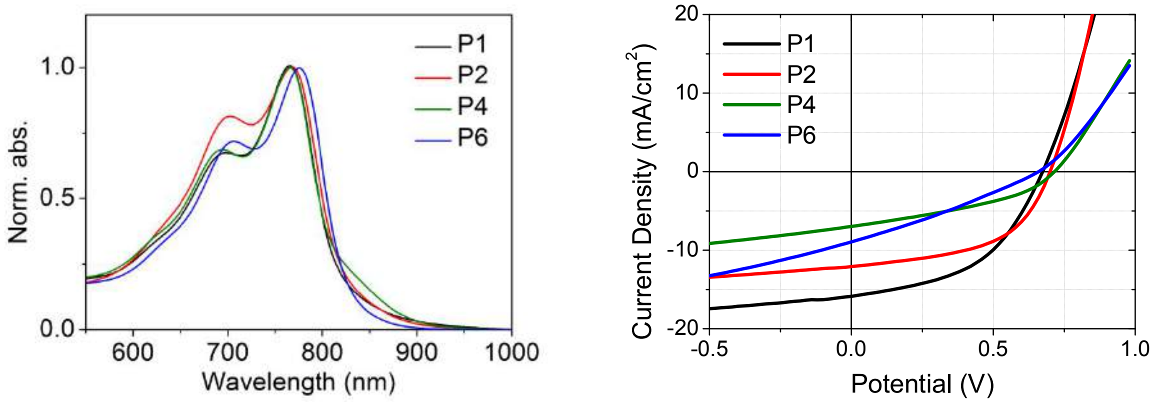

Figure 2.23 - Normalized absorbance in the polymer region of P1, P2, P4 and P6 pristine blends (left) and JV curves of optimized inverted solar cells (right).

The open circuit voltage of the polymer series were between 660 mV and 700 mV which is in good agreement with the model developed by Scharber based on their IP positions.[129] Despite having similar ionization potentials, minor variations in open circuit voltage are observed which we attribute to their difference in side chains and morphology.[130] Fill factors across the series were lower in the inverted architecture than in standard architecture which suggests that hole or electron blocking layers in the inverted architecture are causing a space charge effect at the interface. This loss could be mitigated using alternative blocking layers, however substitution was not explored because of the reported device stability of this inverted architecture selected for this study.[125]

Reducing the $PC_{60}BM$ ratio to 1:1 led to similar device performance for P2 and P4, with P1 and P6 being significantly lower. The concentrations of the inks were reduced at this ratio to compensate the high viscosity resulting from increased polymer concentration. Although device performance amongst the polymer series was lower with 1:1 ratio, the results represent non-optimized devices.

Polymer	Fullerene	D:A ratio	Architecture	Ink conc.	Voc	Jsc	FF (%)	n (%)	T_{80} (hr)	Slope in first 24h (%/day)	Slope in last 24h (%/day)
P1	PC$_{60}$BM	1:2	Standard	12	0.64	11.27	60.2	4.35			
	PC$_{60}$BM	1:2	Inverted	12	0.66	15.9	48.9	5.12	22.9	0.904	0.102
	PC$_{60}$BM	1:1	Inverted	10	0.66	8.50	31.2	1.75	60.3	0.289	0.0311
P2	PC$_{60}$BM	1:2	Standard	10	0.71	10.5	57.7	4.26			
	PC$_{60}$BM	1:2	Inverted	10	0.70	12.1	52.4	4.43	110	0.407	0.0729
	PC$_{60}$BM	1:1	Inverted	8	0.72	10.6	46.3	3.52	>110	0.165	0.0340
P4	PC$_{60}$BM	1:2	Standard	20	0.70	5.91	53.9	2.22			
	PC$_{60}$BM	1:2	Inverted	20	0.68	8.75	45.3	2.69	10.4	0.486	0.0598
	PC$_{60}$BM	1:1	Inverted	16	0.70	7.39	43.5	2.25	>110	0.207	0.0116
P6	PC$_{60}$BM	1:2	Standard	15	0.69	8.96	39.4	2.45			
	PC$_{60}$BM	1:2	Inverted	15	0.66	13.6	32.9	2.95	37.4	0.721	0.132
	PC$_{60}$BM	1:1	Inverted	12	0.70	6.26	28.8	1.26	48.9	0.168	0.04153

Table 2.7 - Device properties and stability of P1, P2, P4 and P6.

- *Photodegradation of polymer/PC$_{60}$BM blends*

The evolution of encapsulated films of the polymer/PC$_{60}$BM blends coated on glass and KBr substrates were followed by UV-Vis and FTIR spectroscopy during light exposure (**Figure 2.24**, Additional information on pristine absorbance of polymer/blend can be obtained in the Morse et al.[109] paper. (Supporting information of the paper)

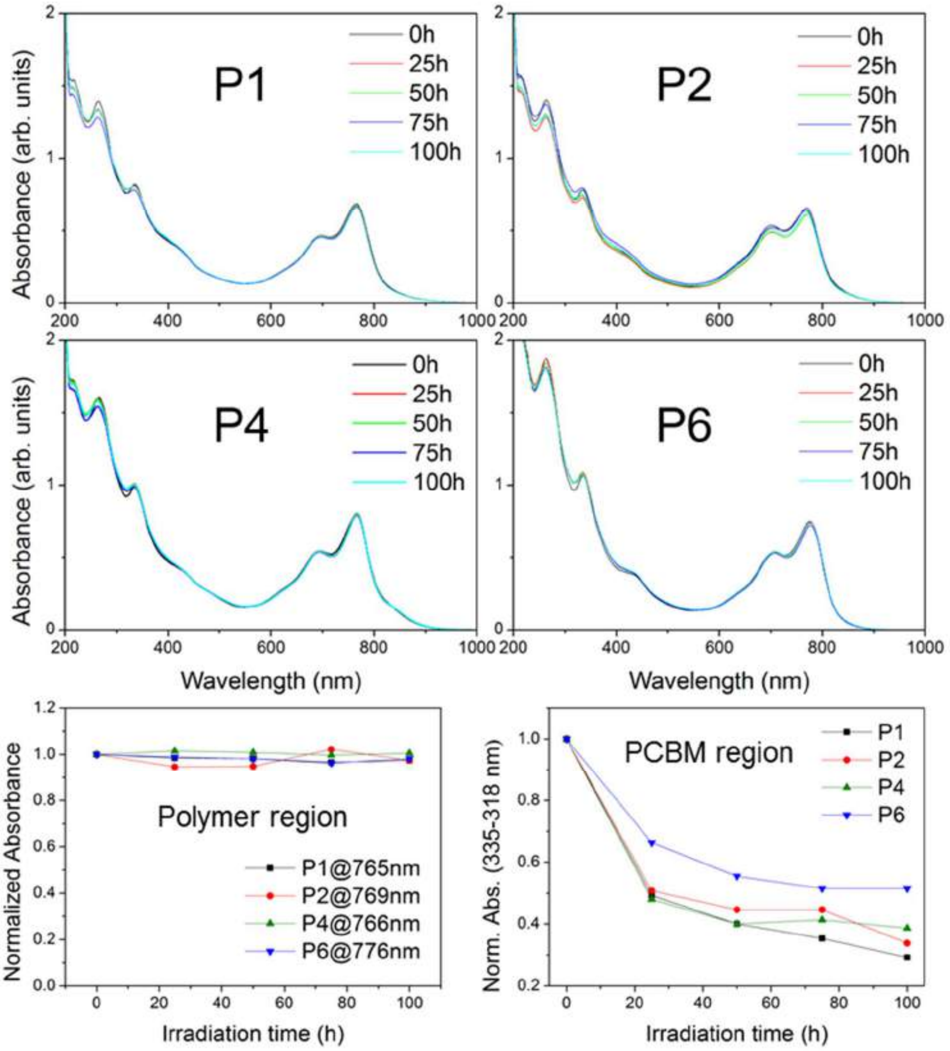

Figure 2.24 - Absorbance changes of the polymer:P$_{60}$CBM (1:2) blends after ageing under AM1.5 simulated solar irradiation. Figures in the bottom left and right show changes in the polymer λ_{max} and the PC$_{60}$BM 355 nm and 318 nm absorption respectively.

During 100 hours exposure, the polymer region of the UV-Vis spectrum was not impacted for each of the films (**Figure 2.24**, 600 – 800 nm region, bottom left). This confirms that the polymers are not photochemically damaged after 100 hours of light exposure (~45 °C) or at least the conjugated backbones are unchanged. From FTIR spectroscopy, no significant evolution of the vibrational modes assigned to the polymers was observed confirming that the chemical structure of the polymers are unchanged after 100h of irradiation. However, the PC$_{60}$BM region (200 – 350 nm) was significantly modified. The evolution is given in **Figure 2.24** (bottom right). This behavior has already been observed in many polymer blends exposed to light in inert atmosphere.[131-134] Authors attributed this modification to the PC$_{60}$BM dimerization/oligomerization. After 25 hours an important decrease of the ΔAbs is observed for each blend suggesting that the PC$_{60}$BM dimerization is relatively independent of the polymer as

Manca et al. have observed (explanation of the ΔAbs measurement is described in Appendix 2.8 and supporting information of Morse et al.[133]) Indeed, the evolution is very similar for P1, P2 and P4, however the $PC_{60}BM$ is less impacted when it is mixed with the P6 polymer. Due to similarities of each polymer studied, we believe this change is a result of P6's unique morphology, its propensity to form crystallites and is potentially linked to its polymer physical properties (polymer Mn) and/or the thienyl-ethyl hexyl side chain. The mechanism of dimerization of fullerenes has been studied in the past[131] and occurs by a photochemical 2+2 cycloaddition when fullerene cages are in close proximity (~4.2 Å). In the case of the P6 blend, the miscibility of $PC_{60}BM$ within the polymer may be low which would favour crystallite formation over dimerization in the film. IR analysis found similar small changes for each of the polymer/$PC_{60}BM$ with a decrease of the fullerene squeleton vibrational mode (526 cm^{-1}) due to the 2+2 cycloaddition on the fullerene moieties from dimerization. Crystallization of films can significantly affect IR stretches which complicates the interpretation.[135]

In parallel, topographic images were recorded by AFM (**Figure 2.25**). The surfaces of pristine polymer samples are shown in supplementary information of Morse et al.[109]

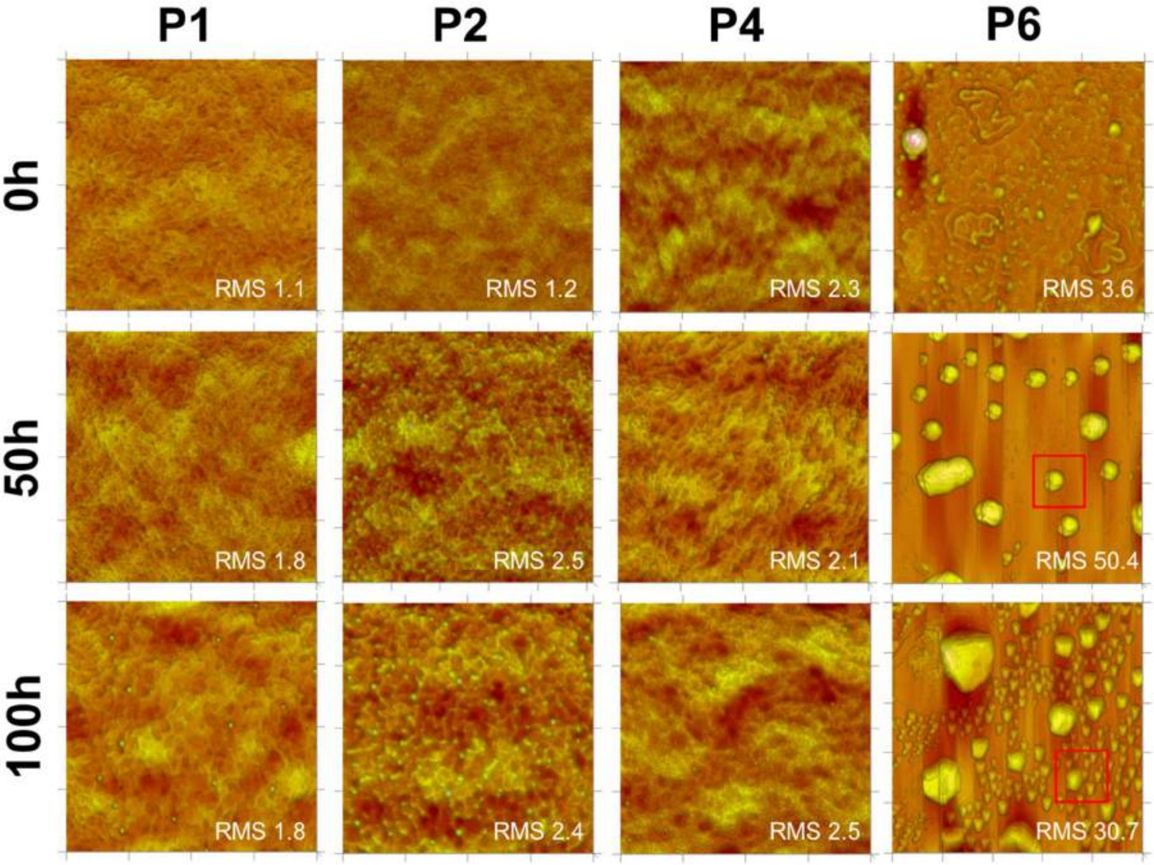

Figure 2.25 - AFM images (Height) of P1, P2, P4 and P6 blend films before (0h) and after 50h and 100h of light exposure at 45°C. The scales are: X=Y=2 μm and Z=20 nm for P1, P2, P4 and pristine P6 images. For P6 50h and 100h, the scale is X=Y=10 μm and Z=600 nm. The red squares are 2x2 μm.

The polymer fullerene blends were smooth with RMS values of 1.1 nm (P1), 1.2 nm (P2), 2.3 nm (P4) and 3.6 nm (P6). The surfaces of P1, P2 and P4 presents a desirable fibrous network similar in appearance to other literature reports of DPP based polymers.[136] The P6 surface is very different with the formation of irregular shapes. After 50 hours of light exposure (45 °C) we can observe a modification of the surface with the formation of dots (20 – 80 nm diameter) for P1, P2 and P4. The isotropic shapes of the crystallites suggest that the process of their formation is diffusion limited.[137] The amount of crystallites increases with the ageing time. For P6, we observe the formation of very large blocks homogenously spread at the surface. In order to have an idea of the very large size of those blocks, the P6 images (50 and 100 hours) are presented at a larger scale (2×2 μm, Z=20 nm for P1, P2, P4 and pristine P6 and 10×10 μm, Z=600 nm for 50 and 100 hours P6). The red squares on the 50 and 100 hours represent the 2×2 μm scale of the other images. These large blocks have a crystalline shape more visible with the phase mode (supplementary information of Morse et al.[109]) and are attributed to $PC_{60}BM$ crystals. This is due to the $PC_{60}BM$ diffusion through the polymeric matrix. $PC_{60}BM$ crystallization is a thermally induced process that occurs even at relatively low temperature (45 °C)[138-142] depending on the thermal stability of the BHJ. From our results, it is clear that the P6 BHJ evolved the fastest. It is then more difficult to assign an order of BHJ evolution between P1, P2 and P4.

As prepared, the polymer blend films display broad 21-25° reflections from alkyl chain packing and π-π stacking (~4 Å). Polymer P4 also displayed additional XRD reflections from the polymer lamella at 4° indicating 22 Å d-spacing. Upon ageing while exposed to AM1.5 illumination in vacuum, structural ordering progressively increased in each of the films. P1, P2 and P4 displayed additional reflections between 2-4° after 100 hours which are commonly associated with inter-chain lamella distances in polymers (**Figure 2.26**).

An increase in the d-spacing (space between polymer lamella) of polymer P4 upon ageing from 21 Å (0 hours) to 21.5 Å (50 hours) and 22 Å (100 hours) suggests possible $PC_{60}BM$ interdigitation as observed in P3HT films.[143] At 100 hours the inter-chain lamellas are spaced at 36.8 Å (P1), 19.2 Å (P2), 22.1 Å (P4) while P6 maintains its amorphous appearance. P1 and P6 uniquely displayed a sharp reflection between 25-35°, associated with π-π stacking distances of 2.6 and 3.4 Å respectively. In combination with the AFM analysis, it is possible to conclude that both the surface and the bulk of the polymer/$PC_{60}BM$ blends experience an increase in molecular ordering over 100 hours of illumination. Observations of both nanoclusters of $PC_{60}BM$ and ordered polymer diffraction confirm the occurrence of the active layer morphological ripening. It is important to note that these measurements were made on films which were confined on a single side (without the physical constraint of the top electrode) which has been identified to reduce the rate of morphological $PC_{60}BM$ ripening.[137] These results should thus be considered as an accelerated test used to identify active layer changes to be expected in a double sided confined device.

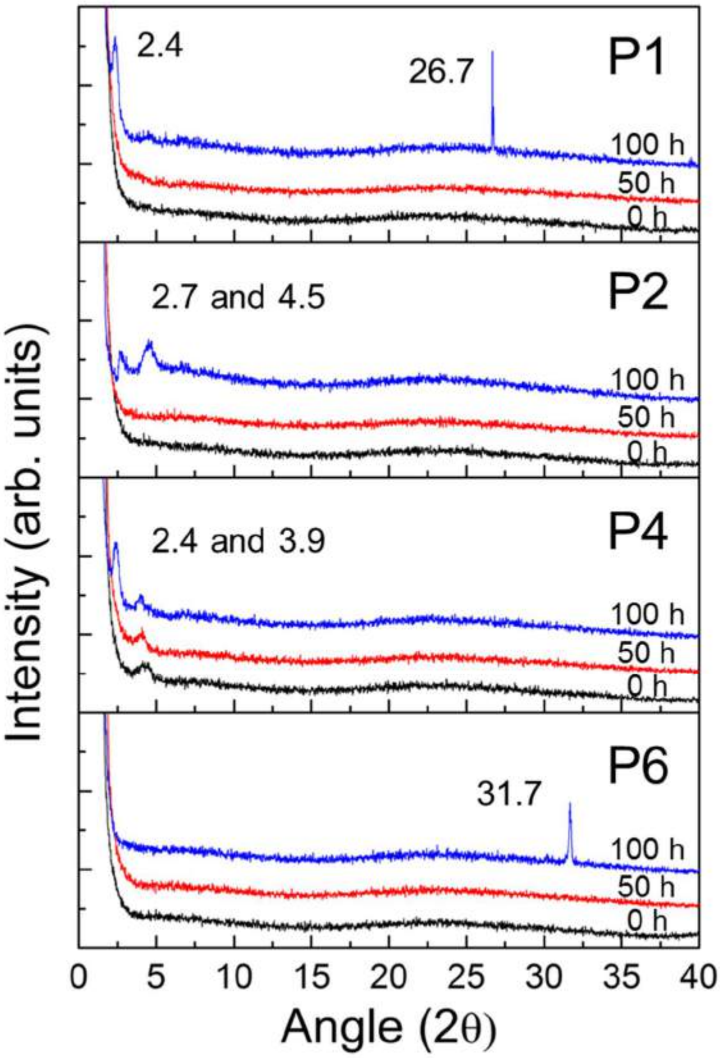

Figure 2.26 - XRD patterns of active layers at different intervals of AM1.5 solar illumination.

- *Degradation of P polymers containing devices*

The devices in this study were encapsulated with a glass cover slide and a UV curable epoxy glue. Encapsulation was performed in a nitrogen glovebox to prevent exposure to oxygen because it is known to promote OPV degradation.[65] The observed degradation of OPV devices in this analysis can be stated to be relatively oxygen free, and that oxygen exposure is not the dominate cause for degradation. This claim is also supported by the similarity in degradation of encapsulated devices to those degraded without encapsulation within a nitrogen filled glovebox.[109]

Our investigation into the degradation of the optimized polymer devices was performed for 110 hours. Upon illumination, the devices reach a surface temperature of 45±2 ˚C, however, it is likely that the OPV film reaches a higher temperature due to the additional energy absorbed in the light absorbing active layer and the insulating ~200 μm nitrogen filled gap incorporated in the glass cover slide and epoxy encapsulation. The device architecture used in each device was identical. Differences in the stability between the devices can be attributed to differences in the active layer, albeit from potentially many different causes. These causes could include morphological changes, polymer photostability, polymer/blocking layer interactions, polymer/$PC_{60}BM$ interactions and migration rates of the electrode materials or blocking layers through the polymer.[63] Each device was photothermally degraded from an optimized performance starting point thus each device had different starting active layer thicknesses which may impact the analysis. The average combined active area and interlayer thickness was measured on glass by profilometry to be 120 nm, 120 nm, 330 nm, and 220 nm for P1, P2, P4 and P6 respectively.

Photothermal degradation of the devices progressed differently for each of the active layers. P6 showed a sharp increase in performance in the first two hours of illumination resulting from increased FF and Jsc likely cause by thermal annealing of the active layer leading to improved nanoscale morphology. Each of the polymers displayed a decrease in performance after 25 hours of light soaking. Amongst the four polymers, P2 was shown to be the most stable retaining 80% of its initial PCE after 110 hours of AM1.5 exposure, known as its T_{80} (**Table 2.7**). The T_{80} for P6 (37 hours), P1 (23 hours) and P4 (10 hours) were significantly shorter. In terms of degradation rate, in the first 25 hours P2 showed the highest stability. Each of the polymers had reduced degradation rates beyond 25 hours, however relative to their starting PCE, P2 was still the most stable of the series. This initial degradation period, termed "burn-in", can be caused by $PC_{60}BM$ dimerization, morphological changes or by the formation of sub-bandgap states.[144] In this case the rapid depreciation of the performance can be attributed to the dimerization observed by UV-Vis in these films (**Figure 2.24**) which is supported by the detailed work of Distler.[134]

Current-voltage analysis during degradation identified different degradation trends. Over the 110 hours there was a minimal change in shunt resistance, however a slow increase in series resistance was noted for each of the polymers (supplementary information of Morse et al.[109]). The normalized change in series resistance was nearly identical for P1, P4 and P6, with P2 showing much slower changes. For each polymer the degradation was observed to be dominated by FF and Jsc losses. Each of the devices degraded in FF in a similar fashion, with an initial rapid drop which slows after the first 25 hours. P1 and P2 displays a slow gradual Jsc loss, P2's losses are significantly slower than P1's with only minimal losses in Jsc observed in the 110 hour time-frame. For P4, the Jsc degraded at the same rate as FF. For P6, Jsc dropped rapidly in the first 40 hours followed by a secondary more gradual decrease. P6 uniquely displayed a loss of Voc over the 110 hour experiment. Voc losses commonly indicate a change in nature of blocking layers/active layer interface (interaction, reaction or migration) which could indicate that P6 and $PC_{60}BM$ are vertically migrating to opposite electrodes or delamination of the active layer.[145] This corroborates a theory that the morphology of the active layer is changing during degradation that is further supported by the vertical $PC_{60}BM$ cluster formation observed in our AFM investigation in the previous section. Generally, across the polymer series degradation occurs at different rates implying that the nature of the polymer (i.e. variation of the side-chain) itself is directly affecting the rate of PCE loss.

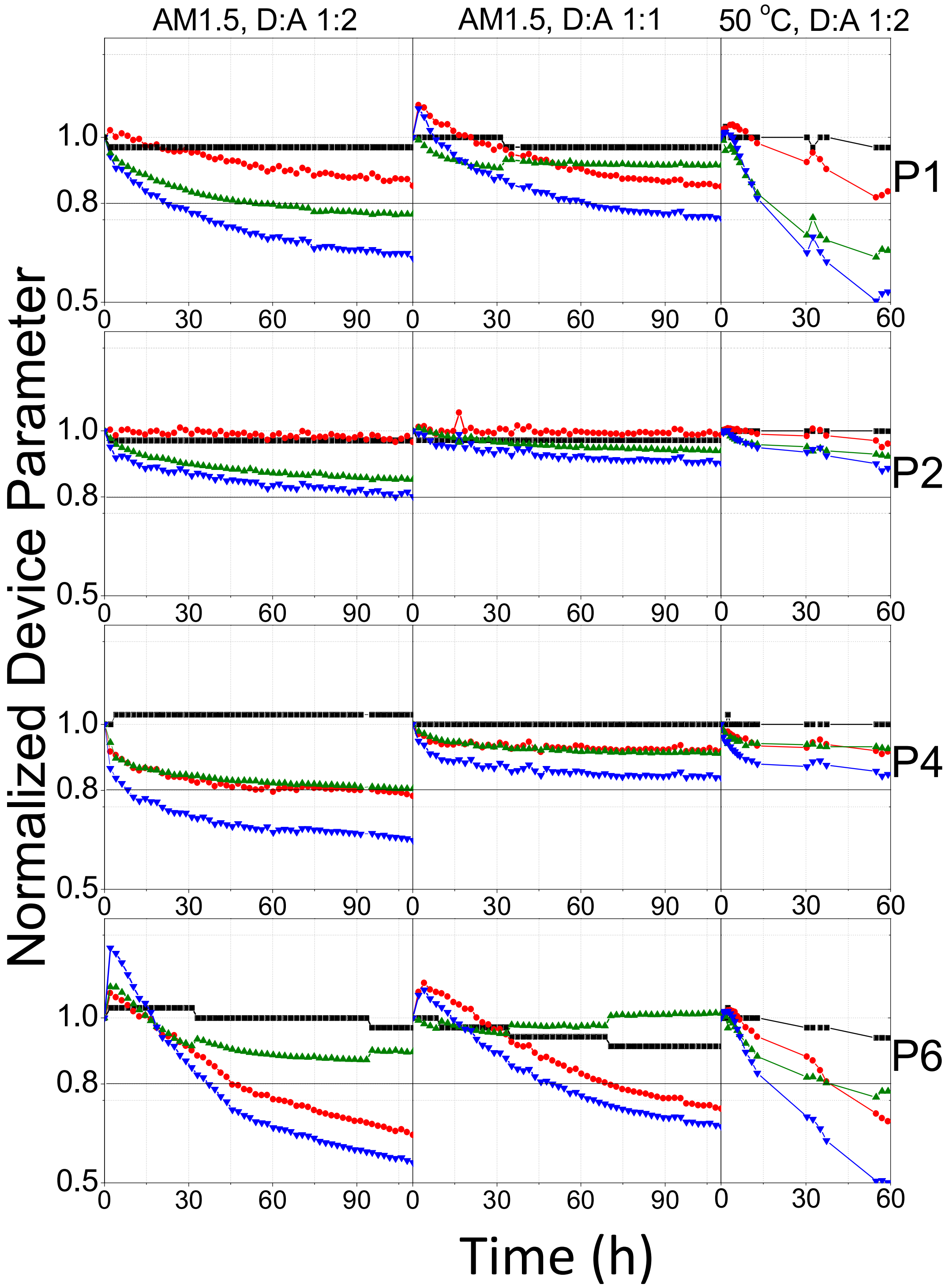

Figure 2.27 - Normalized Jsc (♦), Voc (■), FF (▲) and PCE (▼) degradation of P1-P6/$PC_{60}BM$ blends under AM1.5 illumination or thermal exposure.

- *Controlled morphological ripening*

If the rate of degradation of these devices is dependent on the active layer, then their degradation can be managed by changing active layer parameters. It is possible that the main source of degradation arises from crystallization or Ostwald ripening in the active layer. Ripening[146] and precipitation from supersaturation[147] are known processes which have been shown to occur in OPV devices containing $PC_{60}BM$. It is a process which is dependent on the diffusion of the fullerene derivative through the polymeric matrix and is a thermally activated process.[139] In the polymer fullerene blends, deposits have been observed to grow with ageing by AFM imaging which is further supported by a progressive increase in film order observed in XRD. The shape of the deposits observed in the blends by AFM was isotropic, suggesting that the process for their growth is diffusion limited.[137] If morphological changes are indeed caused by Ostwald ripening of the active layer then it would be expected that (1) the process could be adequately mimicked using an equivalent thermal treatment, and (2) that the process would be dependent on $PC_{60}BM$ loading. It is important to note that although temperature is a factor in the crystallite growth it also affects the $PC_{60}BM$ diffusion rate, $PC_{60}BM$ solubility, and surface tension rendering its relationship to crystal growth complex.

Fresh encapsulated devices were heated at a constant temperature of 50±4 ˚C, to closely match the temperature during AM1.5 illumination, and performance was measured over 60 hours. The thermal exposure led to similar device degradation to AM1.5 illumination. The rates of degradation for P2, P4 and P6 mimicked the rate of degradation under AM1.5 simulated solar irradiation. The absolute performances of the devices were also similar and within expected batch to batch variation. P1 and P6 displayed a faster rate of degradation upon thermal stress than illumination. This discrepancy may arise from differences in heating uniformity, $PC_{60}BM$ dimerization kinetics and/or polymer thermal properties (thermal transition temperatures, crystallization energy or thermal heat capacities). A critical finding was that the trends in thermal degradation of the current-voltage parameters were similar to the trends observed for AM1.5 illumination (**Figure 2.27**). These similarities suggest that degradation is strongly associated with thermal morphological changes over these timeframes.

The rate of Ostwald ripening is proportional to the concentration of $PC_{60}BM$. Ergo, reducing $PC_{60}BM$ concentration should reduce the rate of morphological change and therefore degradation. To test this hypothesis, devices with a polymer to $PC_{60}BM$ ratio of 1:1 were aged under AM1.5 for 110 hours. Across each of the polymers tested, the rate of degradation was reduced significantly (**Figure 2.27**; **Table 2.7**). The chemical kinetics of the photodimerization of fullerene should also be dependent on its concentration and therefore this process is convoluted.

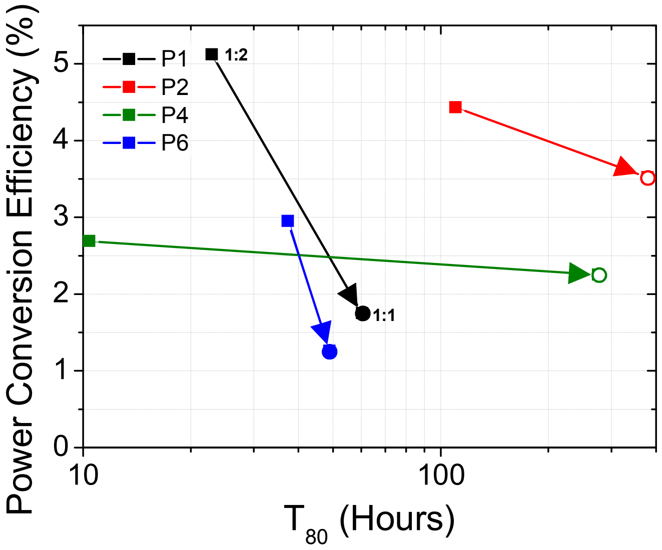

Figure 2.28 - Solar cell power conversion efficiency plotted versus T_{80} (log scale) under AM1.5 illumination for inverted devices containing polymers P1-P6 blended with $PC_{60}BM$. The effect of changing the $PC_{60}BM$ loading from 1:2 (square symbol, ■) to 1:1 (circle symbol, ●) polymer:$PC_{60}BM$ ratio is visually represented across the series showing a tendency towards more stable devices. A data point with an open circle (○) represents T_{80} estimate by extrapolating the slope observed in the last day of ageing.

The T_{80} stability has been improved for all devices for each polymer (**Figure 2.28**). Therefore lowering the $PC_{60}BM$ concentration may be a general approach to increase the PSC device stability. As we can observe in Table 2, this improvement of stability can also reduce the initial performance of the devices. Thus, for P1 and P6, this loss of initial performance is too high to be attractive. However for P2 and P4, a good tradeoff is obtained between efficiency and increasing stability. We can speculate that the charge percolation pathway preserved when reducing $PC_{60}BM$ loading which is not likely the case for P1 and P6. It is important to note that once again the current-voltage parameters which lead to the degradation are the same and trends in their degradation match the trends observed for the devices containing a ratio of 1:2 polymer:$PC_{60}BM$. This suggests that although the rate of degradation is reduced, the same failure mechanisms are causing the devices to degrade.

2.4.4. Discussion

- *Dimerization/crystallization competition*

$PC_{60}BM$ dimerization (i) and ripening (ii) have been evidenced from UV-visible spectroscopy and AFM/XRD respectively (**Figure 2.29**). Both of these processes are affected by similar parameters however they are distinct processes.

(i) *Dimerization:* requires a light exposure without oxygen (to avoid triplet state quenching) and a confined fullerene close proximity (3-4 Å).[131] The reversibility is possible at temperatures greater than 100 °C.[134] The reaction is dependent on fullerene concentration and diffusion rates (a thermally activated process).

(ii) *Ripening*: is a consequence of the $PC_{60}BM$ diffusion and is a purely thermal process. The diffusion strongly depends on the polymer matrix, in other words, the $PC_{60}BM$ diffusion is favoured if the polymer chains are relatively mobile at the considered temperature.

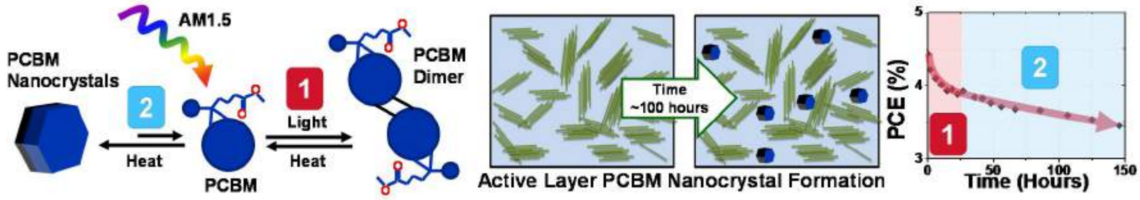

Figure 2.29 - Illustration of the reaction/mass transport kinetics of $PC_{60}BM$ to form $PC_{60}BM$ dimers or $PC_{60}BM$ nanocrystals. Illumination of the device will cause dimer formation which slows the formation of nanocrystallites. The heat generated by solar irradiation will slowly evolve nanocrystallites during exposure causing ultimate device failure.

In our case, the samples were exposed to light without oxygen and at a temperature below 100 °C. Therefore a competition between dimerization and ripening is expected. The 2+2 cycloaddition between two fullerene moieties leads to the formation of dimers. These dimers are less soluble and larger than $PC_{60}BM$ which will physically limit their diffusion in the BHJ. Thus, dimerization and crystallization together impact the device performance. Crystallization drives ultimate device failure, while dimerization can lead to very rapid losses in performance over a short timeframe. Dimerization losses are expected to stabilize after 20-30 hours as shown in **Figure 2.27**. The picture is however more complex because $PC_{60}BM$ dimers are expected to be less soluble and diffuse more slowly than $PC_{60}BM$ in a BHJ, thereby reducing crystallization rates. These convoluted processes are further influenced by the initial morphology dictated by the polymer which complicates interpretation. The dimerization process will thus limit changes in the BHJ over time, albeit with lower mobility and performance.[134] The dimers (and potential trimers and/or oligomers) themselves are present as a collection of isomers and do not possess the needed molecular symmetry to crystallize from the BHJ (**Figure 2.29**).

The nucleation density of small molecules on a 2D surface is inversely proportional to the diffusion rate of the material.[148] If we assume that the nucleation rate is diffusion limited, it is possible to deduce that the number of nucleation sites formed is inversely proportional to the diffusion rate of $PC_{60}BM$ within the polymer matrix. As a qualitative tool it is possible to rank the diffusion processes in P1-P6 by counting the nucleation density of crystallites observed in AFM.

This qualitative analysis reveals that the diffusion, *D*, of fullerene is different within each polymer matrix. The diffusion in P2 is slowest such that $D_{P2} \propto 8D_{P1} \propto 15D_{P6} \propto 16D_{P4}$. By AFM is it also possible to estimate the solubility of fullerene within the polymer matrix at operational conditions. As a first approximation we assume that the surface and bulk are similar and that the crystallites are approximated as circles, allowing us to estimate the mass of fullerene which is excluded from the BHJ over time. By this estimate the most mass is excluded from P6 suggesting that is has a low fullerene solubility/miscibility (C) and the polymers can be roughly estimated that $C_{P6} \propto 2C_{P2} \propto 15C_{P1} \propto 120C_{P4}$.

- *Influence of the polymer structure*

The rate of ripening and dimerization is dependent on similar physical parameters: $PC_{60}BM$ diffusion rate, temperature and $PC_{60}BM$ solubility in the polymer. $PC_{60}BM$ has been found to diffuse at low temperatures in P3HT, as low as 40-50 ˚C, and is observed to occur at ~50 ˚C in P1-P6.[137-142] The diffusion rate of $PC_{60}BM$ through a polymer has also been previously shown to correlate with alkyl chain length.[149] The diffusion rate of a small molecule within a polymer matrix depends more on the nature of the polymer than its molecular weight. Once above a threshold Mw of 10 kg mol^{-1} the polymer Tg and small molecule diffusion constants show little change with a further increase in Mw[150] which suggests it is a function of the chemical structure of the polymer relating to the nature of the side-chain and rigidity of the backbone.[151] The diffusion coefficient of a small molecule within a host matrix below its Tg is strongly correlated to the fractional volume of the amorphous polymer matrix.[152] It can thus be expected that the polymer which has the most evenly distributed and ordered side-chains, being lowest in void fraction, would most likely limit diffusion. Additionally, branched side-chains cause steric hindrance in solid films[153] which increases π-π stacking distances[154] and in turn increase the void fraction and therefore the $PC_{60}BM$ diffusion rate. As a corollary, increasing side-chain order decreases π-π stacking distances; locking in place the polymer chains and reducing the paths in 3-dimensional space for fullerene migration (**Figure 2.30**). Using these general rules, our results can be explained in light of the impact of void fraction on $PC_{60}BM$ diffusion (kinetic) and $PC_{60}BM$ solubility (thermodynamic).

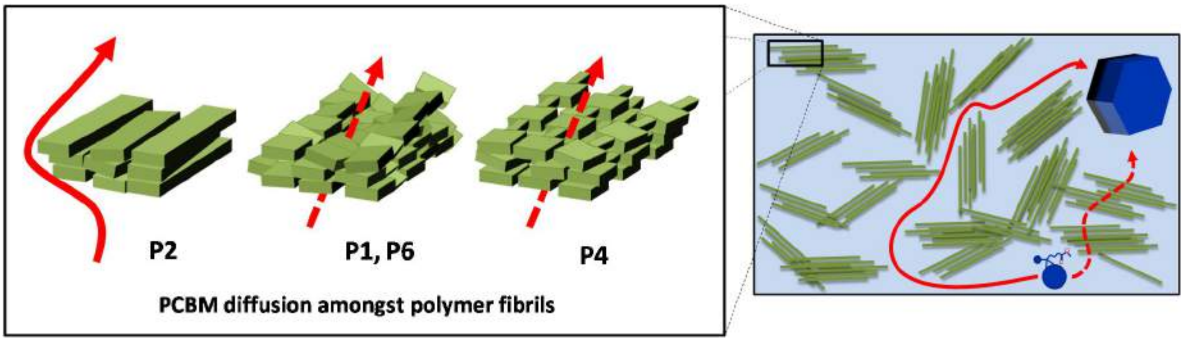

Figure 2.30 - Illustration of different formations of polymer aggregates based on backbone side chain distribution and rotation (left). In the BHJ these aggregates mediate the transport of $PC_{60}BM$ which can either pass through the aggregates or around them in a circuitous path (right).

***P2**, Linear alkyl-chain:* P2 is the most stable polymer with ordered linear side-chains and an even distribution of side-chains along the polymer backbone. The polymer aggregates of P2 are densely packed and have the shortest lamella spacing observed by XRD (once exposed to AM1.5) which is likely to reduce the $PC_{60}BM$ diffusion rate. The linear C_{12} chain is expected to lead to the lowest $PC_{60}BM$ miscibility as it displays the lowest solvent solubility of the polymer in the series and excluded a large quantity of crystallites in the AFM images at 50 and 100 hours. These nanocrystals, being small and evenly distributed, should not greatly impact performance.

***P1**, Linear alkoxy-chain:* Alkoxy side-chains can rotate freely around the oxygen molecule which should enhance $PC_{60}BM$ solubility over P1 which is reflected in a high solvent solubility. The higher $PC_{60}BM$ solubility will cause less mass to precipitate in the film. P1 also shows a large lamella spacing suggesting that the free rotation of the alkoxy chain increases disorder and hinders packing which in turn should increase $PC_{60}BM$ diffusion rates.

***P4**, No side-chain:* the lack of side-chain on the BDT core in P4 and larger branched chain on the DPP unit has two effects (i) increased $PC_{60}BM$ diffusion due to the voids in the polymer backbone and (ii) increased $PC_{60}BM$ solubility caused by potential $PC_{60}BM$ interdigitation/void filling. The interdigitation of $PC_{60}BM$ can be inferred from the increase in lamella spacing with ageing observed by XRD. The $PC_{60}BM$ solubility will be highest in this polymer which is reflected in its high solubility, and therefore nanocrystal formation is expected to be greatly reduced (as seen in AFM). Its high solubility and diffusion make it most prone to dimerization but resilient to crystal formation. P4 shows the slowest rate of decay beyond its initial losses (**Table 2.7**).

***P6**, Branched alkylthienyl-chain:* The branched alkylthienyl sidechain with both its twisted thienyl group[155] and its branched side-chain will sterically hinder solid state packing. The branched chain is however bulky and evenly distributed which should reduce the $PC_{60}BM$ solubility (reduced void fraction). In this case, low solubility but high diffusion will lead to rapid and large $PC_{60}BM$ crystal formation, which does in turn lead to rapid device failure.

2.4.5. Conclusion

A series of four low band-gap polymers of poly(BDT-*alt*-DPP) with differing side chains were synthesized by Stille polymerization. The physical properties of the polymers were similar in absorption, mobility, energy levels, and molecular weights. It was shown that a 5:1 CF:DCB solvent formulation resulted in a balance of solubility and drying time to provide adequate nanoscale phase separation with $PC_{60}BM$ when processed by doctor blade. The device PCEs ranged from 5.1% (P1) to 2.2% (P4) in inverted architecture devices with ZnO and PEDOT:PSS as transport layers. The devices were subsequently exposed to AM1.5 solar irradiation at 50°C and their degradation was monitored over 110 hours. Generally, across the polymer series degradation occurs at different rates, suggesting that the nature of the polymer chemical structure itself is directly affecting the rate of PCE loss. We have shown that this process is strongly linked to active layer morphology changes and $PC_{60}BM$ dimerization occurring with time observed by AFM, XRD, and UV-Vis analysis of the blend films. The devices could be further stabilized by decreasing the fullerene content to a 1:1 polymer:$PC_{60}BM$ ratio suggesting that the device degradation and $PC_{60}BM$ migration is diffusion limited in these films. Furthermore, the device degradation was mimicked by thermal treatment of the films (50°C, no light) indicating that morphological changes largely contribute to the device failure. Amongst the polymer series studied, BDT with a linear dodecyl chain was most stable. We demonstrate that stability of the devices is linked to the fullerene diffusion rate for the series of polymers due to the thermal instability of the polymer/$PC_{60}BM$ bulk heterojunctions. Amongst the polymer series it was shown that an even distribution of side-chains, preferably linear alkyl, promoted device stability by reducing $PC_{60}BM$ diffusion rates. On the contrary, alkoxy and thienyl-ethylhexyl side-chains increase the $PC_{60}BM$ diffusion rates in the BHJ by increasing the rotational freedom and steric hindrance of the side-chains. Removing the side-chain promoted $PC_{60}BM$ interdigitation and high diffusion rates in the films. These observations made from the data presented herein, combined with other literature precedence, can be used as rule of thumb for reducing morphology changes over time in polymer:$PC_{60}BM$ bulk-heterojunction solar cells.

2.5. Summary of chapter 2

Chapter 2, devoted to the impact of the side chain structure of a series of low ban gap polymers, explored three main issues.

Firstly, the influence of side chain structure on the photooxidative stability of a polymer series was investigated. It is well-known that the evaluation and comparison of polymers in terms of photostability is complex and depends on numerous parameters. Therefore, we have compared the photostability of a series of polymer with the same backbone structure, with similar pristine morphology, processed in comparable way and exposed to the same degradation conditions. We have shown that the photostability of the studied polymer series was dictated by two main factors, the chemical structure of the side chain and the polydispersity (PDI) of the macromolecular chains. The nature of side chain has a role on the main step of the chain radical oxidation, more precisely on the lability hydrogen atoms. The PDI seems to be related to the amount of initial defects or impurities which can play an important role on the polymer photostability. Thus, our results suggest that alkoxy side chains are promising candidate to design soluble and photo-resistant pi-conjugated polymers due to the protecting effect of the oxygen atom versus the lability of H atom on the methylene group in alpha position. Additionally, a low PDI appears to be a favorable factor regarding the polymer photostability as it could be indirectly related to a low amount of defects/traps potentially source of radicals which can then initiate or react during the photodegradation process.

Secondly, we have investigated the role of the polymer side chain on the thermal stability of the polymer:$PC_{60}BM$ blend films. In a first step we have shown that the Tg values of the studied polymer series do not change drastically. Our attempt to determine the Tg values by Raman spectroscopy were not in line with data obtained by RHC measurements and hypothesis were proposed to explain these conflicting results. Possible sub-transitions due to the film formation might be an explanation. However, we have shown then that the thermal stability of the polymer blends, in other word the ability of $PC_{60}BM$ molecules to diffuse and agglomerate, depends on the polymeric matrix. Therefore, the Tg values in our polymer series cannot be considered as the main parameter influencing the polymer blend stability. The annealing at sub-Tg temperature can be enough to modify the BHJ morphology and device performance.[116] We have suggested that the difference of thermal stability, that is to say the $PC_{60}BM$ diffusion through the polymeric matrix evidenced in the studied polymer series, could be explained by the presence or absence of sidechain on donor building blocks and by the polymer physical properties such as the molecular weight of the macromolecular chains.

Finally, we have shown that the polymer side-chains have an influence on the competition between $PC_{60}BM$ dimerization and diffusion, impacting then the global stability of the device when they are encapsulated and submitted to light soaking. We observed that lowering the $PC_{60}BM$ content can significantly increase the lifetime of the devices.

Chapter 3

The role of the “third component” on polymer blend stability

3.1. Introduction to Chapter 3

Recently, many investigations were carried out by the scientific community regarding the role of a “third component” in a polymer blend film. By “third component” we mean the role of an undesired or desired component mixed with polymer:PC$_{60}$BM film which could be residues of solvent or additives most of the time. Additives are frequently used for optimizing the Bulk Heterojunction (BHJ) of the polymer blend films (See 1.2.4) which is one of the key points for boosting the device performance.

The first part will concern the crucial role of confined residual additives on the polymer blend photostability. After processing, residues of additives (used for optimizing the BHJ) remain in the active layer and are susceptible to influence the polymer blend photostability.[40,156]

The second part will deal with the use of Hindered Amine Light Stabilizers in polymer blends. HALS is a well-known family of additives widely used in the polymer industry in order to improve their stability when exposed outdoor. We have investigated the effect of HALS incorporation in pi-conjugated polymer blend film.

The last part will focus on the use of a polyfullerene as BHJ thermal stabilizer. The underlying idea is to use a “ready to use” material as additive for restricting the PC$_{60}$BM diffusion and thus increasing the BHJ thermal stability.

Scientific contribution

The present work is the result of a collaborative work within the *Establis* project. The synthesis and characterization of the polyfullerene was performed by Hasina Ramanitra (ESR12, University of Pau) and the device fabrication and degradation done by Dr. Simon Dowland (ER2, Belectric compagny). The thermal degradation of the polymer blends with and without the polyfullerene was done in collaboration with Hasina Ramanitra.

3.2. The crucial role of confined residual additives on the photostability of polymer blends

3.2.1. Introduction

Polymer Solar Cells (PSCs) are based on bulk hetero-junction (BHJ) photoactive blends composed of a mixture of an electron-donating polymer and an electron-accepting fullerene derivative.[26,157] An optimized BHJ layer requires specific phase separation of the donor-acceptor components to enable optimum charge carrier generation in the blend and charge percolation pathways for efficient electron and hole collection to the respective electrodes.[34,158] The donor and acceptor domain sizes must be in the order of the exciton diffusion length, which typically ranks from 3 to 10 nm for conjugated polymers.[159,160] Optimized phase segregation can be promoted by post-deposition film processing such as thermal or solvent annealing as well as by using appropriate solvent(s) and/or specific solvent additives.[47,161] This latter strategy has been recently investigated by testing different additives. [39-42,162-167] Promising results were obtained with alkane derivatives such as R-$(CH_2)_8$-R (3% in volume).[42] The chemical nature of the alkyl substituents (R) modifies the physicochemical properties of the additive and especially its boiling point (Bp). Two criteria have been identified for successfully processing additives: a selective solubility of the fullerene in the component on the one hand and a higher Bp than the host solvent on the other hand.[42] The selective solubility is necessary to preform donor and acceptor domains in solution and the difference of Bp to preserve the domains during the drying process. Chlorobenzene (CB) and Dichlorobenzene (DCB) are the two main solvents used for efficiently solubilize and process P3HT and $PC_{60}BM$. (**Figure 3.1**) The Bp of CB and DCB is 132 and 180°C respectively, and therefore additives must have a higher Bp. Diiodoctane (DIO, Bp=366°C) and octanedithiol (ODT, Bp= 270°C) have been identified as efficient additives with a significant improvement of the power conversion efficiency (PCE) in various polymer blend systems.[5-9]

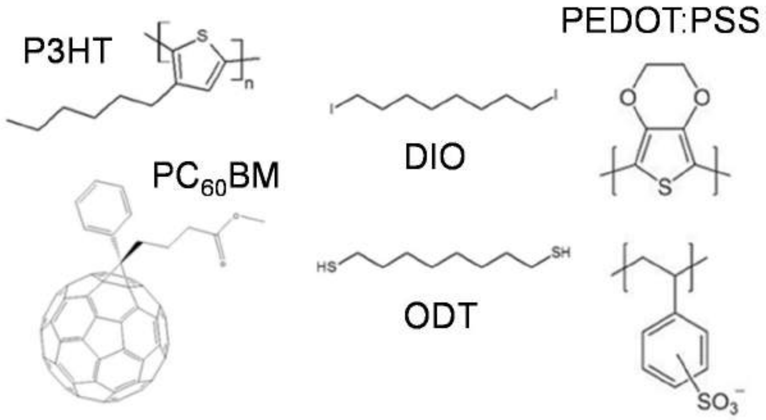

Figure 3.1 - Chemical structure of organic materials used in this work.

An undesired consequence of their high Bp is that part of the additives remains trapped in the film. In this regard, Ye et al.[40] have recently reported the negative impact of residual additives on the reproducibility of PSC performance. Besides, for a promising industrial future, the PSCs technology has to take into account not only the performance but also the stability. To our knowledge, the impact of additives on PSCs stability has been hardly studied. Distler et al.[90] compared the polymer blend photooxidation with unconfined films processed with and without DIO. These authors studied the impact of the morphology (dictated by the presence or not of additives) on the rate of photooxidation. However, they did not focus on the impact of residual additives, especially in confined environment. Moulé et al.[168] have reported on the role of solvent and additive traces on the thermal stability in inert atmosphere of P3HT:PC$_{60}$BM blends. However it is important to keep in mind that PSCs are exposed to light under operating conditions and that oxygen can diffuse in the bulk of devices.

In this context, the main objectives of the present work were i) evaluate the impact of ODT and DIO residues on the P3HT:PC$_{60}$BM blends photostability ii) identify the mechanism(s) of degradation and iii) propose strategies to improve the polymer blends photo stability.

3.2.2. Experimental

Please, refer to the appendix (A1) for additional details on the experimental techniques.

- *Sample preparation and degradation*

Phenyl-C61-butyric acid methyl ester (PC$_{60}$BM) was obtained from Nano C. Diiodooctane (DIO) and octanedithiol (ODT) were purchased from Aldrich with a purity of 98%. Poly(3-hexylthiophen) (P3HT) was purchased from Rieke Metals, Inc. with a molecular weight (Mn) of ~50.000 and a regioregularity (RR) of 96%. P3HT and PC$_{60}$BM in 1:1 weight ratio were both dissolved in chlorobenzene (CB) w/wo 3% in volume of DIO or ODT and were deposited by spin coating (~100 nm) on glass and KBr substrates. (**Figure 3.2**) To get statistical results, series of three samples were prepared for each experiment. The series of samples casted with DIO and ODT additives are called “DIO” and “ODT” respectively. The series of films without additives was optimized by a standard thermal annealing treatment of 15 min at 120°C under inert atmosphere, and called “TA”. By analogy to a typical inverted PSC structure, a standard PEDOT:PSS layer (~50 nm) was deposited on the top.[169] The PEDOT:PSS used is a standard Clevios HTL solar. Finally the impact of the confinement on the active layer photostability (w/wo residual additives) was investigated by comparing the degradation of P3HT:PC$_{60}$BM layers with the PEDOT:PSS on the top without top layer and with a KBr substrate.

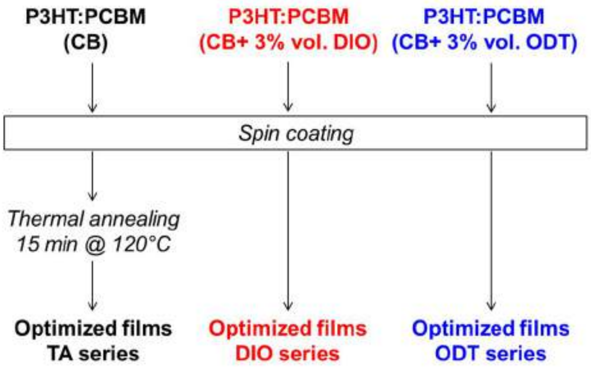

Figure 3.2 - Experimental design of samples preparation.

Irradiations were carried out in ambient air (30-35% humidity) in SUNTEST device (from Atlas) equipped with a xenon lamp. The light intensity was 750 W m^{-2} in the 300−800 nm domain, and the temperature of the samples was ca. 42 °C.

- *IR and UV-visible spectroscopy*

Infrared spectra were recorded in transmission with a Nicolet 760-FTIR spectrophotometer working with OMNIC software. Spectra were obtained using 32 scan summations and a 4 cm^{-1} resolution. Changes in UV-Vis spectra were followed with a Shimadzu UV-2101PC spectrophotometer equipped with an integrating sphere. UV-vis and IR measurements were performed approximately one hour after the samples deposition and the time between spin coat deposition and pristine characterization for all individual samples was very similar.

3.2.3. Results and discussion

- *Initial characterization*

Pristine samples were characterized by UV-visible and IR spectroscopy. The general UV-visible spectrum of a P3HT:$PC_{60}BM$ film in the 300-800 nm region consists of a main and broad band in the 400-650 nm region related to P3HT absorption, and another band in the UV region (~330 nm) related to $PC_{60}BM$. The shape of the P3HT band depends on the polymer organization and can be impacted by different factors: solid/solution state, solvent used, intrinsic morphological characteristics such as regioregularity (RR) or the molecular weight (Mn), blend effect or post-treatment.[3,4,170] The as-casted P3HT:$PC_{60}BM$ film (**Figure 3.3**, dotted line) presents a broad band centered at 480 nm with a weak shoulder around 600 nm which suggests a no-well defined ordering of the polymer mainly attributed to the $PC_{60}BM$ plasticizer effect.[171] It is known that this partial ordering can be significantly improved by thermal annealing treatment.[3,4,172] After thermal treatment (15 min @120°C under inert atmosphere), the corresponding UV-Vis spectrum (TA series) shows drastic modification related to significant improvement of the blend morphology. The shift of λ_{max} (from 480 to 510 nm), the increase of the absorbance (+20% at λ_{max}, +55% at 600 nm) as well as the emergence of a new band at 550 nm translate a higher ordering of the P3HT packing. The UV-Vis spectra of DIO and ODT series exhibit well-defined and intense bands at 550 and 600 nm and the λ_{max} observed at longer wavelength (517 nm) compared to the TA series reveal a higher degree of crystallinity of the polymer. These observations are in good agreement with previous studies.[3-4] The presence of residues in DIO and ODT series can be easily detected by IR spectroscopy.(**Figure 3.3**) DIO can be identified by two bands at 1206 and 1175 cm^{-1} attributed to C-H wagging (from CH_2-I) and one from the C-I stretching at 505 cm^{-1}. Regarding ODT, the stretching mode of the S-H bound at 2560 cm^{-1} can be used, even if the intensity is weak, to detect the presence of additive. For both additives, a modification of the alkyl side chain vibrations region (2980-2850 cm^{-1}) was observed as well.

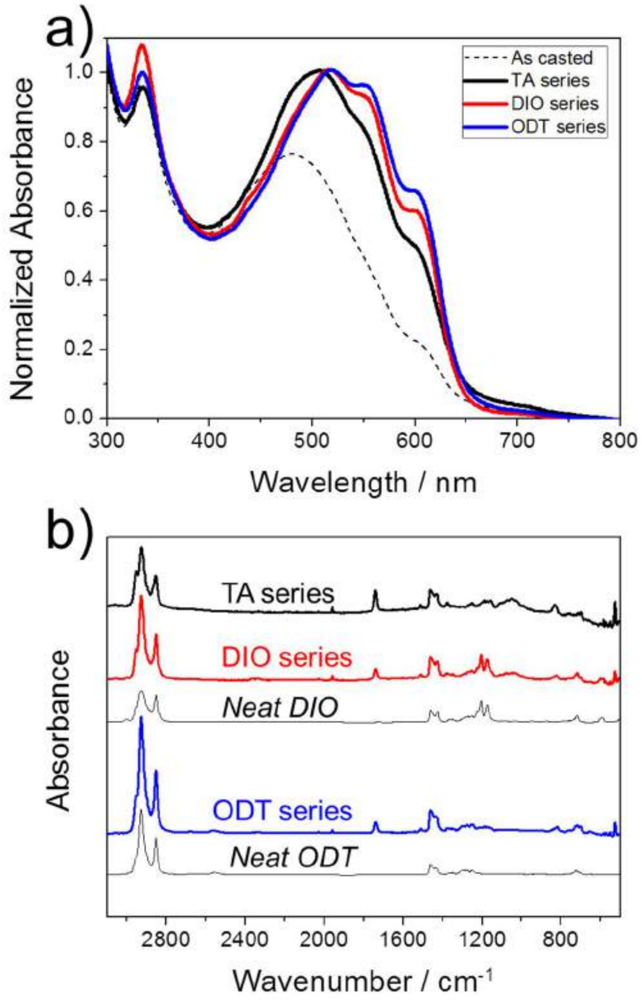

Figure 3.3 - UV-visible (a) and IR spectra (b) of the TA (black), DIO (red) and ODT (blue) series. The UV-vis spectrum of an as-casted film (dots) and IR spectra of neat DIO and ODT complete the picture.

We also focused on the reproducibility of the deposits which is crucial for scientific interpretation and for the development of industrial production with appropriate reliability. The variations of the initial absorbance (measured for each sample at λ_{max}) were 2 %, 7 % and 16 % for TA, DIO and ODT series respectively. The higher fluctuation of the absorbance for DIO and ODT series is likely to be caused by the variation of morphology due to the use of additives. The amount of residual additives observed by IR is well reproducible and cannot fully explain the higher fluctuation observed by UV-visible spectroscopy. This is in good agreement with the observation of Ye. et al.[14] who suggested that the use of additives affects the reproducibility of device performance due to a fluctuation of the BHJ morphology.

Pristine characterizations allowed us to evidence that annealing treatment as well as process additives allow optimizing the BHJ morphology on the one hand, but the use of additives gives residues trapped in the BHJ and results in BHJ morphological distortion from sample to sample on the other hand.

- *Photodegradation*

In a second step, all samples (from all series) were covered by a standard PEDOT:PSS layer and were submitted to photooxidation (Xe lamp, 750W/m², 45-50°C, ambient air). Blends degradation was monitored by measuring the evolution of the absorbance of the samples (in the range 300-800 nm) versus irradiation duration as reported in **Figure 3.4**. We essentially focused on the initial stages of degradation, which plays an important role for applications as a loss of few percent of the polymer absorbance can lead to a drastic change of the device performance.[173]

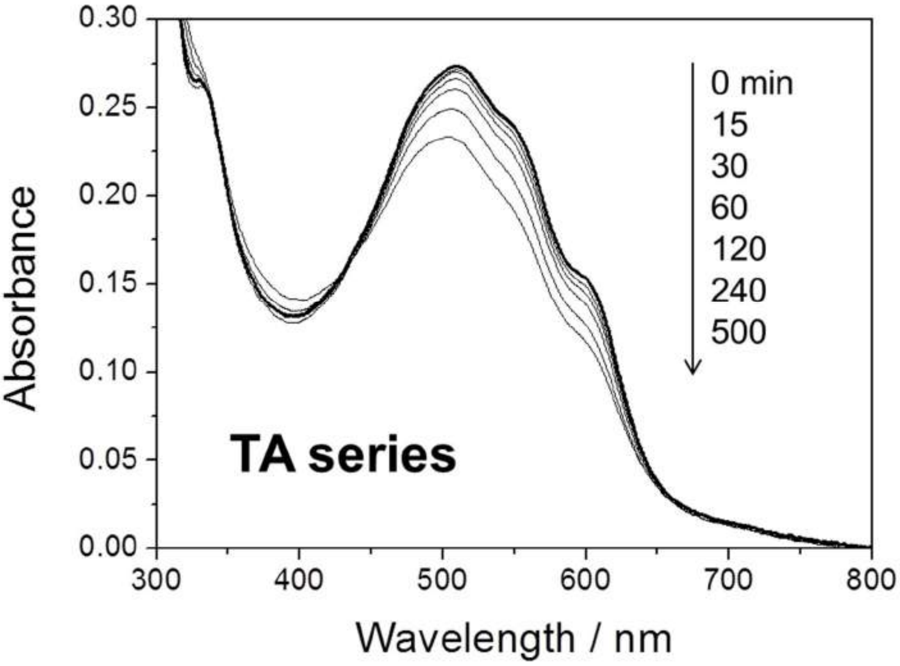

Figure 3.4 - Evolution of the P3HT:PC$_{60}$BM absorbance (300-800 nm) of the TA series versus time of photooxidation. (0-500 min).

The normalized decays of absorbance at λ_{max} for all series of samples are compared in **Figure 3.5**. Focusing on the degradation of the TA series, a linear and well reproducible decrease of the absorbance is observed, with a low and constant deviation. (-9% of the initial absorbance after 250 min of irradiation with a deviation of 3%) Regarding samples treated with ODT, similar decay is observed but with a higher fluctuation. (23% of deviation) For DIO, a rapid drop of the absorbance (-10%) occurs within the first 15 min of exposure, and then a linear and less pronounced decay is observed. This rapid decay could be likely attributed to i) a morphological reorganization of the BHJ (due to a metastable initial morphology) and/or ii) a photochemical reaction involving the DIO additive with its environment i.e. P3HT, PC$_{60}$BM or PEDOT:PSS. The first option corresponds to a thermally-assisted process and the second one to a photochemically-assisted one. It has been observed that the reorganization (thermally induced) of P3HT:$PC_{60}BM$ films affects the $PC_{60}BM$ absorption band (330 nm) due to the formation of $PC_{60}BM$ clusters in the P3HTdomains, which progressively scatter the incident light but the P3HT absorption remains constant.[174] In the present case both P3HT and $PC_{60}BM$ bands are impacted suggesting that the initial decay may be likely attributed to a photochemical reaction. In this context, IR spectroscopy can provide valuable information. Unfortunately the presence of the PEDOT:PSS layer hinders the IR analysis in transmission mode. The PEDOT:PSS absorbs in a large domain (1700-500 cm^{-1}) masking the main vibrational modes P3HT and $PC_{60}BM$.

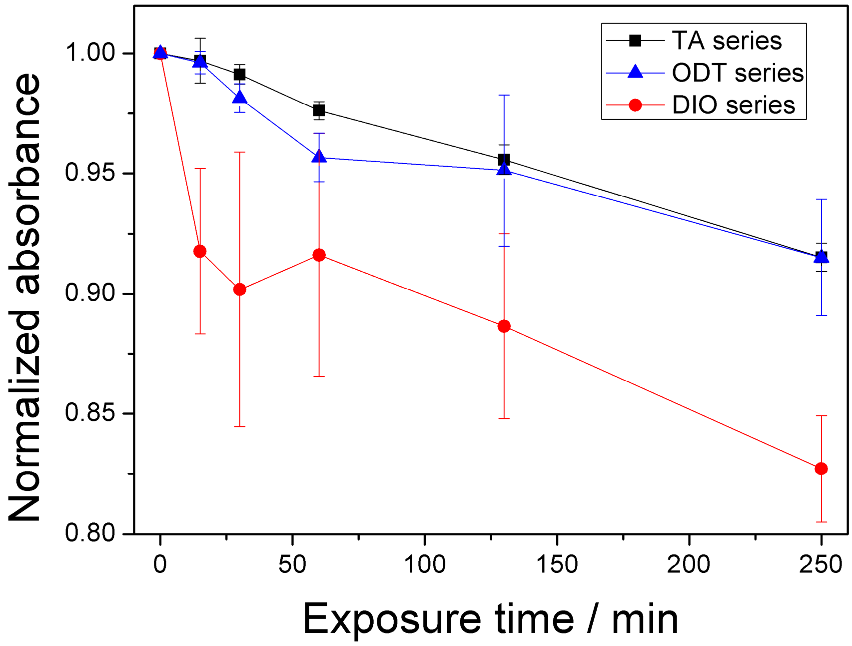

Figure 3.5 - Decay of the normalized P3HT absorbance (measured at λ_{max}) for the TA (black), DIO (red) and ODT (blue) series upon light exposure in air. Each symbol represents the averaged absorbance obtained from three samples and the error bars represent the corresponding standard deviation. All the active layers were covered by a standard PEDOT:PSS layer.

Therefore, in order to achieve a better understanding of the observed phenomena and obtain information related to the chemical structure of the components of the blend, the same series of samples were prepared and exposed to the same degradation conditions but without PEDOT:PSS top layer (See **Figure 3.7** for all series). The presence of residual additives was evidenced by IR spectroscopy as previously shown. (**Figure 3.3**) In an unconfined environment data reported in **Figures 3.7** reveal similar rate of degradation and deviation for all series w/wo residual additives. Additionally, the initial important drop of absorbance previously observed with DIO series covered by PEDOT:PSS is not observed without top layer. Looking at the IR spectra, we can observe that after 15 min of exposure, the entire DIO residue (in the limit of IR detection) has vanished suggesting a significant photo-instability of DIO molecules. (**Figure 3.6**) A simple physical desorption is not considered as a dominant phenomenon as DIO has a low saturated vapor pressure at room temperature[14] which hinder an efficient evaporation of the molecules even at 50°C (in the dark). (See Appendix 3.1 or Figure S1 of Tournebize et al.[156]) The fast DIO disappearance is not accompanied by a concomitant modification of the chemical structure of P3HT and $PC_{60}BM$. (**Figure 3.6**) The IR spectra obtained after 15 min of exposure corresponds to a virgin P3HT:$PC_{60}BM$ film. The comparison of the DIO series w/wo PEDOT:PSS top layer suggests the following comments. Without a top layer, DIO residues are simply eliminated without damaging P3HT and $PC_{60}BM$ probably by a light-induced decomposition of the DIO molecules into by-products which then migrate out of the solid film. In other words, the residues are cleanly removed. However, the presence of PEDOT:PSS top layer seems to act as a barrier even if this film is relatively thin (~50 nm), and consequently the DIO molecules (or by-products) are trapped in the BHJ and may react with P3HT and/or $PC_{60}BM$. Focusing now on the ODT series, this additive is not easily detectable due to overlapping with P3HT vibrational modes but no clear changes in the IR spectra are observed after short irradiation duration.

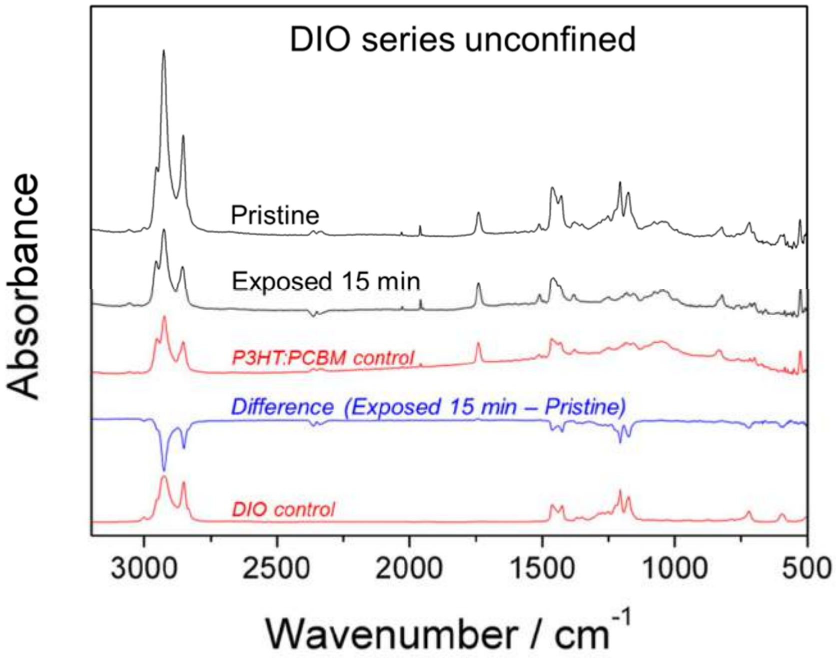

Figure 3.6 - Direct IR spectra of a sample from the DIO series (unconfined) before and after 15 min of irradiation. (black) The “Exposed 15 min” spectrum as well as the “Difference (Exposed 15 min – Pristine)” (blue) can be compared to a pristine P3HT:$PC_{60}BM$ film and a pure DIO spectra (red).

In order to analyze the impact of additives on the chemical structure of the polymer blend materials in a confined configuration, the use of a transparent top layer to the IR beam is required. For this, new series of samples (TA, DIO and ODT) were submitted to irradiation with a KBr substrate as a top layer. KBr was chosen for several reasons: i) it is an inert substrate and no potential reactions could occur which cannot be guaranteed for an organic layer like PEDOT:PSS layer, ii) it is a thick top layer (4 mm) therefore the barrier effect is much more pronounced than with the PEDOT:PSS layer which can facilitate the observation of the mechanism, and iii) the substrate is transparent in the range of the irradiation source as well as in the range of the IR beam allowing therefore an accurate analysis. Thus, TA, DIO and ODT series inserted between two KBr substrates were exposed in the same irradiation conditions. We assume that the oxygen content is not a limiting factor as oxygen can diffuse from the sides of the "KBr-sandwiched' active layers. The results are shown in **Figures 3.7** and can be compared to the unconfined series or covered by a PEDOT:PSS top layer.

As previously observed, a weak and approximately linear decay of the absorbance (3-4%) is observed, with good reproducibly, for the all TA series (TA/none ~ TA/PEDOT:PSS ~ TA/KBr) during the time frame of the irradiation. This result suggests that the presence of a top layer and especially KBr does not perturb the conditions of degradation. (oxygen content, light scattering …) Focusing then on the DIO/KBr series, a rapid decay is observed. This decay is similar to that observed for the DIO/PEDOT:PSS series, but with a higher rate : indeed, a 30% drop (in average) of the absorbance occurs after only 60 min of exposure. Comparing the different top layers, we can classify the impact of DIO on the polymer blend photostability as following: TA = DIO/none < DIO/PEDOT:PSS < DIO/KBr. It can therefore be concluded that the presence of the top layer pushes the DIO to react with the active layer materials due to the barrier effect and this effect is reproducible within the DIO series.

The interpretation of the impact of ODT on the polymer blend stability is delicate as the reproducibility is very bad (except for ODT/none series), but again an important role of the top layer is observed according to: TA = ODT/none ~ ODT/PEDOT:PSS < ODT/KBr. We can note that the kinetic of the degradation is different for ODT and DIO series. Covered by a KBr substrate, we can observe that for the DIO series, a rapid and brutal impact occurs while an almost linear and progressive evolution is observed for ODT series. This may suggest a different mechanism of degradation.

With KBr top layer, we have access to the evolution of the chemical structure thanks to IR spectroscopy in the transmission mode. (**Figure 3.8**)

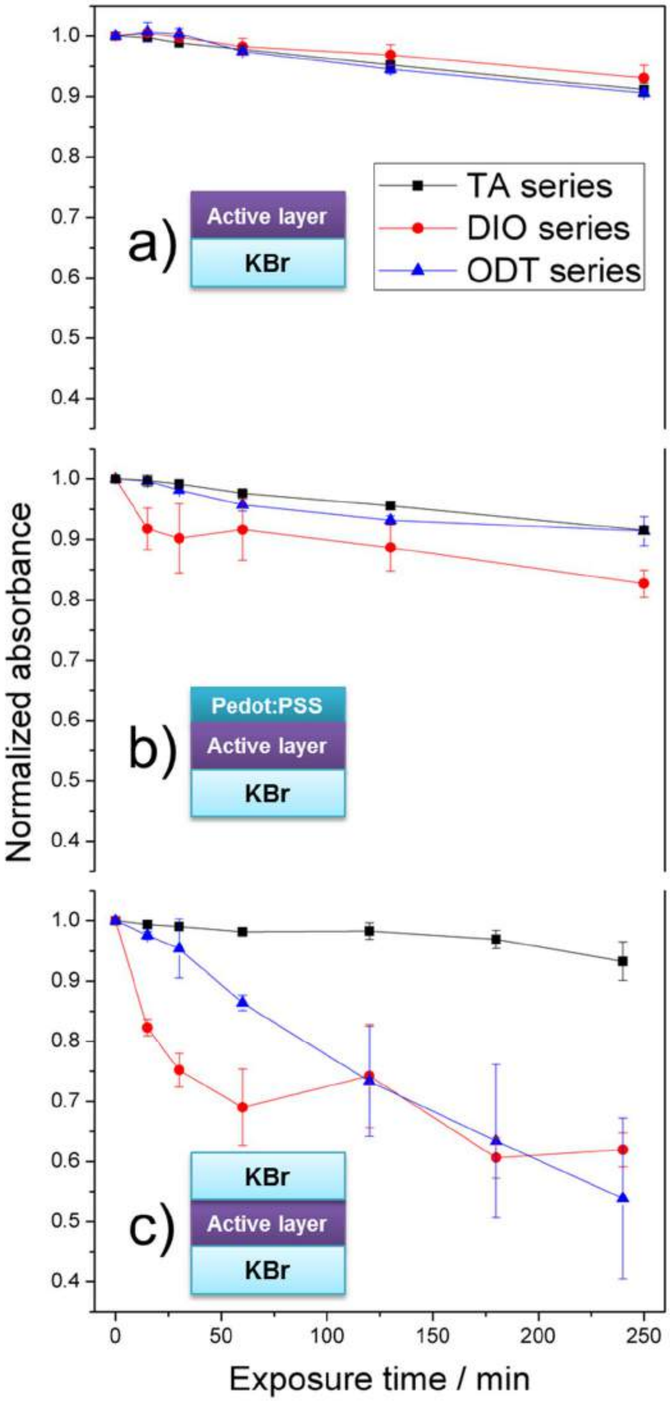

Figure 3.7 - Evolution of the P3HT absorbance (taken at λmax in the visible region) of the TA (black), DIO (red) and ODT (blue) series versus time of photooxidation in the different confinement conditions: without top layer (a) with PEDOT:PSS (b) and KBr (c) top layer. Each symbol represents the averaged absorbance obtained from three samples and the error bars represent the corresponding standard deviation.

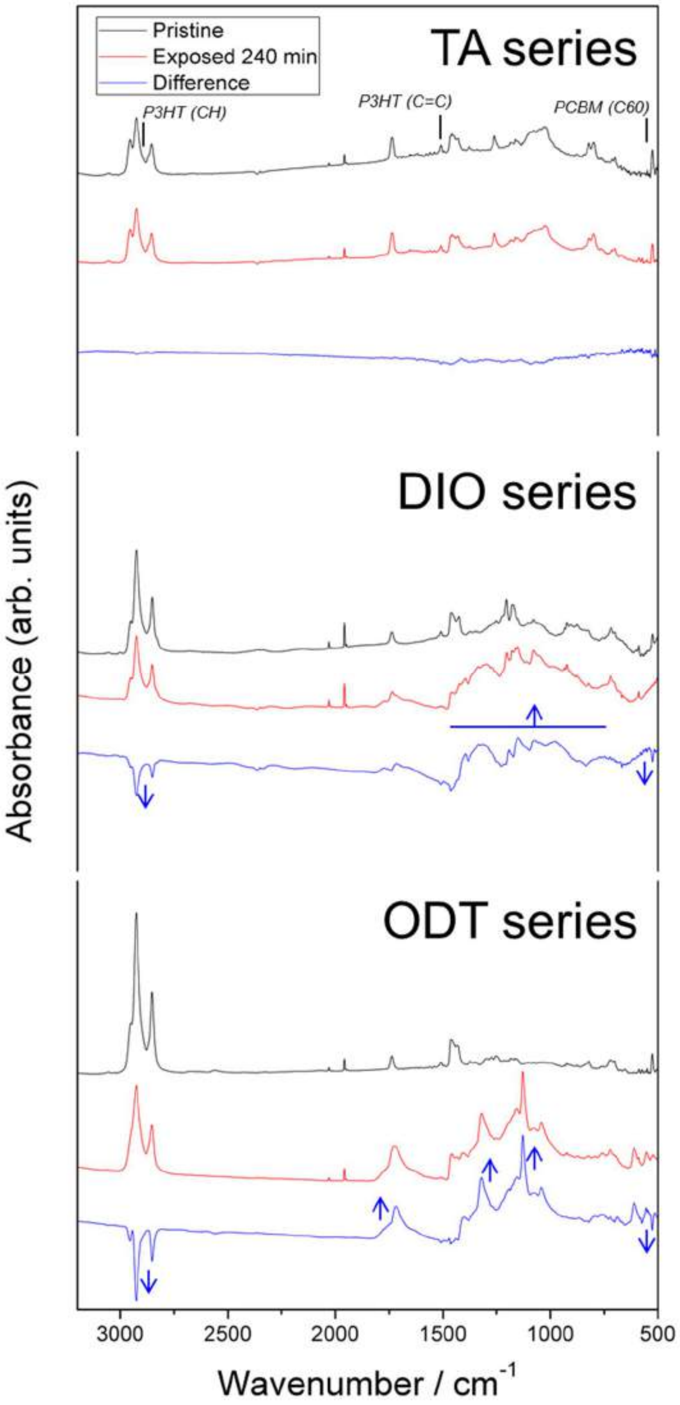

Figure 3.8 - Direct (Pristine and after 240 min of irradiation) and subtracted (“Exposed 240 min – Pristine”) FTIR spectra of TA (a), DIO (b) and ODT (c) series covered by a KBr. Arrows on subtracted spectra indicate the vibrational modes consumed (pointed down) i.e. CH (2925 cm^{-1}), C=C (1510 cm^{-1}) and C60 (526 cm^{-1}) moieties and formed (pointed up) i.e the carbonyl region (1775-1630 cm^{-1}) and sulfoxide species (1320 and 1120 cm^{-1}).

For the TA/KBr series, a mean 3-4% drop of the UV-vis absorbance is measured after 240 min of irradiation. No clear formation of degradation product is observed, likely due to the limit of detection of the IR apparatus and a possible low molar extinction coefficient of formed photodegradation species. Nevertheless, a loss of 5%, 14% and 22% in average of the CH, C60 and C=C vibration is observed respectively. (**Figure 3.8** and **Table 3.1**) For ODT/KBr series, the drastic 50% drop of absorbance observed after 240 min of exposure is accompanied by main modifications of the chemical structure. Indeed, a loss of 39, 46 and 59% was measured for the CH, C=C and C60 groups respectively. The consumption of initial chemical groups is concomitant with the formation of carbonyl (1775-1630 cm^{-1}) and sulfoxide (1320, 1120, 1040 and 614 cm^{-1}) species.(**Figure 3.8**) These photoproducts result from the photooxidation of the active layer materials and can be ascribed to the photooxidation of P3HT (carbonyl and sulfoxides) and PC$_{60}$BM (carbonyls) in agreement with Manceau et al.[72]

	TA series			DIO series			ODT series		
Vib. Mod.(cm^{-1})	CH	C=C	C60	CH	C=C	C60	CH	C=C	C60
Av. Loss (-%)	5 +/- 2	22 +/-6	14 +/-7	44 +/-14	53 +/-26	99 +/-1	39 +/-6	46 +/-24	59 +/-28

Table 3.1 - Summary of loss of the main vibrational modes: CH (2925cm^{-1}), C=C (1510 cm^{-1}) and C60 skeleton (526 cm^{-1}) after 240 min of irradiation of the different series.

We can note that the presence of high amounts of photo oxidation species in the aged ODT/KBr series indicates that the availability of oxygen is definitely not a limiting factor in our study (lateral diffusion). The presence of ODT residues apparently accelerate the photooxidation process of P3HT:PC$_{60}$BM. The acceleration of the degradation was observed for all samples but with high fluctuation (important error bar). Focusing lastly on the DIO/KBr series, an important decrease of the initial absorbance is observed after 240 min of exposure (40%) as previously observed for ODT/KBr series. However a quite different evolution of the chemical structure is observed. Indeed, a drastic consumption of the initial bands is observed with a loss of 44, 53 and 99% of the CH, C=C and C60 groups respectively. (See **Table 3.1**) Besides, no well-defined photoproducts are observed to be formed, and especially low amount of photoxidized species conversely to the ODT/KBr series. An increase of absorbance in the 1400-1100 cm^{-1} region is observed which provokes a shift of the baseline but no-well defined products can be identified. Therefore, we suggest that a different mechanism of degradation occurs in the case of DIO. As a very important consumption of the C=C and C60 is observed with no well-defined photooxidation products formation, it is reasonable to propose that the degradation of DIO molecules involves a photo-induced radical process which is the case for any chromophoric organic material submitted to light irradiation.[66] Thus, the radicals formed in the photochemical decomposition of the DIO molecules are susceptible to saturate the C=C bonds resulting in an important loss of absorbance. Additionally, the radical so-formed can be trapped by the PC$_{60}$BM which is a radical scavenger[88] and this process could account for the total disappearance of the C60 skeleton vibration. The two different mechanisms proposed for DIO and ODT series can be supported by the evolution of the visible absorbance (**Fig. 3.7**). A linear decay of the absorbance is observed for the TA series (no residues) during the first stage of photooxidation. Regarding the DIO series, the degradation involves a first exponential decay. This evolution supports the radical mechanism proposed in the sense that the DIO molecules react very rapidly and saturate their neighboring environment. Once all molecules transformed, the standard photoxidation process can occur (as for the TA series). This is completely different for the ODT series. The decay of the absorbance is linear from the beginning of exposure which confirms a different mechanism of degradation compared to the DIO series. Nevertheless, the slope is more important than the one of the TA series suggesting a progressive involvement of ODT in the radical photooxidation mechanism of P3HT:PC_{60}BM resulting in an acceleration of the degradation rate. In other words, ODT residues could act as a radical initiator. In order to get more insights into the degradation mechanism of DIO and ODT, a droplet of each additive and the host solvent (CB) was inserted between two KBr substrates. In a first experiment, samples were only submitted to soaking at 50°C in the dark which only provoke hardly reductions of absorbance. (See Appendix A3.1 or Figure S1/S2 of Tournebize et al.[156]) This result confirms the low ability of these two additives to migrate into the gas phase (by lateral diffusion) under atmospheric conditions and even at 50°C. However after long time of soaking in the dark at 50°C (500h) the presence of oxidized species was detected by IR spectroscopy for ODT samples only, suggesting that this additive is not thermally stable in air even in the dark. (See Appendix A3.2 or Figure S4 of Tournebize et al.[156]) In a second experiment, samples were submitted to the same conditions of soaking (50°C) but under light exposure (Xe lamp, 750 W/m^2). (See Appendix A3.3 or Figure S1/S3 of Tournebize et al.[156]) No significant modification on the chemical structure was observed for ODT after 50h, but after longer exposure (300h) (photo)oxidized species were observed confirming therefore that this additive is sensitive to oxidation. (See Appendix A3.2 or Figure S4 of Tournebize et al.[156]). Similar oxidation products are formed w/wo light, but light drastically accelerate oxidation kinetics. The weakness of ODT appears to be related to the S-H end-group. Indeed, the vibrational signature of S-H at 2556 cm^{-1} disappears the most rapidly compared to other vibrations, and sulfoxide derivative are formed (1410, 1040 cm^{-1}). Nevertheless, the alkane part is also impacted as indicated by the decrease of the C-H groups and the concomitant formation of the carbonylated oxidation species. Focusing now on DIO samples, the molecules are stable in the dark but light provokes a rapid and important disappearance of the initial bands of the additive, but no photoproducts are formed in parallel. This means that DIO is decomposed by light and that by-products are not trapped in the film.

3.2.4. Conclusion

Herein, we have demonstrated that DIO and ODT residual additives are not stable upon light exposure in air and strongly impact the polymer blend stability. Two different mechanisms were proposed for DIO and ODT. DIO molecules are highly sensitive to light and the radicals formed are susceptible to saturate instantaneously the neighbor pi-conjugated backbone of the polymer and or be trapped by the fullerene. ODT molecules are sensitive to (photo)oxidation (light accelerates the oxidation) and participate/accelerate the radical photooxidation mechanism of the polymer blend materials. We have demonstrated that the confinement of the active layer plays a major role on the residual additives reactivity. When confined in the BHJ by a top layer, residual additives, or more precisely the photoproducts issue from their degradation, cannot migrate out of the film and strongly react with the polymer and fullerene provoking their rapid degradation. However, we have observed that a light soaking process before the deposition of the top layer appears to be an efficient way to remove cleanly the residual additives.

The two required criteria for successfully use the additives are: a selective solubility of the fullerene with/in the component on the one hand and a higher Bp than the host solvent on the other hand.[5] However, it was demonstrated recently that the BHJ of P3HT:PC$_{60}$BM and PCDTBT:PC$_{60}$BM can be optimized by the use of additives with a lower Bp as the host solvent.[175] They found that THF (Bp~65°C) has a similar effect on the device property as ODT (BP~270°C) with ODCB (BP~180°C) as host solvent. Our results encourage the use of low Bp solvents and additives in order to avoid residues and therefore crucial effect on the photostability of the active layer.

3.3. The use of HALS (Hindered Amine Light Stabilizers) in polymer blend films

3.3.1. Introduction

As shown in part **3.2**, residual additives can drastically impact the polymer blend stability especially in the confined environment of the device. Additives (or a certain amount of additives) remain trapped in the polymer matrix due to their high boiling point (Bp) and are susceptible to negatively impact the polymer blend photostability.[40,156] In the present section, we have investigated the effect of additives which are usually used as stabilizers for a wide range of plastics. Technical polymers of our daily life are always formulated with additives in order to improve their resistance to outdoor exposure. One of the most famous family of additives is the so-called Hindered Amine Light Stabilizers (HALS). The mechanism of stabilization of HALS is very complex. The commonly accepted mechanism is represented in **Figure 3.9** and known as the Denisov cycle.[176,177] When HALS molecules are in presence of a polymer exposed to light and oxygen, tempo radicals (N-O°) are created. These tempo radicals can intercept radicals (R) created along the chain radical oxidation mechanism of polymers (see the radical mechanism in 1.3.2) and transform them into non-radical products thus stopping the propagation of radical chain oxidation. The very positive point of HALS is that this stabilization process is not sacrificial as the –N-O° form is regenerated.

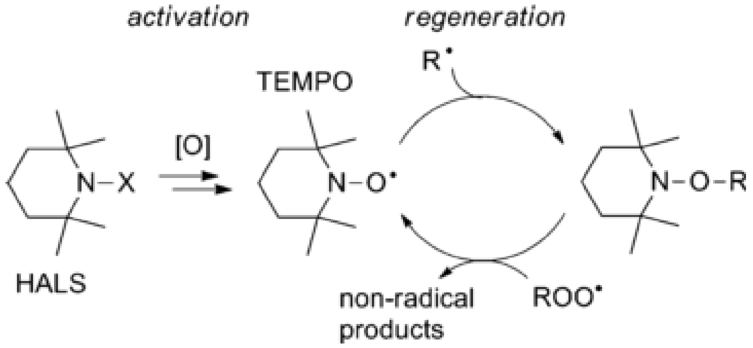

Figure 3.9 - Mechanism of Hals stabilization (Denisov cycle).[176]

Here we have studied the possibility to use HALS molecules as additives in polymer solar cells (PSCs). We used P3HT:PC$_{60}$BM as standard polymer blend materials. Firstly, we have explored the issue of tuning the bulk hetero-junction (BHJ) morphology with HALS as other well-known additives such like DIO or ODT do it. Then, we investigated the effect of HALS on P3HT photostability. Both the chemical structure of HALS and its content in the polymer film formulation were investigated. Finally, HALS were incorporated and evaluated in polymer blend films with a special attention to the photoreactivity between HALS and PC$_{60}$BM.

3.3.2. Experimental

Please, refer to the appendix (A1) for additional details on the experimental techniques.

Figure 3.10 and **Table 3.2** show the chemical structure and physical properties of the investigated additives. All the thin films of prepared in this section were spin coated and the additives were added to the P3HT, $PC_{60}BM$ or P3HT:$PC_{60}BM$ solution (chlorobenzene) in different proportions (% in volume).

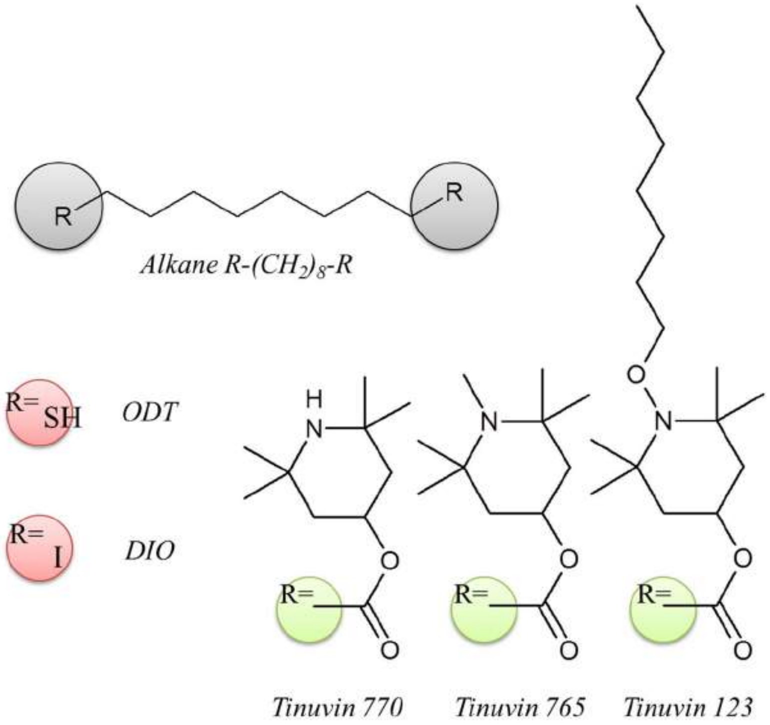

Figure 3.10 - Chemical structures of the investigated additives.

Name	State	M g/mol	Bp °C	Density g/ml	Purity %
Chlorobenzene (CB)	Liquid	112	132	1.11	98
Diiodooctane (DIO)	Liquid	366	366	1.84	98
Octanedithiol (ODT)	Liquid	178	270	0.97	98
Tinuvin 770 (T770)	Solid	481	>350	1.05	-
Tinuvin 123 (T123)	Liquid	737	280	0.97	-
Tinuvin 765 (T765)	Liquid	509/370	220	1.00	Mix

Table 3.2 - Physico chemical properties of the investigated solvent and additives.

3.3.3. Results and discussion

- *HALS as BHJ optimizer ?*

First, we have tried to determine if HALS molecules are potential BHJ morphology optimizers such as DIO and ODT. We used Tinuvin 765 as it is one of the most used HALS additives. (**Figure 3.10**) We prepared P3HT:PC$_{60}$BM films from various solutions: pure chlorobenzene (CB), CB+3%DIO, CB+3%ODT and CB+3%T765. The addition of 3% in volume of additives is the percentage usually used for optimizing the BHJ of polymer blends.[42] UV-vis spectroscopy is a valuable tool to check the degree of ordering of P3HT chains in solid films.[178] The UV-vis spectra of the P3HT:PC$_{60}$BM series thus obtained are presented in **Figure 3.11**.

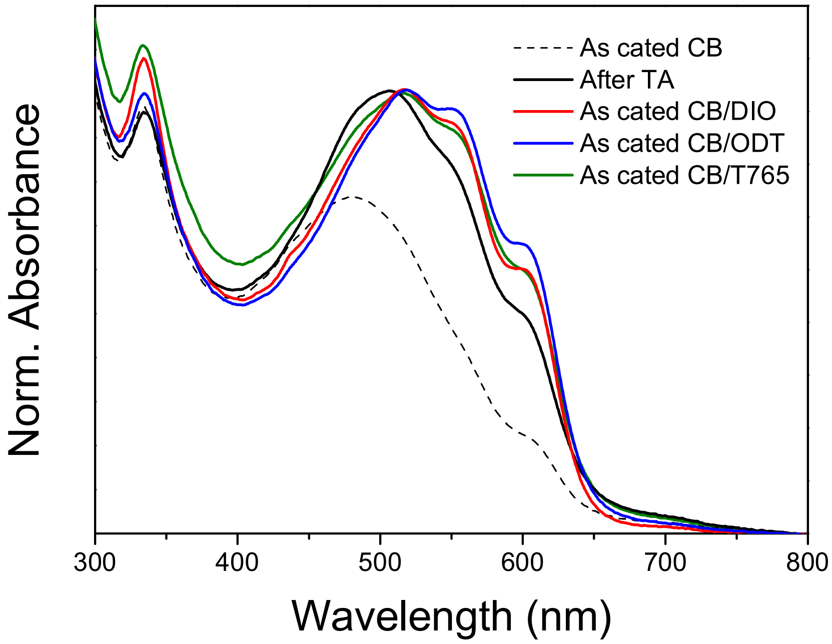

Figure 3.11 - UV-vis spectra of P3HT:PC$_{60}$BM films casted from pure CB (dashed line), CB+3%DIO (red), CB+3%ODT (blue) or CB+3%T765 (green). The black cure corresponds to the “as casted CB” after a thermal annealing of 15 min at 120°C in inert atmosphere.

We can observe the well-known reorganization of the P3HT after thermal annealing. This phenomenon has been largely depicted and explained in the literature.[34] The increase of absorbance can be attributed to the increase of ordering of the polymer chains. As expected, the same effect, even more pronounced, can be observed when DIO and ODT are used. Interestingly, a comparable effect was also observed with T765. This is a first encouraging result as T765 could be used as a BHJ morphology optimizer such as DIO or ODT (besides the expected stabilizing effect). As shown in the previous section, DIO and ODT are high boiling point additives and residues trapped in the polymeric matrix are susceptible to drastically impact the polymer blend photostability.[156] T765 has a high boiling point (220°C) which is a property as HALS need to remain trapped in the polymer matrix to act as stabilizers.

- *HALS, a potential class of P3HT:$PC_{60}BM$ photostabilizers ?*

After the promising first results in terms of BHJ morphology optimization, the photostabilizing properties of T765 were evaluated. Thus, P3HT:$PC_{60}BM$ materials were dissolved in CB+3%T765 and series of films were prepared and exposed to photooxidative conditions. Three samples were prepared in order to get statistical results. The films with T765 were compared to a control series without additives. **Figure 3.12** shows that the absorbance of P3HT in the P3HT:$PC_{60}BM$ T765 deposits slightly increases during the first 30 min of exposure probably due a reorganization of the P3HT phase. Then, the absorbance decreases and interestingly the rate of degradation is more important compared to the control series (without T765).

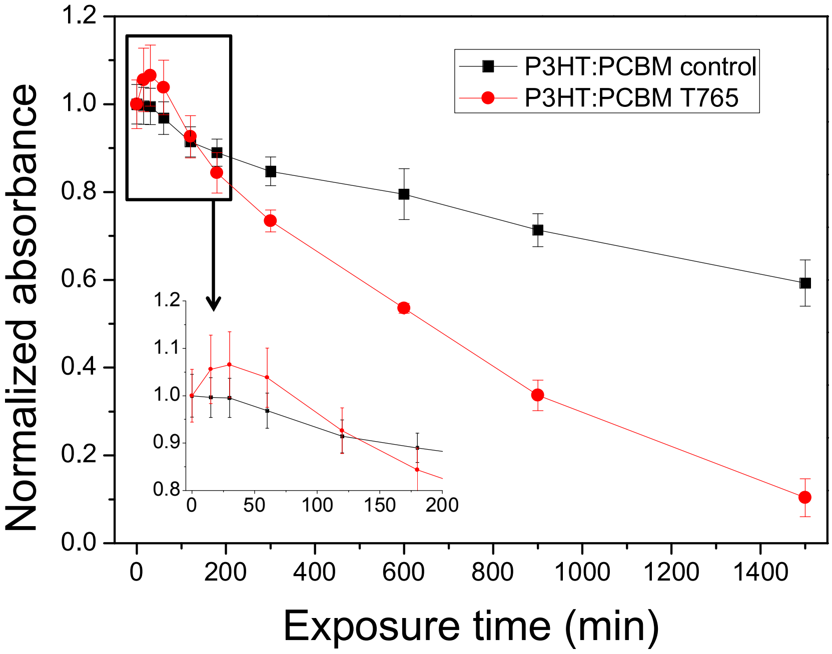

Figure 3.12 - Evolution of the P3HT absorbance (taken at maximum absorbance) versus time of exposure for P3HT:$PC_{60}BM$ films casted from pure CB (control) or CB+3%T765. Three samples per series were investigated and the deviations are represented by the error bars.

It is clear that T765 has a negative impact over the exposure on the polymer blend photostabiltiy. Antagonist reactions may occur between the HALS molecules and P3HT and/or $PC_{60}BM$. Tinuvin molecules are known to be very efficient light stabilizers when they are used as single additive. However antagonists effects were observed when anti-oxidants were used as co-additives.[179,180] It is important to note that $PC_{60}BM$ can be considered as an anti-oxidant in general. Thus, antagonist reactions may occur between T765 and $PC_{60}BM$.

- *Reactivity between HALS and PC$_{60}$BM*

In order to get further information concerning potential antagonist reactions between T765 and PC$_{60}$BM, we have recorded infrared spectra along the degradation of the previous samples without and with T765 (**Figure 3.13**).

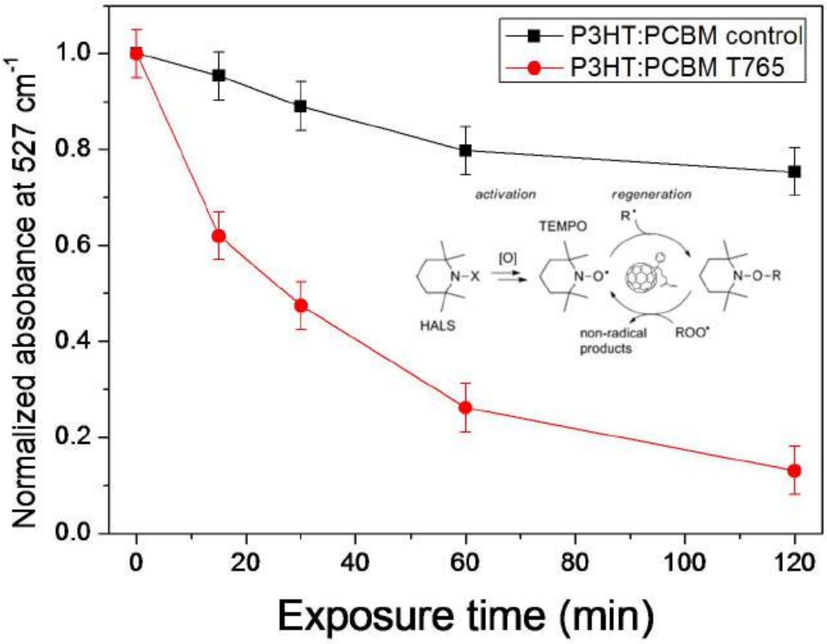

Figure 3.13 - Evolution of the C60 vibrational mode (527 cm^{-1}) of PC$_{60}$BM versus time of exposure for P3HT:PC$_{60}$BM films casted from pure CB (control) and from CB+3%T765.

Figure 3.13 clearly shows that T765 drastically impacts the PC$_{60}$BM molecules, especially its C60 moieties. The rapid drop of the C60 vibrational mode of PC$_{60}$BM when mixed with T765 suggests that T765 radicals may add on the C60 moieties of PC$_{60}$BM. In the case of P3HT:PC$_{60}$BM films casted without additives, PC$_{60}$BM acts as a stabilizer thanks to its radical scavenger properties and exited state quenching effects mainly.[88,90] Thus, PC$_{60}$BM molecules can interact with the radicals coming from the P3HT degradation increasing thus P3HT photostability. In presence of T765, PC$_{60}$BM molecules may create antagonist effects according to the complex Denisov cycle.

- *Hals, a potential P3HT photostabilizer? Impact of HALS structure and content*

As $PC_{60}BM$ seems to interact with T765, we decided to prepare films of P3HT (without $PC_{60}BM$) casted from pure CB as a control sample and we compared the photostability with a film casted from CB+T765. As a negative impact on the polymer stability was observed in **Figure 3.14**, we have also included films of P3HT prepared with additives known to have a negative impact on P3HT stability such as DIO and ODT.[156] We used an exaggerate amount of additives (30%) to see more easily the effect of each additives. After casting, films were exposed to the sun test simulator in air (see experimental part) and the evolution of the P3HT absorbances in the four types of deposits are reported in **Figure 3.14**. The P3HT film prepared without additives has a linear rate of photodegradation. DIO and ODT additives drastically impact the stability of the polymer. This is in line with the previous part of the chapter.[156] Here, the deposit is not confined, but as 30% of high boiling point additives corresponds to a huge amount a non-negligible fraction of additives remains in the none confined deposit.

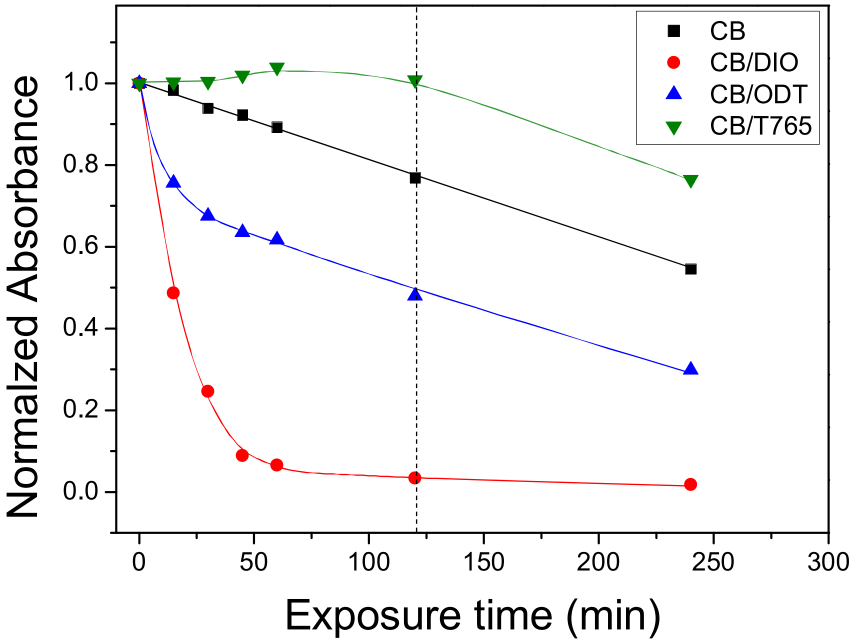

Figure 3.14 - Evolution of the P3HT absorbance (taken at the maximum absorbance) versus time of exposure for P3HT films casted from pure CB, CB+30%DIO, CB+30%ODT or CB+30%T765.

After one hour of photooxidation, the entire P3HT absorbance has vanished in the case of DIO, and 40% when ODT is used. Interestingly, when mixed with T765 the absorbance of P3HT slightly increases probably due to some polymer reorganization. Thus, an induction period of 120 min is observed when T765 is used. Although the amount of additives was very high (usually the amount of HALS is in the range 0.1-1%), the use of T765 has a positive impact on P3HT stability.

In a further step, films of P3HT were prepared with a more realistic amount of additive (1 and 5%) and were exposed to the same degradation conditions. Results are presented in **Figure 3.15**. We have previously seen that P3HT with 30% of T765 has an induction period of about 120 min. When P3HT is mixed with 5% of T765, we still observe an induction period but reduced to about 60 min. However, in all the cases we can observe an increase of the degradation rate after the induction period compared to the control sample. When P3HT is mixed with 1% of T765, we observe no induction period (or is very short) and the rate of degradation is higher than the one of the control sample. These results clearly show that P3HT is not stabilized when a small amount of T765 is used, and antagonist effects most probably occur over exposure resulting in a decrease of the P3HT stability.

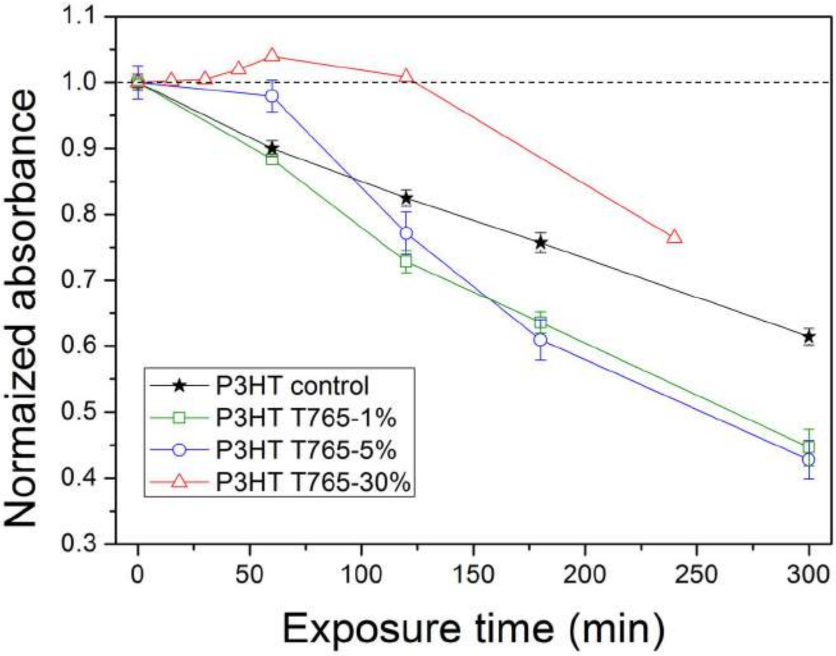

Figure 3.15 - Evolution of the P3HT absorbance (taken at maximum absorbance) versus time of exposure for P3HT films casted from pure CB (control), CB+1%T765, CB+5%T765 or CB+30%T765.

It is known that the reactivity of Tinuvin additives depends on the chemical group attached on the nitrogen atoms.[176] Thus, we tested two other Tinuvin, T770 and T123 with a hydrogen atom and alkoxy groups respectively. (See **Figure 3.10**) We have compared the P3HT stability mixed with 1 or 5% of T770 (N-H), T765 (N-CH3) and T123 (N-OR). (**Figure 3.16**) T765 and T123 also have negative impact on P3HT stability. As a general trend, we can observe that when HALS molecules are used at 1% the decrease of the P3HT stability is the most important. The induction period observed for T765 was not observed for T770 and T123 even at 5%. We note also that T123 has the most negative impact on the P3HT stability. The N-OR ending group is design to facilitate the formation of NO° necessary for the stabilization process (See Denisov cycle, **Figure 3.9**). However, the degradation of P3HT is even more severe when T123 is used.

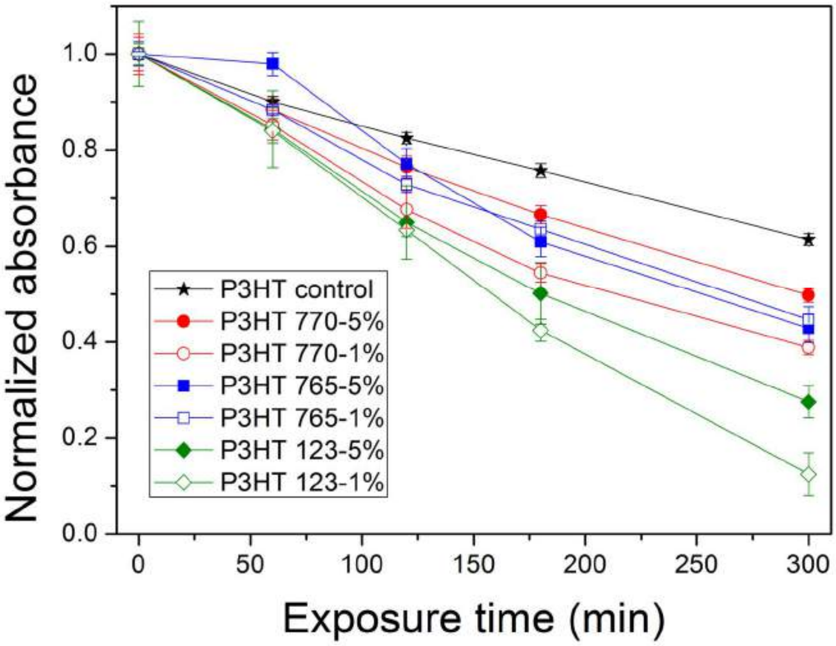

Figure 3.16 - Evolution of the P3HT absorbance (taken at the maximum of absorbance) versus time of exposure for P3HT films casted from pure CB (control), CB+T770 1 and 5%, CB+T765 1 and 5% or CB+T123 1 and 5%.

- *Evolution of the chemical structure when T765 is mixed with P3HT or $PC_{60}BM$ and exposed to photooxidative conditions (See IR spectra in Appendix A3.5)*

Finally, thin films containing pure T765, T765+P3HT and T765+$PC_{60}BM$ were casted on KBr substrates in order to follow the IR spectra when exposed to photooxidative conditions. A exaggerate amount of T765 (30% in volume) was used in order to maximize the qualitative observation of the potential photochemical reactions. All the IR spectra are available in Appendix (A3.5). From the spectra of the pristine samples, it is very difficult to identify the vibrational modes of P3HT and $PC_{60}BM$ which are masked by the T765 vibrational modes. No significant evolution of the chemical structure of T765 alone was observed even after 33h of photooxidation. When mixed with P3HT, an induction period was observed (1-2h) and is in line with the UV-vis spectra of **Figure 3.14**. A lot of vibrational modes are impacted suggesting complex reactions. The C-H vibration of the N-CH_3 bonds seems to be particularly impacted. When mixed with $PC_{60}BM$, clearly photoreactions occur without induction period leading to important modifications of the chemical structure in few minutes of exposure.

3.3.4. Conclusion

We have seen that using 3% of HALS additives can optimize the P3HT:$PC_{60}BM$ morphology. Due to their high boiling points, HALS molecules remain in the polymer blend films (and this is a mandatory property). However, we have observed a decrease of the polymer blend stability when T765 was used at 3%. One reason could be the antagonist effects with $PC_{60}BM$. Nevertheless, the use of low amount of HALS do not increase the polymer stability whatever the ending group of HALS is (-H, -R or –OR). We observed important and different modifications of the chemical structure when T765 is mixed with P3HT or $PC_{60}BM$ suggesting complex probable antagonist reactions.

HALS seems to be not relevant additives for polymer blend stabilization. Recently, Turkovic et al.[181] successfully used hindered phenols and improved the stability of polymer blend devices. They did not report antagonist effects with $PC_{60}BM$.

A huge amount of stabilizers are available in the polymer area, and most of the times a package of several stabilizers is incorporated in the polymer matrix. Research for finding appropriate combination and formulation of additives is thus a long process. Even if the mechanisms of stabilization of additives are broadly understood, the detailed mechanisms of interaction, and antagonist effects, are often difficult to unravel. For example, HALS molecules are widely used in industry since several decades, but the mechanism of stabilization was fully elucidated only several years later. In 2012, Gryn’ova provided a deeper understanding in the various possible mechanism of HALS stabilization.[176] Therefore, in conclusion, the use of stabilizers for BHJ blend is challenging especially because the mechanism of stabilization must not interfere with the charge transfer during the PV conversion.

3.4. The use of a poly-fullerene as BHJ thermal stabilizer

3.4.1. Introduction

The morphology of the BHJ, and more precisely how the donor and acceptor materials are mixed together in the solid film is a key factor of device performances.[34] However, once the pristine BHJ morphology is optimized, PC$_{60}$BM molecules have the natural tendency to diffuse trough the polymeric matrix thus forming large domains.[182] The direct consequence is a drastic drop of the device performance due to a decrease of donor/acceptor interfaces. Therefore it is crucial to preserve the optimized BHJ morphology when the devices are submitted to thermal stress during device fabrication and upon operational conditions.

Different approaches were investigated in the past for stabilizing the BHJ morphology.[183] (See 1.3.4 section) A straight forward idea consists to create chemical bonds via crosslinking between materials in order to freeze the BHJ. The chemical structures of pi-conjugated polymer and fullerene derivatives have to be modified in order to make the crosslink possible. Polymer-polymer, fullerene-fullerene and polymer-fullerene crosslinking were tested.[93,96,184,185] The use of a third component was also investigated as crosslinker.[97]

When a modified material is used for crosslinking, it is necessary to activate the reaction by a post thermal treatment or light exposure once the film is fabricated. Undesired reactions can occur and intensive studies are needed in order to find the appropriate post-treatment conditions.[186] Here, we propose the use of a “ready-to-use” additive. Thus, there is no need to modify the device fabrication methods or to add a post treatment step. We have investigated the use of a polyfullerene (HHR-19) as an additive (10% of PC$_{60}$BM mass content) for increasing the thermal resistance of polymer blend BHJ. We tested the additive for P3HT:PC$_{60}$BM (1:1) and EP10:PC$_{60}$BM (1:2) polymer blend films. (**Figure 3.17**) We used optical microscopy and UV-vis spectroscopy for investigating the impact of the additive on the polymer blend thermal stability.

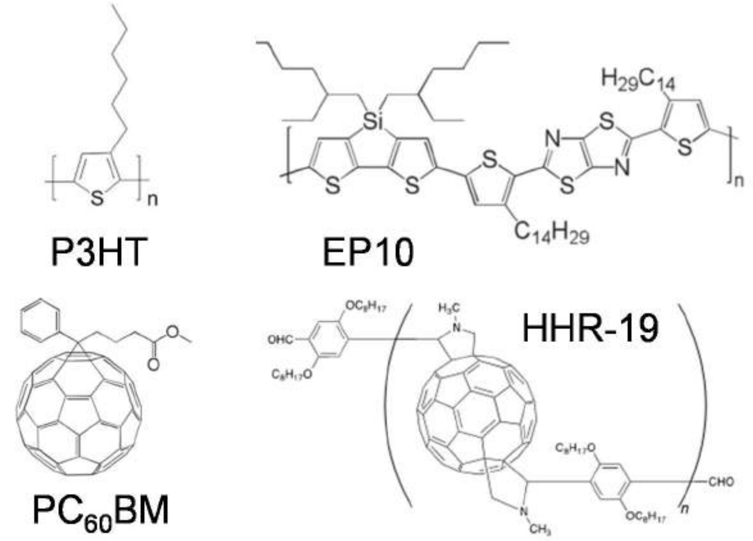

Figure 3.17 – Chemical structures of the investigated materials.

3.4.2. Experimental

Please, refer to the appendix (A1) for additional details on the experimental techniques.

- *Poly-fullerene synthesis (Hasina Ramanitra, ESR12)*

You can refer to the PhD of Hasina Ramanitra (University of Pau) for a complete description of the material synthesis and characterization.

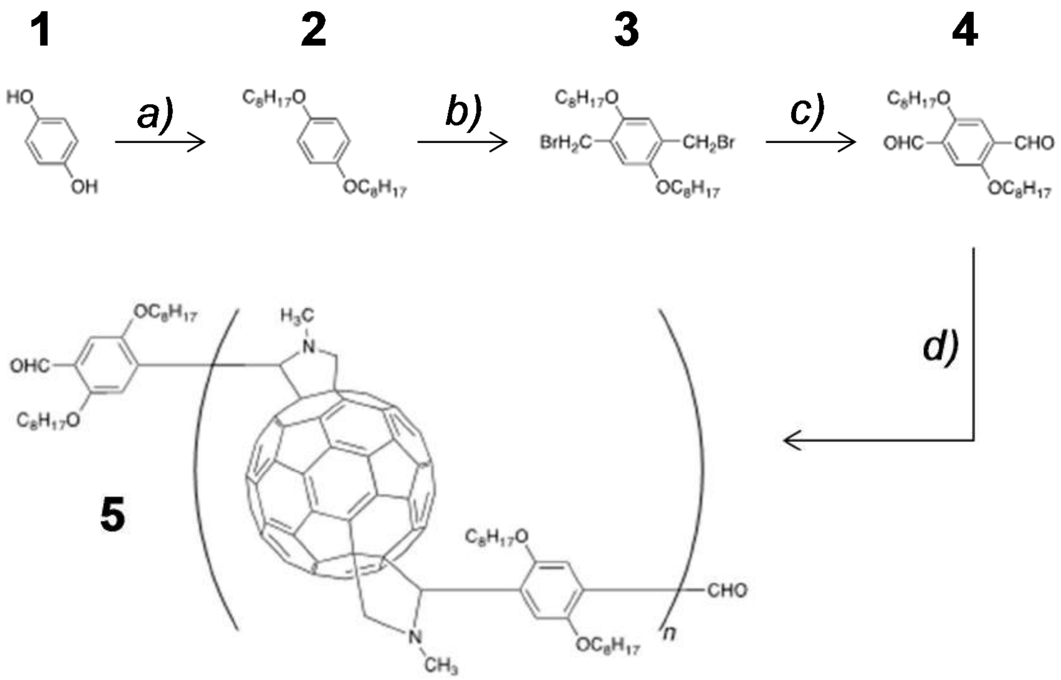

Figure 3.18 - Synthesis route of the polyfullerene HHR-19. a) 1-bromooctane, K_2CO_3, **1**, acetonitrile, 70%; b) (CH_2O), acetic acid, **2**, HBr, 73%; c) $NaHCO_3$, **3**, dimethyl sulfoxide, 47%; d) C_{60}, *N*-methylglycine, **4**, DCB, 58%.

- *Film and device fabrication (Dr. Simon Dowland, ER2)*

Glass/ITO substrates were cleaned by wiping with an IPA (isopropanol/acetone) soaked tissue before being sonicated in acetone and IPA for 15 mins each. A suspension of ZnO nanoparticles (5wt%) in EtOH was sonicated for 30 mins before being deposited on the substrates by doctor blading. The coater surface was set to 65 °C and the blade run 700 µm over the samples at a speed of 5 mm/s. The ZnO layer was subsequently annealed at 140 °C for 10 mins before deposition of the active layer. The active layer was coated at 65 °C at a speed of 35-40 mm/s with a blade height of 700 µm in all cases except where explicitly stated. Absorption spectra were taken here to ensure consistency of the active layer thickness between samples. A PEDOT:PSS solution was filtered using 0.45 µm hydrophilic filters before being deposited on the active layer at 65 °C, a speed of 20 mm/s and a blade height of 700 µm. Samples were then annealed for 5 mins at 120 °C under nitrogen to drive of residual water before being placed in an evaporator. 150 nm of silver was then evaporated onto the samples under vacuum. The current voltage characteristics of the devices were measured using a Keithley source meter both in the dark and under illumination by a Xenon lamp calibrated to approximately a 1 sun intensity using a silicon photodiode.

- *Optical microscopy*

Film morphology was observed by an optical microscope (OLYMPUS, BH) equipped with a CCD camera. The threshold color treatment was done by using Scion Image software.

- *UV-vis spectroscopy*

UV/VIS spectra were recorded in transmission mode using a homemade set up containing fiber optic, spectrometers from ocean optics (Maya2000) and a combination of deuterium and halogen lamps as light sources.

3.4.3. Results and discussion

Films based on P3HT:PC$_{60}$BM (1:1) and EP10:PC$_{60}$BM (1:2) were prepared without (control sample) and with HHR-19 as additive (10% of PC$_{60}$BM mass content). We first observed the evolution of the film morphology at the macroscopic scale by optical microscopy. **Figure 3.19** shows the P3HT:PC$_{60}$BM blend films, without and with the HHR-19 additive, before and after 5h thermal treatment at 120°C. Threshold color treatments were used to help the visualization of the PC$_{60}$BM crystals. This technique also highlights the imperfections of the pristine film. Thus, 0.1% of the surface of the pristine sample is covered by imperfections from film fabrication. After 5h at 120°C, the black area increases but remains weak. No significant difference can be observed when the additive is used in the film.

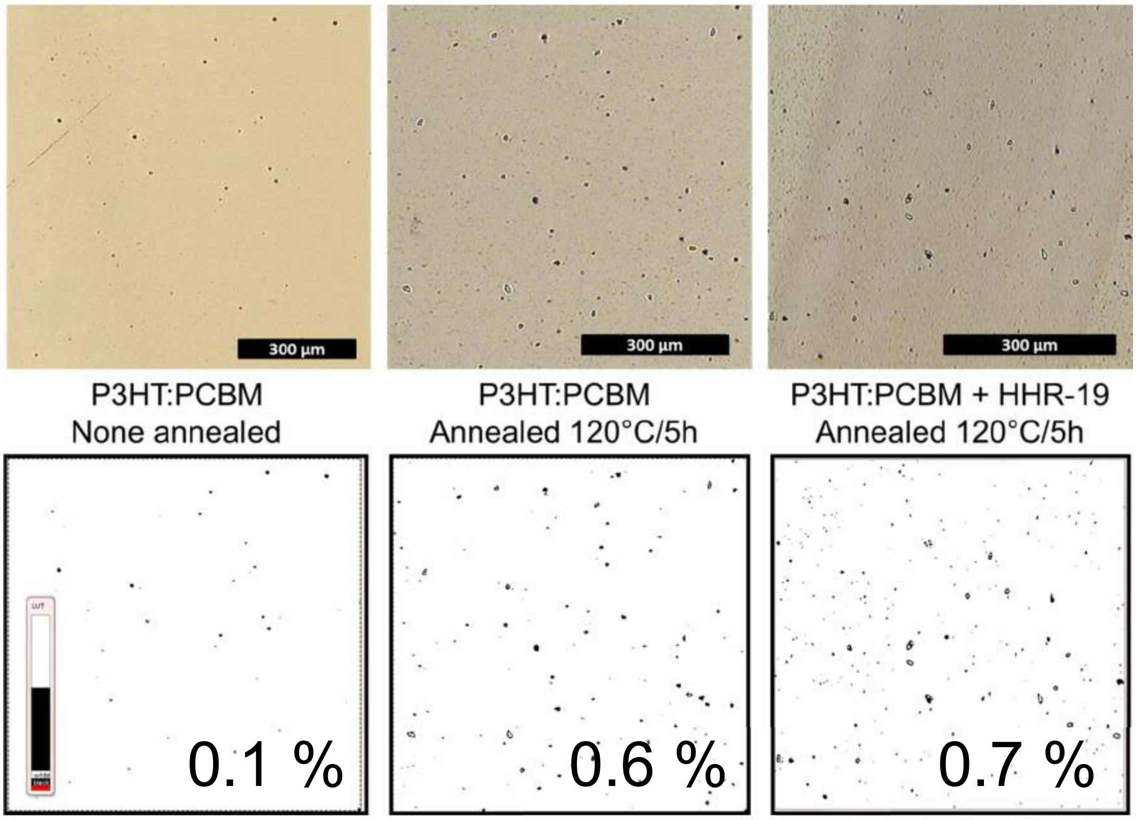

Figure 3.19 - On the top side, images of P3HT:PC$_{60}$BM films before thermal annealing (left) after 5h at 120°C without additive (middle) with additive (right). On the bottom side, the same images with a threshold color treatment. The values indicate the percentage of black spots versus the white background. The films before annealing of polymer blends w/wo HHR-19 were similar.

The same experiment has been performed on polymer blend films based on EP10 polymer. The results are shown in **Figure 3.20**. In this case and after annealing of the sample without additive, we observe a clear increase of the black spots (x64) suggesting the formation of large PC$_{60}$BM domains. With the additive, the surface is the same as the pristine one without additives. (not shown) It seems therefore that the additive efficiently stabilizes the EP10 polymer blend morphology by hindering the $PC_{60}BM$ diffusion.

At this step, the additive seems to be efficient for EP10, but in the case of P3HT, the phase separation was not large enough to observe differences at the macroscopic scale between samples w/wo additive. Thus, we performed thermal treatment for both polymer blends in more severe conditions: 10h at 140°C.

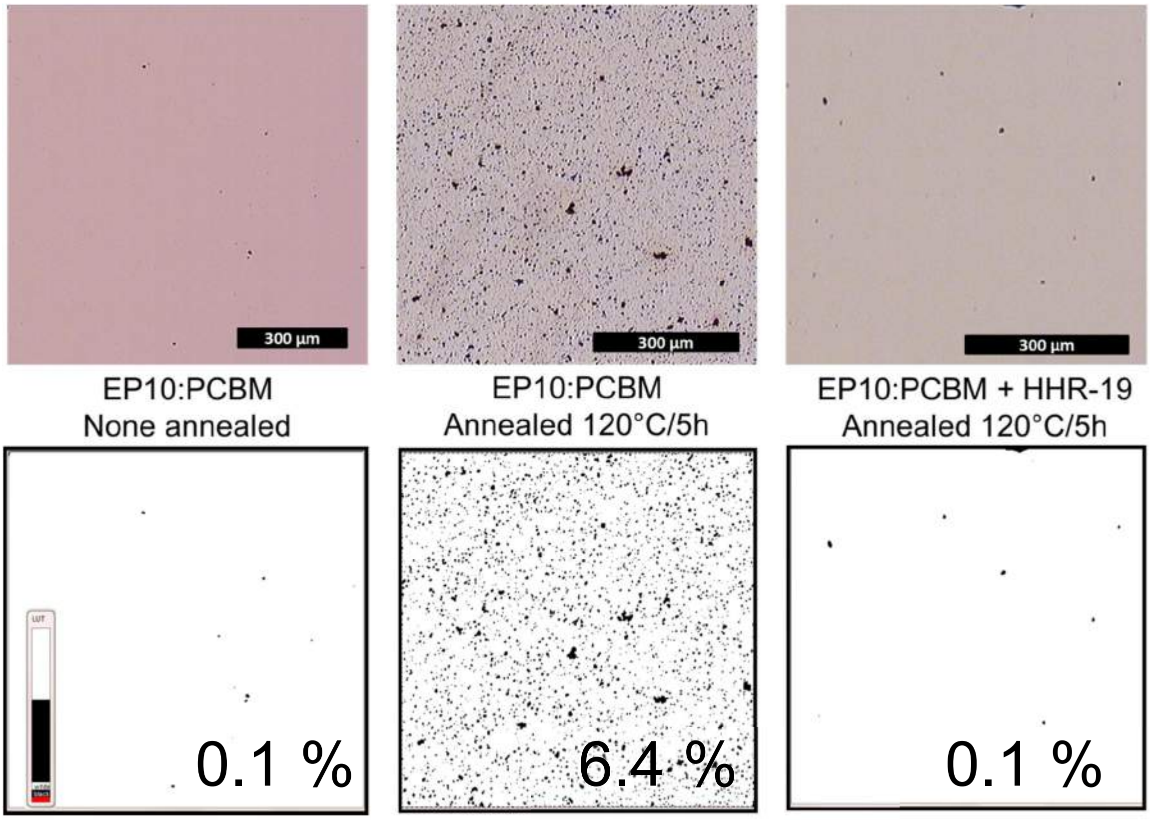

Figure 3.20 - On the top side, images of $EP10:PC_{60}BM$ films before thermal annealing (left) after 5h at 120°C without additive (middle) with additive (right). On the bottom side, the same images with a threshold color treatment. The films before annealing of polymer blends w/wo HHR-19 were similar.

Figure 3.21 shows the results obtained with $P3HT:PC_{60}BM$. The $PC_{60}BM$ crystallization is clearly present and the black area covers 8% of the total surface. The structure of the crystals exhibits the needle like structure as reported in previous studies.[104] When the additive is added, the $PC_{60}BM$ crystallization is different. First, the covered surface is slightly less important and the crystals are smaller but in larger amount. This indicates a different phase separation. With additive, the nucleation points are more abundant but the growing is limited. Without additive, nucleation points are less abundant but the growing is faster.

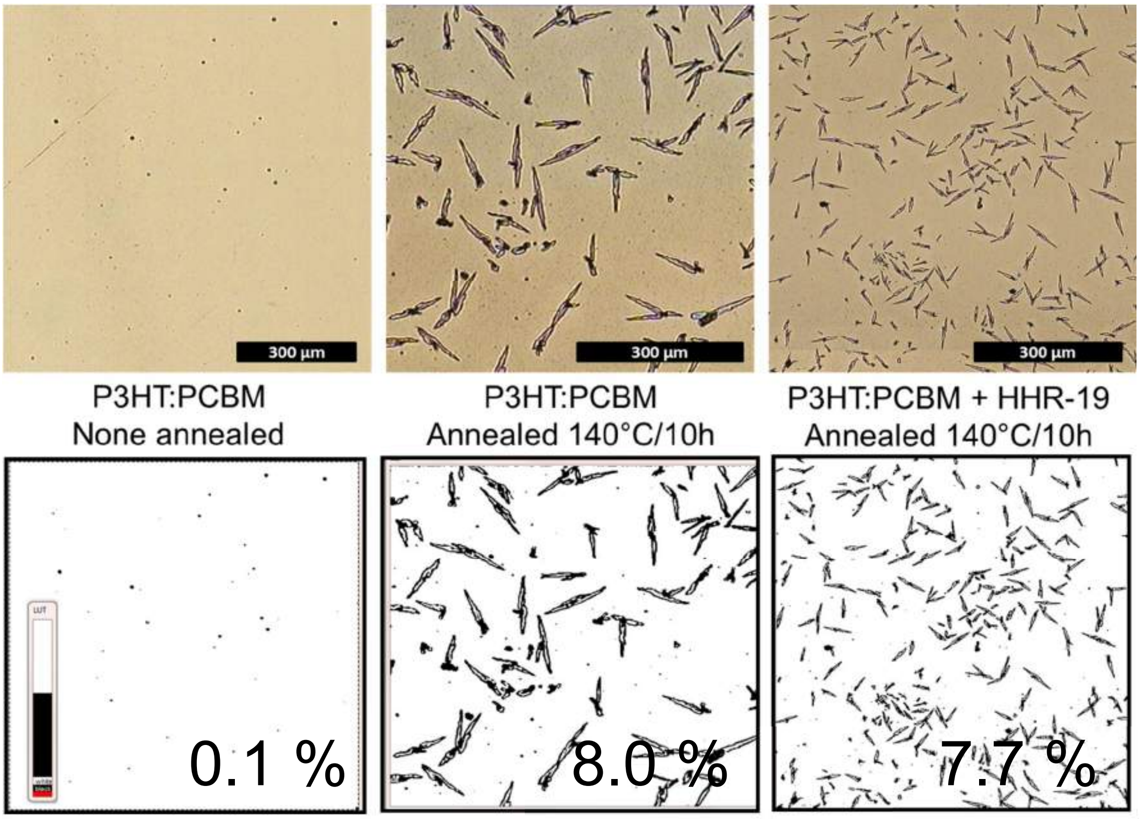

Figure 3.21 - On the top side, images of P3HT:$PC_{60}BM$ films before thermal annealing (left) after 10h at 140°C without additive (middle) with additive (right). On the bottom side, the same images with a threshold color treatment.

In the case of EP10, we have shown that the additive is efficient in the conditions of annealing treatment of 5h at 120°C. For EP10 blends, the annealing treatment at 140°C for 10h without additive results in the formation of $PC_{60}BM$ aggregates which surface area represents 31% of the total surface area. This is not surprising as $PC_{60}BM$ aggregates were already observed in a less severe condition (5h/150°C) With additive, the $PC_{60}BM$ crystallization is not suppressed as it is the case for the milder annealing treatment at 120°C but is much more attenuated compared to the blend wo additive (factor 5). **Figure 3.23** summarizes the $PC_{60}BM$ aggregation as a function of the annealing conditions and when the HHR-19 additive is added. The additive is clearly more effective in the case of EP10 than P3HT blends. It means that the effectiveness of the polyfullerene depends of the chosen donor conjugated polymer.

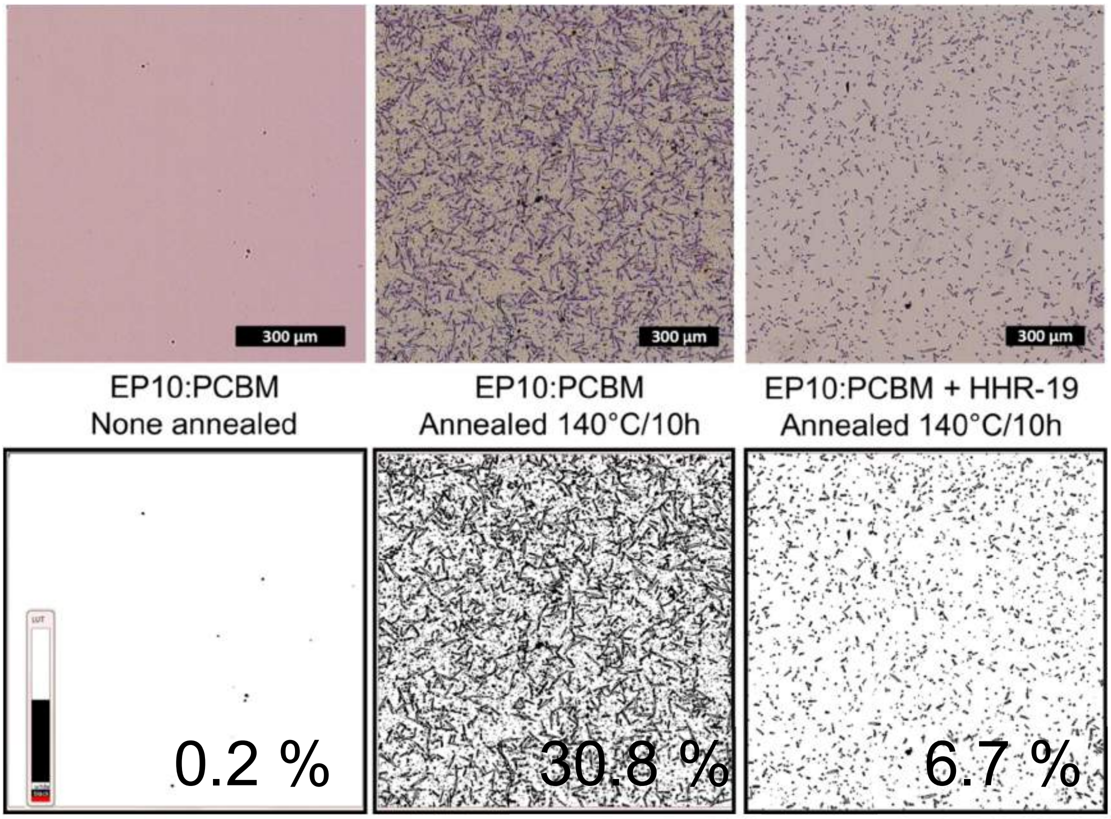

EP10:PCBM
None annealed

EP10:PCBM
Annealed 140°C/10h

EP10:PCBM + HHR-19
Annealed 140°C/10h

Figure 3.22 - On the top side, images of P3HT:PC$_{60}$BM films before thermal annealing (left) after 10h at 140°C without additive (middle) with additive (right). On the bottom side, the same images with a threshold color treatment.

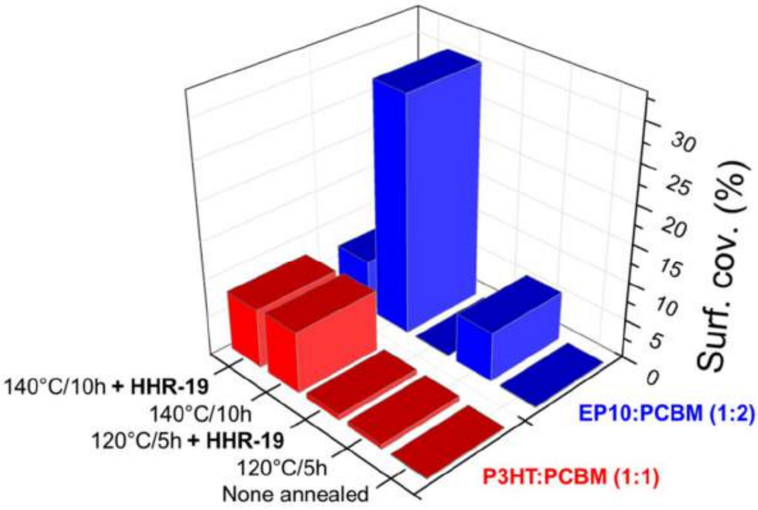

Figure 3.23 - Summary diagram of the PC$_{60}$BM aggregates surface of all the investigated blends.

UV-Vis spectroscopy is a valuable tool to investigate morphological change in polymer blend such as $PC_{60}BM$ crystallization.[97,187] The crystallization of $PC_{60}BM$ results in a decrease of its absorption band at 334 nm due to the scatter of the light. **Figure 3.24** shows the absorbance of the pristine polymer blends.

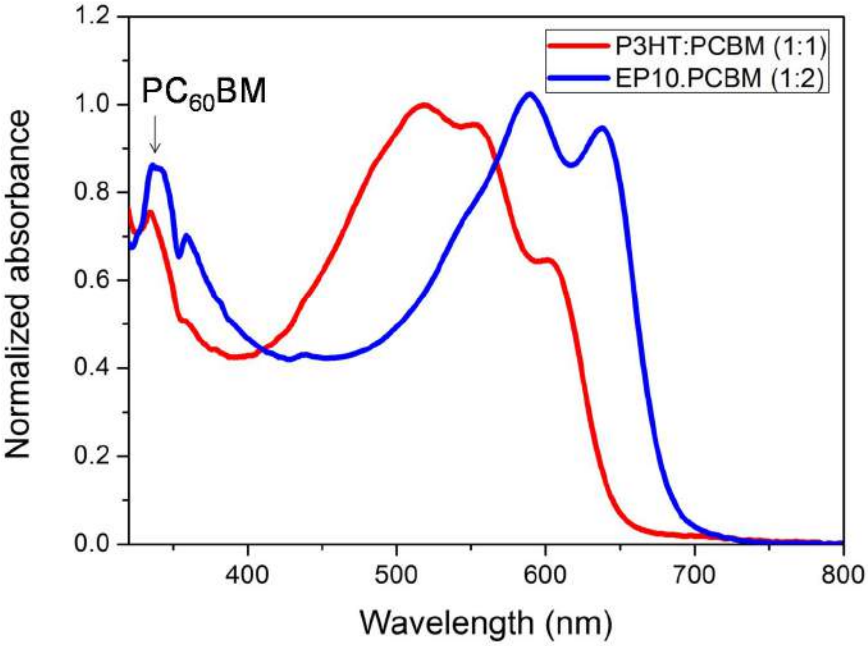

Figure 3.24 - UV-vis spectra of pristine P3HT:$PC_{60}BM$ (1:1) and EP10:$PC_{60}BM$ (1:2) films.

$PC_{60}BM$ molecules absorb mostly in the UV domain (300-400 nm). The evolution of the band at 334 nm was monitored during the different annealing processes and the results are presented in **Figure 3.25**. Due to the formation of large crystals, transmittance is favored resulting in a decrease of $PC_{60}BM$ absorbance. This observation is valid for both P3HT and EP10 blends. In presence of HHR-19, we can clearly observe that the decrease of the $PC_{60}BM$ band (334 nm) is reduced for both polymer blends which is in line with the optical images. (**Figure 3.25)**

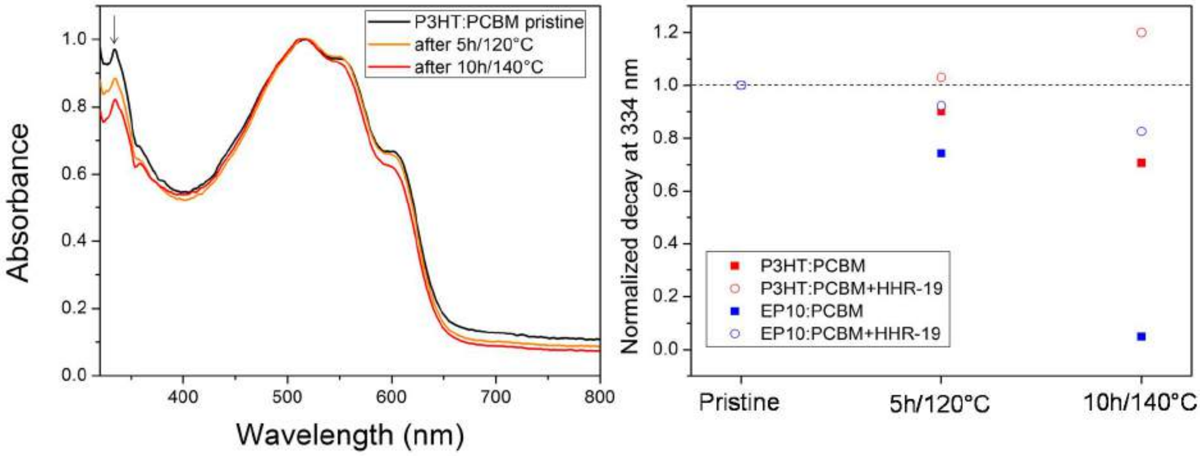

Figure 3.25 - Evolution of the UV-vis P3HT:$PC_{60}BM$ (1:1) without HHR-19 after 5h at 120°C and 10h at 140°C (left). Evolution of the $PC_{60}BM$ band (334 nm) after annealing for P3HT:$PC_{60}BM$ (1:1) and EP10:$PC_{60}BM$ (1:2) with and without HHR-19.

The results are fully in line with the optical images: For P3HT, no significant difference was observed for the annealing at 120°C but the difference becomes significant for the harsher annealing treatment. Concerning EP10, we already note a clear difference for the annealing at 120°C and the difference becomes even more important upon the annealing treatment at 140°C.

Finally, the impact of the poly-fullerene HHR-19 was tested when inserted in inverted devices Ag/PEDOT:PSS/P3HT:$PC_{60}BM$/ZnO/ITOglass. Devices were submitted to thermal soaking at 100, 120 and 140°C and **Figure 3.26** shows the evolution of the device performance with or without HHR-19.

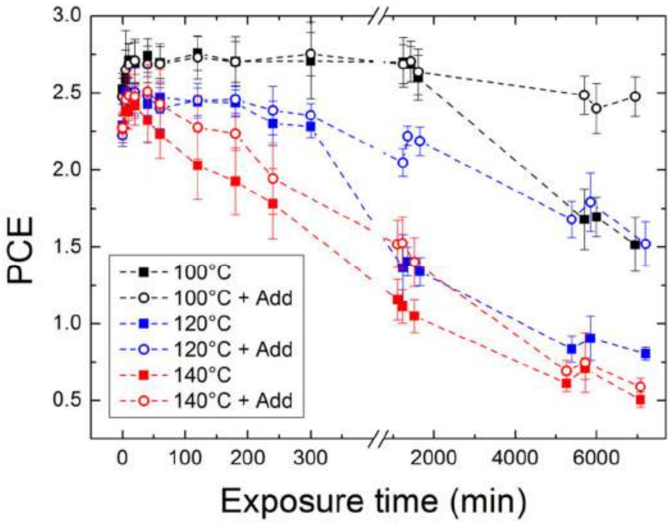

Figure 3.26 – Evolution of device performance with or without HHR-19 when exposed to different thermal soaking.

For devices without HHR-19 and exposed to 100 and 120°C we can clearly observe that the device performances remain constant before suddenly decreasing when a critical time is achieved. This time is at about 300 and 2000 min when exposed to 120 and 100°C respectively. We clearly observe the device performances are significantly stabilized when HHR-19 is used. Even if the effect is less pronounced, HHR-19 stabilizes also the devices exposed to 140°C.

3.4.4. Conclusion

Here, we have investigated the use of a poly-fullerene as an additive for improving the thermal stability of the BHJ. The $PC_{60}BM$ crystallization can be easily detected by optical microscopy and UV-vis spectroscopy. By using a poly-fullerene additive (10% of $PC_{60}BM$ content), we have demonstrated that the thermal stability of polymer blends can be significantly enhanced. Thus, the use of a poly-fullerene additive appears to be an interesting way to stabilize BHJ morphology and therefore device performances.

3.5. Summary of Chapter 3

In this chapter 3, the role of the "third component" was studied.

First, we have demonstrated that residual additives such as DIO or ODT are not stable upon light exposure in air and strongly impact the polymer blend stability. We have evidenced that the confinement of the active layer plays a major role on the residual additives reactivity. When confined in the BHJ by a top layer, residual additives, or more precisely the photoproducts issue from their degradation, cannot migrate out of the film and strongly react with the polymer and the fullerene moieties provoking their rapid degradation. However, we have shown that a short light soaking process before the deposition of the top layer appears to be an efficient way to cleanly remove the residual additives.

Secondly, we have shown that using 3% of HALS additive allows the optimization the P3HT:PC$_{60}$BM BHJ morphology on the one hand. Due to their high boiling points, HALS additives remain in the polymer blend films. But on the other hand, we have observed a decrease of the polymer blend stability when 3% HALS additives were incorporated in the BHJ One reason could be the antagonist effects between HALS and PC$_{60}$BM. Nevertheless, the use of low amount of HALS does not increase the polymer stability as well, whatever the ending group of HALS is. The successful use of stabilizers for polymer blend seems highly challenging especially because it is crucial that the mechanism of stabilization must not interfere with the charge transfer process. The search of efficient and cheap barrier materials for the encapsulation appear to be the most effective way to stabilize polymer blends from oxidation.

Finally, in a last part, the use of a poly-fullerene as BHJ thermal stabilizer was explored. When used as an additive (10% of PC$_{60}$BM content), the insertion of poly-fullerene can significantly reduce the PC$_{60}$BM crystallization and therefore improve the polymer blend thermal stability.

Chapter 4

Identification of the mechanical breaking point in OSCs

4.1. Introduction to Chapter 4

This Chapter concerns the delamination issue in OSCs. As we have seen in the Chapter 1 (1.3.5) layers in the device can delaminate resulting in a drastic loss of the device performance. The lack of adhesion between layers is not surprising as the fabrication of OSCs devices consists (except the top electrodes) of successive layer deposition steps of organic materials from solutions. Thus, different or orthogonal solvents are required in order to avoid a (re)solubilization of the already deposited layer by the new one. Due to the natural lack of solubility at the interface, materials in these regions could suffer from a lack of adhesion. The PEDOT:PSS layer is one of the most used hole transporting layer (HTL) materials in OPV and its interface with the active layer (AL) was pointed as the weakest mechanical point in standard and inverted device structure.[102,103] Although the PEDOT:PSS formulation allow a good wettability on various types of layers (ITO in the case of standard structure and active layer for inverted structure) the natural affinity between the active layer and the PEDOT:PSS remains relatively weak during the layer deposition and post thermal annealing treatment. OSC devices or modules are submitted to various stresses during their fabrication such as successive layer depositions, thermal cycles and air exposure. The delamination issue was not intensively investigated as it is a problem which arises especially at the industrial production step. The conception of flexible modules via the roll to roll process which the most realistic low cost way to produce cheap and flexible OSCs, leads to various mechanical stresses of the module. This mechanical stress added to various other ones (thermal cycles, successive layer deposition, air exposure etc…) can impact the inter-layer adhesion in pristine modules. Once fabricated, the modules are exposed to environmental conditions meaning exposed to light in air. Depending of the encapsulation cost and efficiency, the oxygen and humidity can be more or less reduced. The humidity was found to have a crucial impact on the delamination effect especially due to the water solubility of the PEDOT:PSS layer.[188,189] Thus, the initial relatively weak adhesion between PEDOT:PSS and active layer can be strongly impacted in working conditions.

In this Chapter, we investigated the delamination process in pristine and aged OSCs devices. For that, inverted OSC devices (Ag/PEDOT:PSS/Polymer:$PC_{60}BM$/ZnO/ITOglass) were fabricated and submitted to the so-called "Tack tests". The Tack test is a mechanical analysis used to investigate adhesion properties. The general idea is described in the experimental section 4.2.2. (**Figure 4.3**) With this technique, we obtain the force at break conditions which is a quantitative value of the force needed to delaminate completely the device. Thus, we have compared the force or stress at the break conditions of devices based on different p-type polymers or type of PEDOT:PSS. At the end of the Tack test experiment, the OSCs are divided in two parts, the so-called *"upper part"* and *"lower part"* (**Figure 4.4**). However, the Tack test technique cannot identify precisely where the breaks occur. Therefore, the *"upper part"* and *"lower part"* surfaces obtained after the Tack tests were analyzed by surface sensitive techniques such as AFM and XPS in order to identify the breaking points in our OSC devices. The two techniques are complementary as the chemical composition of the first nanometers can be extracted from XPS while the AFM shows the surface topography.

The first part of the Chapter 4 concerns the identification and strengthening of the mechanical breaking point in pristine OSCs. OSCs devices based on three different donor polymers were fabricated and submitted to Tack test experiments. We will see the influence of the donor polymer used in the active layer on the breaking points location. Then, two strategies were studied in order to improve the adhesion. First, the formulation of a new type of PEDOT:PSS was studied as new hole transporting layer (HTL). In order to improve the intermixing behavior with the active layer, an organic solvent (instead of water) was used for PEDOT:PSS. Secondly, the introduction of interlayers based on copolymers was investigated. The copolymers are based on one part with high affinity with the active layer and the other part has a good affinity with the PEDOT:PSS. These interlayers are expected to improve the adhesion behavior between active layer and PEDOT:PSS.

The second part will be about the identification of the mechanical breaking point in aged OSCs. The OSCs devices were submitted to damp heat exposure (85°C/85% rH) and a mechanism of delamination was proposed based on AFM and XPS analysis.

Scientific contribution

The present work is the result of a collaborative work within the *Establis* project. The synthesis of the new PEDOT:PSS (HTL2) and the fabrication of OSC devices was done by Dr. Stefan Schumann (ER4, Heraeus Company). Dr. Dargie Deribew did additional OSCs fabrication and degradation (ER1, Belectric Company). The development of the Tack test technique and the results associated were done by Alberto Gregori (ESR2, University of Pau). The synthesis and characterization of interlayers was done by Joanna Kolomanska (ESR6, Aston University).

4.2. Identification of the mechanical breaking point in pristine OSCs

4.2.1. Introduction

As mentioned in Chapter 1 and the general introduction of Chapter 4, the adhesion between the PEDOT:PSS (HTL) and the active layer (AL) appear to be the limiting interface in terms of adhesion.[102,103]

Herein, we investigated first the role of the p-type polymer (donor) on the device delamination. The device design and the chemical structure of the studied polymers are shown in **Figure 4.1**. The p-type polymers investigated are P3HT, SiPCPDTBT and PDTSTzTz. The different devices were submitted to Tack tests (see experimental 4.2.2 and **Figure 4.3**) in order to analyze the impact of the p-type polymer on the stress conditions required to break or delaminate the device.

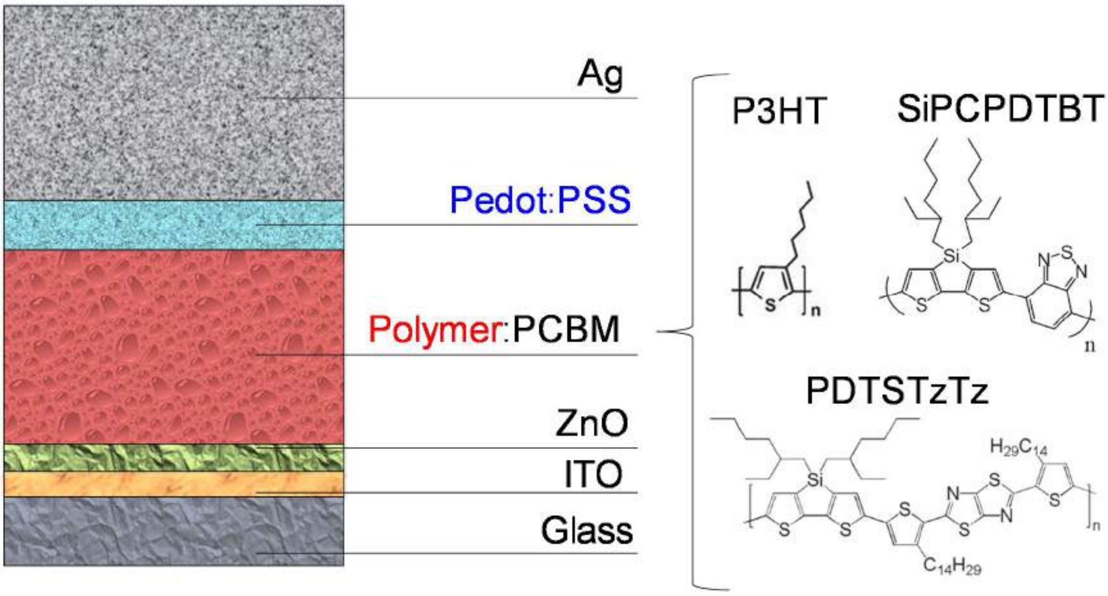

Figure 4.1 - The investigated inverted OSCs structure based on three different p-type polymers.

The surface of each polymer blends was analyzed in terms of chemical composition (XPS) and topography (AFM) in order to characterize the surface where the PEDOT:PSS is deposited. The analysis of the delaminated surfaces enables the detection of the breaking point for each device.

In a second part, two strategies were investigated in order to improve the adhesion between the HTL and AL: the use of a new type of PEDOT:PSS based on organic solvent 1) and the insertion of an interlayer 2). (**Figure 4.2**) The P3HT:$PC_{60}BM$ active layer was used as reference.

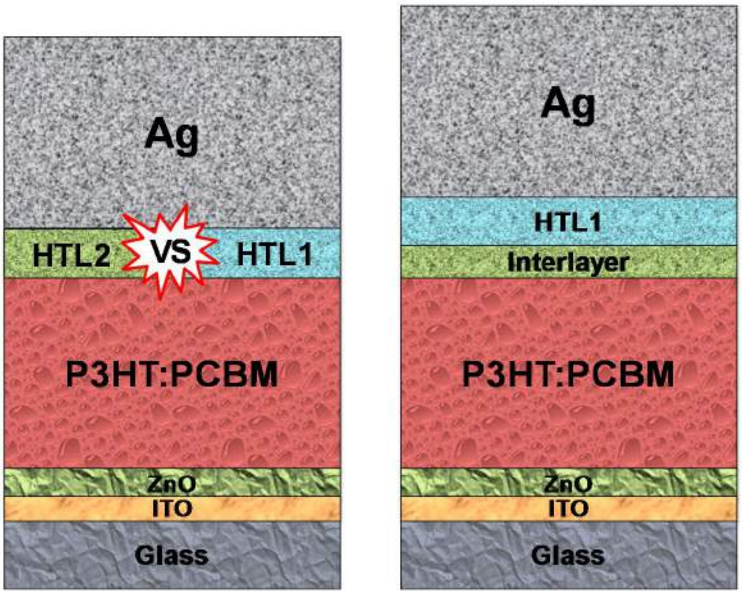

Figure 4.2 - Investigated OSCs structures and the two strategies involved: the use of an organic based PEDOT:PSS (HTL2) as new HTL (left) instead of HTL1 which is a water based PEDOT:PSS (HTL1) or the use of an interlayer based of copolymers (right).

4.2.2. Experimental

Please, refer to the appendix (A1) for additional details on the experimental techniques.

- *PEDOT:PSS formulation and OPV devices fabrication (Dr Stefan Schumann, ER4)*

The non-aqueous PEDOT:PSS (HTL2) dispersion was prepared by a solvent exchange process. The solvent system used includes a mix of higher alcohols such as diethylene glycol and propanediol which was then diluted in ethanol. In the formulation step a surfactant system for better wettability and film formation as well as the non-polar solvent additive are added in low quantities. The water content was determined by Karl-Fischer titration and solids content by gravimetric analysis. Before use, the dispersion was filtered over a 5 µm syringe filter (Minisart, Sartorius) at room temperature. The inverted OPV devices are based on the model system ITO/ZnO/ P3HT:PC$_{60}$BM, 1:1/ PEDOT:PSS/Ag with the following layer thicknesses: ZnO (20 nm), P3HT:PC$_{60}$BM (170 nm) and PEDOT:PSS with either HTL1 (50nm) or HTL2 (120 nm). All layers where spin coated followed by a drying step of 15 minutes at 130 °C after each step. P3HT (BASF):PC$_{60}$BM (Nano-C) was processed from o-dichlorobenzene (Sigma-Aldrich) containing 3wt./% of diiodooctane (Sigma-Aldrich). The sol-gel process for ZnO was described elsewhere. More details are available in a recent article of Schumann et al.[2]

- *Interlayer synthesis and characterization (Joanna Kolomanska, ESR6)*

The complete synthesis and characterization of the investigated copolymers used as interlayers (JK189, JK190 and JK195) are available in the thesis of Joanna Kolomanska (ESR6, Aston University).

- *Tack tests (Alberto Gregori, ESR2)*

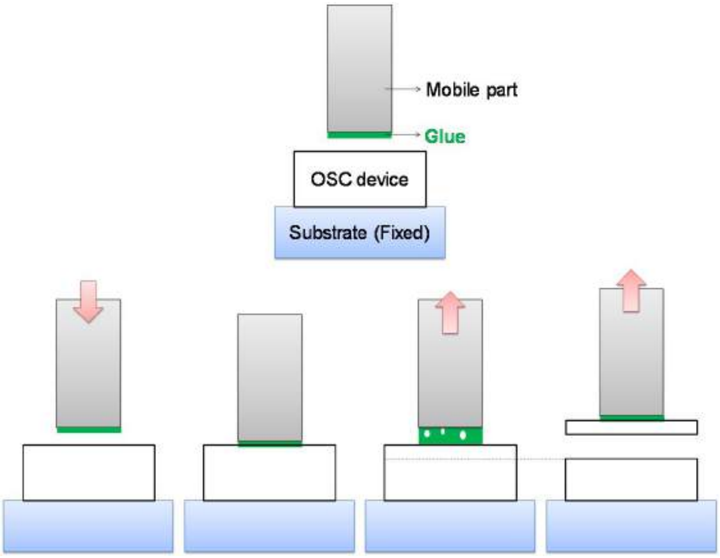

Figure 4.3 - General principle of Tack test experiments.

For this series of experiments a circular probe with a diameter of 12 mm has been used. The adhesive of choice (denoted glue in **Figure 4.3**) has been an epoxy adhesive under the commercial name of SADER® from Bostik S. A (5 min hardening, maximum load 130 kg/cm^2). The mixture of epoxy resin and hardener was prepared before each measurement and the time between the deposition of the adhesive drop and the probe contact was always kept around 30 s. The approaching speed of the probe was 50 mm/s, with a sampling frequency of 100 Hz, and the force sensor used was a TME F108TC, with an operating range of 1-100 N and a sensitivity of 0.05 N. The calibration for the linearity factor was repeated at the beginning of every day of measurement. The contact threshold force was of 5 N and it was kept constant during the curing of the adhesive (30 min), with a sampling frequency of 0.1 Hz. The pulling speed was 10 mm/s with a sampling frequency of 100 Hz. The pictures were taken with a Canon IXUS 132 and the software utilized to treat the images was ImageJ (National Institutes of Health, Open source under Title 17, Section 105 of USA code).

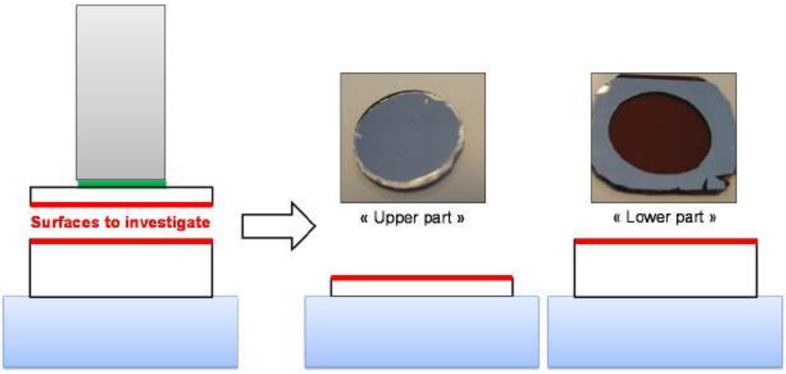

Figure 4.4 - The so called *"upper part"* and *"lower part"* obtained after the Tack tests. The red surfaces are the regions of interest for identifying the breaking points.

- *Surface investigation*

XPS measurements were carried out using a multichamber UHV system (base pressure 10^{-10} mbar), equipped with a SPECS Phoibos 150 cylindrical hemispherical analyzer and a monochromatic Al Kα source (Focus 500 monochromator XR50m X-ray source, Al Kα 1486.74 eV).

A Nanoscope IIIa atomic force microscope (AFM) from Veeco Instruments was used for surface topography measurements. Images were obtained using the repulsive mode in intermittent contact, more commonly called the “tapping” mode. The RMS (root mean square) represents the standard deviation of the Z-axis values of a given surface.

4.2.3 Results and discussion

- *Identification of the breaking point in OPV devices, influence of p-type polymer*

The devices based on three different p-type polymers (**Figure 4.1**) were submitted to the Tack test analysis. **Figure 4.5** shows the stress force at the breaking point for the different devices.

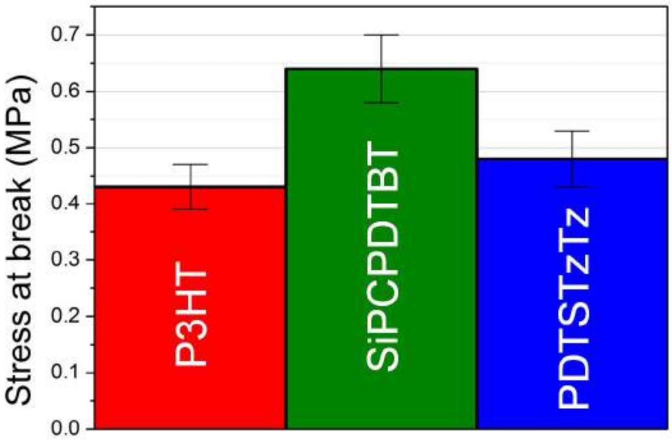

Figure 4.5 - Stress at break for OSCs based on P3HT, SiPCPDTBT and PDTSTzTz polymers as donor materials.

As a general rule, one can say that the smaller the stress at the breaking point is the weaker is the adhesion in the device. We can observe that significantly different values are obtained depending of the polymer. The weakest stress at break was found for devices based on P3HT, followed by PDTSTzTz and finally SiPCPDTBT. The fact that different stresses at break were obtained suggest that the breaking point involve directly or indirectly the p-type polymer. Therefore, it seems that the choice of the p-type polymer influences the overall resistance of the device against delamination. A closer look on the upper and lower parts already suggest that the breaking region lies somewhere between the silver and top of the active layer. (**Figure 4.6**) Indeed, one can see already by eyes the silver on the upper part possibly covered by transparent) PEDOT:PSS. Thus the colorless aspect of the upper part suggests that no or a weak part of the active layer adhere to silver/PEDOT:PSS.

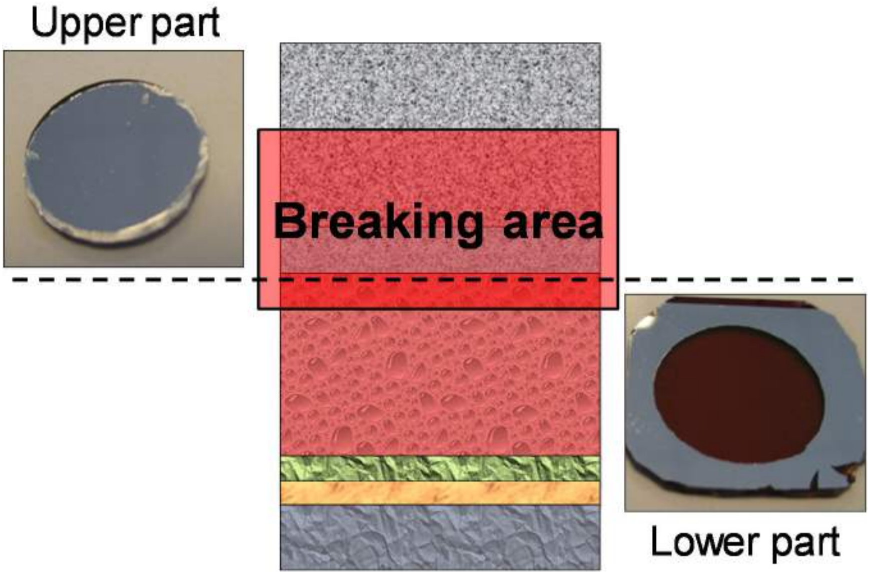

Figure 4.6 - Breaking area estimated from the photographs of the so called upper and lower parts in the case of the devices based on P3HT p-type polymer.

By eyes, the breaking point seems to be similar, independent on the p-type polymer used. Nevertheless, we decided to use surface sensitive techniques (XPS and AFM) in order to reveal possible differences in the three different cases.

Before analyzing the OSC devices, it is necessary to analyze the individual layers as references. If several layers are involved in the breaking process, a complex chemical composition of the upper and/or lower parts can be expected. First, we have analyzed the glass/ITO substrate by XPS and AFM in order to get the chemical composition and morphology of the surface. Then, each layer which constitutes the OSCs was coated on the glass/ITO substrate and analyzed in the same manner in order to get the “id” of each individual layer. The AFM images of each layer are available in Appendix (A4.1). **Figure 4.7** summarized the topography of the different surfaces. The interfaces in **Figure 4.8** correspond to the AFM profiles of the individual layers. In reality, the interfaces most probably are somewhat different than the profiles of none confined layers due to the intermixing after deposition of the upper layers. However, it gives us a more realistic picture than the flat lines (left side of **Figure 4.8**). We can observe that the roughness of the active layer fluctuates significantly by changing the p-type polymer. **Figure 4.7** shows the AFM images of the different active layer surfaces. We can observe that P3HT:$PC_{60}BM$ has a different surface morphology than the others. When we look at the 10x10 µm images or the AFM profile (**Figure 4.6**), the surface of P3HT:$PC_{60}BM$ has a large roughness most probably due to the thermal annealing step. The two other polymer blends seem to be less sensitive or at least the surfaces remain relatively smooth. We show polymer blend surfaces in **Figure 4.7** only, as they are the device-relevant surfaces on where the PEDOT:PSS will be deposited.

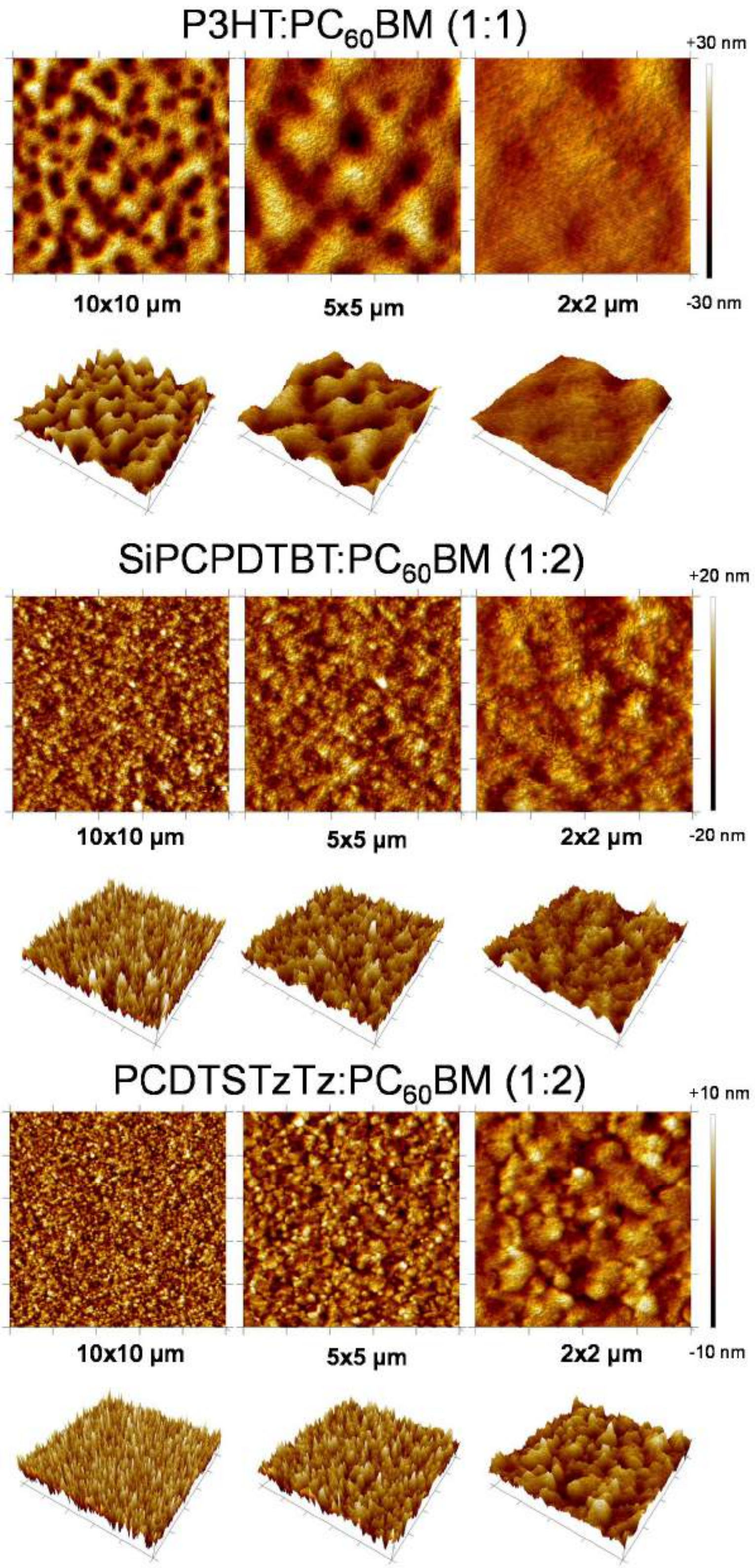

Figure 4.7 - AFM images of P3HT:PC$_{60}$BM (1:1), SiPCPDTBT:PC$_{60}$BM (1:2) and PDTSTzTz:PC$_{60}$BM (1:2) films at different scales. The samples were dried 15 min at 130°C.

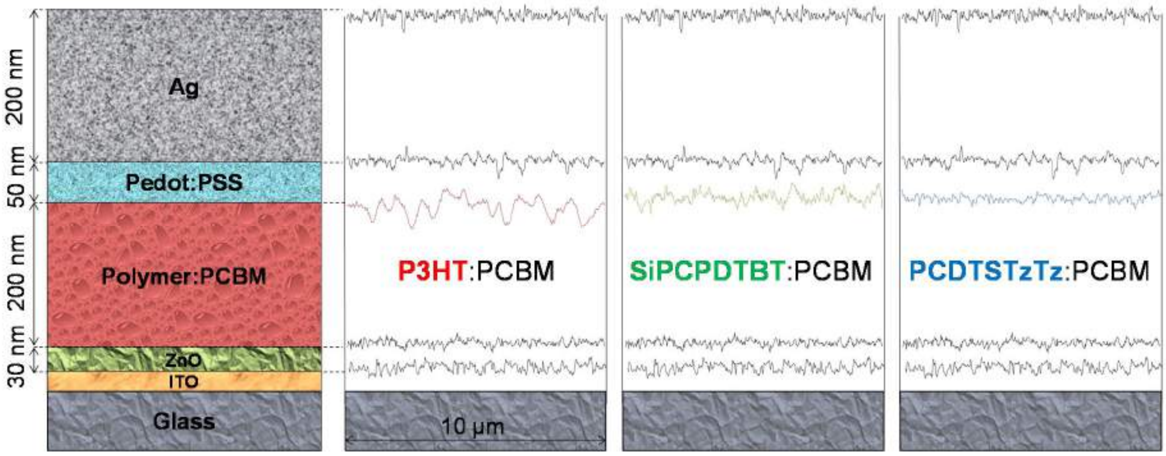

Figure 4.8 - General structure of the device associated to the individual layer profiles and thicknesses obtained by AFM.

In some polymer blend films, it is known that the $PC_{60}BM$ has the tendency to sediment at the bottom resulting in a gradient of composition with more polymer at the surface and more $PC_{60}BM$ at the bottom.[190,191] In order to know more precisely the chemical composition of our polymer blend surfaces, we have compared the carbon/sulfur element ratio extracted from XPS spectra of neat polymer films with the blend versions. The results are also compared to the expected value from the chemical structure and are shown in **Table 4.1**.

	Expected C/S (Polymer)	**C/S from XPS (Polymer)**	**C/S from XPS (Polymer:$PC_{60}BM$)**
P3HT	10.1	10.5	13.2
SiPCPDTBT	11.0	11.6	16.0
PCDTSTzTz	10.4	10.5	18.0

Table 4.1 - Expected and measured carbon / sulfur (C/S) ratio in polymer and blend films.

First of all, it is important to mention that XPS gives us the chemical composition at the surface meaning less than 10 nm. We can observe that the C/S element ratios for the neat polymers are in line with the theoretical ratio. Although the survey spectra of blend and neat polymer films for the three cases are very similar, the calculated C/S ratios show that additional carbons are located at the surface and can be attributed to the $PC_{60}BM$. We can note that the amount of $PC_{60}BM$ seems to be relatively higher in the case of SiPCPDTBT and PDTSTzTz than for P3HT. This is probably due to the fact that the optimal polymer:fullerene ratio (best device performances) for both SiPCPDTBT and PDTSTzTz case are (1:2) while it is (1:1) in the case of P3HT. We can note that the difference of $PC_{60}BM$ content at the surface does not have a negative effect on the adhesion. (**Figure 4.5**) Although we see that the $PC_{60}BM$ is also at the surface, the most abundant component is by far the polymer which may also explain the observed large difference of surface roughness.

In a next step, we investigated the chemical composition and morphology of the upper and lower samples (after Tack tests) for the different devices. (See experimental for more information) We start with the devices based on P3HT:PC$_{60}$BM. **Figure 4.9** shows the XPS spectra of the upper and lower surfaces compared to the neat (reference/control) P3HT:PC$_{60}$BM and PEDOT:PSS.

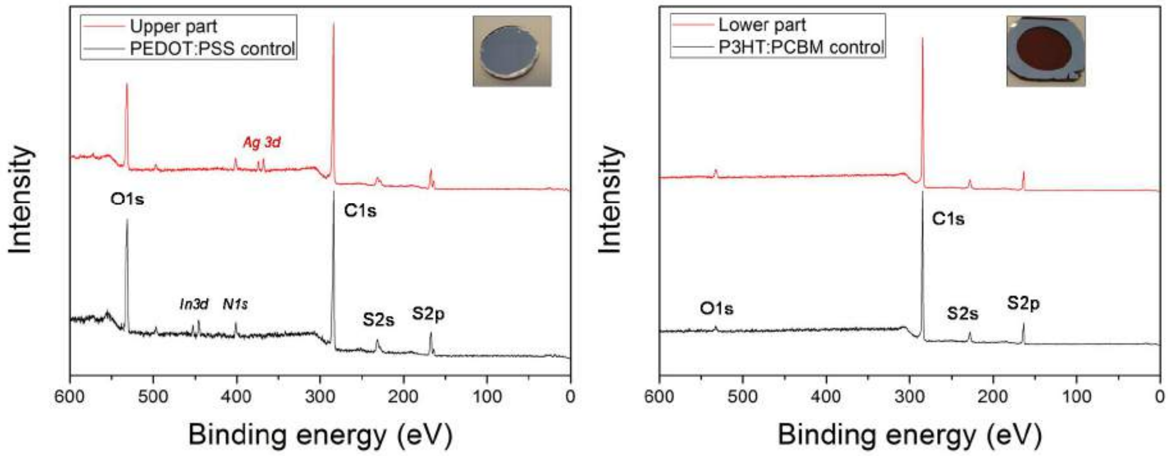

Figure 4.9 - XPS survey spectra of the P3HT:PC$_{60}$BM and PEDOT:PSS control samples compared to the upper (left) and lower (right) parts.

From the survey spectra, the breaking point seems to be located at the exact interface between the P3HT:PC$_{60}$BM and PEDOT:PSS layer. Indeed, the upper and lower parts match very well with the PEDOT:PSS control and P3HT:PC$_{60}$BM control spectra respectively. Nevertheless, two differences can be observed regarding the upper part. First, the signal at about 445 and 443 eV are present on the control sample and are attributed to In3d core levels. This is due to the fact that the PEDOT:PSS control layer was very thin (close to the 10 nm) and the In3d signal from the ITO substrate even small is visible. Secondly, we can observe signals at 368 and 374 eV on the upper part sample only. These peaks are attributed to silver atoms from the electrode. Two reasons can explain why we observe a small amount of silver. First, the breaking point is not perfectly flat and as the spot of the XPS is relatively large (< 5mm) it is possible to have very locally, breaking points located deeper in the PEDOT:PSS layer and close to the silver electrode. The other explanation can be that some silver atoms can diffuse into the PEDOT:PSS during the device fabrication or Tack test analysis. The survey spectra support more the second hypothesis as the lower part spectrum does not show any trace of residual PEDOT:PSS which should be visible if locally the breaking would be close to the Ag/PEDOT:PSS interface.

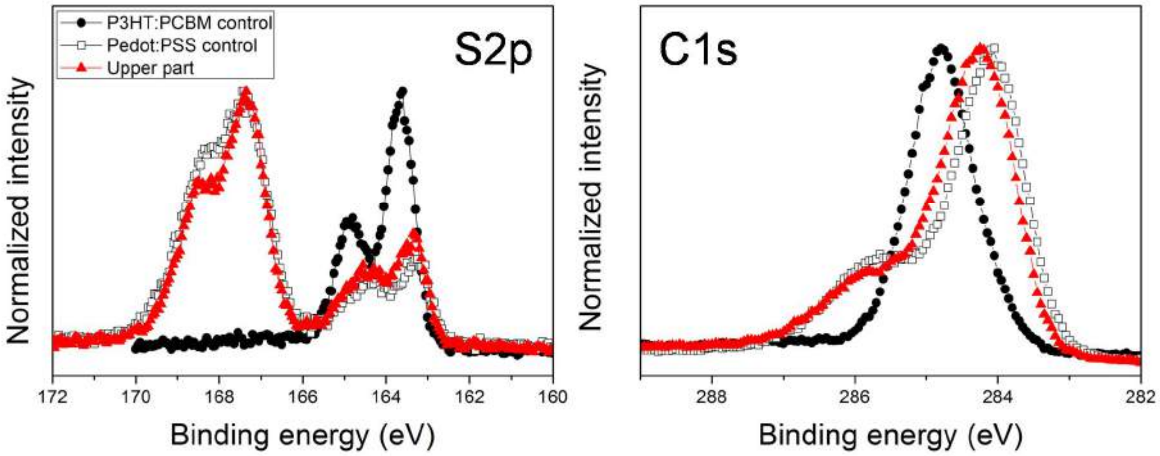

Figure 4.10 - XPS spectra of the S2p (left) and C1s (right) core levels for the control samples and the upper part.

Figure 4.10 shows more details related to the C1s and S2p core levels. We observe clearly that the S2p and C1s spectra of the upper sample are very similar to the PEDOT:PSS control sample. Thus, from the XPS spectra, we confirm that the PEDOT:PSS/P3HT:PCBM interface is definitely the weak point in terms of mechanical adhesion. We also performed AFM measurements on the upper and lower samples.

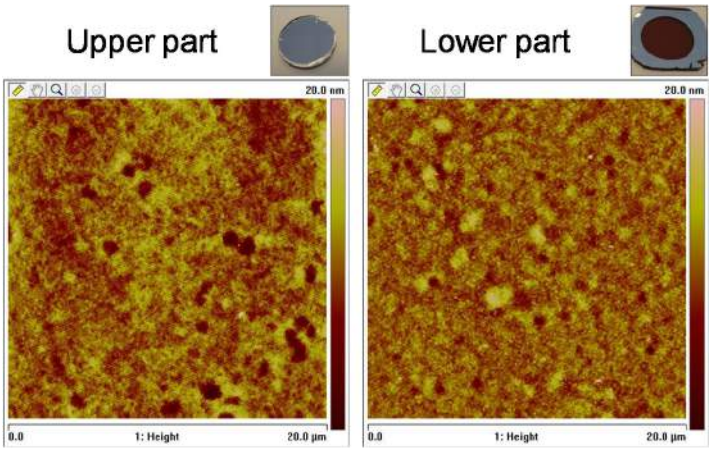

Figure 4.11 - AFM images of the upper and lower parts in OSCs based on P3HT:PC$_{60}$BM.

We note again that the morphology of the neat P3HT:PC$_{60}$BM and PEDOT:PSS control samples is different, probably due to interlayer mixing which can modify interface properties. However, holes (diameters are between 0.5 and 1 µm) are present on both upper and lower surfaces but not on the control samples. This suggests that the holes were formed during the deposition of the PEDOT:PSS on P3HT:PC$_{60}$BM. The holes are deeper and more well defined in the upper part (PEDOT:PSS side).

Thus, the AFM results confirm that the breaking point is very close to the PEDOT:PSS/P3HT:PC$_{60}$BM interface and the holes observed by AFM suggest a poor intermixing between the two layers probably due to their hydrophobic/hydrophilic properties. Additionally holes at the interface may represent potential none-adhesive regions and decrease the overall adhesion between the layers.

The same procedure has been done for devices based on SiPCPDTBT and PCDTSTzTz blends. **Figure 4.12** shows the survey spectra of the upper parts.

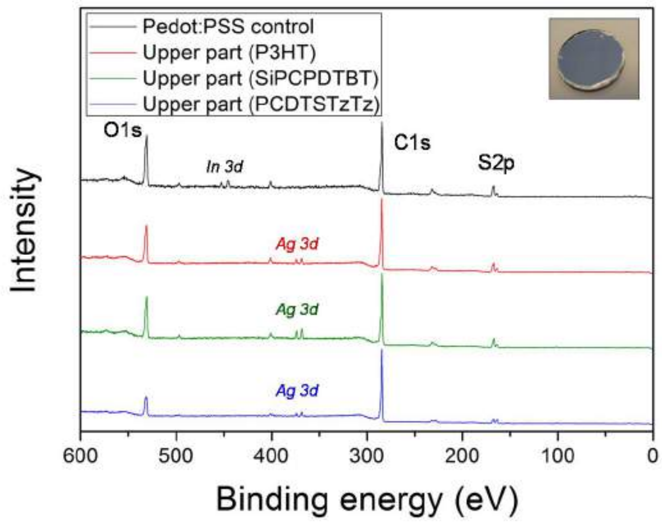

Figure 4.12 - Survey spectra of PEDOT:PSS control and upper parts of devices based on P3HT:PC$_{60}$BM, SiPCPDTBT:PC$_{60}$BM and PCDTSTzTz:PC$_{60}$BM.

Ag/PEDOT:PSS/P3HT:PC$_{60}$BM/ZnO/ITOglass			
C/S PEDOT:PSS Control	C/S blend Control	C/S Upper part OSC	C/S Lower part OSC
7.4	13.2	8.3 =0.17blend+0.83Pedot:PSS	12.7 =0.91blend+0.09Pedot:PSS
Ag/PEDOT:PSS/SiPCPDTBT:PC$_{60}$BM/ZnO/ITOglass			
C/S PEDOT:PSS Control	C/S blend Control	C/S Upper part OSC	C/S Lower part OSC
7.4	16.0	8.9 =0.17blend+0.83Pedot:PSS	17.9 >
Ag/PEDOT:PSS/PCDTSTzTz:PC$_{60}$BM/ZnO/ITOglass			
C/S PEDOT:PSS Control	C/S blend Control	C/S Upper part OSC	C/S Lower part OSC
7.4	18.0	11.5 =0.39blend+0.61Pedot:PSS	21.3 >

Table 4.2 - C1s/S2p element ratio from survey XPS spectra of PEDOT:PSS, P3HT:PC$_{60}$BM (1:1), SiPCPDTBT:PC$_{60}$BM (1:2) and PCDTSTzTz:PC$_{60}$BM (1:2) control samples compared to their corresponding upper and lower parts from devices after Tack tests.

The results in **Table 4.2** give a more precise idea of the breaking point near the PEDOT:PSS/AL interface. In the case of devices based on P3HT:$PC_{60}BM$, the upper part has a C/S ratio which corresponds to a mixture of 83% of PEDOT:PSS and 17% of blend assuming an homogeneous distribution of these components. Thus, the breaking point is close to the PEDOT:PSS/AL interface, only slightly in the active layer. According to that, the lower part should be composed only of the blend. Indeed, we found that the C/S ratio of the lower part is very close to the neat blend value. **Table 4.2** confirms the outcome of the survey and detailed C1s and S2p core levels and gives more precise idea on the breaking point.

For SiPCPDTBT:$PC_{60}BM$, the upper part show similar results than for P3HT:$PC_{60}BM$ meaning the surface of the upper part consists mainly of PEDOT:PSS. However, the lower part shows a higher C/S ratio (17.9) compared to the blend control sample (16.0) suggesting the presence of additional carbon most likely from the $PC_{60}BM$. This could be explained by a heterogeneous vertical polymer:fullerene composition. After delamination (or Tack tests), the first nanometers of the active layer (rich in polymer, see **Table 4.1**) are more strongly bound to PEDOT:PSS and remain therefore at the PEDOT:PSS of the upper part. As a consequence, the lower part has a higher fraction of $PC_{60}BM$ as expected for layers closer to the bulk of the blend. This effect was not found in the case of P3HT:$PC_{60}BM$ probably because the polymer:$PC_{60}BM$ ratio is only 1:1 resulting in a weaker amount of $PC_{60}BM$ at the surface even after delamination.

For PCDTSTZTz:$PC_{60}BM$, the upper part shows a significantly higher C/S ratio with respect to the PEDOT:PSS control sample meaning a probable higher amount of polymer blend compared to the other cases. Assuming a homogeneous distribution of the materials, the amount of blend has been evaluated from XPS intensities to be around 39% (and 61% of PEDOT:PSS). The high amount of blend materials on the upper part means that the breaking point is probably localized deeper in the active layer than for P3HT and SiPCPDTBT based devices. As for SiPCDTBT, the lower part shows a distinctly higher C/S ratio than the blend control. Again, this could be explained for the same reason meaning that the polymer rich surface observed for polymer blend control samples is now on the upper part and a higher content of $PC_{60}BM$ is observed because the delamination point is deeper in the polymer blend films.

Figure 4.13 - Schematic representation of the interface and breaking points according to XPS and AFM results. The polymer:blend surface topography was extracted from the AFM profiles. The dotted line represents the estimated and proposed mechanical break position.

In this section, we have seen that although the stresses at break varies with the p-type polymer, the weak point in terms of adhesion remains definitely the PEDOT:PSS/Polymer:$PC_{60}BM$ interface. The presence of holes observed in the case of P3HT:$PC_{60}BM$ can be attributed to weak adhesion areas. This may explain why these devices show the weakest stress at break. Since the interface PEDOT:PSS/polymer: $PC_{60}BM$ seems to be the generally limiting mechanical weak point in OSCs, it is necessary to find strategies to improve the stability of this interface. This is the object of the subsequent section.

- *The use of new type of PEDOT:PSS*

A new type of PEDOT:PSS, based on organic solvents (see experimental for more information) was tested in order to improve the intermixing with the active layer. The idea is to increase the affinity between the holes transporting (HTL) and active layers (AL). We denote in the following the standard water based PEDOT:PSS HTL1 and the organic based one called HTL2. IT can be shown that the device performances using HTL2 are very similar to HTL1. The formulation development and successful insertion in OPV devices has been recently published.[2] Analogously to HTL1, Tack tests were performed on inverted devices (**Figure 4.2**) containing HTL2. All data together are summarized in **Figure 4.14.** We observed only effect of the HTL for P3HT:PC$_{60}$BM based solar cells with a slight improvement while a slight decrease for SiPCPDTBT:PC$_{60}$BM was observed although the differences are within the error bars . No significant effect was found in the case of PCDTSTzTz based devices.

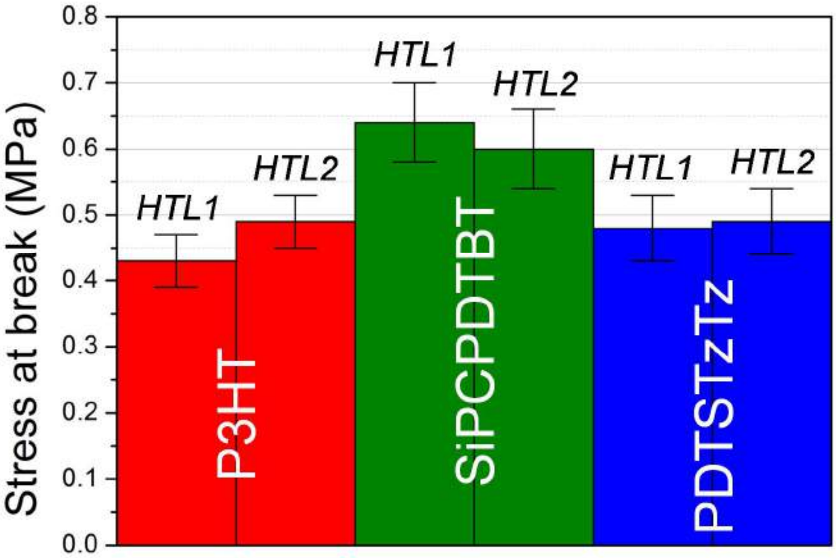

Figure 4.14 - Effect of HTL2 on the stress at break for OSCs based on P3HT, SiPCPDTBT and PDTSTzTz polymers as donor materials.

The question arises if the weak point in these devices is also the PEDOT:PSS/AL interface. As an example, we focus on devices based on P3HT:PC$_{60}$BM as a slight improvement was observed. As for HTL1, XPS and AFM investigations were carried out on upper and lower parts after Tack test in order to identify the breaking points.

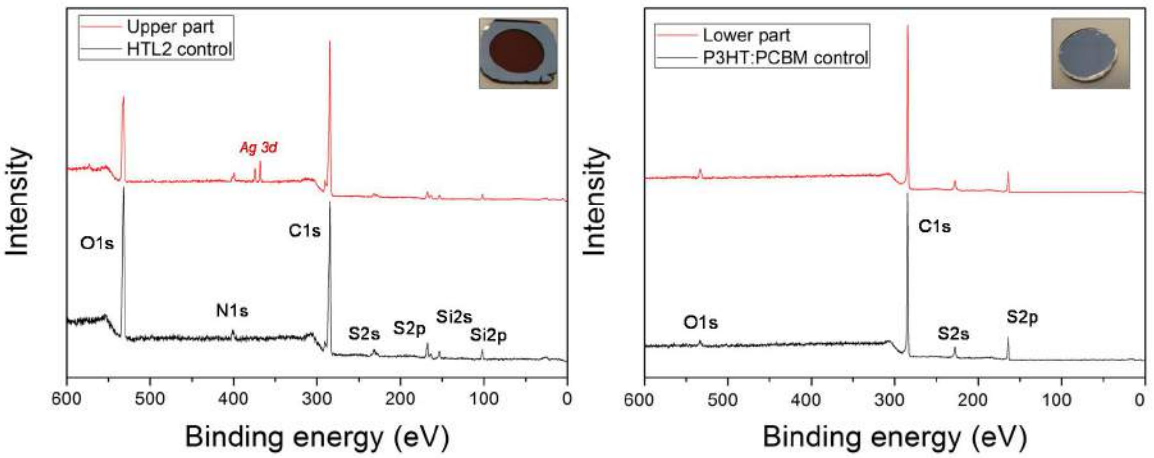

Figure 4.15 - XPS survey spectra of upper and lower parts compared to the control P3HT:PC$_{60}$BM and HTL2 samples.

From the survey spectra (**Figure 4.15**), we can observe that, as observe for HTL1, the spectrum of the upper part is similar to the PEOT:PSS (HTL2) control sample and the spectrum of the lower part comparable to the P3HT:PC$_{60}$BM control sample suggesting that the breaking point is also close to this interface. **Figure 4.16** shows the detailed core level spectra of C1s and S2p of the upper part. It is clearly visible that the C1s spectrum of the upper part can be only described by a superposition of the C1S spectra of the AL and HTL2. The component at 286.5 eV from the HTL2 is clearly visible, but their relative intensity is lower. Additionally, the peak at 284.7 eV shows a small energetic shift, similar to the position of the P3HT:PC$_{60}$BM control. Concerning the S2p, we observe a somewhat higher relative intensity of features in the low binding energy range (163-166 eV) with respect to the HTL2 spectrum, most probably due to the superposition of signals from P3HT and PEDOT. To confirm this observation, we performed a peak fitting of the S2p core level spectra, shown in (**Figure 4.17**)

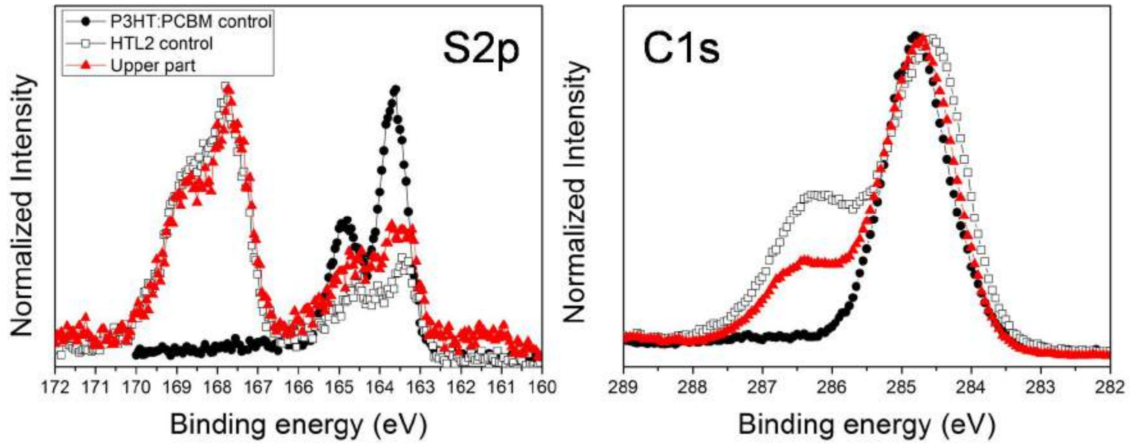

Figure 4.16 - S2p (left) and C1s (right) core levels of the upper part (HTL2 based devices) compared to the control samples.

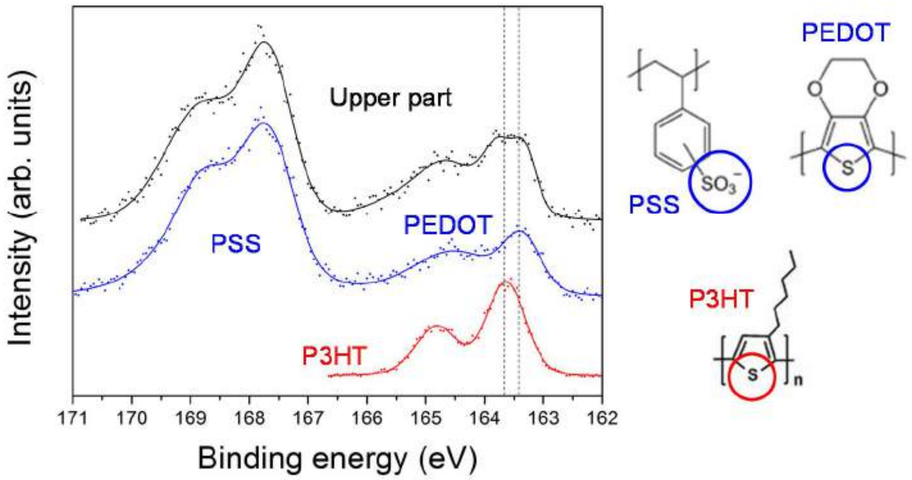

Figure 4.17 - S2p signal of control P3HT (red), HTL2 (PEDOT:PSS) and the upper part obtained after Tack tests (black). Experimental spectra are in dots and the fitting in full lines for each case. The chemical structures of the involved polymers are shown on the right side.

S2p signal consists of a spin-slit doublet (S2p$_{3/2}$ and S2p$_{1/2}$) with an energy splitting of 1.2 eV and intensity ratio (1:2).[192] From **Figure 4.17**, we can observe that the control P3HT S2p is in line with the expected splitting energy and intensity ratio. It is not the case for HTL2 and this can be explained by the various chemical states present when PEDOT and PSS are mixed together.[192] Indeed, several components for PSS and PEDOT can be expected as positive and negative charges are localized on PEDOT and PSS respectively resulting in a broadening of the S2p signals for both polymers. The S2p signal of PEDOT:PSS is well documented in the literature.[192-195] Concerning the upper part of the HTL2/P3HT:PC$_{60}$BM based devices, we can observe that the experimental S2p spectrum around 163.5 eV is larger than the individual HTL2 and P3HT. **Figure 4.17** reveal that qualitatively, the signal of the upper part consists likely of the superposition of the PEDOT and the P3HT. This is again in line with the fact that the upper part has a significant part of the active layer.

Ag/**HTL1**/P3HT:PC$_{60}$BM/ZnO/ITOglass			
C/S **HTL1** Control	C/S blend Control	C/S Upper part OSC	C/S Lower part OSC
7.4	13.2	8.3 =0.17blend+0.83HTL1	12.7 =0.91blend+0.09HTL1
Ag/**HTL2**/P3HT:PC$_{60}$BM/ZnO/ITOglass			
C/S **HTL2** Control	C/S blend Control	C/S Upper part OSC	C/S Lower part OSC
16.4	13.2	20.3 >	11.7 <

Table 4.3 - Comparison of the C1s/S2p element ratio for P3HT:PC$_{60}$BM, HTL1 and HTL2 control samples with to the upper and lower parts.

In **Table 4.3**, we compare the C/S intensity ratio of the upper and lower parts after Tack tests for devices based on P3HT:PC_{60}BM and HTL1 or HTL2 (data for the HTL1 based device are taken from **Table 4.2**). The HTL2 itself is richer in carbon compared to HTL1. For the HTL2 based device, the upper part the C/S ratio is even higher than the HTL2 control ratio. This suggests that PC_{60}BM from the active layer is present on the upper part. The lower part shows a C/S ratio lower than the blend control sample; the value of 10.7 is in fact close to neat P3HT control (10.5, see **Table 4.1**).

Thus, from XPS, we may conclude that in the case of HTL2 the breaking point is located deeper in the active layer (even if it is still close to the surface) compared to HTL1.

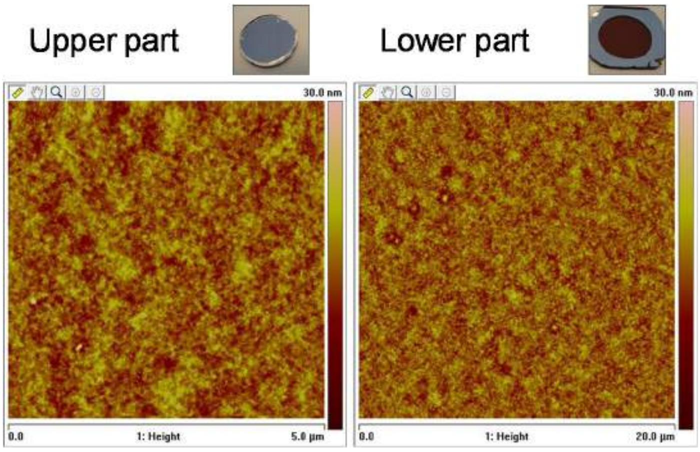

Figure 4.18 - AFM images of the upper and low parts in OSCs based on HTL2/P3HT:PC_{60}BM.

Figure 4.18 shows that the upper and lower parts are comparable and relatively smooth without holes as it was the case for HTL1. This may support the initial assumption that HTL2 allows a better intermixing with the active layer.

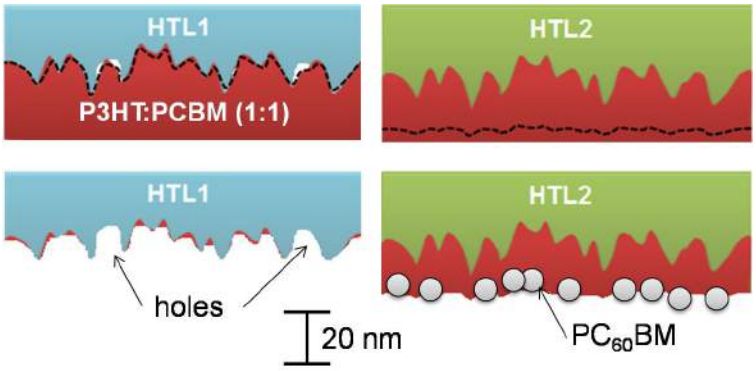

Figure 4.19 - Carton of the estimated breaking points in the case of HTL1/P3HT:PC_{60}BM and HTL2/P3HT:PC_{60}BM interfaces.

- *The use of interlayers*

The second tested strategy to improve the AL/HTL adhesion was the use of an interlayer (IL). An additional layer between the AL and HTL based on a block copolymer poly(isobutyl p-styrene sulfonate)-b-poly(dodecyl p-styrene sulfonate) (PiBSS-b-PDDSS) was inserted in the device structure. A thin layer (not measured but should be close to 10 nm according to some XPS spectra) of PiBSS-b-PDSS was deposited on the AL as described in the experimental section. The intermixing between the AL and the IL is supposed to be better than with PEDOT:PSS as the deposited IL solution is based on an organic solvent. Once the IL deposited on the AL, a thermal annealing was carried out (15 min at 150 °C) in order to de-protect the side chains of the PIBSS-b-PDSS (**Figure 4.20**). Thus, the resulting surface is supposed to be more compatible with PEDOT:PSS. At the end an improvement of the overall adhesion is expected.

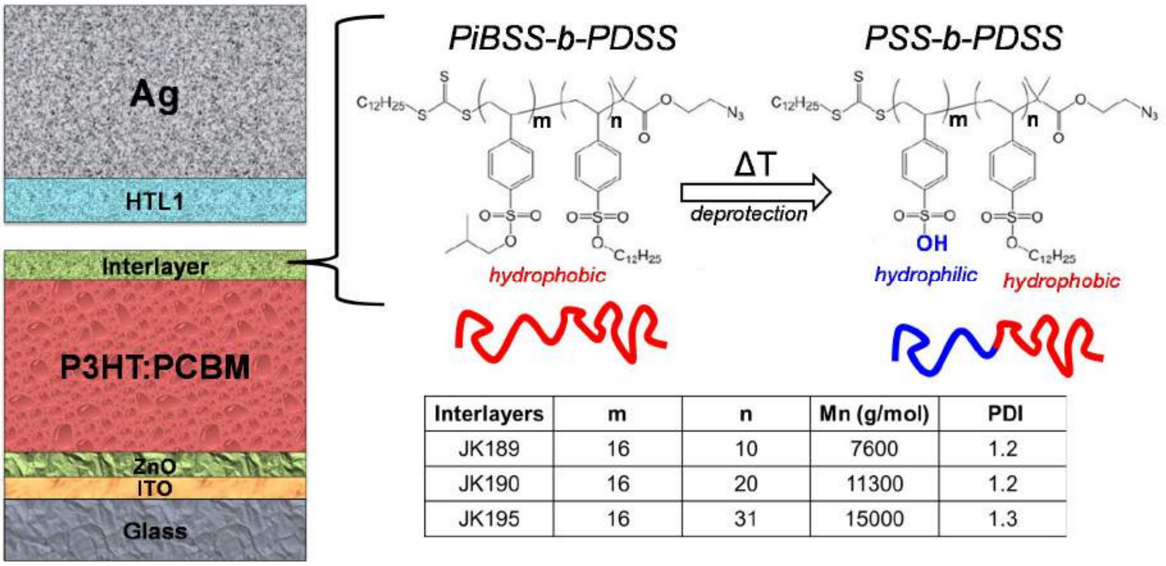

Interlayers	m	n	Mn (g/mol)	PDI
JK189	16	10	7600	1.2
JK190	16	20	11300	1.2
JK195	16	31	15000	1.3

Figure 4.20 - Device structure and chemical structure of the interlayers before and after de-protection. Physical properties of the three interlayers are presented in the inserted table.

Devices were fabricated with the three different interlayers (JK189, JK190 and JK195) de-protected or not and were submitted to Tack tests. Results are shown in **Figure 4.21**. It is clear that the stresses at break are generally lower than the reference when interlayers are inserted. We note that the de-protection (thermal annealing) increases the adhesion strength in all cases. However, the adhesions remain lower than the reference sample without interlayers. In the best case (JK195), the adhesion strength is comparable to the reference. We could explain the weak adhesion without de-protection by the fact that a relative interface dipole may occur between P3HT and PSS. This was proposed for explaining why the interface is stronger in inverted device configuration.[103] By adding the interlayer, the $P3HT^+/PSS^-$ interface is suppressed resulting in a weaker interface. The fact that a better adhesion was observed after de-protection suggest that the de-protected PSS interact favorably with the PEDOT:PSS.

The surface topography of the upper part (obtained after Tack tests) of the reference (without interlayer) was compared to the upper parts when JK189, JK190 and JK195 interlayers were used (**Figure 4.22**). In this case, all the interlayers were de-protected.

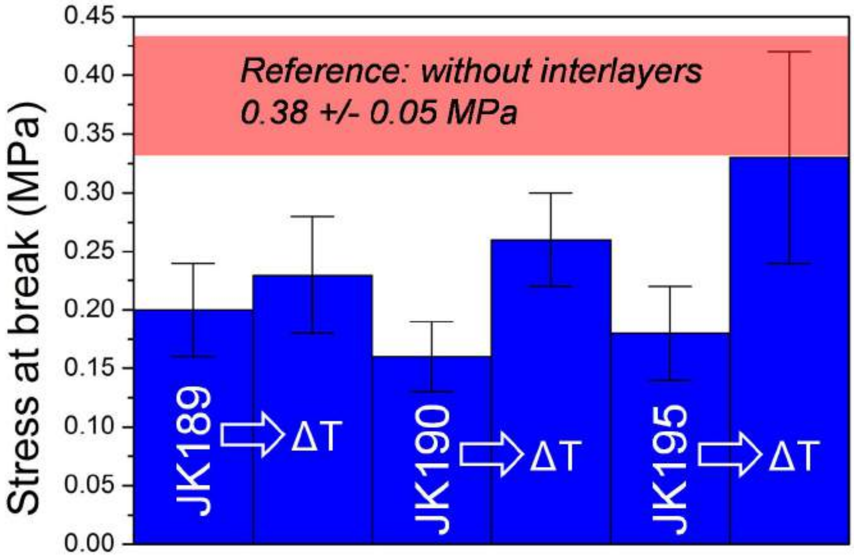

Figure 4.21 - Stresses at break with the different interlayers with or without de-protection compared to the reference without interlayers.

We can clearly observe that dots are visible on all surfaces only when an interlayer is used. These dots are homogeneously distributed in the case of JK189. We ascribe these dots to residues of the interlayer or to PEDOT:PSS from the upper part.

During the de-protection step, cohesion with the PEDOT:PSS can occur resulting an improvement of the adhesion (compared than without de-protection) Clear insights from XPS spectra are difficult to obtain as the chemical structure of PEDOT:PSS and interlayers are very similar.

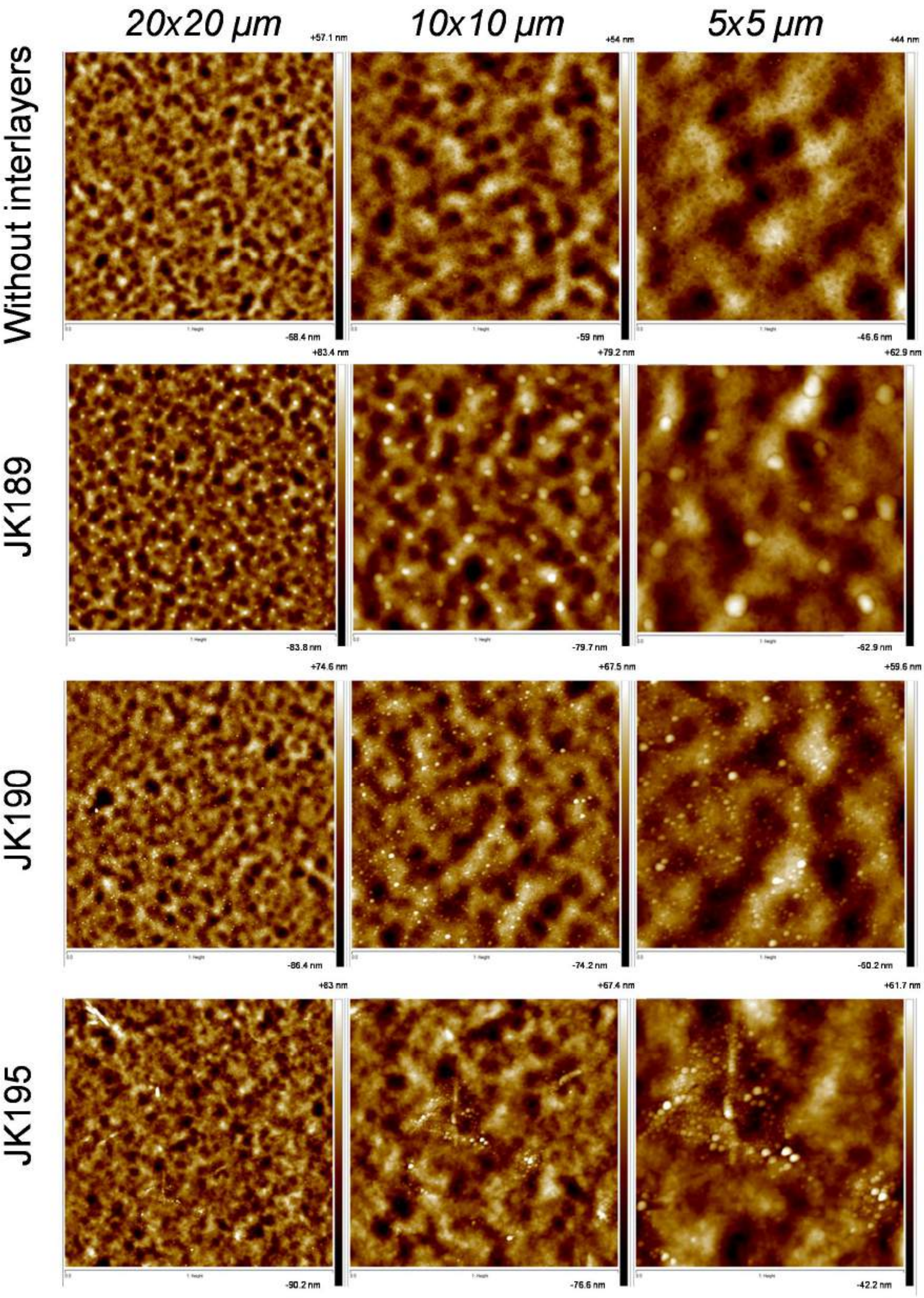

Figure 4.22 - AFM images of the upper part of the reference (without interlayer) and with JK189, JK190 and JK195. All the interlayers were de-protected by thermal annealing (15 min at 150°C).

4.2.4. Conclusion

In this part, we have identified the weakest mechanical point in inverted OSCs. We have seen that although the choice of the p-type polymer has an influence on the stress at break. The limiting interface remains the PEDOT:PSS/Polymer:PC$_{60}$BM interface. The breaking point was found to be very close to the interface for P3HT:PC$_{60}$BM and SiPCPDTBT:PC$_{60}$BM based devices while it was slightly deeper in the active layer for PCDTSTzTz:PC$_{60}$BM based devices. The presence of holes at the surface in the case of P3HT:PC$_{60}$BM may explain the weakest adhesion in the series.

The use of an organic based PEDOT:PSS (HTL2) results in an improvement for P3HT:PC$_{60}$BM based device, the breaking point was found to be deeper in the active layer. Even if the effect of HTL2 on the stress at break was rather small, this approach could be a promising route which needs further investigations. The use of interlayers did not improve the overall adhesion. However, the de-protection of the copolymers increases clearly the stress at break.

4.3. Identification of the mechanical breaking point in aged OSCs

4.3.1. Introduction

The previous part was dedicated to the delamination process on pristine, undegraded devices. We have seen that the delamination occur whatever the p-type polymer used between the hole transporting layer (HTL) and the active layer (AL). The use of an organic based PEDOT:PSS improved slightly the adhesion between the two layers on pristine devices in the case of devices based on P3HT:PC$_{60}$BM. Now, the current part is devoted to the understanding of the delamination process during ageing. It is known that humidity is the main factor responsible of the delamination process due to the water solubility of the PEDOT:PSS (HTL1).[63,189] Therefore, the damp heat test (85°C/85% rH in the dark) is the most severe degradation process for testing the delamination resistance.

Thus, Tack tests on fresh and aged devices were performed and the breaking point analyzed by XPS and AFM (**Figure 4.23**). We concentrate on the inverted devices based on P3HT:PC$_{60}$BM as the active layer.

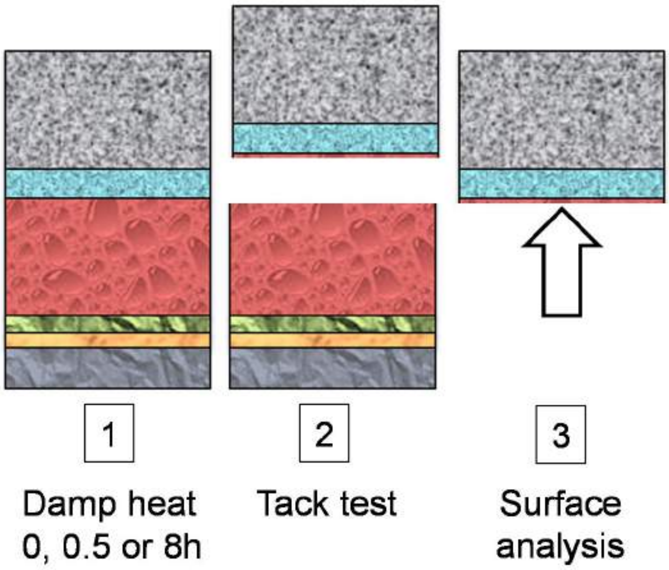

Figure 4.23 - Experimental protocol with first the exposure to damp heat (85°C/85% rH in the dark) followed by the Tack tests and then the surface analysis of the breaking point.

Firstly, the standard water soluble PEDOT:PSS (HTL1) was first investigated as a reference in order to understand the delamination process of a standard device during ageing. Then, the organic based PEDOT:PSS (HTL2) was compared to the water soluble version. Finally, the use of interlayers between the PEDOT:PSS (HTL1) and the active layer was tested as a way to improve the resistance to delamination.

4.3.2. Experimental

Please, refer to the appendix (A1) for additional details on the experimental techniques.

- *OSCs fabrication and characterization damp heat exposure (Dr. Dargie Deribew, ER1)*

Inverted devices glassITO/PEI/P3HT:$PC_{60}BM$/PEDOT:PSS/Ag were fabricated using standard procedures. First, the glass/ITO substrate was cleaned in an ultrasonic bath of acetone and propan-2-ol for 10 min each. Following cleaning, the substrates were dried and treated by UV-ozone for 10 min. PEI, which is used as an electron transporting layers (ETL), was subsequently coated directly on top of the cleaned substrates. The coated ETL films were dried at 100 °C in air for 10 min. Following the drying process, approximately 250 nm of P3HT:$PC_{60}BM$ (1:0.8 w/w, from Xylene stirred overnight) photoactive layer was then coated on top of the PEI layer. A thin layer of Poly(isobutyl p-styrene sulfonate)$_m$-*b*-poly(dodecyl p-styrene sulfonate)$_n$ (PiBuSS-*b*-PDSS) interfacial layer (0.5 mg/mL in Acetone) was then subsequently coated on top of the active layer. Prior to coating the PEDOT:PSS, the samples were heated at 150 °C for 12 to 18 min (depending on the length of Poly(isobutyl p-styrene sulfonate block)) in a controlled nitrogen atmosphere (glove box). Following the thermal deprotection process, PEDOT:PSS used as hole transporting layer, was subsequently coated directly from the commercial aqueous dispersion on top of the interfacial layer. All layers were coated using a doctor blade. The devices were then completed by thermally evaporating 300 nm of Ag electrode on customized mask. Before the evaporation of the metal electrode, the photoactive layer was annealed in nitrogen at 140 °C for 5 min. For the moisture induced degradation, devices were exposed to damp heat in a climate chamber (85 °C/85% humidity) for specific period of time. Cells were illuminated with a simulated solar spectrum from Steuernagel Solartest 1200 Oriel solar simulator at 100 mW/cm^2. The current density − voltage (J − V) characteristics of the devices were recorded using Keithley 2400 SMU in combination with Keithley 7001 Multiplexer system and custom software. The mismatch in the simulated solar spectrum is corrected by measuring the external quantum efficiency (EQE) of each cell.

- *Interlayer synthesis and characterization (Joanna Kolomanska, ESR6)*

See 4.1.1

- *Tack tests (Alberto Gregori, ESR2)*

See 4.1.1

- *Surface investigation*

See 4.1.1

4.3.3. Results and discussion

- *Damp heat exposure: evolution of device performance and stress at break*

Inverted devices based on P3HT:PC$_{60}$BM and containing HTL1 were fabricated and exposed to damp heat tests (85°C/85% rH in the dark). The evolution of the device performance is represented in **Figure 4.23**.

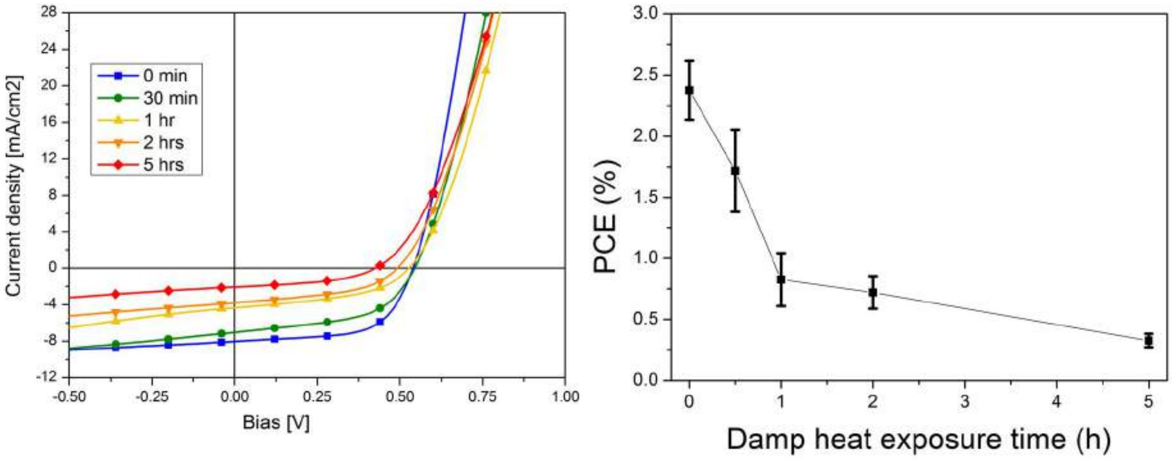

Figure 4.24 - Evolution of the device performance versus time of damp heat (85°C/85% rH in the dark) exposure.

As the devices were not encapsulated, the exposure to damp heat induces a rapid drop of the device efficiency. The stress at break was measured for pristine and exposed devices. **Figure 4.25** shows the stress at break for pristine and devices exposed 0.5 and 8 h to damp heat. We note that the forces are higher than in the previous part (**4.1**). This is due to a modification of the experimental parameters of Tack test. In this part, the devices were prepared by another partner and the Tack tests needed to be adapted.

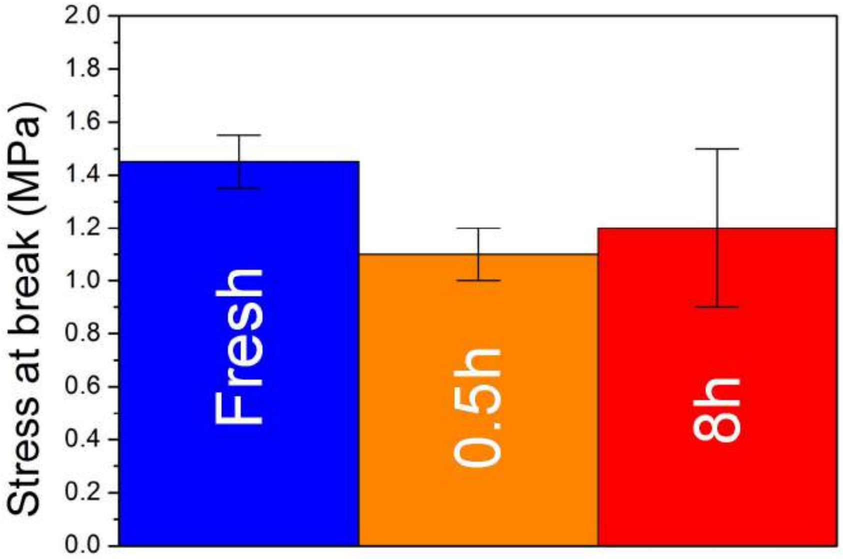

Figure 4.25 - Stress at break for fresh and exposed to damp heat devices.

We can observe that devices submitted to 0.5h of damp heat have a significant drop of adhesion strength resulting in a lower stress at break. In order to characterize the breaking points in mire details, the surface of the upper part was analyzed by XPS and AFM. The XPS survey spectra are shown in **Figure 4.26**.

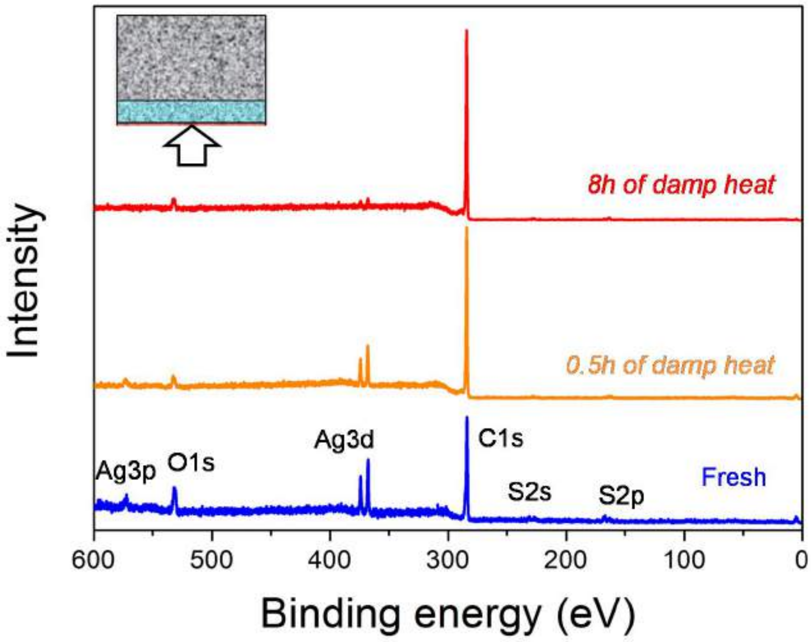

Figure 4.26 - Survey spectra of the upper parts of delaminated fresh and exposed devices.

From the survey spectra, we can observe that the fresh delaminated surface is based on carbon, silver, oxygen and sulfur. The composition is listed in **Table 4.4**. It is in line with the previous part where the upper surface was found to be almost based on PEDOT:PSS with silver.

Samples	C1s	O1s	S2p	Ag3d
Control / Fresh	79.56	9.92	7.17	3.35
Control / 0.5h	84.67	11.21	2.17	1.96
Control / 8h	93.91	3.88	1.82	0.39

Table 4.4 - Evolution of the atomic composition of samples exposed to damp heat (85°C/85% rH in the dark).

After damp heat, we can observe increase of carbon content resulting in a relative decrease of the other elements. The question arises if the chemical state of the carbon is also changing.

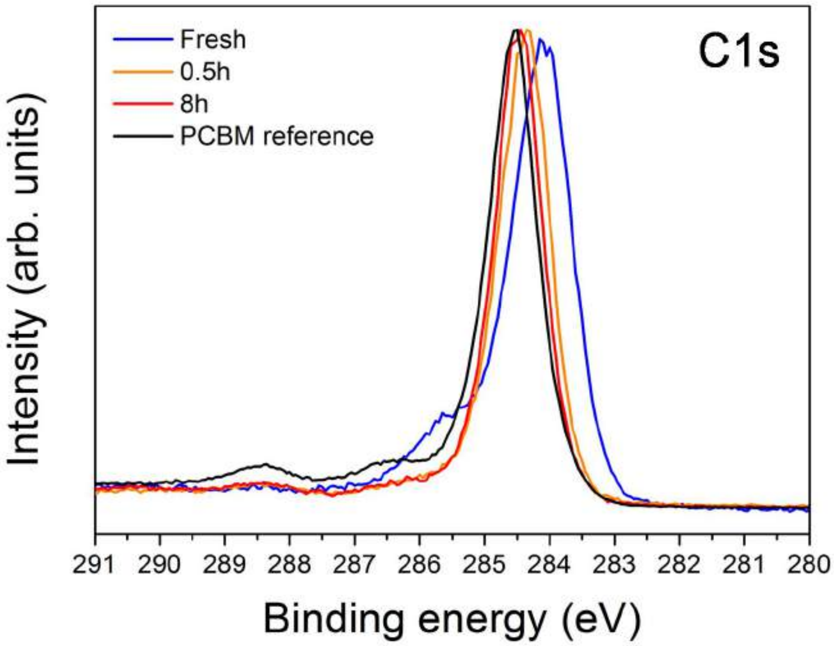

Figure 4.27 - C1s signal of the upper parts of delaminated fresh and exposed devices.

Figure 4.27 shows the detailed shape of the C1s signal, normalized to the same intensity for all three samples and a $PC_{60}BM$ reference. We observe that very rapidly (0.5h of DH exposure) the C1s signal evolves from the PEDOT:PSS like shape to a shape comparable to $PC_{60}BM$. We can even detect the two signals characteristic of the “$PC_{60}BM$ legs”, the C-O (286.5 eV) and C=O (288.5 eV) and additional satellite features. The observation that only the carbon content is increasing with exposure time, indicates that the breaking point is in a $PC_{60}BM$-rich region. The initial sulfur content, originated from PEDOT:PSS, is vanishing like the silver and the oxygen. Nevertheless, these elements did not fully disappear meaning that the breaking point for devices exposed to damp heat is still close to the PEDOT:PSS/AL interface.

The enrichment of $PC_{60}BM$ on the surface, as concluded from XPS data, is even visible by eye. **Figure 4.28** shows photographs of the samples before and after DH. We see the metallic appearance of the silver electrode on the fresh sample. The color and reflectivity of the surface change after damp heat exposure. After 8h, the surface becomes yellowish. This is points to a $PC_{60}BM$ enrichment as a pure thin layer of $PC_{60}BM$ absorbs the UV but also a part of the visible light thus showing a yellow color.

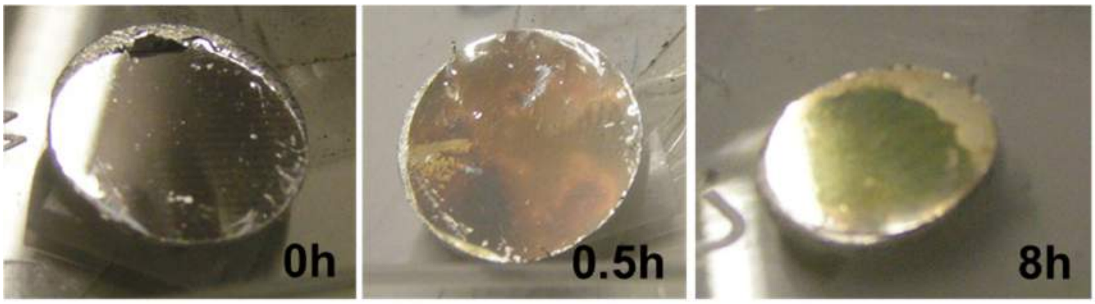

Figure 4.28 - Photographs of fresh and exposed upper delaminated parts.

Thus, we conclude that the limiting mechanical point in degraded P3HT:$PC_{60}BM$ devices is still the interface between the PEDOT:PSS and the active layer. The surface analysis of the upper delaminate part suggests that the breaking point do not move deeper in the active layer as the elements of P3HT are still not detected after damp heat exposure. However, the analyzed surface becomes richer of $PC_{60}BM$ exclusively. It is known that the $PC_{60}BM$ diffuse and can even crystallize when exposed to annealing.[34,196] Here, we propose that $PC_{60}BM$ molecules diffuse to the PEDOT:PSS/AL interface and form progressively a thin layer of pure $PC_{60}BM$ molecules. The thickness of $PC_{60}BM$ after 8h of damp heat can be estimated of few nanometers. The formation of this layer probably decrease the initial P3HT/PSS interface which has been observed in inverted device configuration.[103] Thus, the insertion of $PC_{60}BM$ molecules at the P3HT/PSS interface probably reduces the adhesion strength. (**Figure 4.25**) The proposed mechanism id proposed in **Figure 4.29**.

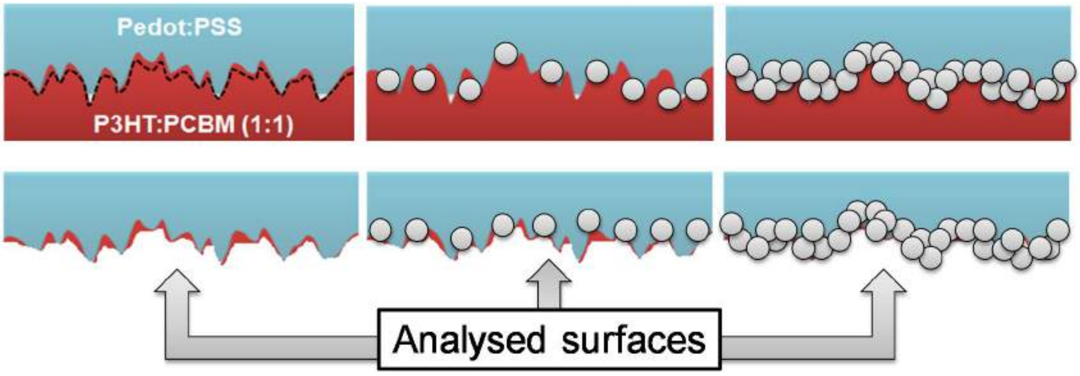

Figure 4.29 - Proposed mechanism of delamination in inverted devices based on P3HT:$PC_{60}BM$/PEDOT:PSS exposed to damp heat. $PC_{60}BM$ diffusion (gray spheres) at the interface during damp heat exposure (top) and the corresponding upper parts (bottom) after Tack tests.

The enrichment of $PC_{60}BM$ at the hole transporting layer is problematic for the device performance. $PC_{60}BM$ is the electron acceptor material in devices that transports the electrons towards the electron transporting layer (ETL). On the other hand, in P3HT the holes are collected and a percolation pathway with the HTL is required. Thus, the extraction of holes at the HTL/P3HT interface could be blocked by the enrichment of $PC_{60}BM$ at this interface. Moreover, the $PC_{60}BM$ layer most probably increases the recombination process and thus impact drastically the device performance.

- *Influence of interlayers on delamination mechanism and device stability*

Figure 4.30 shows the influence of interlayers on device stability. We note that the interlayers initially slightly decrease the initial performance. In addition, from **Figure 4.30**, it is clear that the interlayers do not stabilize the device performance. If we focus on the first 0.5h of exposure, we can even observe that the device performance is more impacted with an interlayer.

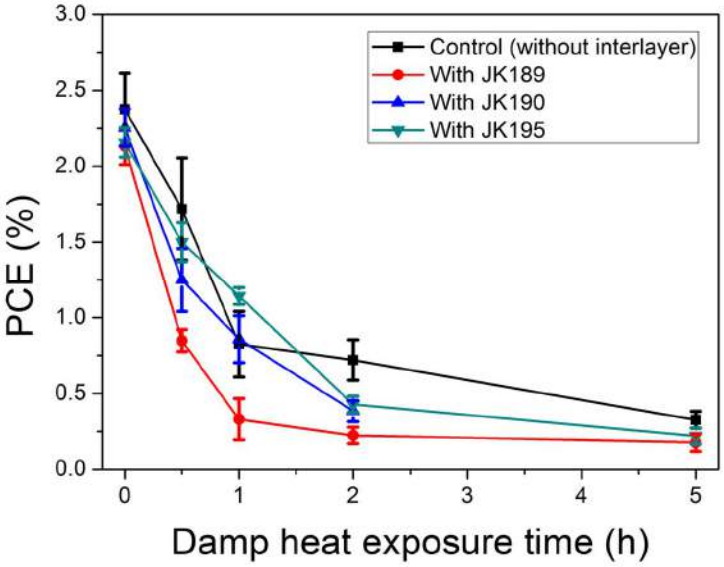

Figure 4.30 - Evolution of the device performance versus time of damp heat (85°C/85% rH in the dark) exposure.

As for the control devices, the upper delaminated part was analyzed by XPS and AFM. **Table 4.5** shows that with or without interlayers, the surface gets enriched in $PC_{60}BM$ after damp heat exposure. AFM images (**Figure 4.31**) show the formation of fibril structures in the JK189 series most probably due the agglomeration of $PC_{60}BM$ molecules. From the AFM images, the JK189 interlayer may induces specific morphologies of $PC_{60}BM$ agglomerates.

Samples	C1s	O1s	S2p	Ag3d
Control / 0h	79.56	9.92	7.17	3.35
Control / 0.5h	84.67	11.21	2.17	1.96
Control / 8h	93.91	3.88	1.82	0.39
JK189 / 0h	75.29	14.06	6.89	3.76
JK189 / 0.5h	91.85	4.31	2.40	1.43
JK189 / 8h	94.27	4.75	0.98	0
JK190 / 0h	75.56	13.16	7.36	5.93
JK190 / 0.5h	83.08	6.36	4.55	6.02
JK195 / 0h	88.02	6.38	2.72	2.88
JK195 / 0.5h	91.53	5.03	1.89	1.55

Table 4.5 - Evolution of the chemical composition of the pristine or exposed to damp heat upper parts.

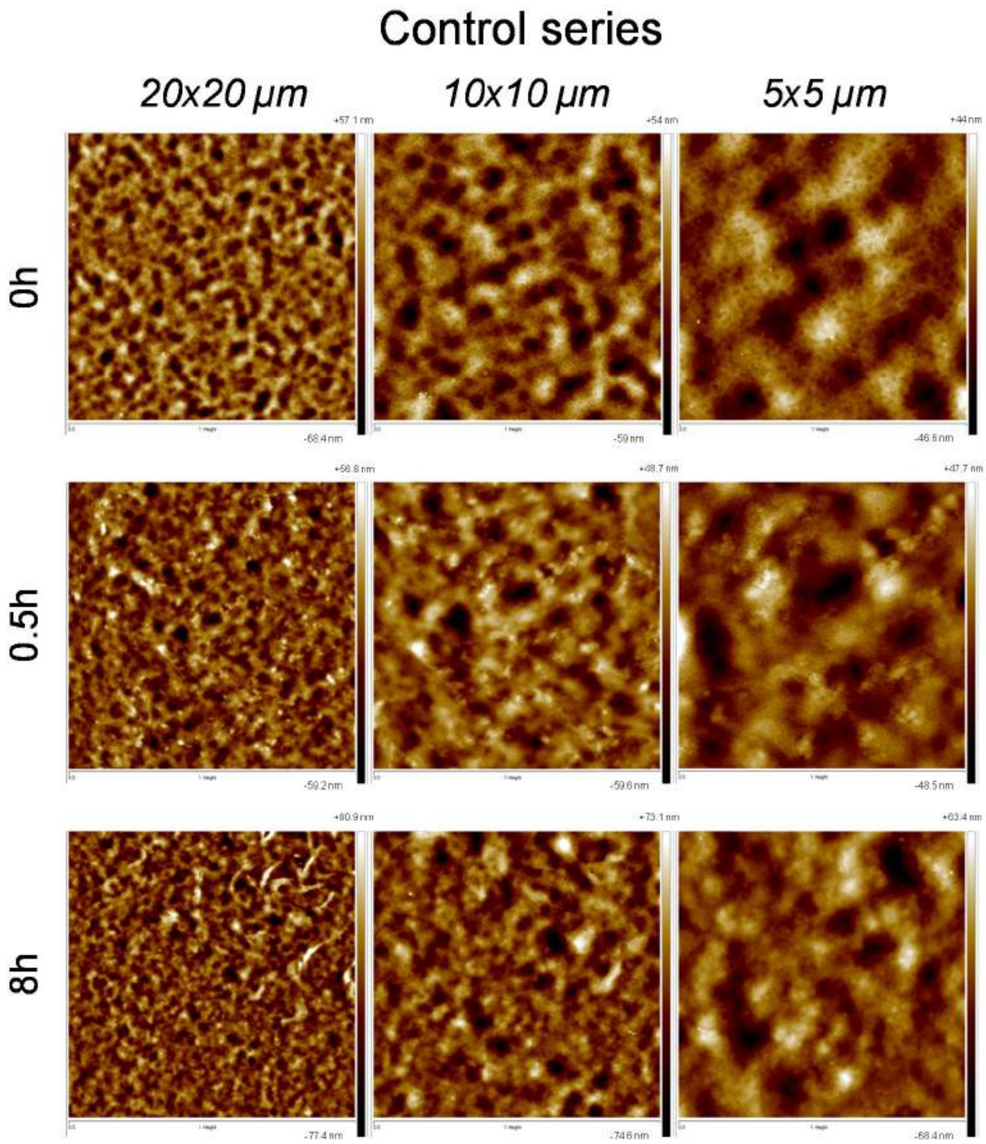

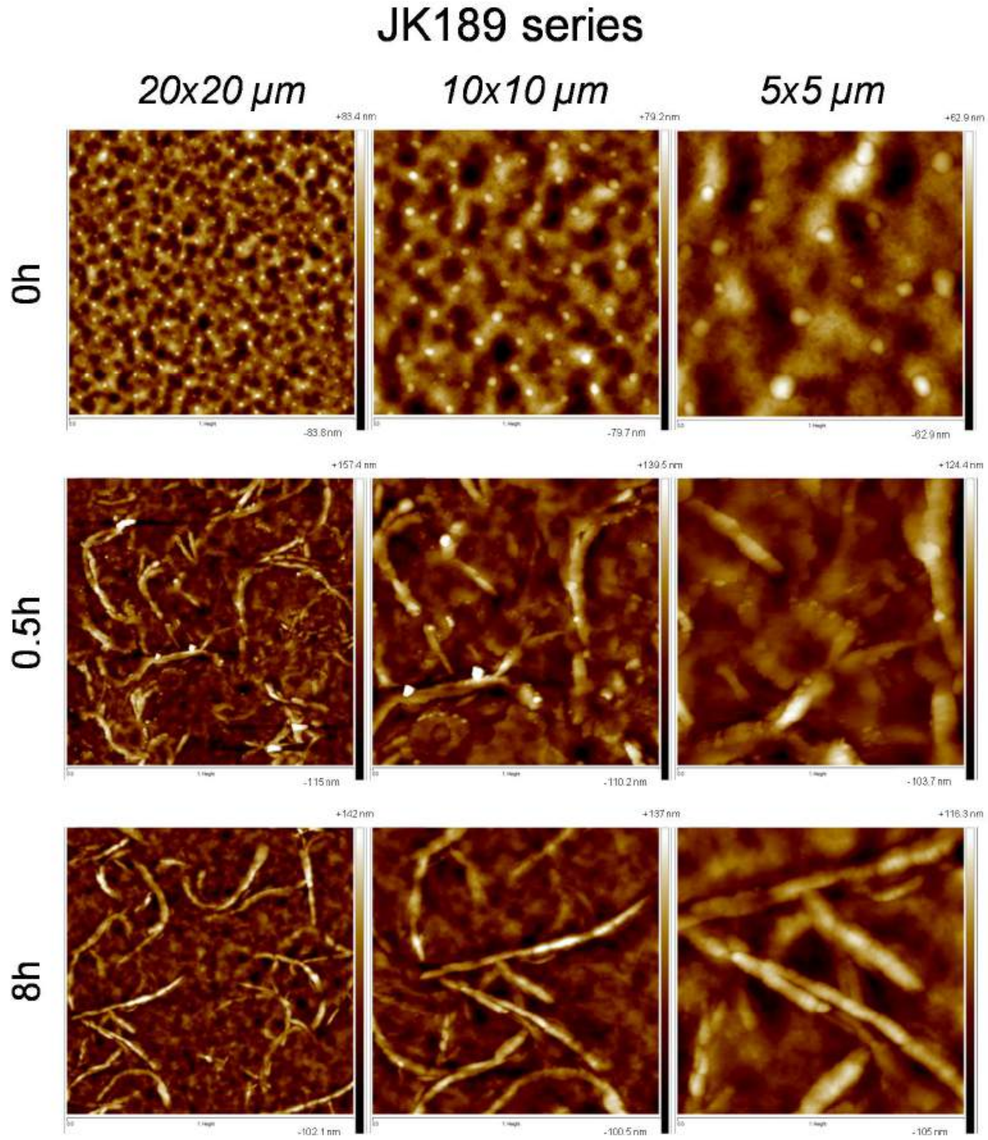

Figure 4.31 - AFM images of pristine and exposed (damp heat) upper parts without (control series) and with interlayer (JK189 series).

4.3.4. Conclusion

Exposed to damp heat (85°C/85% rH in the dark), the device performance is drastically and rapidly reduced. We observed a decrease of adhesion strength when the devices are submitted to damp heat. We proposed the rapid drop of performance as well as the decrease of adhesion strength to the agglomeration of $PC_{60}BM$ molecules at the interface between the active layer and PEDOT:PSS.

4.4. Summary of Chapter 4

In the first part (**4.2**), we have identified the weakest mechanical point in inverted OSCs. We have seen that although the choice of the p-type polymer has an influence on the stress at break, the weakest interface remains the PEDOT:PSS/Polymer:$PC_{60}BM$ interface. The use of a new type of PEDOT:PSS (HTL2, based on organic solvents) shown a slight improvement for P3HT:$PC_{60}BM$ and the breaking point was found to be deeper in the active layer.

The use of interlayers did not improve the global adhesion and the device stability when exposed to damp heat (85°C/85% rH).

In the second part (**4.3**), we have exposed inverted devices based on HTL1/P3HT:$PC_{60}BM$ to damp heat (85°C/85% rH in the dark). From our results, we propose that the decrease of stress at break and the rapid drop of performance are due to the agglomeration of $PC_{60}BM$ molecules at the PEDOT:PSS/AL interface. The agglomeration of $PC_{60}BM$ can favor the delamination process and at the same time block the holes extraction.

Chapter 5

Electronic structure (ES), energy level alignments (ELA) and interactions between the active layer (AL) and the electron transporting layer (ETL)

5.1. Introduction to Chapter V

The electronic structure and energy level alignments (ELA) of organic semi-conductors at charge transporting layers or electrodes are crucial for optimizing the performance of electronic devices. **Figure 5.1** shows the most important energetic levels considered for a metal/semiconductor interface.

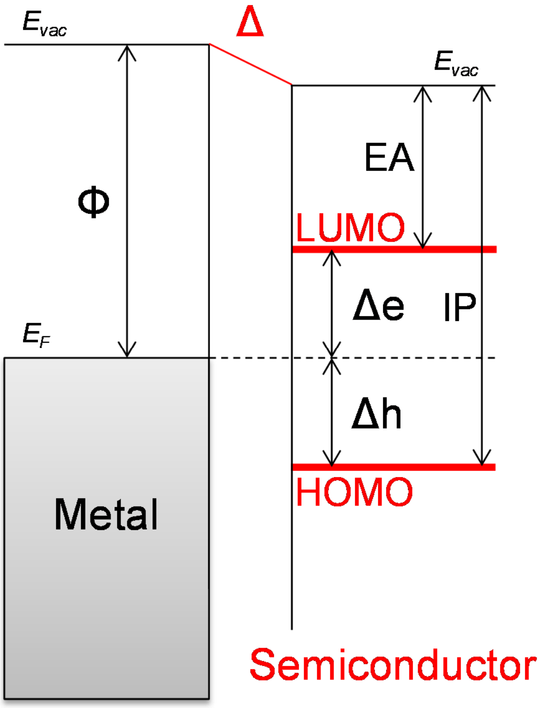

Figure 5.1 - Illustration of the energy level alignment at a typical metal/semiconductor interface. The energy difference between the Fermi energy (E_F) and the vacuum energy (E_{vac}) is the work function (Φ) of the metal. The difference in binding energy between the (E_F) and the onsets of occupied and unoccupied density of states on the semiconductor side are the charge injection barriers, Δh for holes and Δe for electrons, respectively. The energy differences between the highest occupied molecular orbital (HOMO) and the lowest unoccupied molecular orbital (LUMO) to the vacuum energy (E_{vac}) define the ionization potential (IP) and the electron affinity (EA) of the semiconductor, respectively. A shift of the E_{vac} between materials indicates the formation of an interface dipole (Δ).

The main experimental techniques used to investigate the electronic structure and energy level alignments are photoemission spectroscopies (PES) such as X-ray and UV photoemission spectroscopy. (XPS and UPS) Please refer to the appendix (A1) for details regarding the techniques.

5.1.1. Models[197-199]

Many models were established in order to explain the different experimental observations regarding the ELA. A recent review of the group of A. Kahn summarizes the basic established approaches which can explain the ELA at metal-organic interfaces.[199] Hwang et al. divide these models in two types: models excluding gap states at the interfaces such as the Schottky model (no interface dipole, Δ=0) and models explaining the ELA by presence of gap states. Gap states are localized between the HOMO and LUMO levels of the organic material and different origins are discussed. At interfaces, gap states can be induced by defects or chemical reactions between the metal and organic material. The metal electron wave function can penetrate into the organic material resulting in metal induced gape states. Recently, Oehzelt et al. present a more detailed work related to how the organic semiconductor density of states controls the energy level alignment at electrode interfaces.[200] Also the groups of W.R. Salaneck and M. Fahlman intensively investigated the ELA at organic/inorganic and organic/organic interfaces with focus on polymer materials.[198,201] They introduced the Integer Charge Transfer (ICT) model for explaining the ELA between organic semiconductors and various substrates used as electrodes. **Figure 5.2** illustrates the basic approach of the ICT model. The ICT states are energetic levels located in the HOMO/LUMO gap of conjugated organic molecules or polymers. ICT^+ is defined as the energy required for extracting an electron at the interface. The difference between ICT+ and IP (VL→HOMO) is that the model considers the electronic and geometrical relaxation of the molecule as a consequence of the charge transfer. Therefore ICT^+ is related to the HOMO level. Similarly ICT^-, it is defines as the energy gained by the molecule to accept an electron after all relaxation processes considered. Thus, ICT^- is related unrelaxed LUMO level, determined e.g. by inverse photoemission measurements. **Figure 5.2** illustrates the three possible scenarios for the ELA depending on the work function (WF) of the substrate relative to the ICT+/- levels of the deposited organic material. A pinning regime is obtained, when WF of the substrate is larger than the ICT^+ level. Analogously, when the WF of the substrate is smaller than ICT^-, the Fermi level will align with ICT^-. If the substrate WF lies in between ICT^+ and ICT^-, no pinning occurs and a vacuum level alignment is observed.

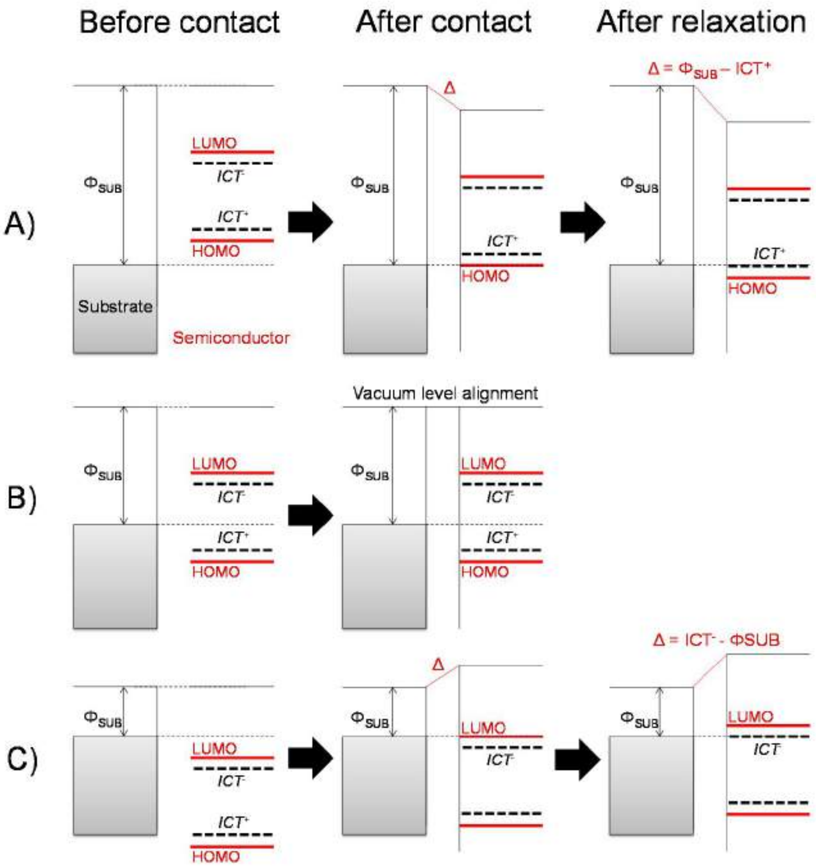

Figure 5.2 - Adapted from Fahlman et al.[198] Schematic illustration of the evolution of the energy level alignment when a p-conjugated organic molecule or polymer is physisorbed on a substrate surface when A) $\phi_{SUB}>E_{ICT+}$: Fermi-level pinning to a positive integer charge-transfer state, B) E_{ICT}-<$\phi_{SUB}<E_{ICT+}$: vacuum level alignment, and C) $\phi_{SUB}<_{EICT}$-: Fermi-level pinning to a negative integer charge-transfer state. The charge-transfer-induced shift of the vacuum level (corresponds to the interface dipole Δ) is observed in the pinning regime.

5.1.2. OPV devices, active layer (AL) / electron transporting layer (ETL) interface

In the present study, we focus on inverted OPV devices and the interface between the active layer (AL) and electron transport layer (ETL). After exciton splitting at the polymer/PC$_{60}$BM interfaces, the electrons are transported in the active layer by percolated PC$_{60}$BM molecules and transferred to the ETL. Cho et al. demonstrated that an additional PC$_{60}$BM thin layer between the AL and ETL can significantly increase the inverted device performance.[202] In the inverted structure, it is therefore helpful to have a vertical gradient of materials with more donor polymer at the top (interface with HTL) and more acceptor PC$_{60}$BM at the bottom (interface with ETL) in order to be close to the ideal BHJ morphology (See Chapter 1).[203]

In a first part (**5.1**), we investigated the ELA between C60 and different materials susceptible to be used as ETL such as ITO, ITO/PEI and ZnO. We used C60 instead of PC$_{60}$BM in order to exclude a possible alteration of the molecule due to the evaporation process, which cannot be excluded for $PC_{60}BM$. The evaporation of C60 molecules is well controlled (monolayer by monolayers on the targeted materials). We also investigated the insertion of interlayers on top of ZnO to modify the electronic structure and therefore ELA with C60.

In a second part (**5.3**), we investigated the stability (photo/thermal) of devices based on ZnO or PEI/ITO, the two current most used ETL in inverted OPV devices. We tried to understand the reasons why differences of thermal/photostabilities were observed.

Scientific contribution

The present work is the result of a collaborative work within the *Establis* project. The fabrication and degradation of OSC devices have been performed by Dr. Dargie Deribew (ER1, Belectric Company). The synthesis of the polymers used as interlayers was done by Anna Isakova (ESR7, Aston University). Thin films of bear and modified ZnO were prepared by Dr. Simon Dowland (ER2, Belectric Company).

5.2. ES and ELA between C60 and various ETLs

5.2.1. Introduction

The interface between the active layer (AL) and the electron transport layer (ETL) in the inverted OPV device structure is crucial for the performance. We have selected there different ELSs: ITO, ITO/PEI and ITO/ZnO. The polyethylenimine (PEI) was recently used as a surface modifier of various electrodes.[55,56] The PEI is an insulator polymer which therefore must be coated as ultra-thin layer. It is chemically or physically adsorbed onto the conductor surface and reduce the work function of a large type of metals resulting in strong interface dipoles to subsequently deposited organic materials.[55] We used C60 as a molecule related to $PC_{60}BM$, easy to evaporate in ultra-high-vacuum conditions. The precise control of the evaporation rate allows a detailed study of interface properties of C60 in the monolayer range on various types of substrates using photoemission spectroscopy (XPS/UPS).

5.2.2. Experimental

Please, refer to the appendix (A1) for additional details on the experimental techniques.

- *Surface analysis*

Photoemission measurements were carried out using a multichamber UHV system (base pressure 10^{-10} mbar), equipped with a SPECS Phoibos 150 cylindrical hemispherical analyzer and a monochromatic Al Kα source (Focus 500 monochromator, XR50 M X-ray source, Al Kα 1486.74 eV) for XPS a UVS 300 He discharge lamp (21.2 eV excitation energy) for UPS. During UPS measurements, a bias voltage of 7 V was applied in order to overcome the work function of the analyzer.

A Nanoscope IIIa atomic force microscope (AFM) from Veeco Instruments was used for surface topography measurements. Images were obtained using the repulsive mode in intermittent contact, more commonly called the “tapping” mode. The RMS (root mean square) represents the standard deviation of the Z-axis values of a given surface.

- *Substrates preparation*

ITO substrates were cleaned by a successive ultrasonic baths in acetone and isopropanol (15 min). Finally, the samples were treated by ozone for 10 min before being inserted in the UHV chamber. For the preparation of PEI/ITO substrates, the polyethylenimine PEI (Aldrich) was solubilized in isobutanol (1 mg/mL) and blade casted (5 mm/sec at 85°C) in inert atmosphere on cleaned ITO substrates. Then, the films were dried 15 min at 110°C still in inert atmosphere.

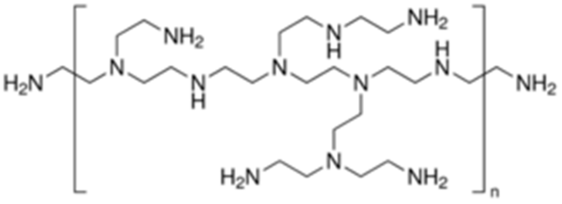

Figure 5.4 - Chemical structure of the branched polyethylenimine (PEI).

The ZnO substrates were made from nanoparticles. The nanoparticles in ethanol were sonicated 30 min and blade casted (5 mm/sec) on cleaned ITO. The substrates were dried 10 min at 140°C in air.

- *C60 evaporation*

The organic films were evaporated in ultra-high-vacuum from a temperature-controlled crucible. The pressure during the evaporation of the organic was less than 2.0 10^{-8} mbar and the temperature adapted in order to control the evaporation. For C60, the evaporation rate was about 0.1 nm/min.

- *Interlayers synthesis (Anna Isakova, ESR7)*

The synthetic route towards catechol and fullerene-functionalised catechol polymer is illustrated by **Figure 5.5**. At first, the precursor poly(3,4-dimethoxystyrene) (PDMS) is synthesised by reversible addition-fragmentation chain transfer (RAFT) polymerisation [step (i)], allowing fabrication of well-defined polymers of targeted molar masses and low polydispersities. Interestingly, PDMS was also demonstrated to have high affinity for zinc-binding, although lower than that of its demethylated version, poly(3,4-dihydroxystyrene) (PDHS). Demethylation of PDMS to yield PDHS is achieved by treating the polymer with boron tribromide, a very strong Lewis acid [step (ii)]. Alternatively, to increase the compatibility of PDMS and PDHS with the $PC_{60}BM$ of the photoactive blend PDMS is coupled to the fullerene derivative to yield PDMS-FUL [step (iv)].[3] The coupling is made before demethylation in order to avoid any parallel unwanted reactions. To achieve addition of the fullerene moiety to every polymer chain in step (iv) excess fullerenol (FUL-OH) was used. The PDMS-FUL is subsequently demethylated to give PDHS-FUL [step (v)].

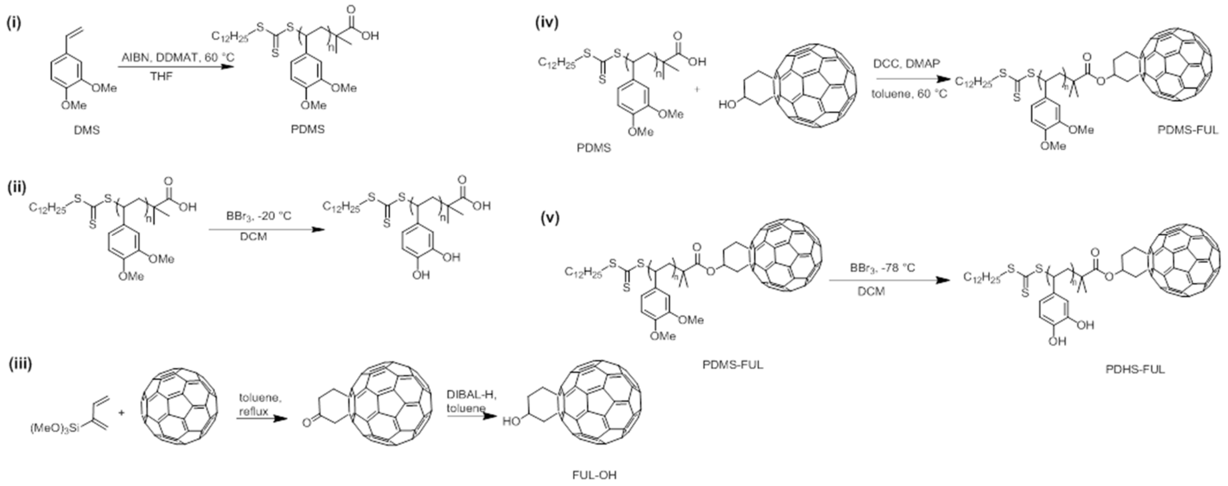

Figure 5.5 - Synthetic route towards PDHS-FUL: (i) RAFT polymerisation of DMS; (ii) demethylation of PDMS to yield PDHS; (iii) synthesis of the fullerenol precursor FUL-OH; (iv) coupling of PDMS and FUL-OH towards fullerene-functionalised PDMS-FUL; (v) demethylation of PDMS-FUL to obtain PDHS-FUL.

5.2.3. Results and discussion

- *Surface Characterization of the different ETL substrates.*

We first prepared ITO, ITO/PEI and ITO/ZnO substrates as described in the experimental part. In a first step, it is important to characterize the different neat substrates. Indeed, the specific chemical composition or morphology of the substrate can significantly impact the subsequent evaporation of C60. Therefore, the substrates were analyzed by XPS, UPS and AFM. **Figure 5.6** shows the XPS survey spectra of the different substrates as prepared.

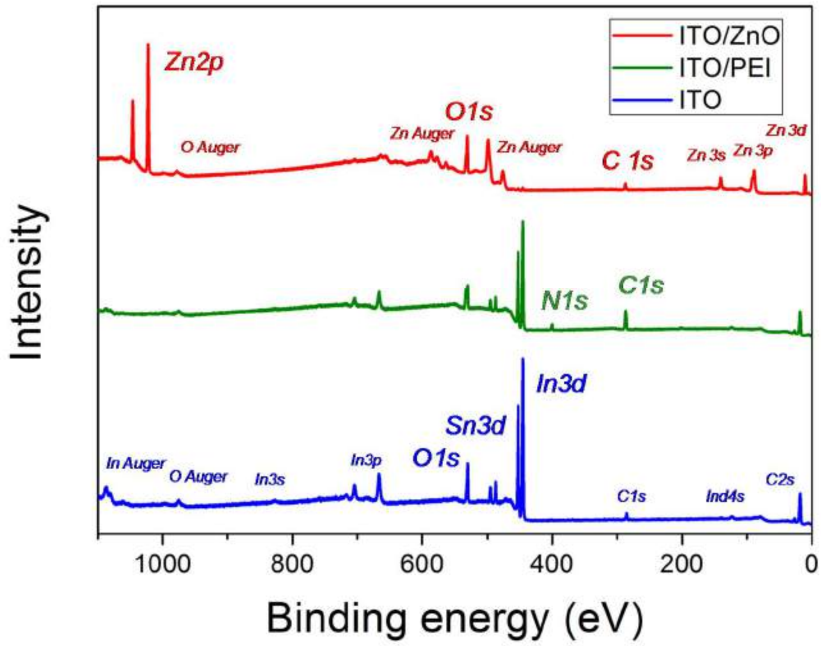

Figure 5.6 - XPS survey spectra of ITO, ITO/PEI and ITO/ZnO with assignment of each signal.

For ITO, we observe the expected signals of the different elements (In3d, Sn3d and O1s as main signals). As the substrates were prepared ex-situ (although maximum protection), contamination from the ambient air cannot be avoided. Such a contamination can be quantified via the intensity of the carbon C1s core level signal.

In the case of ITO/PEI, the polymer was casted on top of ITO as an ultra-thin layer. From XPS measurements, we estimated the PEI thickness was about 3 nm.

Concerning ZnO, the expected core level related to Zn and O elements can be observed. The C1s signal may indicate some contamination which can be attributed to remaining acetate ligands coming from the preparation procedure according to the shape of C1s (More information in the subsequent **5.3** section).

Figure 5.7 shows the surface topography of the three different substrates. The typical surface structure was observed for ITO.[204] For ITO/PEI, the AFM image suggests that the PEI covers not homogenously the ITO substrate, and ITO related features are still visible as a background. This observation is in good agreement with a recently published work by Zhou et al.[55] Additionally, it can be observed that the passivation of ITO by PEI slightly reduces the RMS (See profiles in **Figure 5.7**) even if significant variation can be observed locally. With ZnO on the top, the mean RMS is higher than the one of ITO and ITO/PEI.

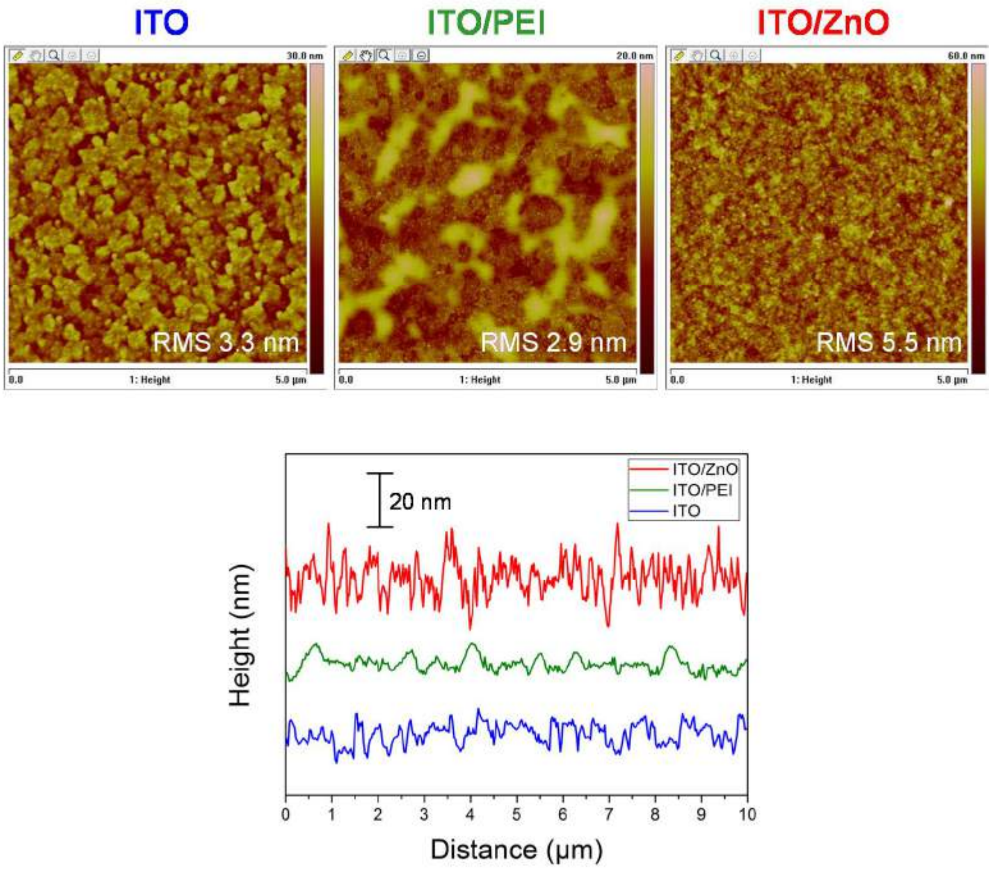

Figure 5.7 - AFM images of ITO, ITO/PEI and ITO/ZnO associated to their profiles.

Figure 5.8 shows the UPS spectra of the different substrates. The work functions (WF) and valence bands (VB) of the different substrates were determined from the UPS spectra (secondary electron cut-off (SECO) and valence band (VB) region respectively) and the values are summarized in **Table 5.1**. It is important to note that for a broad range of WF values can be reported in the literature for the “same” material. Indeed, the absolute value of a WF can drastically change depending on the sample preparation, cleaning procedures or the calibration of the equipment.[205,206] In the present study, we found WF values of 4.0, 3.4 and 3.0 eV for ITO, ITO/ZnO and ITO/PEI respectively. Although the absolute values are somewhat lower compared to data reported in the literature, the relative differences between WF of the three materials are in good agreement.[55,56]

	ITO	ITO/PEI	ITO/ZnO
Valence band (VB)	3.4 eV	3.2 eV	3.7 eV
Work function (WF)	4.0 eV	3.0 eV	3.4 eV

Table 5.1 - Valence band (VB) and work function (WF) of ITO, ITO/PEI and ITO/ZnO.

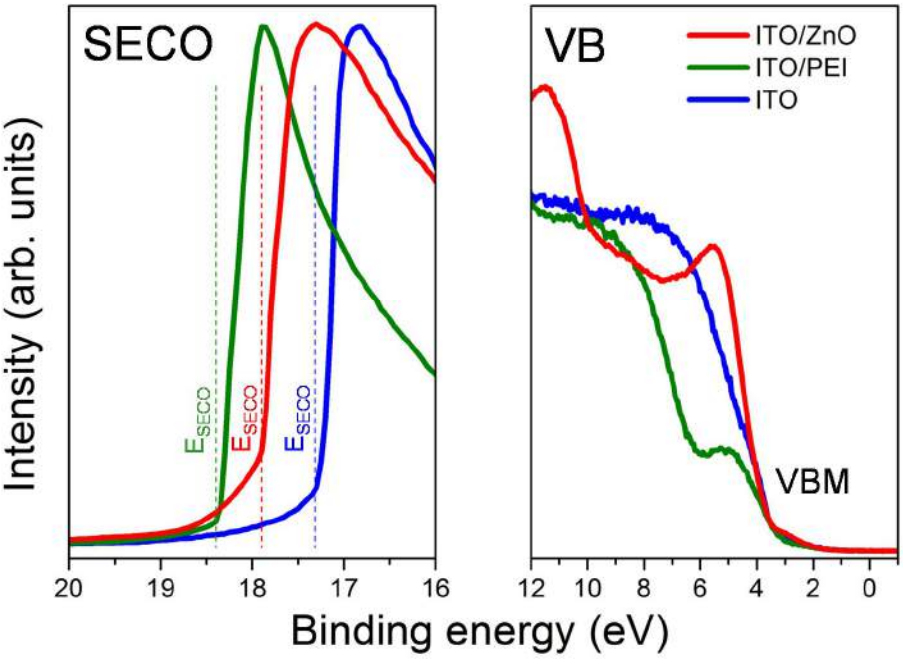

Figure 5.8 - UPS spectra of ITO, ITO/PEI and ITO/ZnO. The secondary electron cut-off (SECO, left) and valence band region (VB, right) are shown.

- *Interface with C60*

After characterization of the different substrates, we evaporated stepwise C60 molecules as described in the experimental section. XPS and UPS measurements were performed after each step of C60 evaporation. The C60 thicknesses were calculated from XPS intensity ratios of overlayer and substrate related peaks. (See Appendix A1) XPS and UPS spectra of ITO, ITO/PEI and ITO/ZnO substrates with increasing C60 coverage are presented in **Figure 5.9**, **5.10** and **5.11** respectively. From XPS spectra, a progressive attenuation of the signals from the substrates concomitant with the increase of C1s signal can be observed along the C60 deposition for the three substrates. The UPS spectra show the valence band region (right panels), a zoom into the secondary electron cut-off region (SECO, left panels). In particular the ELA was extracted from UPS, as described in the general introduction.

The UPS spectra for C60 on ITO in **Figure 5.9** show the development of the HOMO of C60 with increasing film thickness, whereas ITO related features disappear. In the UPS cut-off region an energetic shift of the SECO to higher binding energies ca be observed, indicating a shift of the vacuum level resulting in an increase of the work function (WF) by 0.25 eV. In other words, an interface dipole of 0.25 eV is formed after deposition of C60 molecules. The extracted values of

WF and the energetic positions of the HOMO, C1s and In3d signals are summarized in **Table 5.2**. We can observe that the C1s signal is shifted by around 0.13 eV to the lower binding energies (BE), probably indicating an energetic relaxation.

/ITO	**In3d**	**C1s C60**	**HOMO edge/max**	**WF**
Bare	444.56	-	3.13	4.00
0.9 nm	444.79	285.22	2.08/2.69	4.06
1.9 nm	444.69	285.09	2.16/2.67	4.14
3.1 nm	444.76	285.09	2.18/2.67	4.22
4.3 nm	444.78	285.09	2.17/2.66	4.24
5.7 nm	444.80	285.10	2.15/2.64	4.25
6.3 nm	444.79	285.10	2.16/2.64	4.25
7.0 nm	444.71	285.10	2.16/2.64	4.25
8.5 nm	444.78	285.09	2.16/2.64	4.25
/ITO/PEI	**In3d/N1s**	**C1s C60**	**HOMO edge/max**	**WF**
Bare	444.69/400.10	-	3.23	3.00
0.7 nm	444.77/399.62	285.11	2.14/2.87	3.92
2.4 nm	444.79/399.69	285.10	2.29/2.83	4.13
3.3 nm	444.80/399.72	285.10	2.29/2.80	4.26
4.8 nm	444.84/399.79	285.05	2.30/2.78	4.29
5.7 nm	444.86/399.87	285.06	2.31/2.76	4.29
/ITO/ZnO	**Zn2p**	**C1s C60**	**HOMO edge/max**	**WF**
Bare	1022.17	-	3.73	3.35
0.1 nm	1022.09	285.00	1.85/2.80	3.36
0.2 nm	1022.09	285.00	2.03/2.74	3.53
1.0 nm	1022.09	284.88	2.06/2.70	3.72
1.7 nm	1022.09	284.84	2.06/2.65	3.78
2.6 nm	1022.01	284.84	2.06/2.63	3.80
3.1 nm	1022.05	284.79	2.06/2.59	4.07
3.6 nm	1022.05	284.75	2.06/2.56	4.12
4.7 nm	1022.05	284.75	2.06/2.54	4.19

Table 5.2 - Evolution of the main signals as a function of the C60 film thickness: HOMO, WF, C1s, Zn2p, In3d and N1s along the C60 evaporation.

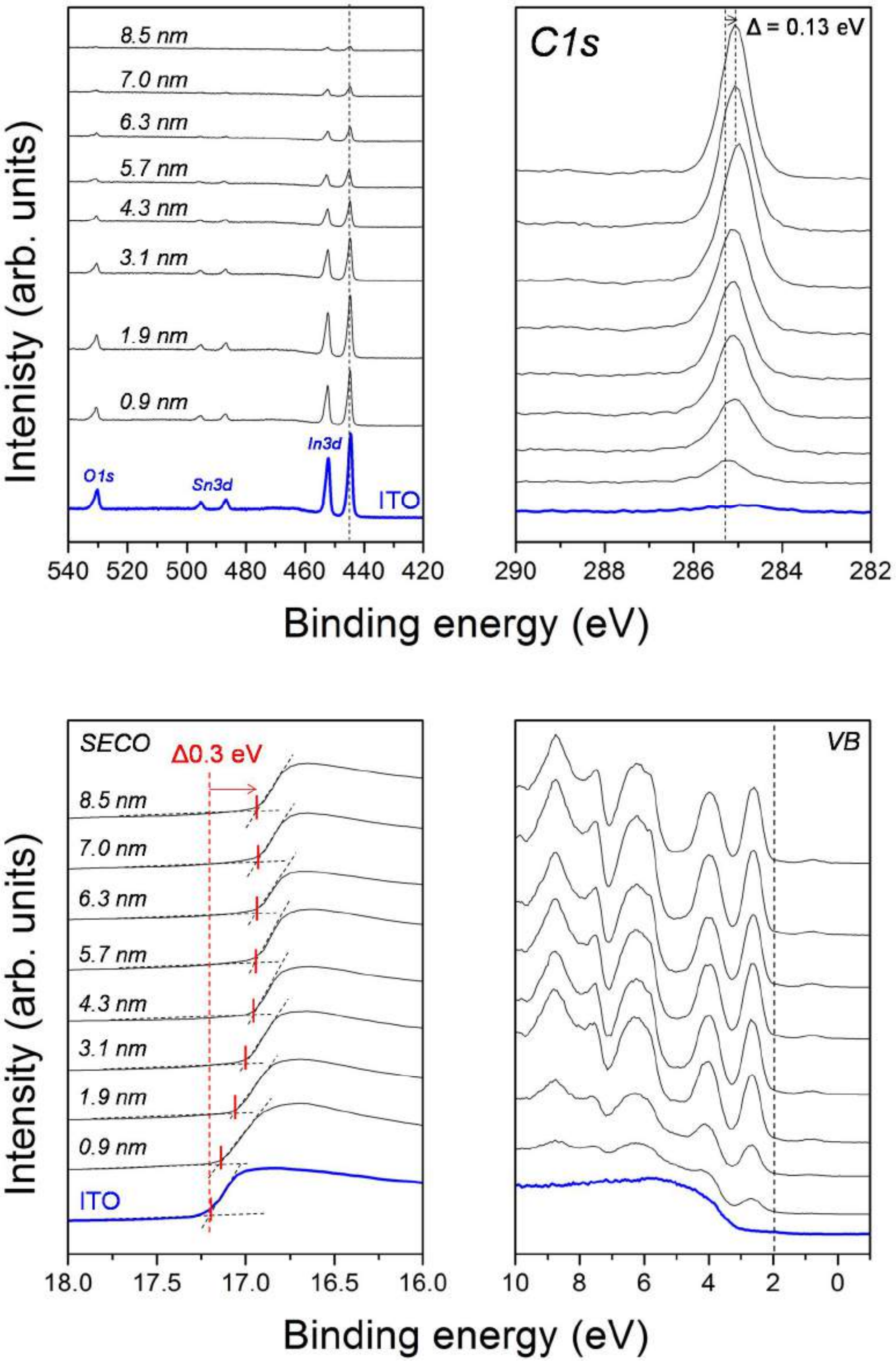

Figure 5.9 - XPS (top) on UPS (bottom) of bare ITO (blue) and after several C60 evaporations. For UPS, The secondary electron cut-off (SECO, left) and valence band region (VB, left) are represented.

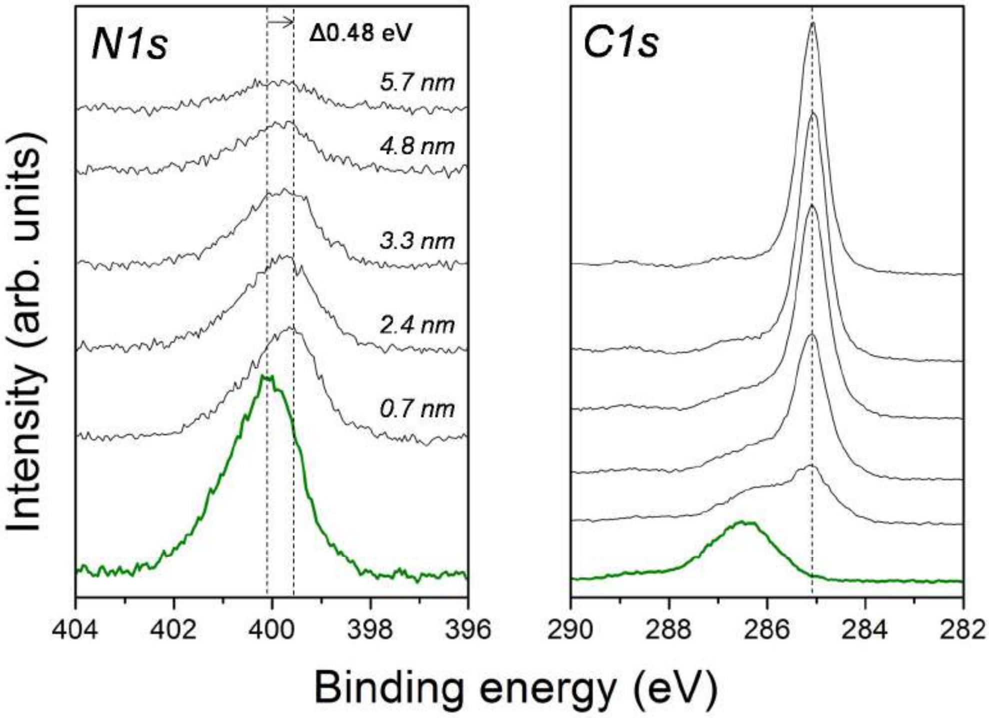

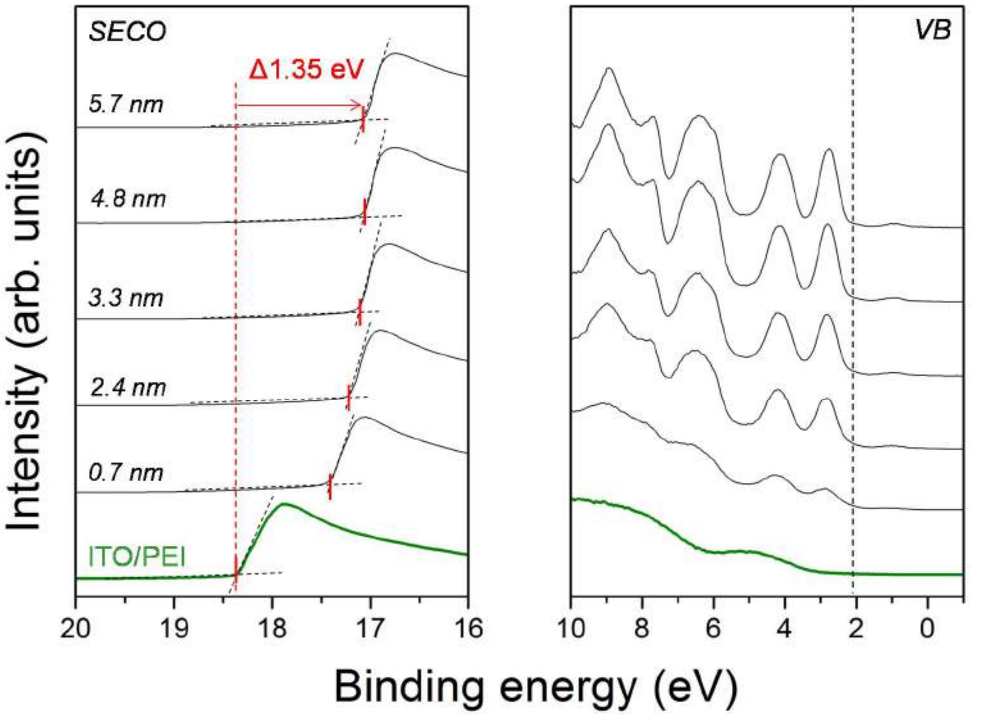

Figure 5.10 - XPS (top) on UPS (bottom) of bare ITO/PEI (green) and after several C60 evaporations. For UPS, The secondary electron cut-off (SECO, left) and valence band region (VB, left) are represented.

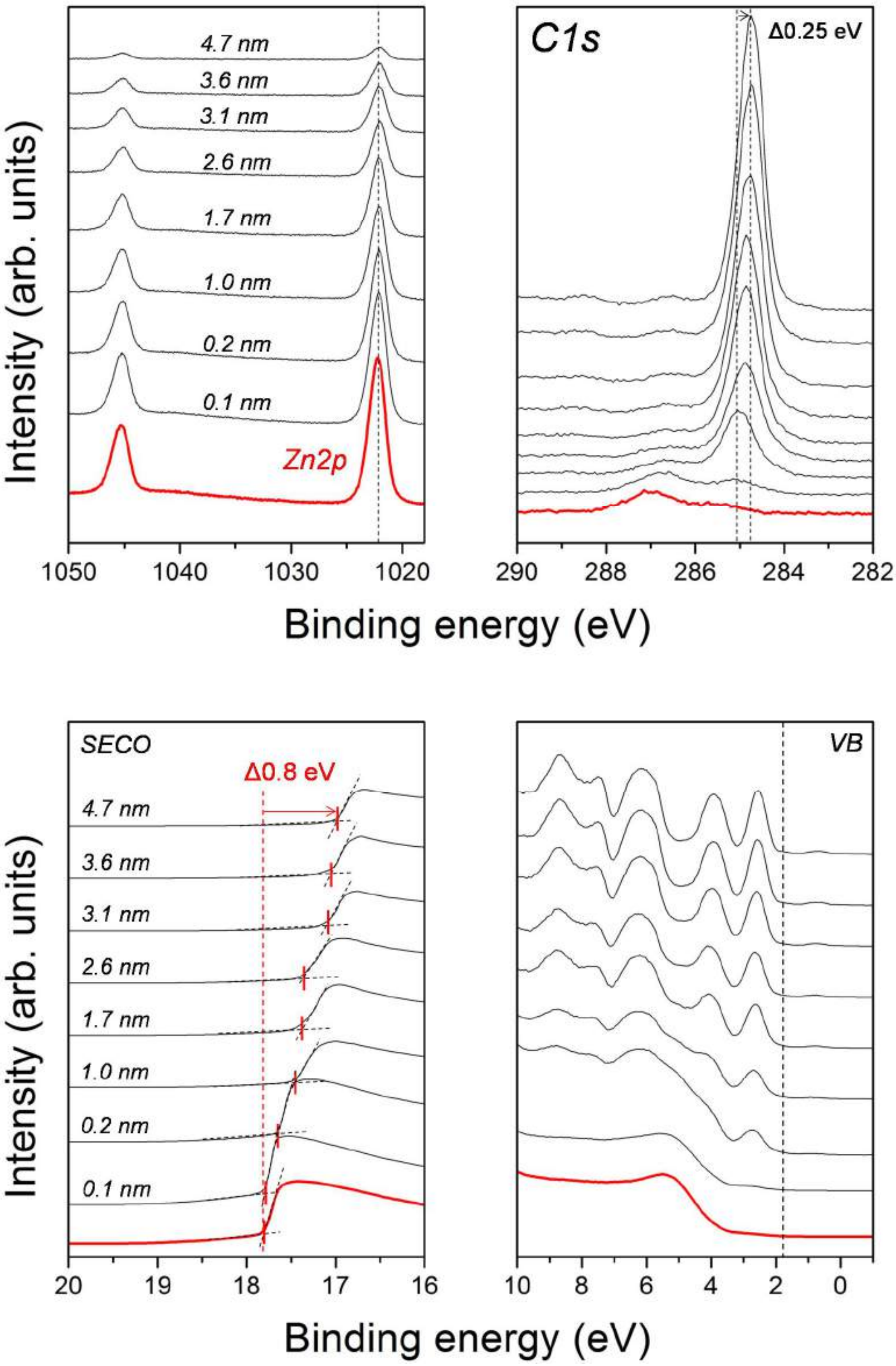

Figure 5.11 - XPS (top) on UPS (bottom) of bare ITO/ZnO (red) and after several C60 evaporations. For UPS, The secondary electron cut-off (left) and valence band region (left) are represented.

In the case of ITO/PEI, we can clearly observe that the N1s core level is shifted to lower BE after the first evaporation. The large energetic shift of 0.55 eV suggests a significant change in the electronic environment of the nitrogen atoms when the first layer of C60 deposited. From UPS (SECO) spectra, it can be observed that the WF after evaporation of C60 is comparable to the one of C60 on pristine ITO. Thus, the lowering of WF of ITO/PEI with respect to ITO is compensated by the formation of a large interface dipole of 1.35 eV (**Figure 5.12**). For both the lowering of the substrate WF and the ELA to C60, chemical groups containing nitrogen atoms play a key role. A possible route to modify the WF of a substrate is the deposition of self-assembly monolayers (SAMs) of molecules with molecular dipoles.[207-209] In the case of polymers, it is essential that electronegative atoms compose the chemical structure such as oxygen (PEO) or nitrogen (PEI).[55,56,210,211] According to the ICT model, although after dipole formation a charge transfer from the substrate to the C60 is expected (pinning at ICT$^-$, cf. **Figure 5.2**), we observe a higher electron density at the N-atoms of PEI, suggesting a complex redistribution of the electrons in PEI. This discrepancy is also observed in **Figure 5.12**: whereas the work function is increasing, indicating a charge transfer to C60, the binding energy of N1s is decreasing.

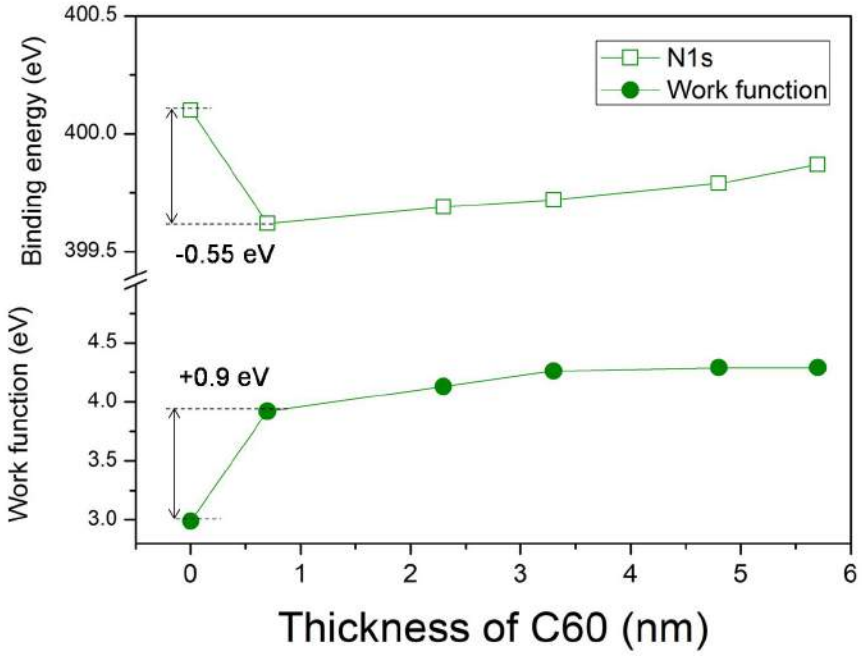

Figure 5.12 - The evolution of the work function (WF) and N1s signal of ITO/PEI with C60 coverage.

Finally, an interface dipole was also observed for ITO/ZnO with an intermediate value of 0.75 eV compared to ITO (0.25 eV) and ITO/PEI (1.35 eV). We can observe a shift of the C1s signal of 0.25 eV to the lower BEs accompanied by a rigid shift of the HOMO (0.25 eV) during the first steps of deposition which is ascribed to the film formation.

Figure 5.13 illustrates the ELA of C60 on the three different substrates. The ELA can be understood by the Integer Charge Transfer (ICT) model previously described in the general introduction (**Figure 5.2**). The WF of the three substrates (ITO, ITO/PEI and ITO/ZnO) is smaller than the ICT^- of C60 as illustrated in **Fig 5.13** (top) (4.5 eV[201,212]). The WF after evaporation of C60 is very similar for the three interfaces (4.2-4.3 eV), suggesting the alignment of the Fermi level of the substrates with common level of C60 resulting in a shift of the vacuum level of 0.25, 0.75 and 1.35 for ITO, ITO/ZnO and ITO/PEI, respectively (see **Figure 5.13**). Thus, our results are in line with the ICT model, and we determine that the pinning level of C60 (ICT^-) is 4.25 ± 0.05 eV.

The surface topography of each substrate before and after C60 evaporation are available in Appendix (A5.2). After the C60 evaporation, all samples show similar roughness as before C60 evaporation suggesting a relative homogenous C60 film formation (no island formation).

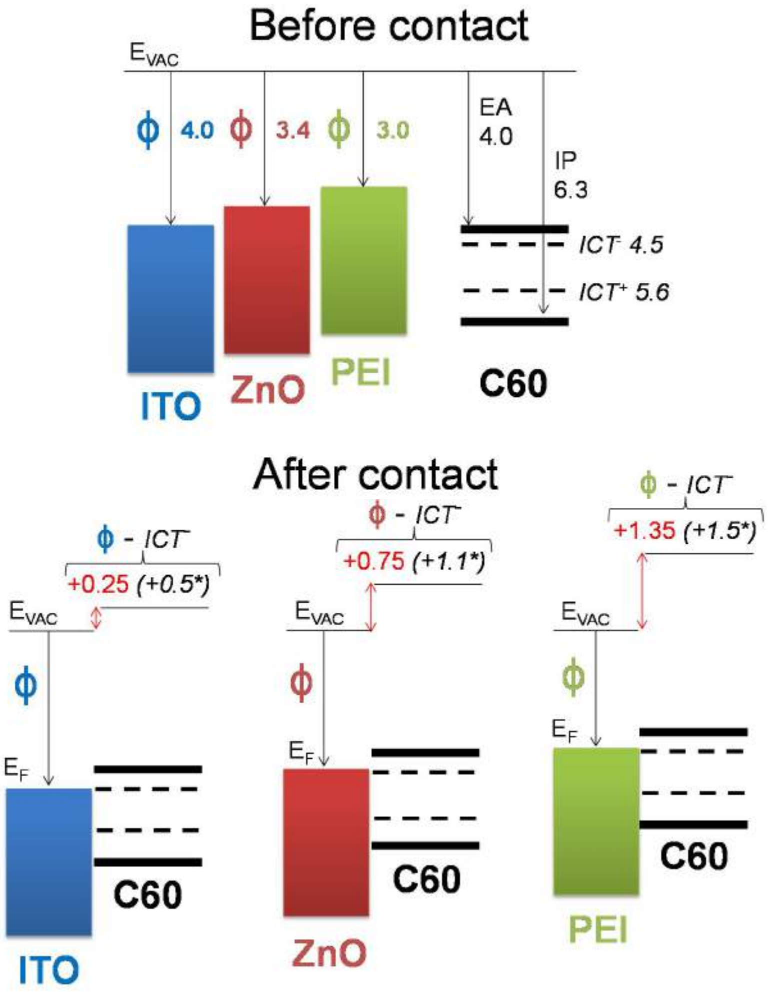

Figure 5.13 - Illustration of the ELA between C60 and ITO, ITO/PEI and ITO/ZnO. The values of EA, ICT^-/ICT^+ and IP of C60 are extracted from Fahlman et al.[201]

- *New interlayers between ETL and AL: relationship between work function and device performance*

In this section we focus on the inverted device structure with a P3HT:PC$_{60}$BM/ZnO interface. Four polymers (AX) were synthetized and tested as surface modifier (similar to PEI discussed above). The chemical structure of these new polymers is shown in **Figure 5.14**. The underlying idea was to add an ultra-thin layer of polymer strongly bounded to ZnO which could increase the adhesion with the organic materials of the active layer.

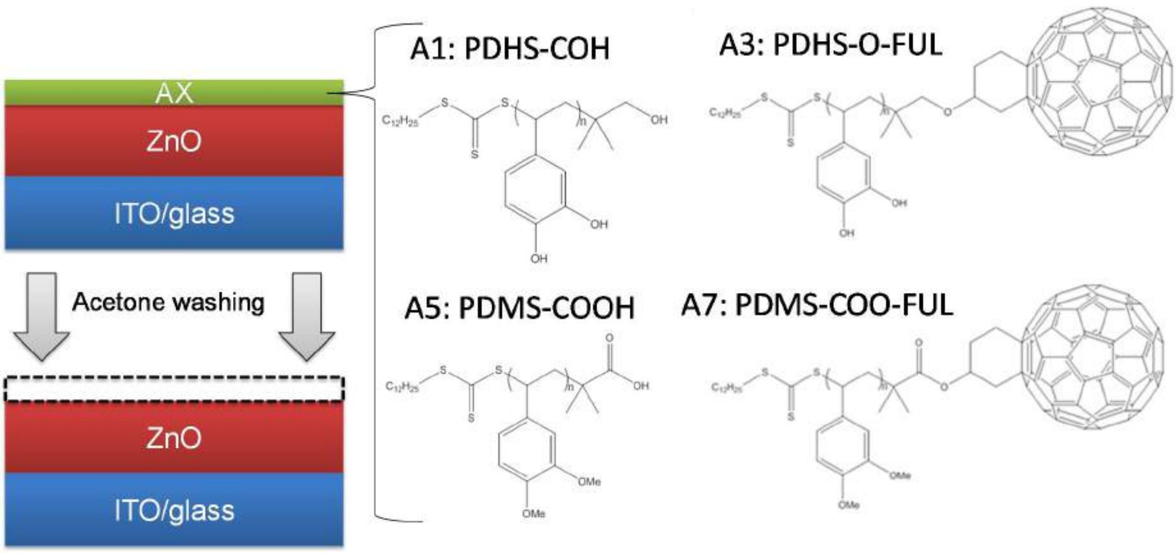

Figure 5.14 - Chemical structure of the different AX polymers used as interlayers between P3HT:PC$_{60}$BM and ZnO in inverted device structure.

First, the insertion of AX interlayers in devices was tested. **Figure 5.15** compares the device performance with or without the different interlayers. It is important to note that once the interlayer deposited, the polymer was washed by acetone in order to get ultra-thin layer. (Estimated to few nanometers) The presence of a very thin layer is a precondition for the successful application in devices as the polymers are insulators (same reason as PEI). From **Figure 5.15** it can be observed that the device performance is not impacted when A5-6-7-8 are used while we can observe a significant decrease for A1-2-3-4 interlayers. We selected A1-3-5-7 to investigate their interactions (physical/chemical binding) with ZnO. When A1 and A3 are inserted, we can measure a loss of 60% and 100% respectively, whereas the device performances are preserved when A5 and A7 are used.

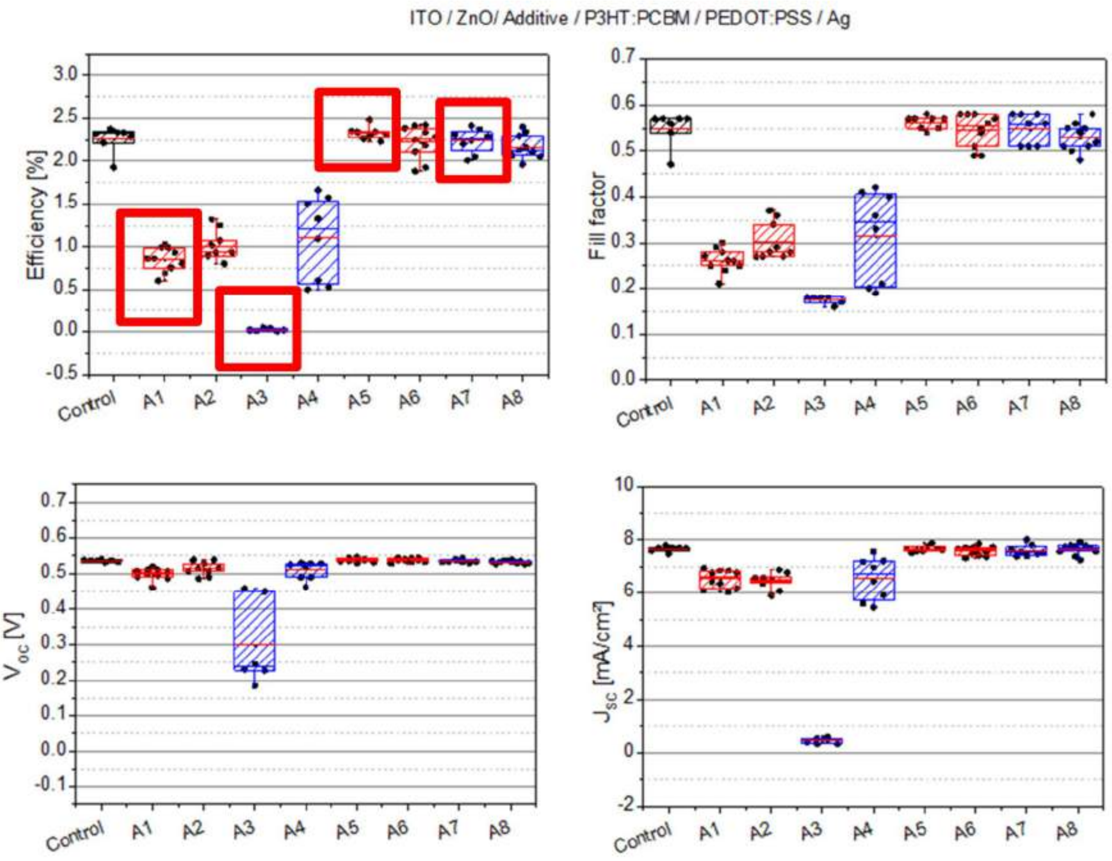

Figure 5.15 - Comparison of device performance with or without the insertion of interlayers. The devices were based on ITO/ZnO/AX/P3HT:$PC_{60}BM$/PEDOT:PSS/Ag.

In order to study interface properties of A3, A5 and A7 interlayers, we performed photoemission measurements of the modified electrodes. Analogously to the device fabrication, the interlayers were deposited by blade casting on ZnO and then they were then washed with acetone before being analyzed by XPS/UPS. The first issue was to determine if the interlayer materials remain on the ZnO surface or if they were totally washed out. **Figure 5.16** shows XPS survey spectra after acetone washing. Clearly, A1 and A2 remain on the ZnO substrate while A5 and A7 are fully washed out. In the case of A5-7, after washing features of the clean ZnO substrate are observed with intensities very similar to the XPS spectrum of the ZnO control. In contrast, for A1-3, we can clearly observe the expected core levels of A1-3 (C1s and O1s) concomitant with the disappearance of ZnO signal (except Zn2p). The thicknesses of A1 and A3 on ZnO were calculated comparing XPS spectra of the ZnO substrate and the overlayer. We obtain 7.6 and 6.0 nm, respectively. This means that the materials cover well the ZnO substrate suggesting a stronger interaction with the ZnO substrate. Additionally, the thickness of A1 and A3 are low enough for enabling the electron transfer to the ETL. When we look at the chemical structure of the different polymers, we can most probably attribute the strong interaction most probably to the hydroxyl ending groups (-OH) on the styrene unit for A1 and A3. Thus, the ending groups have direct influence on the interaction with ZnO. A5-7 have methoxy (-OMe) groups and cannot interact strongly with the substrate and do not resist to the washing step.

In a next step, we analyzed the interface electronic properties by UPS. As expected, for A5-7 the UPS spectra are almost the same as for a ZnO control. This is in good agreement with the XPS results confirming that the polymers were fully washed out.

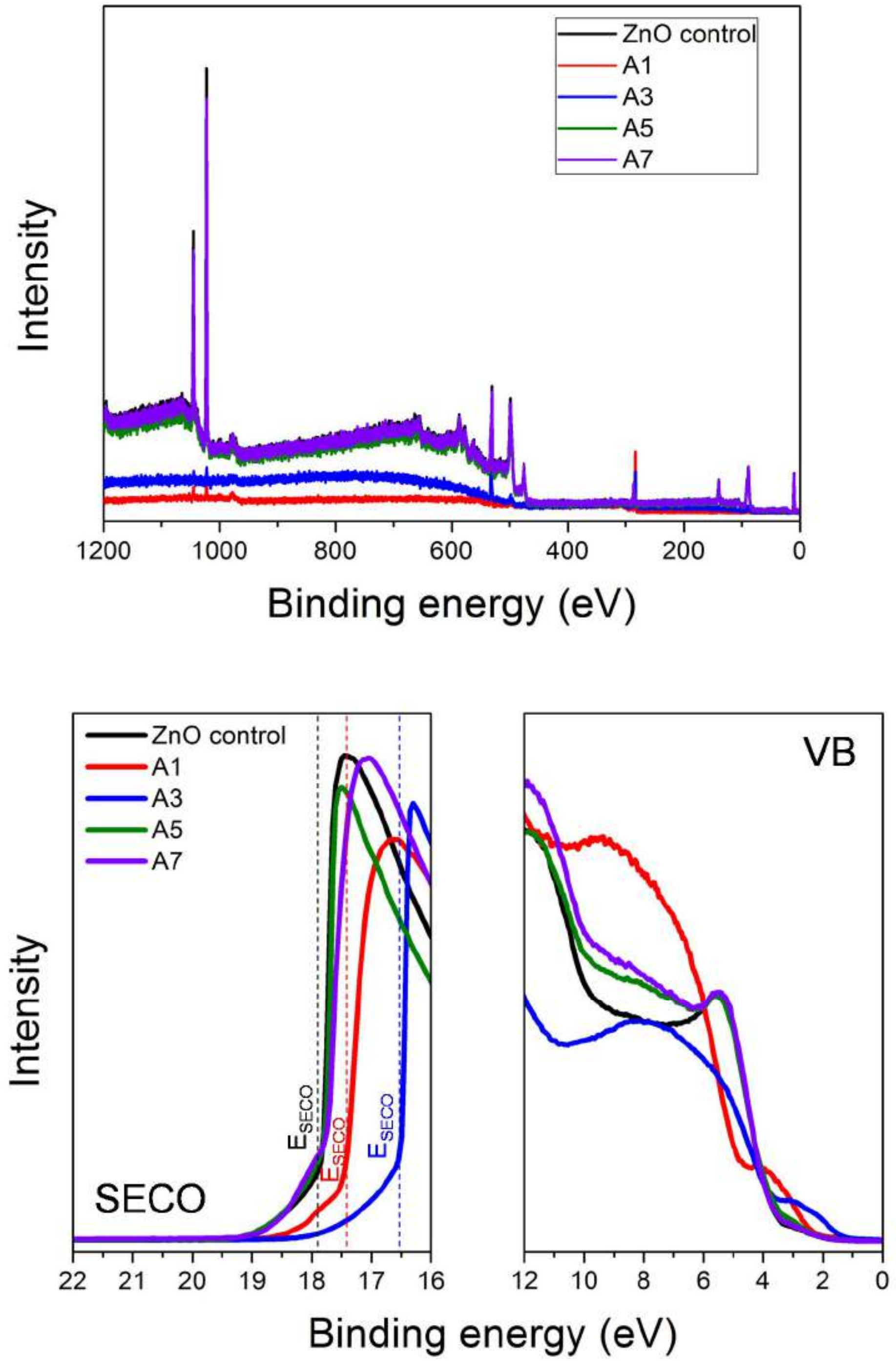

Figure 5.16 - XPS (top) and UPS (bottom) spectra of ZnO control, A1/ZnO, A3/ZnO, A5/ZnO and A7/ZnO after the washing step.

In the case of A1-3, the deposition of the polymer layers has a drastic influence on the valence band (VB) features and in particular on the work function (WF). The VB is 3.8 eV for the control ZnO and is 2.4 and 1.3 eV for A1 and A3 respectively. The WF is 3.5 eV for the control ZnO and is 3.8 and 4.7 eV for A1 and A3 respectively. Thus, the introduction of A1 and A3 increases the WF of ZnO while PEI has the opposite effect.

Sample	**XPS**	**UPS (WF)**	**UPS (VB)**	**Chemical group on the styrene**
ZnO (control)	Trace of carbon from ligands/contamination	3.5 eV	3.8 eV	-
A5/ZnO	No trace of A5 (=ZnO)	3.5 eV	3.8 eV	-OMe
A7/ZnO	No trace of A7 (=ZnO)	3.5 eV	3.8 eV	-OMe
A1/ZnO	Polymer + ZnO	3.8 eV	2.4 eV	-OH
A3/ZnO	Polymer + ZnO	4.7 eV	1.3 eV	-OH

Table 5.3 - Summary of the XPS/UPS results.

The increase of WF (+0.3 and +1.2 eV for A1 and A3 respectively) may explain the loss of the respective device performance as observed in **Figure 5.15**. As the insertion of A3 induced a drastic increase of 1.2 eV, the substrate WF might be now higher than ICT$^-$ of the fullerene. We decided therefore to investigate the interface between ZnO/A3 and C60. We proceeded in the same manner as for ITO, ITO/PEI and ITO/ZnO with evaporation of successive C60 layers.

XPS/UPS results are shown in **Figure 5.17**. Clearly visible again, there is an increase of the C1s intensity accompanied by a decrease of the substrate related Zn2p intensity due to the C60 evaporation. The SECO region of the UPS spectra shows almost no change, i.e. the vacuum level remains constant and we observe a vacuum level alignment (VLA) regime between ZnO/A3 and C60. This VLA can be expected according to the ICT model described in the general introduction (**Figure 5.2**), and previously when we have been discussing the dipoles formed between C60 and ITO, ITO/PEI and ITO/ZnO. The WF of ZnO/A3 is slightly larger than the ICT$^-$ level of C60, and therefore the WF is in between ICT$^-$ and ICT$^+$ resulting in the observed VLA.

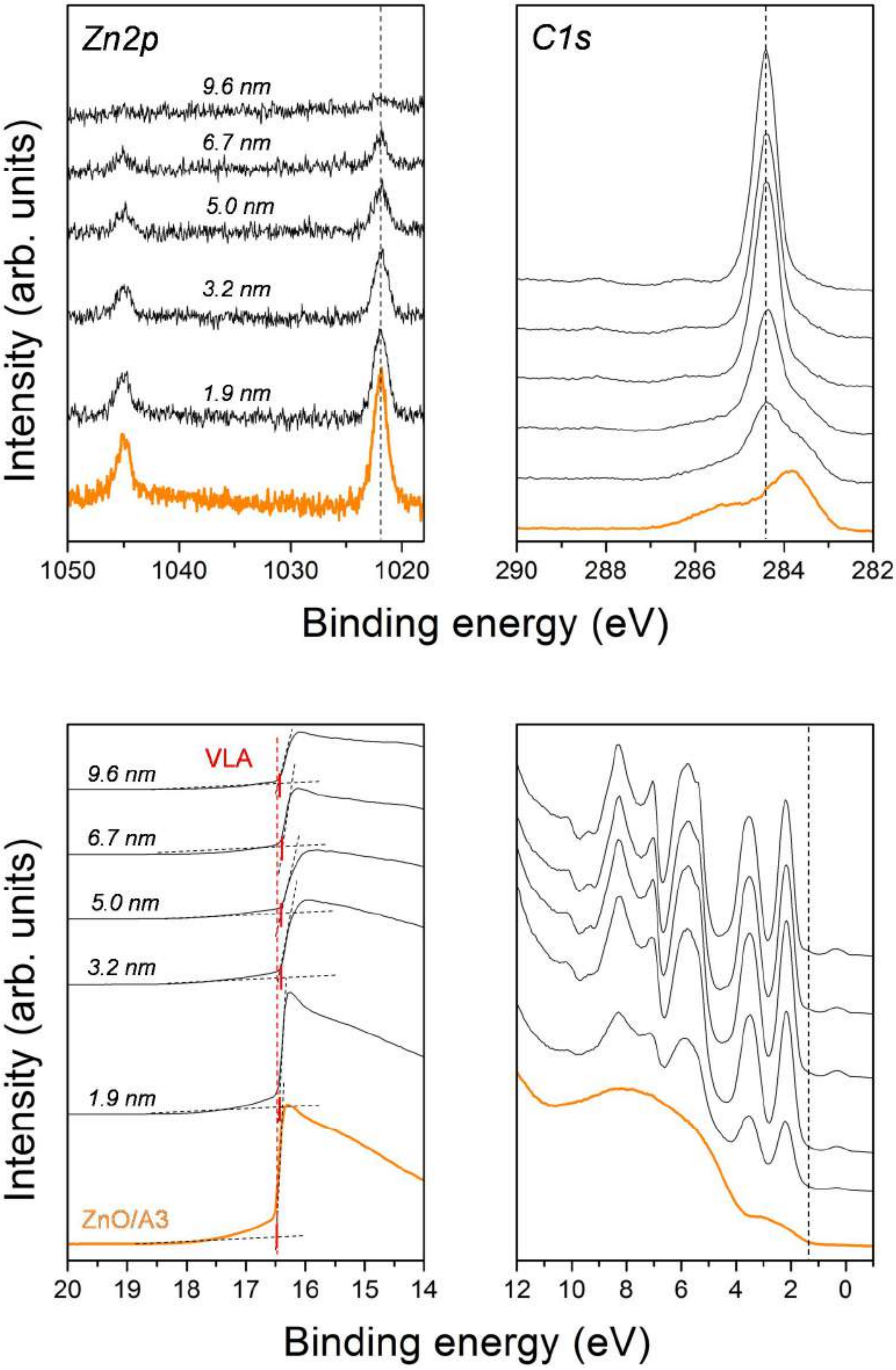

Figure 5.17 - XPS (top) on UPS (bottom) of bare ZnO/A3 (orange) and after several C60 evaporations. For UPS, The secondary electron cut-off (SECO, left) and valence band region (VB, left) are represented.

5.2.4. Conclusion

In this part, we have investigated the ELA between C60 and various ETLs in the context of inverted structure devices. Interface dipoles were observed for ITO (0.25 eV), ITO/PEI (1.35 eV) and ITO/ZnO (0.75 eV) while a VLA was observed in the case of ZnO/A3. (**Figure 5.18**) Our results are fully in line with the ICT model which predicts the formation of dipoles equal to the difference between ICT^- and WF_{ETL}.

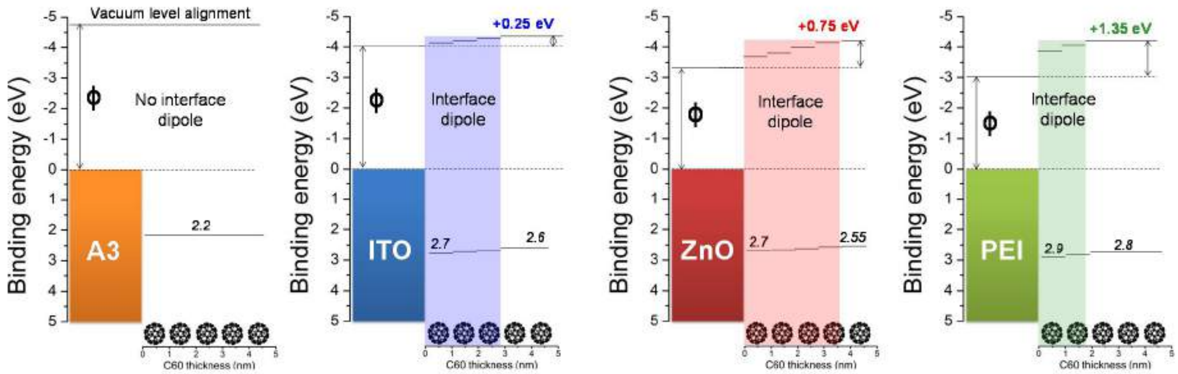

Figure 5.18 - Summary of the ELA between C60 and various ETL substrates.

Figure 5.19 represents the $WF_{ORG/SUB}$ versus WF_{SUB} dependence predicted by the ICT model. In our investigation, the ICT^- of C60 is estimated to 4.3 eV +/- 0.05 eV. In the literature, the ICT^- of C60 was found to be 4.5 eV.[190,198] The difference of 0.2 eV might be due to a difference of calibration.

Interestingly, we can observe a link between the device performance (inverted structure) and the WF_{SUB}. It is important to remind that in the case of devices, the acceptor used is $PC_{60}BM$ and the ICT^- of $PC_{60}BM$ is 0.25 eV lower than C60.[201] Thus, the ICT^- of $PC_{60}BM$ is close to the WF_{ITO} and the S shape of the corresponding J(V) curve suggest a not optimal electron transfer. The effect is much more clear in the case of ZnO/A3, where an energy barrier (Δe) of 0.6 eV is estimated (energy difference between ICT^- of $PC_{60}Bm$ and $WF_{ZnO/A3}$), thus making the electron transfer very difficult resulting in a not working device. In the case of ZnO and ITO/PEI, we are in the pinning regime which according to the J(V) curves seems to favor the electron extraction. Thus, the obtained results suggest a correlation between the energy difference between the ICT^- of the acceptor and the WF of the ETL and the device performance. In the case of $WF_{SUB} < ICT^-$, the pinning regime seems to favor the electron transfer while a vacuum level alignment induces the formation of an energy barrier impacting the electron transfer and at the end the device performance.

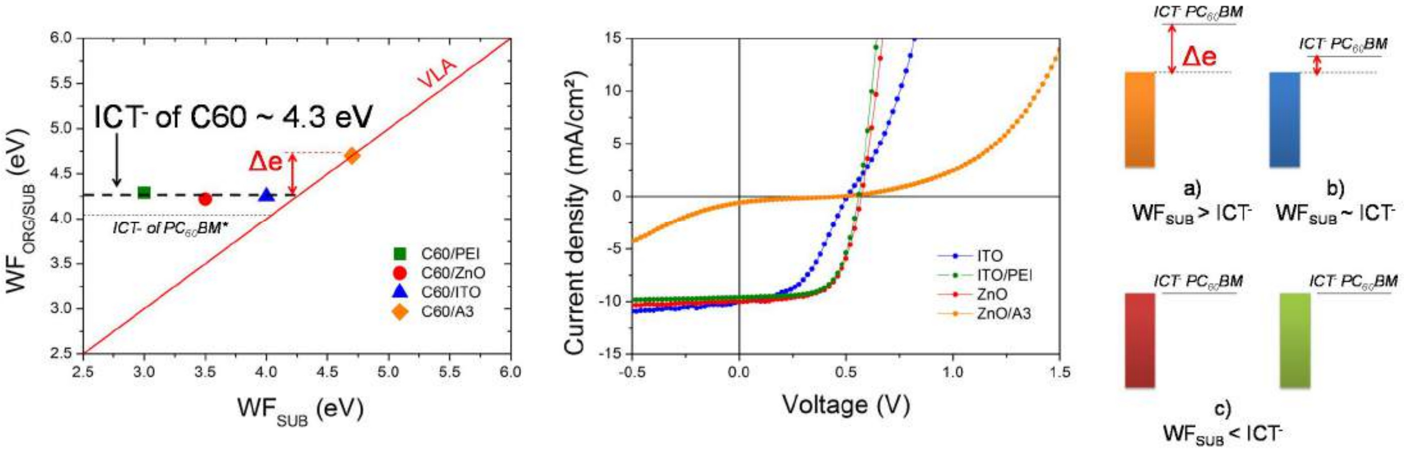

Figure 5.19 – On the left side is shown the dependence of C60 WF evaporated on various substrates of different WFs. The Integer Charge Transfer (ICT$^-$) of C60 is estimated of 4.3 eV +/- 0.05. The ICT$^-$ of PC$_{60}$BM is estimated from Fahlman et al.[201] In the middle is shown, light J(V) curves of inverted devices based on Ag/PEDOT:PSS/P3HT:PC$_{60}$BM/ETL/ITOglass with ETL=ITO (blue), ITO/PEI (green), ZnO (red) or ZnO/A3 (organge). On the right side is shown the relative energy differences between the ICT$^-$ of PC$_{60}$BM and the different WF$_{SUB}$ where WF$_{SUB}$ > IVT$^-$ a) WF$_{SUB}$~ICT$^-$ b) and WF$_{SUB}$ < ICT$^-$ c).

5.3. Influence of ETL on device stability

5.3.1. Introduction

This part is devoted to the photo- and thermal stability of devices based on ZnO or PEI as electron transporting layer (ETL). Inverted devices were fabricated and submitted to AM1.5 exposure in inert atmosphere (light exposure) or exposed at 140°C still in inert atmosphere (thermal exposure). The stability of the devices varies significantly depending on the ETL used and the type of exposure (photo or thermal). Therefore, we investigated first the evolution of the electronic structure (XPS/UPS) of unconfined ETL when exposed to the same light and thermal soaking. In a second step, we exposed ETL confined with the active layer (AL) used in the devices P3HT:PC_{60}BM and we analyzed the interface AL/ETL after washing out the AL.

5.3.2. Experimental

Please, refer to the appendix (A1) for additional details on the experimental techniques.

- *Device/sample preparation and degradation*

Inverted device glass ITO/ETL/P3HT:PC_{60}BM/PEDOT:PSS/Ag with ETL = ZnO or PEI were fabricated using standard procedures. First, the glass/ITO substrate was cleaned in an ultrasonic bath of acetone and propan-2-ol for 10 min each. Following cleaning, the substrates were dried and treated by UV-ozone for 10 min. ZnO or PEI, both used as an electron transporting layers, was subsequently coated directly on top of the cleaned substrates. The coated ETL films were dried at 100 °C and 140 °C in air for 10 min for the PEI and ZnO, respectively. Following the drying process, approximately 250 nm of P3HT:PC_{60}BM (1:0.8 w/w, from Xylene stirred overnight) photoactive layer was then coated on top of the ETLs. PEDOT:PSS used as hole transporting layer, was subsequently coated directly from the commercial aqueous dispersion. All layers were coated using a doctor blade. The devices were then completed by thermally evaporating 300 nm of Ag electrode on customized mask. Before the evaporation of the metal electrode, the photoactive layer was annealed in nitrogen at 140 ° C for 5 min. Cells were illuminated with a simulated solar spectrum from Steuernagel Solartest 1200 Oriel solar simulator at 100 mW/cm^2. The current density − voltage (J − V) characteristics of the devices were recorded using Keithley 2400 SMU in combination with Keithley 7001 Multiplexer system and custom software. The mismatch in the simulated solar spectrum is corrected by measuring the external quantum efficiency (EQE) of each cell.

Following fabrication, devices were exposed to 1 sun conditions (AM1.5, 100W/cm^2) for in-situ photodegradation study, or placed on hot plate at 140 °C for thermal degradation study. Both degradations were performed under inert atmosphere. In order to elucidate the degradation mechanisms occurring in devices submitted to light or thermal exposure, half-finished devices were also fabricated using procedure similar to that of the devices and were exposed to the same light or thermal soaking. After exposure, the top AL was washed off using chloroform in ultrasonic bath (5 min). Then, the samples (ITO/ETL) were dried and inserted in ultra-high vacuum for photoemission analysis.

- *Surface analysis*

See 5.2.2 section

5.3.3. Results

- *Device degradation: PEI vs ZnO as ETL*

Devices were fabricated and exposed to light and thermal soaking as described in the experimental part. **Figure 5.20** shows the effect of the photo and thermal degradation on the electrical parameters of the devices based on ZnO or PEI. We note that very similar initial device performances were obtained when ZnO or PEI are used as ETL (3%). However, **Figure 5.20** shows that the ETL has a direct or indirect impact on the device stability.

Regarding the devices based on ZnO, the light exposure results in a distinct drop (from 3 to 2.5%) of the initial performance due to a loss of current (J_{SC}) during the very first hours of light exposure. After that, the device performance is relatively stable (2.2%) up to more than 100h illumination. Devices based on PEI have a different behavior when exposed to light: a slower and progressive loss (3 to 2%) occurs until 40h. Then the performance remains relatively constant (1.9%) up to more than 100h illumination. The rapid and sometimes exponential loss of performance at the very beginning of exposure is called burn-in period. This phenomenon has been observed many times and is well-documented in the literature.[144,213,214]

From **Figure 5.20**, we can observe that the thermal soaking at 140°C is more severe for the devices stability compared to the light soaking. A drastic performance loss can be observed after 15h of thermal exposure for both PEI (3 →2%) and ZnO (3→1%) based devices. Thus, PEI based devices are more thermally resistant than ZnO based devices.

Photo- and thermal soaking in inert atmosphere impact differently the device performances probably due to involvement of different mechanisms of degradation. In order to get more insight, we investigated interface properties in detail. In a first step, the electronic structure of unconfined ETL (no active layer deposited on the top) exposed to light or thermal soaking was studied.

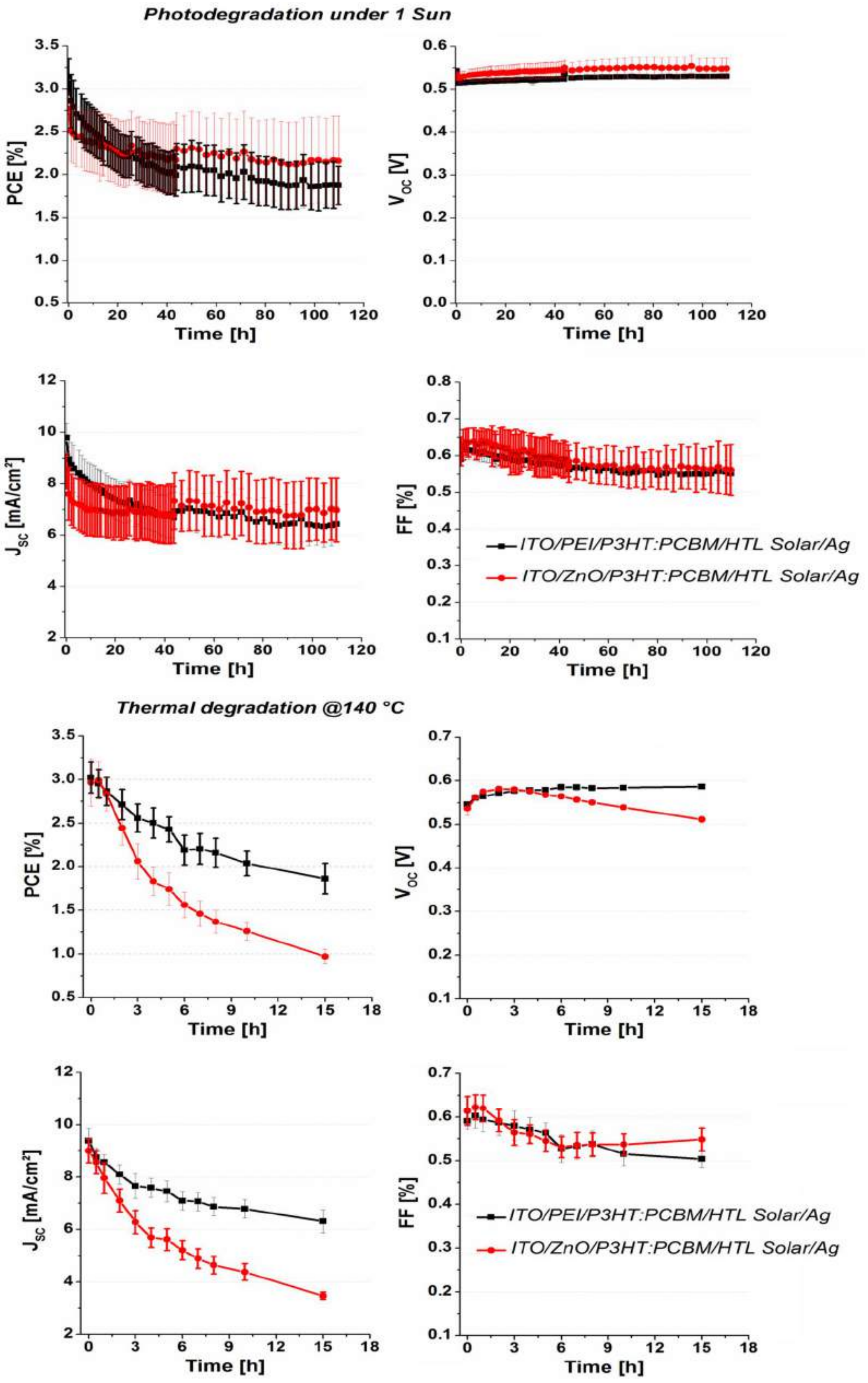

Figure 5.20 – Evolution of the electrical parameters of inverted devices base on PEI or ZnO as ETL exposed to thermal and light soaking.

- *Stability of unconfined ETL*

Light degradation - We used XPS and UPS to investigate the evolution of the electronic structure of unconfined glass/ITO/ZnO and glass/ITO/PEI samples when exposed 15h and 70h to light irradiation (AM1.5).

We first focus on the effect of light exposure on ZnO substrates. **Figure 5.21** shows the Zn2p and C1s core level regions. (Survey in Appendix A5.1)

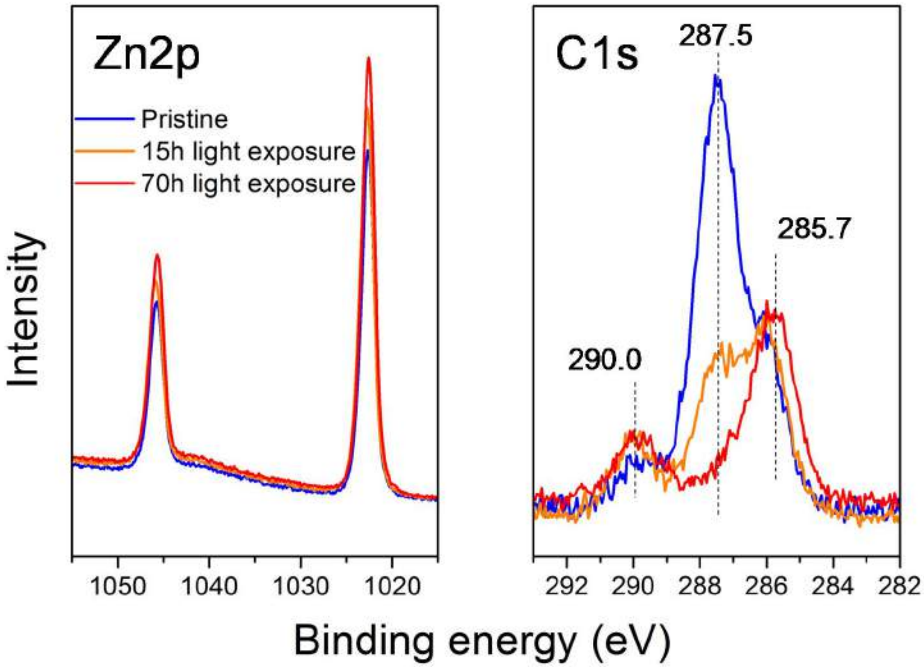

Figure 5.21 - Zn2p and C1s core level regions of pristine ZnO (blue) exposed 15h (orange) and 70h (red) to light.

For the pristine ZnO, the C1s signal (blue) exhibits three components which can be attributed to C(=O)-O (290.0 eV), C-O (287.5 eV) and C-C (285.7).[215] The presence of these groups reflects the presence of traces of residual acetate ligands coming from the ZnO preparation. A possible carbon contamination of the ex-situ prepared ZnO could contribute to the C1s signal, but, such contamination would consist mainly of C-H carbon expected around 285 eV. The calculated thickness of organic material (residual ligands with possible contaminants) is about 1.4 nm. (See Appendix A1 for details on calculation) After 15h and 70h of exposure, we can clearly observe the disappearance of the component at 287.5 eV while the two others are still preserved after 70h exposure. The increase of Zn2p signal intensity indicates that part of the over-layer, i.e. residual ligands, most probably leave the film and migrate in gas phase. This is in line with the evolution of the calculated organic material thickness. After 15h and 70h of light exposure, we calculated a thickness of 0.8 nm (-0.6 nm) and 0.6 nm (-0.8 nm) respectively. XPS results indicate that the organic material on ZnO (residual ligands with possible contaminants) reacts when exposed to light and desorbs from ZnO. As only the C-O component is impacted, it is interesting to have a closer look to the O1s signal of pristine and 70h exposed ZnO. (**Figure 5.22**) The O1s core level of pristine ZnO is based on three components. We attributed the different components according to a recent work of Zhang et al.[216] : O^{2-} species in the lattice (O_L), oxygen vacancies or defects (O_V) and chemisorbed species oxygen (O_C). We can observe that the light exposure has selectively provoked a shift of the O_C component (-0.4 eV). This shift suggests a change in chemical environment of the organic materials and the fact that the shift goes to lower binding energy support the disappearance of electronegative atoms such as oxygen. It is in line with the disappearance of the C-O (287.5 eV) and desorption of organic species probably coming from residual ligands.

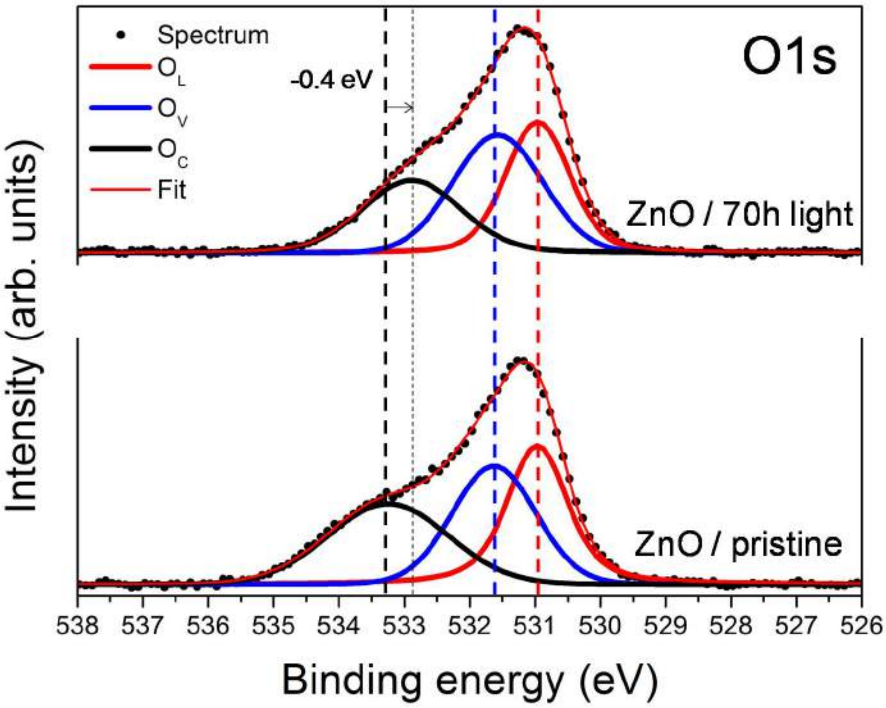

Figure 5.22 - Deconvolution of the O1s core level of pristine and 70h light exposed ZnO.

Another important issue is the modification of electronic interface properties upon light soaking. In **Figure 5.23** we show the evolution of the UPS spectra of the pristine and 70h exposed ZnO samples. Whereas the valence band onset remains constant, the light exposure induces clearly an increase of the work function (WF), which might affect the ability for charge extraction in devices. The increase of WF is probably due to the desorption of organic material previously mentioned with XPS results.

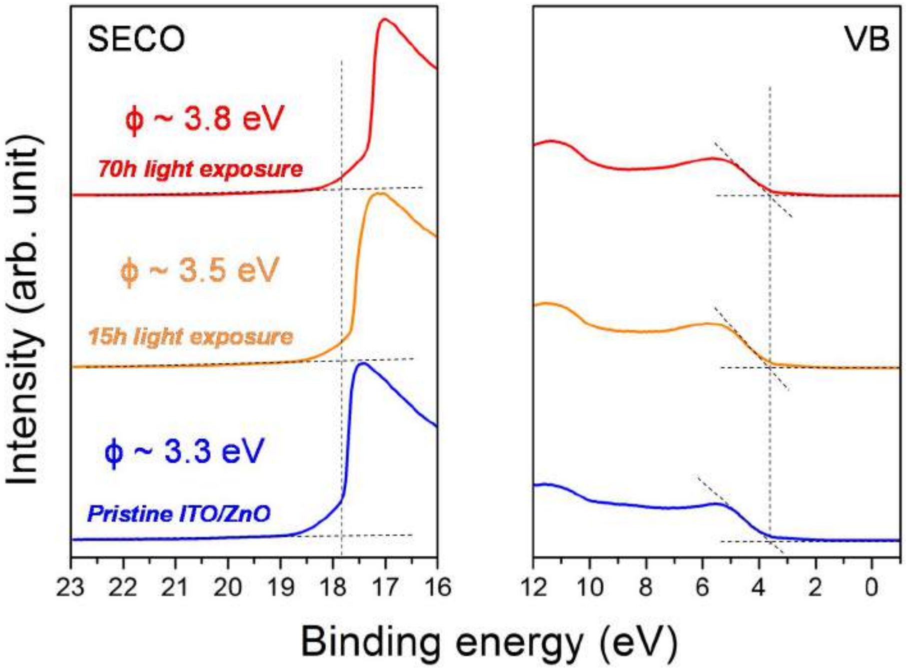

Figure 5.23 - UPS spectra of pristine ZnO and after 15h and 70h light exposure.

We focus now on the photo-degradation of ITO/PEI irradiated in the same conditions as ZnO samples. **Figure 5.24** shows the XPS survey spectra and the corresponding N1s and C1s detail spectra. Changes of both shape and intensity of the N1s signal are clearly observed, especially after 70h of light exposure. The N1s of pristine PEI can be described with two components corresponding to the peak fit shown in **Figure 5.25**. According to the literature, the component at lower binding energy (BE) can be assigned to neutral amines (N) while the other component at higher BE represents the protonated amine (N^+)[56,217]. After 70h exposure to light, the intensity of the N component has decreased accompanied by a change in the N/N^+ ratio. These changes suggest that the neutral amines were more prone to react and probably a small fraction migrates in the gas phase when exposed to light. This is supported by the slight increase of the intensity of the substrate, as revealed for instance by the increase of the In3d intensity from the ITO substrate. The thickness of PEI on ITO was calculated to be 2.4 for pristine and 15h exposed samples, and 2.2 nm for exposed 70h. **Figure 5.26** shows the UPS spectra of the same samples. In contrast to ZnO samples, only a small increase of the work function (+0.1 eV) was observed after 70h of light exposure.

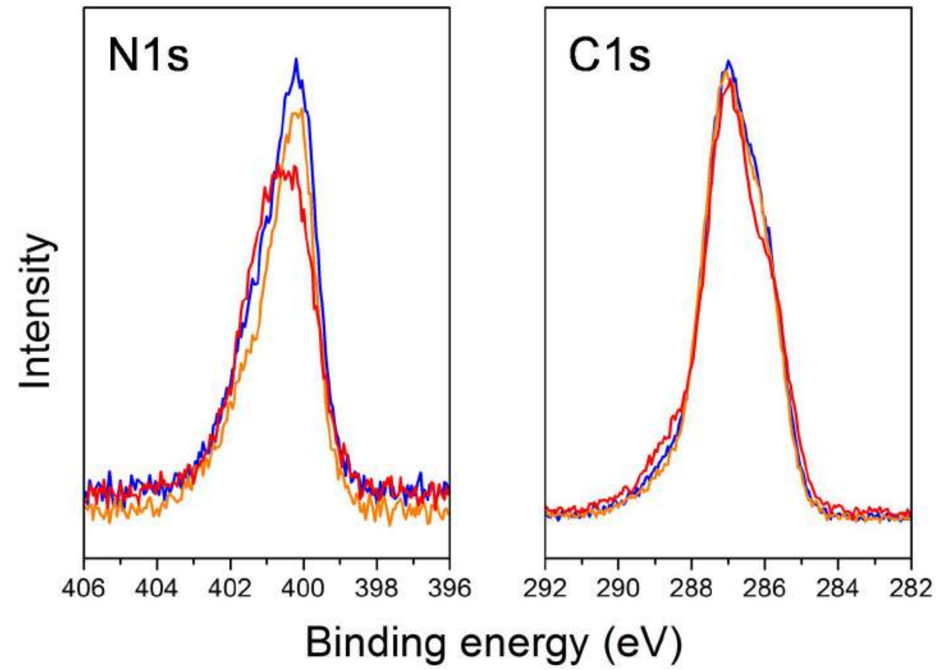

Figure 5.24 - XPS survey (top) and focus on N1s and C1s core levels of pristine ITO/PEI and submitted to 15h and 70h of light exposure.

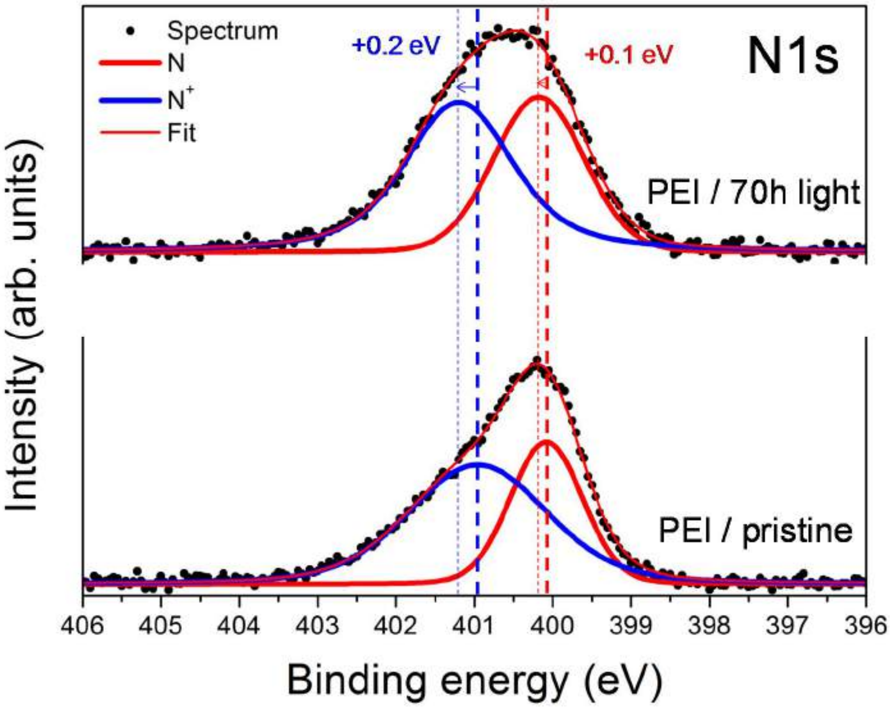

Figure 5.25 - Deconvolution of the N1s core level of pristine and 70h light exposed ITO/PEI.

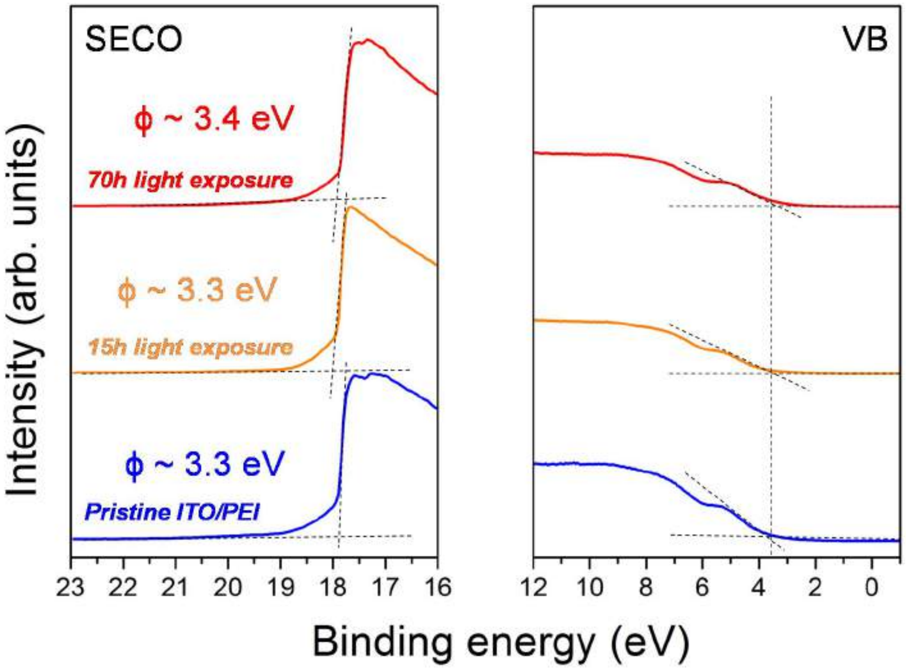

Figure 5.26 - UPS spectra of pristine ITO/PEI and submitted to 15h and 70h of light exposure.

To summarize the main evolutions resulting from the light exposure of ITO/ZnO and ITO/PEI samples, we have shown that organic matter is present on both substrates (residual ligands for ITO/ZnO, and PEI for ITO/PEI), and is sensitive to light exposure. For ZnO, light provokes the photodegradation of the ligands and part of the by-products migrates in the gas phase; these phenomena are concomitant with a significant increase of the work function (+0.2 and +0.4 eV after 15 and 70h respectively). For PEI, it seems also that a small part of the neutral amines migrate in gas phase due to photodegradation processes. The fairly weak increase of WF (+0.1 eV after 70h of light exposure) may suggest that most of the amines, which are bonded to ITO, are unaffected by photodegradation after 70h exposure. Thus, the interface ITO/PEI is still unchanged up to 70h of light exposure. **Figure 5.27** illustrates the proposed processes involved upon light soaking.

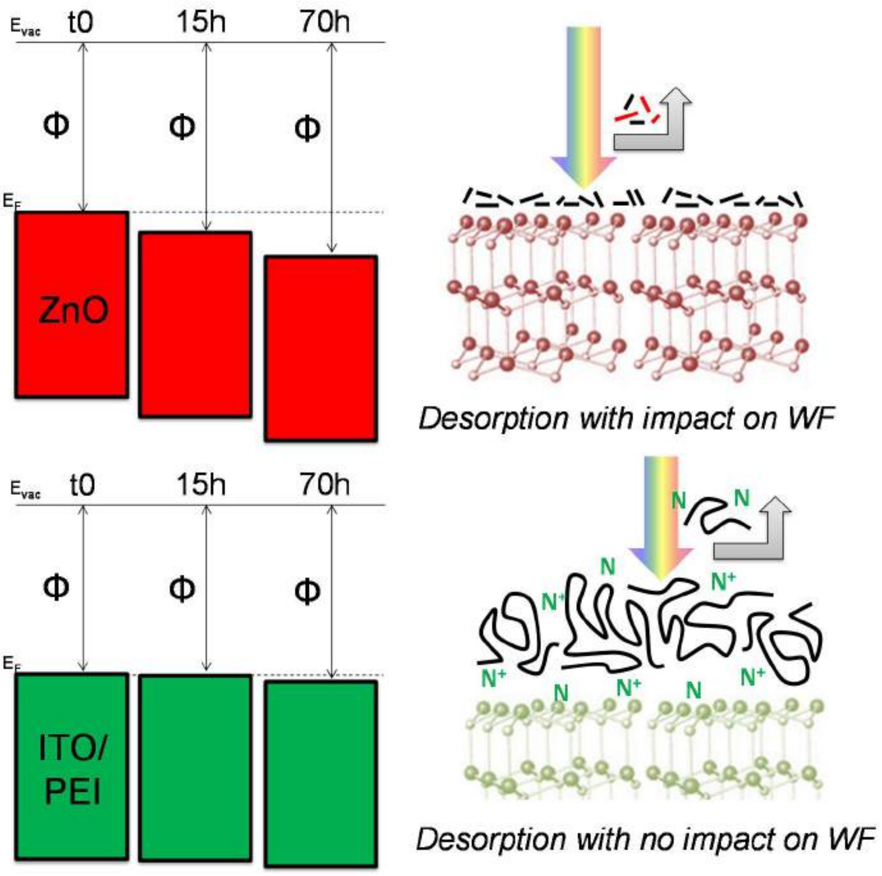

Figure 5.27 - Proposed mechanism of photodegradation of organic matter at the surface of ITO/ZnO and ITO/PEI substrates.

Thermal degradation - Due to the drastic effect of the thermal degradation on the PCE, the study of the influence of the ETL was of particular interest. The same series of XPS/UPS measurements were performed on thermally degraded (inert atmosphere) ITO/ZnO and ITO/PEI unconfined substrates. As example, **Figure 5.28** shows the evolution of the C1s signal of ZnO and the N1s signal of ITO/PEI, i.e. the core levels which where the most significantly affected upon light exposure. In contrast to light exposure, the chemical composition at the surface remains unchanged suggesting that the organic materials are not thermally sensitive (up to 8h at 140°C) for both substrates. Also the UPS spectra show almost no changes (Appendix A5.3). It seems that the chemisorbed organic materials on ZnO are not thermally sensitive and remain at the surface. In the case of PEI, the polymer is not degraded by the thermal soaking.

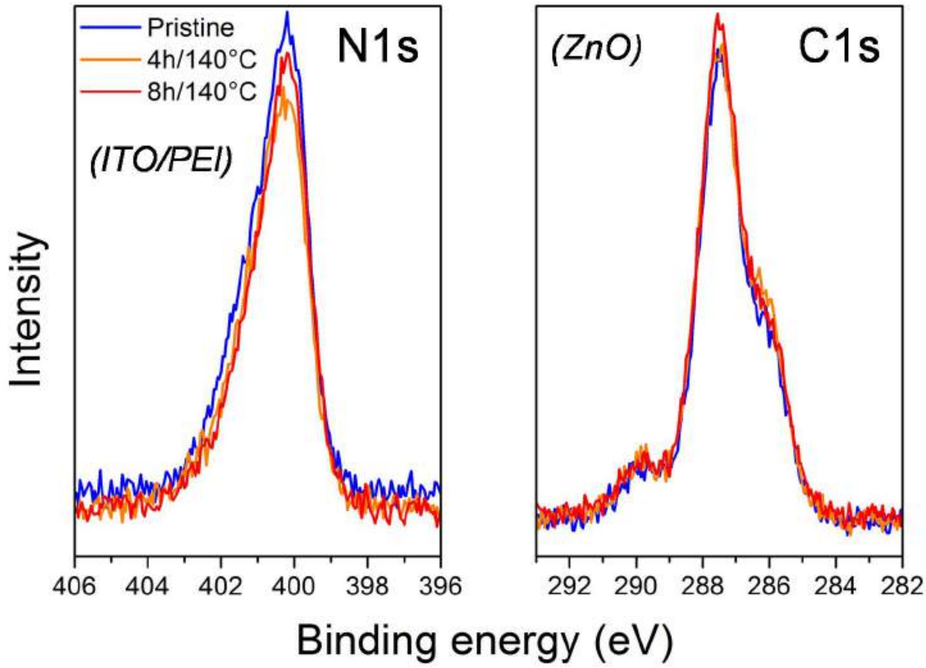

Figure 5.28 - N1s and C1s core levels of ITO/PEI and ZnO respectively thermally exposed.

- *Stability of confined ETL*

Light exposure - Here, the ETL layers (ZnO or PEI) were covered by the active layer (AL) (P3HT:$PC_{60}BM$) before being exposed to thermal or light soaking. After thermal or light soaking, the active layer was washed out by immersion in chloroform (See experimental part). Then, the samples were analyzed by XPS/UPS. The underlying idea was to analyze remaining materials from the active layer on the ZnO or PEI substrates.

Figure 5.29 shows the XPS spectra obtained for ZnO/AL (washed) pristine and exposed to light for 15 and 70h. The spectrum of a control ZnO (none exposed) is shown as a reference. The blue spectrum corresponds to a ZnO sample obtained after deposition and removal of the active layer. We can observe that the two spectra are different. Indeed, we can observe that after deposition and removal of the AL, additional materials remain at the surface resulting in an attenuation of the Zn2p signal (and other signals from the substrate) compared to the ZnO control sample. The presence of carbon and sulfur elements indicates that P3HT and probably also $PC_{60}BM$ are present at the surface. This suggests that even without exposure, a spontaneous binding is formed between AL materials and ZnO or ZnO/organic matter (ligands, contamination). Thus, the resulting binding is strong enough to make the remaining materials insoluble to a chloroform immersion. (5 min in ultrasonic bath). Interestingly, more organic materials remain at the surface of ZnO after light exposure. This suggests additional photo-induced interactions between AL and ZnO. We observe similar XPS intensities after 15 and 70h of light exposure, i.e. the amount of residual AL is only marginally affected by the irradiation duration indicating that additional photo-induced interactions are mainly created during the very first step of exposure. Remarkably, this timescale is in good agreement with the time scale of the burn-in process observed in **Figure 5.20.**

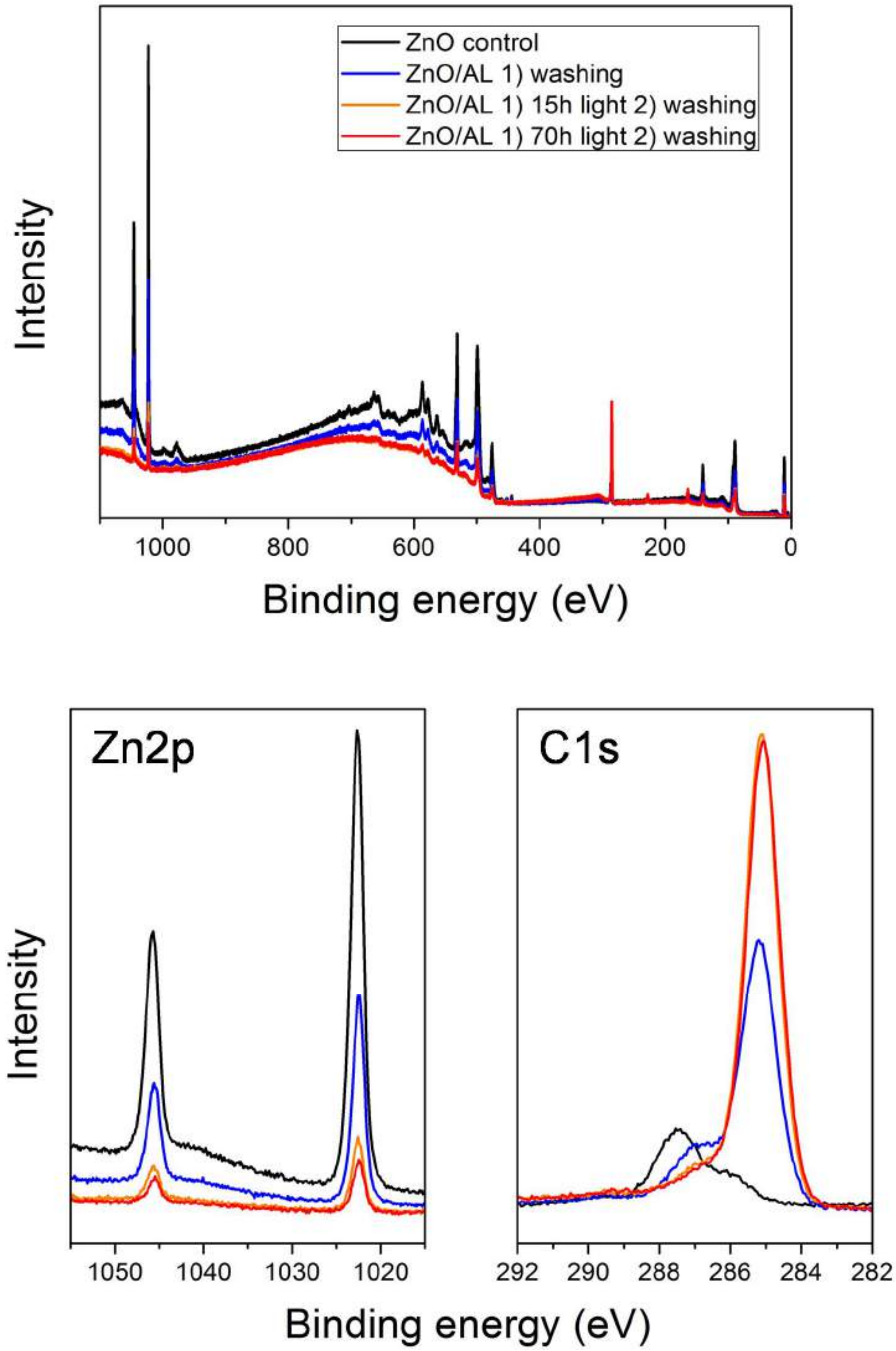

Figure 5.29 - XPS survey (top) and Zn2p and C1s core level spectra for control ZnO (black), ZnO/AL→washed (blue), ZnO/AL→15h of light exposure→washed (orange) and ZnO/AL→70h of light exposure→washed (red).

The same series of experiments were performed for ITO/PEI/AL samples and the data are available in Appendix A5.4. As for ZnO, residual amount of AL is clearly observed after CHCl3 washing without exposure. Similarly to ITO/ZnO/Al samples, light exposure provokes a decrease of the intensity of the substrate In3d signal suggesting the presence of more residual AL compared to the un-irradiated ITO/PEI/AL sample.

Thermal soaking - Concerning the thermal treatment, the same set of XPS spectra as observed after light exposure of ITO/PEI and ZnO respectively are available in Appendix A5.5 and A5.6. As for light exposure, additional AL residue can be observed but with a different amount.

The discrepancy between the thicknesses of the residual organic layers for all the studied samples is shown in **Figure 5.30**.

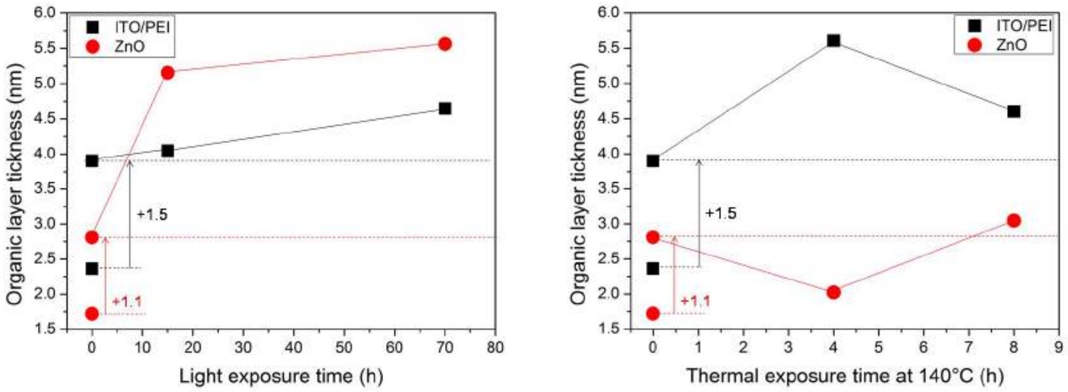

Figure 5.30 - Residual organic layer thickness on pristine and exposed (light left, thermal right) ITO/PEI and ITO/ZnO.

Figure 5.30 shows the residual organic layer thickness extracted from the XPS spectra. As observed for unexposed ZnO, a 1.7 nm layer of organic material of from residual ligands and contamination was measured. In the case of bear ITO/PEI, the PEI thickness is estimated to be 2.4 nm. We have observed that after the active layer deposition followed by washing (no exposure), organic material from P3HT and $PC_{60}BM$ remain on both ZnO and ITO/PEI. The layer thickness of reaming AL has been estimated to be 1.1 and 1.5 nm for ZnO and ITO/PEI respectively. Regarding the effect of light exposure for ITO/PEI/AL, the remaining AL layer slightly increases along the exposure time (+0.1 and +0.6 nm for 15 and 70h respectively). In the case of ZnO, an increase of +2.3 and +2.7 nm was measured for 15 and 70h of light exposure. The thermal exposure of ITO/PEI/AL results in an increase of the remaining AL layer corresponding to a thickness of +1.7 and +0.7 nm, while in the case of ZnO a variation of -0.8 and +1.2 nm was measured after 4 and 8h of thermal soaking at 140°C respectively.

5.3.4. Discussion

From **Figure 5.20**, it is clear that the nature of the ETL has an impact on the device photo and thermal stability.

We first focus on thermal degradation (140°C, inert atmosphere). From our results on unconfined ETLs, we observed that both ITO/PEI and ZnO were thermally stable at 140°C up to 8h with no significant change of the chemical composition and electronic properties. The limiting degradation process is probably the phase separation in the bulk heterojunction (BHJ) P3HT:$PC_{60}BM$ which was widely investigated in the scientific literature. It is also known that the surface energy of the substrate has an important impact on $PC_{60}BM$ diffusion and therefore BHJ thermal stability.[79] Therefore, here we propose that the device thermal stability is governed by the difference of surface energy of ITO/PEI and ITO/ZnO. Additionally, we have observed for confined substrates a higher amount of AL residue on ITO/PEI than ZnO suggesting that AL interacts better with PEI via physical and/or chemical binding. Thus, the mobility of AL materials at the interface with PEI might be partially reduced implying a stabilization of the BHJ compared to ZnO.

Then, for light exposure, we have observed for unconfined substrates that the residual ligands of ZnO are light sensitive resulting in an important increase of the work function (+0.2 and +0.4 eV for 15 and 70h respectively). In a confined environment, the relative high amount of residual AL remaining at the ZnO surface (+2.3 nm after 15h) suggests photo-induced interactions which could explain the burn-in process observed in **Figure 5.20**. For unconfined ITO/PEI, we have observed a change in the N1s signal suggesting photo-induced reaction with the amine groups. In confined configuration, the change of N1s is also observed and may suggest that the slight additional AL residue could result from a photo-induced bonding. **Figure 5.30** shows a linear trend (unlike ZnO) which is in line with the time scale of the burn-in process observed in **Figure 5.20**.

5.3.5. Conclusion

In this part, we have investigated the influence of ETLs: ITO/PEI vs ZnO on device photo and thermal stability. From our results, we propose that the difference of surface energy from ETL can influence the $PC_{60}BM$ diffusion and therefore the phase separation rates in the polymer blend and at the end, the device thermal stability. Exposed to light, we propose that photo-induced reaction between AL and ETL can partially come into play the burn-in process observed in the device photostability.

5.4. Summary of Chapter 5

In the first part (**5.2**), we have investigated the energy level alignment between C60 and various electron transporting layer (ETL) such as ITO, ITO/PEI, ZnO and ZnO/A3. Our results are in line with the ICT model which predicts interface dipole for ITO, ITO/PEI and ZnO while vacuum level alignment was observed for ZnO/A3. The obtained results suggest a correlation between the energy difference of WF_{ETL} and ICT^- of the acceptor with the device performance.

In the second part (**5.3**), we compared the photo and thermal stability of devices based on ITO/PEI or ZnO. The difference of thermal stability might be explained by the different surface energies from ETLs thus influencing the $PC_{60}BM$ diffusion and thereforethe rate of phase separation. Exposed to light, photo-induced reactions of the organic material of ETLs (residual ligands and/or contamination for ZnO and PEI itself for ITO/PEI) with the active layer materials might explain the burn-in period of the devices.

General conclusion

Considerable efforts for increasing the organic solar cells performances were achieved during this last decade. In 2013, Heliatek GmbH announced 12% of efficiency for a tandem organic solar cell, with the aim to reach 15% in the near future. Even if additional efforts are needed for getting modules performances as high as those obtained with small devices (the so-called lab/fab transfer), reaching long lifetimes is definitely the crucial remaining point. Due to their natural sensitivity to the operating conditions of PV, the structure and properties of organic materials are progressively modified, inducing degradation within the devices. In order to stabilize the devices and get longer lifetimes, it is crucial to understand the different and complex mechanisms which can occur. Thus, the aim of the present work is to provide deeper insights related to the degradation and stabilization of organic materials used in OPV.

- In a first part, we have studied the degradation of a series of low band gap polymers. We concluded that the chemical structure of the side chain can significantly impact the polymer (and blend) photostability, but that additional parameters are important to consider for a fair comparative study. We demonstrated that alcoxy side chains (-OR) and a low polydispersity index are two crucial parameters which can reduce the pi-conjugated polymer degradation rate. Within the same polymer series, we observed that the thermal stability of the polymer blends (phase separation induced by diffusion of $PC_{60}BM$ molecules) is not directly related to the polymer or blend Tg, but rather to sub-transitions dictated by the difference of polymer side chains. Thus, the lack of side chains on one part of the low band gap backbone seems to favor $PC_{60}BM$ diffusion and therefore reduce the thermal stability of the blend films. Finally, we observed that the competition between $PC_{60}BM$ dimerization and crystallization influences the stability of encapsulated devices and depends on the structure of the low bang gap polymer side chain. As a general rule within the studied series, we observed that lowering the $PC_{60}BM$ content results in devices stabilization. The impact was more or less pronounced depending on the low bang gap polymer.
- Secondly, we clearly demonstrated that the use of high boiling point additives such as DIO and ODT induces the presence of residues which, once confined, react with the polymer blend materials resulting in a drastic decrease of polymer blend photostability. We also studied the use of HALS in polymer blends and we observed antagonist effects when mixed with P3HT and $PC_{60}BM$. Finally, we used a polyfullerene as a ready-to-use additive for thermally stabilizing the polymer blends and devices. We observed a reduction of the $PC_{60}BM$ crystallization and an improvement of the device thermal stability when the polyfullerene is used.
- Concerning the interface between the active layer (AL) and the hole transporting layer (HTL), we observed that the interface between the AL and the PEDOT:PSS layer is definitely the mechanical weak point whatever the donor polymer used is. The use of an organic-based PEDOT:PSS formulation instead of a water-based PEDOT:PSS slightly improves the adhesion between the AL and HTL layer in the case of P3HT:$PC_{60}BM$ resulting in a breaking point deeper in the AL. However, the use of copolymers as interlayers did not show promising results. Exposed to damp heat (85°C/85% RH), we observed that the $PC_{60}BM$ agglomerates at the AL/PEDOT:PSS interface can support the device delamination and the holes extraction can be blocked.
- Regarding the interface between the AL and electron transporting layer (ETL) of the inverted device structure, we investigated the energy level alignments between C60 and various potential ETLs such as ITO, ITO/PEI, ZnO and ZnO/AX. In agreement with the ICT model, we revealed the existence of interface dipoles related to the difference of the work function of the

ETL substrate (WF_{sub}) and the ICT^- of C60. The results show that the WF_{sub} must be lower than the E_{ICT}^- of C60 in order to obtain an efficient electron transfer in the pinning regime. Then we compared the photo- and thermal stability of devices based on ZnO or ITO/PEI, the two most currently used ETLs in inverted device configuration. We found that the ETL influence the thermal stability of the devices likely due to the difference of surface energy which impacts the $PC_{60}BM$ diffusion. Exposed to light, we observed that organic materials from the AL can react with the substrates which can possibly explain the burn-in period of the devices.

Exposed to light and/or thermal soaking, we demonstrated that polymer blend materials can be successfully stabilized by different approaches. However, the exposure which is and will remain the Achill's heel of organic materials used in electronic applications is the combination of light with oxygen/humidity. Indeed, even if some strategies are valuable for increasing the stability of organic materials (such as side chain structure) it is important to remind that fairly weak degradation of the organic materials completely "kill" the device performance. Thus, all efforts for stabilizing OPV materials and devices are useless if an efficient encapsulation is not used. Currently, the use of ultra-barrier encapsulation is expensive. Therefore, the search and development of cheap and efficient materials for transparent and flexible packaging[218-220] (Ievgeniia Topolniak, ESR9) appear to be essential for the success of the technology.

Bibliography

(1) Rhodes, R. *The Security Implications of Increased Global Reliance on Nuclear Power Conference* **2007**.

(2) O'Connor, P. A. *THE PARDEE PAPERS* **2010**, *10*.

(3) Smil, V. *Encyclopedia of Energy* **2004**, *6*.

(4) *Intergovernmental Panel on Climate Change* **2013**.

(5) Perez, R.; Perez, M. *IEA/SHC SOLAR UPDATE* **2009**.

(6) Bequerel, M. E. *Compte rendu de l'académie des sciences* **1839**.

(7) Bequerel, M. E. *Compte rendu de l'académie des sciences* **1839**.

(8) Fritts, C. E. **1883**.

(9) Einstein, A. *Annalen der Physik* **1905**, *17*.

(10) Ohl, R. S. **1941**.

(11) Chapin, D. M.; Fuller, C. S.; Pearson, G. L. *Journal of Applied Physics* **1954**, *25*, 676.

(12) Loferski, J. J. *Journal of Applied Physics* **1956**, *27*, 777.

(13) Shockley, W.; Queisser, H. J. *Journal of Applied Physics* **1961**, *32*, 510.

(14) Vos, D. *J. Phys. D: Appl. Phys.* **1980**, *13*, 839.

(15) Mulvaney, D. *solar industry* **2013**, *6*.

(16) Spanggaard, H.; Krebs, F. C. *Solar Energy Materials and Solar Cells* **2004**, *83*, 125.

(17) Pochettino, A. *Acad. Lincei Rend.* **1906**, *15*, 335.

(18) Volmer, M. *Ann. Physik* **1913**, *40*, 775.

(19) Chiang, C. K.; Fincher, C. R.; Park, Y. W.; Heeger, A. J.; Shirakawa, H.; Louis, E. J.; Gau, S. C.; MacDiarmid, A. G. *Physical Review Letters* **1977**, *39*, 1098.

(20) Glenis, S.; Tourillon, G.; Garnier, F. *Thin Solid Films* **1986**, *139*, 221.

(21) Tang, C. W. *Applied Physics Letters* **1986**, *48*, 183.

(22) Kroto, H. W.; Heath, J. R.; O'Brien, S. C.; Curl, R. F.; Smalley, R. E. *Nature* **1985**, *318*, 162.

(23) Sariciftci, N. S.; Smilowitz, L.; Heeger, A. J.; Wudl, F. *Synthetic Metals* **1993**, *59*, 333.

(24) Morita, S.; Kiyomatsu, S.; Yin, X. H.; Zakhidov, A. A.; Noguchi, T.; Ohnishi, T.; Yoshino, K. *Journal of Applied Physics* **1993**, *74*, 2860.

(25) Halls, J. J. M.; Pichler, K.; Friend, R. H.; Moratti, S. C.; Holmes, A. B. *Synthetic Metals* **1996**, *77*, 277.

(26) Yu, G.; Gao, J.; Hummelen, J. C.; Wudl, F.; Heeger, A. J. *Science* **1995**, *270*, 1789.

(27) Kodali, H. K.; Ganapathysubramanian, B. *Modelling and Simulation in Materials Science and Engineering* **2012**, *20*, 035015.

(28) Mei, J.; Bao, Z. *Chemistry of Materials* **2013**, *26*, 604.

(29) Kim, D. H.; Ayzner, A. L.; Appleton, A. L.; Schmidt, K.; Mei, J.; Toney, M. F.; Bao, Z. *Chemistry of Materials* **2013**, *25*, 431.

(30) Cabanetos, C.; El Labban, A.; Bartelt, J. A.; Douglas, J. D.; Mateker, W. R.; Fréchet, J. M. J.; McGehee, M. D.; Beaujuge, P. M. *Journal of the American Chemical Society* **2013**, *135*, 4656.

(31) Tumbleston, J. R.; Collins, B. A.; Yang, L.; Stuart, A. C.; Gann, E.; Ma, W.; You, W.; Ade, H. *Nature Photonics* **2014**, *8*, 385.

(32) Miller, N. C.; Sweetnam, S.; Hoke, E. T.; Gysel, R.; Miller, C. E.; Bartelt, J. A.; Xie, X.; Toney, M. F.; McGehee, M. D. *Nano letters* **2012**, *12*, 1566.

(33) He, X.; Mukherjee, S.; Watkins, S.; Chen, M.; Qin, T.; Thomsen, L.; Ade, H.; McNeill, C. R. *The Journal of Physical Chemistry C* **2014**, *118*, 9918.

(34) Dang, M. T.; Hirsch, L.; Wantz, G.; Wuest, J. D. *Chemical Reviews* **2013**, *113*, 3734.

(35) Bartelt, J. A.; Douglas, J. D.; Mateker, W. R.; Labban, A. E.; Tassone, C. J.; Toney, M. F.; Fréchet, J. M. J.; Beaujuge, P. M.; McGehee, M. D. *Advanced Energy Materials* **2014**, *4*, n/a.

(36) Urien, M.; Bailly, L.; Vignau, L.; Cloutet, E.; de Cuendias, A.; Wantz, G.; Cramail, H.; Hirsch, L.; Parneix, J.-P. *Polymer International* **2008**, *57*, 764.

(37) Scharber, M. C.; Koppe, M.; Gao, J.; Cordella, F.; Loi, M. A.; Denk, P.; Morana, M.; Egelhaaf, H. J.; Forberich, K.; Dennler, G.; Gaudiana, R.; Waller, D.; Zhu, Z.; Shi, X.; Brabec, C. J. *Adv Mater* **2010**, *22*, 367.

(38) Li, Y. *Chemistry, an Asian journal* **2013**, *8*, 2316.

(39) Lou, S. J.; Szarko, J. M.; Xu, T.; Yu, L.; Marks, T. J.; Chen, L. X. *Journal of the American Chemical Society* **2011**, *133*, 20661.

(40) Ye, L.; Jing, Y.; Guo, X.; Sun, H.; Zhang, S.; Zhang, M.; Huo, L.; Hou, J. *The Journal of Physical Chemistry C* **2013**, *117*, 14920.

(41) Aïch, B. R.; Lu, J.; Beaupré, S.; Leclerc, M.; Tao, Y. *Organic Electronics* **2012**, *13*, 1736.

(42) Lee, J. K.; Ma, W. L.; Brabec, C. J.; Yuen, J.; Moon, J. S.; Kim, J. Y.; Lee, K.; Bazan, G. C.; Heeger, A. J. *Journal of the American Chemical Society* **2008**, *130*, 3619.

(43) Norrman, K.; Gevorgyan, S. A.; Krebs, F. C. *ACS Applied Materials & Interfaces* **2008**, *1*, 102.

(44) Reale, A.; Notte, L. L.; Salamandra, L.; Polino, G.; Susanna, G.; Brown, T. M.; Brunetti, F.; Carlo, A. D. *Energy Technol.* **2015**, *3*, 385.

(45) Giri, G.; DeLongchamp, D. M.; Reinspach, J.; Fischer, D. A.; Richter, L. J.; Xu, J.; Benight, S.; Ayzner, A.; He, M.; Fang, L.; Xue, G.; Toney, M. F.; Bao, Z. *Chemistry of Materials* **2015**, 150327123020006.

(46) Ray, B.; Nair, P. R.; Alam, M. A. *Solar Energy Materials and Solar Cells* **2011**, *95*, 3287.

(47) Dang, M. T.; Hirsch, L.; Wantz, G. *Advanced Materials* **2011**, *23*, 3597.

(48) Fan, X.; Fang, G. J.; Qin, P. L.; Cheng, F.; Zhao, X. Z. *Applied Physics A* **2011**, *105*, 1003.

(49) Pearson, A. J.; Wang, T.; Jones, R. A. L.; Lidzey, D. G.; Staniec, P. A.; Hopkinson, P. E.; Donald, A. M. *Macromolecules* **2012**, *45*, 1499.

(50) Yang, X.; Uddin, A. *Renewable and Sustainable Energy Reviews* **2014**, *30*, 324.

(51) Park, J. H.; Kim, J. S.; Lee, J. H.; Lee, W. H.; Cho, K. *The Journal of Physical Chemistry C* **2009**, *113*, 17579.

(52) Po, R.; Carbonera, C.; Bernardi, A.; Camaioni, N. *Energy & Environmental Science* **2011**, *4*, 285.

(53) Sun, K.; Zhang, S.; Li, P.; Xia, Y.; Zhang, X.; Du, D.; Isikgor, F. H.; Ouyang, J. *Journal of Materials Science: Materials in Electronics* **2015**.

(54)

(55) Zhou, Y.; Fuentes-Hernandez, C.; Shim, J.; Meyer, J.; Giordano, A. J.; Li, H.; Winget, P.; Papadopoulos, T.; Cheun, H.; Kim, J.; Fenoll, M.; Dindar, A.; Haske, W.; Najafabadi, E.; Khan, T. M.; Sojoudi, H.; Barlow, S.; Graham, S.; Brédas, J.-L.; Marder, S. R.; Kahn, A.; Kippelen, B. *Science* **2012**, *336*, 327.

(56) Lin, Z.; Chang, J.; Zhang, J.; Jiang, C.; Wu, J.; Zhu, C. *Journal of Materials Chemistry A* **2014**, *2*, 7788.

(57) Brabec, C. J. *Solar Energy Materials and Solar Cells* **2004**, *83*, 273.

(58) McFarland, E. W. *Energy & Environmental Science* **2014**, *7*, 846.

(59) Scharber, M. C.; Sariciftci, N. S. *Prog Polym Sci* **2013**, *38*, 1929.

(60) Kirchartz, T.; Taretto, K.; Rau, U. *J. Phys. Chem. C* **2009**, *113*, 17958.

(61) Li, N.; Baran, D.; Spyropoulos, G. D.; Zhang, H.; Berny, S.; Turbiez, M.; Ameri, T.; Krebs, F. C.; Brabec, C. J. *Advanced Energy Materials* **2014**, *4*, n/a.

(62) Dennler, G.; Scharber, M. C.; Brabec, C. J. *Advanced Materials* **2009**, *21*, 1323.

(63) Jørgensen, M.; Norrman, K.; Gevorgyan, S. A.; Tromholt, T.; Andreasen, B.; Krebs, F. C. *Advanced Materials* **2012**, *24*, 580.

(64) Manceau, M.; Chambon, S.; Rivaton, A.; Gardette, J.-L.; Guillerez, S.; Lemaître, N. *Solar Energy Materials and Solar Cells* **2010**, *94*, 1572.

(65) Seemann, A.; Sauermann, T.; Lungenschmied, C.; Armbruster, O.; Bauer, S.; Egelhaaf, H. J.; Hauch, J. *Solar Energy* **2011**, *85*, 1238.

(66) Rivaton, A.; Tournebize, A.; Gaume, J.; Bussière, P.-O.; Gardette, J.-L.; Therias, S. *Polymer International* **2014**, *63*, 1335.

(67) Gardette, J.-L. *Handbook of Polymer Degradation, 2nd edn* **2000**, *1*, 671.

(68) Gardette, J.-L.; Mailhot, B.; Lemaire, J. *Polymer Degradation and Stability* **1995**, *48*, 457.

(69) Chambon, S.; Rivaton, A.; Gardette, J.-L.; Firon, M.; Lutsen, L. *Journal of Polymer Science Part A: Polymer Chemistry* **2007**, *45*, 317.

(70) Chambon, S.; Rivaton, A.; Gardette, J.-L.; Firon, M. *Polymer Degradation and Stability* **2011**, *96*, 1149.

(71) Manceau, M.; Bundgaard, E.; Carle, J. E.; Hagemann, O.; Helgesen, M.; Sondergaard, R.; Jorgensen, M.; Krebs, F. C. *Journal of Materials Chemistry* **2011**, *21*, 4132.

(72) Manceau, M.; Rivaton, A.; Gardette, J.-L.; Guillerez, S.; Lemaître, N. *Polymer Degradation and Stability* **2009**, *94*, 898.

(73) Manceau, M.; Gaume, J.; Rivaton, A.; Gardette, J.-L.; Monier, G.; Bideux, L. *Thin Solid Films* **2010**, *518*, 7113.

(74) Hintz, H.; Egelhaaf, H. J.; Lüer, L.; Hauch, J.; Peisert, H.; Chassé, T. *Chemistry of Materials* **2010**, *23*, 145.

(75) Hintz, H.; Sessler, C.; Peisert, H.; Egelhaaf, H. J.; Chassé, T. *Chemistry of Materials* **2012**, *24*, 2739.

(76) Tournebize, A.; Bussière, P.-O.; Wong-Wah-Chung, P.; Thérias, S.; Rivaton, A.; Gardette, J.-L.; Beaupré, S.; Leclerc, M. *Advanced Energy Materials* **2013**, *3*, 478.

(77) Fraga Domínguez, I.; Topham, P. D.; Bussiere, P.-O.; Bégué, D.; Rivaton, A. *The Journal of Physical Chemistry C* **2014**, 141219124027006.

(78) Koch, N. *physica status solidi (RRL) - Rapid Research Letters* **2012**, *6*, 277.

(79) He, C.; Germack, D. S.; Joseph Kline, R.; Delongchamp, D. M.; Fischer, D. A.; Snyder, C. R.; Toney, M. F.; Kushmerick, J. G.; Richter, L. J. *Solar Energy Materials and Solar Cells* **2011**, *95*, 1375.

(80) Manceau, M.; Rivaton, A.; Gardette, J.-L. *Macromolecular Rapid Communications* **2008**, *29*, 1823.

(81) Tromholt, T.; Madsen, M. V.; Carlé, J. E.; Helgesen, M.; Krebs, F. C. *Journal of Materials Chemistry* **2012**, *22*, 7592.

(82) Lloyd, M. T.; Peters, C. H.; Garcia, A.; Kauvar, I. V.; Berry, J. J.; Reese, M. O.; McGehee, M. D.; Ginley, D. S.; Olson, D. C. *Solar Energy Materials and Solar Cells* **2011**, *95*, 1382.

(83) Dupuis, A.; Wong-Wah-Chung, P.; Rivaton, A.; Gardette, J.-L. *Polymer Degradation and Stability* **2012**, *97*, 366.

(84) Tournebize, A.; Gardette, J.-L.; Taviot-Guého, C.; Bégué, D.; Arnaud, M. A.; Dagron-Lartigau, C.; Medlej, H.; Hiorns, R. C.; Beaupré, S.; Leclerc, M.; Rivaton, A. *Polymer Degradation and Stability* **2015**, *112*, 175.

(85) Kong, J.; Song, S.; Yoo, M.; Lee, G. Y.; Kwon, O.; Park, J. K.; Back, H.; Kim, G.; Lee, S. H.; Suh, H.; Lee, K. *Nature communications* **2014**, *5*, 5688.

(86) Mateker, W. R.; Douglas, J. D.; Cabanetos, C.; Sachs-Quintana, I. T.; Bartelt, J. A.; Hoke, E. T.; El Labban, A.; Beaujuge, P. M.; Frechet, J. M. J.; McGehee, M. D. *Energy & Environmental Science* **2013**, *6*, 2529.

(87) Taliani, C.; Ruani, G.; Zamboni, R.; Danieli, R.; Rossini, S.; Denisov, V. N.; Burlakov, V. M.; Negri, F.; Orlandi, G.; Zerbettob, F. *J. CHEM. SOC., CHEM. COMMUN.* **1993**, 220.

(88) Chambon, S.; Rivaton, A.; Gardette, J.-L.; Firon, M. *Solar Energy Materials and Solar Cells* **2007**, *91*, 394.

(89) Reese, M. O.; Nardes, A. M.; Rupert, B. L.; Larsen, R. E.; Olson, D. C.; Lloyd, M. T.; Shaheen, S. E.; Ginley, D. S.; Rumbles, G.; Kopidakis, N. *Advanced Functional Materials* **2010**, *20*, 3476.

(90) Distler, A.; Kutka, P.; Sauermann, T.; Egelhaaf, H.-J.; Guldi, D. M.; Di Nuzzo, D.; Meskers, S. C. J.; Janssen, R. A. J. *Chemistry of Materials* **2012**, *24*, 4397.

(91) Razzell-Hollis, J.; Wade, J.; Tsoi, W. C.; Soon, Y.; Durrant, J.; Kim, J.-S. *J. Mater. Chem. A* **2014**, *2*, 20189.

(92) W, O. *Lehrbuch der Allgemeinen Chemie* **1896**, *2*.

(93) Wantz, G.; Derue, L.; Dautel, O.; Rivaton, A.; Hudhomme, P.; Dagron-Lartigau, C. *Polymer International* **2014**, *63*, 1346.

(94) Müller, C. *Chemistry of Materials* **2015**, *27*, 2740.

(95) Miyanishi, S.; Tajima, K.; Hashimoto, K. *Macromolecules* **2009**, *42*, 1610.

(96) Kim, B. J.; Miyamoto, Y.; Ma, B.; Fréchet, J. M. J. *Advanced Functional Materials* **2009**, *19*, 2273.

(97) Derue, L.; Dautel, O.; Tournebize, A.; Drees, M.; Pan, H.; Berthumeyrie, S.; Pavageau, B.; Cloutet, E.; Chambon, S.; Hirsch, L.; Rivaton, A.; Hudhomme, P.; Facchetti, A.; Wantz, G. *Adv Mater* **2014**, *26*, 5831.

(98) Kanai, Y.; Matsushima, T.; Murata, H. *Thin Solid Films* **2009**, *518*, 537.

(99) Wang, M.; Tang, Q.; An, J.; Xie, F.; Chen, J.; Zheng, S.; Wong, K. Y.; Miao, Q.; Xu, J. *ACS Applied Materials & Interfaces* **2010**, *2*, 2699.

(100) Li, J.; Kim, S.; Edington, S.; Nedy, J.; Cho, S.; Lee, K.; Heeger, A. J.; Gupta, M. C.; Yates Jr, J. T. *Solar Energy Materials and Solar Cells* **2011**, *95*, 1123.

(101) Ferreira, S. R.; Lu, P.; Lee, Y.-J.; Davis, R. J.; Hsu, J. W. P. *The Journal of Physical Chemistry C* **2011**, *115*, 13471.

(102) Dupont, S. R.; Oliver, M.; Krebs, F. C.; Dauskardt, R. H. *Solar Energy Materials and Solar Cells* **2012**, *97*, 171.

(103) Dupont, S. R.; Voroshazi, E.; Heremans, P.; Dauskardt, R. H. *Organic Electronics* **2013**, *14*, 1262.

(104) Kesters, J.; Kudret, S.; Bertho, S.; Van den Brande, N.; Defour, M.; Van Mele, B.; Penxten, H.; Lutsen, L.; Manca, J.; Vanderzande, D.; Maes, W. *Organic Electronics* **2014**, *15*, 549.

(105) Silva, H. S.; Tournebize, A.; Bégué, D.; Peisert, H.; Chassé, T.; Gardette, J. L.; Therias, S.; Rivaton, A.; Hiorns, R. C. *RSC Adv.* **2014**, *4*, 54919.

(106) Chambon, S.; Rivaton, A.; Gardette, J.-L.; Firon, M. *Journal of Polymer Science Part A: Polymer Chemistry* **2009**, *47*, 6044.

(107) Aygul, U.; Egelhaaf, H. J.; Nagel, P.; Merz, M.; Schuppler, S.; Eichele, K.; Peisert, H.; Chasse, T. *Chemphyschem* **2014**.

(108) Manceau, M.; Helgesen, M.; Krebs, F. C. *Polymer Degradation and Stability* **2010**, *95*, 2666.

(109) Morse, G. E.; Tournebize, A.; Rivaton, A.; Chasse, T.; Taviot-Gueho, C.; Blouin, N.; Lozman, O. R.; Tierney, S. *Physical chemistry chemical physics : PCCP* **2015**, *17*, 11884.

(110) Avram, M.; Mateescu, G. D. *Editura Tehnica: Bucuresti* **1966**.

(111) Lin-Vien, D.; Colthup, N. B.; Fateley, W. G.; Grasselli, J. G. *Academic Press: San Diego* **1991**.

(112) Dupuis, A.; Wong-Wah-Chung, P.; Rivaton, A.; Gardette, J.-L. *Polymer Degradation and Stability* **2012**, *93*, 366.

(113) Noriega, R.; Rivnay, J.; Vandewal, K.; Koch, F. P.; Stingelin, N.; Smith, P.; Toney, M. F.; Salleo, A. *Nature materials* **2013**, *12*, 1038.

(114) Hopkinson, P. E.; Staniec, P. A.; Pearson, A. J.; Dunbar, A. D. F.; Wang, T.; Ryan, A. J.; Jones, R. A. L.; Lidzey, D. G.; Donald, A. M. *Macromolecules* **2011**, *44*, 2908.

(115) Flores, F.; Abad, E.; Martinez, J. I.; Pieczyrak, B.; Ortega, J. *Journal of physics. Condensed matter : an Institute of Physics journal* **2013**, *25*, 094007.

(116) Bergqvist, J.; Lindqvist, C.; Bäcke, O.; Ma, Z.; Tang, Z.; Tress, W.; Gustafsson, S.; Wang, E.; Olsson, E.; Andersson, M. R.; Inganäs, O.; Müller, C. *J. Mater. Chem. A* **2014**, *2*, 6146.

(117) Liem, H.; Cabanillas-Gonzalez, J.; Etchegoin, P.; Bradley, D. D. C. *Journal of Physics: Condensed Matter* **2004**, *16*, 721.

(118) Liem, H. *Journal of Physics: Condensed Matter* **2007**, *19*, 416106.

(119)

(120) Liu, D.; Osuna Orozco, R.; Wang, T. *Physical Review E* **2013**, *88*.

(121) Kim, J.-H.; Lee, M.; Yang, H.; Hwang, D.-H. *Journal of Materials Chemistry A* **2014**, *2*, 6348.

(122) Dou, L.; Gao, J.; Richard, E.; You, J.; Chen, C. C.; Cha, K. C.; He, Y.; Li, G.; Yang, Y. *Journal of the American Chemical Society* **2012**, *134*, 10071.

(123) White, M. S.; Olson, D. C.; Shaheen, S. E.; Kopidakis, N.; Ginley, D. S. *Applied Physics Letters* **2006**, *89*, 143517.

(124) Cardona, C. M.; Li, W.; Kaifer, A. E.; Stockdale, D.; Bazan, G. C. *Adv Mater* **2011**, *23*, 2367.

(125) Hau, S. K.; Yip, H.-L.; Baek, N. S.; Zou, J.; O'Malley, K.; Jen, A. K. Y. *Applied Physics Letters* **2008**, *92*, 253301.

(126) Wienk, M. M.; Turbiez, M.; Gilot, J.; Janssen, R. A. J. *Advanced Materials* **2008**, *20*, 2556.

(127) Jung, J. W.; Jo, J. W.; Liu, F.; Russell, T. P.; Jo, W. H. *Chemical communications* **2012**, *48*, 6933.

(128) Li, Z.; Zhang, Y.; Tsang, S.-W.; Du, X.; Zhou, J.; Tao, Y.; Ding, J. *The Journal of Physical Chemistry C* **2011**, *115*, 18002.

(129) Scharber, M. C.; Mühlbacher, D.; Koppe, M.; Denk, P.; Waldauf, C.; Heeger, A. J.; Brabec, C. J. *Advanced Materials* **2006**, *18*, 789.

(130) Stevens, D. M.; Speros, J. C.; Hillmyer, M. A.; Frisbie, C. D. *The Journal of Physical Chemistry C* **2011**, *115*, 20806.

(131) Eklund, P. C.; Rao, A. M.; Zhou, P.; Wang, Y.; Holden, J. M. *Thin Solid Films* **1995**, *257*, 185.

(132) Li, Z.; Wong, H. C.; Huang, Z.; Zhong, H.; Tan, C. H.; Tsoi, W. C.; Kim, J. S.; Durrant, J. R.; Cabral, J. T. *Nature communications* **2013**, *4*, 2227.

(133) Piersimoni, F.; Degutis, G.; Bertho, S.; Vandewal, K.; Spoltore, D.; Vangerven, T.; Drijkoningen, J.; Van Bael, M. K.; Hardy, A.; D'Haen, J.; Maes, W.; Vanderzande, D.; Nesladek, M.; Manca, J. *Journal of Polymer Science Part B: Polymer Physics* **2013**, *51*, 1209.

(134) Distler, A.; Sauermann, T.; Egelhaaf, H.-J.; Rodman, S.; Waller, D.; Cheon, K.-S.; Lee, M.; Guldi, D. M. *Advanced Energy Materials* **2014**, *4*, n/a.

(135) Nichols, J. B. *J. Appl. Phys.* **1954**, *25*, 840.

(136) Li, W.; Hendriks, K. H.; Furlan, A.; Roelofs, W. S.; Wienk, M. M.; Janssen, R. A. *Journal of the American Chemical Society* **2013**, *135*, 18942.

(137) Yang, X.; Alexeev, A.; Michels, M. A. J.; Loos, J. *Macromolecules* **2005**, *38*, 4289.

(138) Treat, N. D.; Brady, M. A.; Smith, G.; Toney, M. F.; Kramer, E. J.; Hawker, C. J.; Chabinyc, M. L. *Advanced Energy Materials* **2011**, *1*, 82.

(139) Conings, B.; Bertho, S.; Vandewal, K.; Senes, A.; D'Haen, J.; Manca, J.; Janssen, R. A. J. *Applied Physics Letters* **2010**, *96*, 163301.

(140) Schaffer, C. J.; Palumbiny, C. M.; Niedermeier, M. A.; Jendrzejewski, C.; Santoro, G.; Roth, S. V.; Muller-Buschbaum, P. *Adv Mater* **2013**, *25*, 6760.

(141) Müller, C.; Bergqvist, J.; Vandewal, K.; Tvingstedt, K.; Anselmo, A. S.; Magnusson, R.; Alonso, M. I.; Moons, E.; Arwin, H.; Campoy-Quiles, M.; Inganäs, O. *Journal of Materials Chemistry* **2011**, *21*, 10676.

(142) Vandenbergh, J.; Conings, B.; Bertho, S.; Kesters, J.; Spoltore, D.; Esiner, S.; Zhao, J.; Van Assche, G.; Wienk, M. M.; Maes, W.; Lutsen, L.; Van Mele, B.; Janssen, R. A. J.; Manca, J.; Vanderzande, D. J. M. *Macromolecules* **2011**, *44*, 8470.

(143) Kohn, P.; Rong, Z.; Scherer, K. H.; Sepe, A.; Sommer, M.; Müller-Buschbaum, P.; Friend, R. H.; Steiner, U.; Hüttner, S. *Macromolecules* **2013**, *46*, 4002.

(144) Peters, C. H.; Sachs-Quintana, I. T.; Mateker, W. R.; Heumueller, T.; Rivnay, J.; Noriega, R.; Beiley, Z. M.; Hoke, E. T.; Salleo, A.; McGehee, M. D. *Adv Mater* **2012**, *24*, 663.

(145) Sachs-Quintana, I. T.; Heumüller, T.; Mateker, W. R.; Orozco, D. E.; Cheacharoen, R.; Sweetnam, S.; Brabec, C. J.; McGehee, M. D. *Advanced Functional Materials* **2014**, *24*, 3978.

(146) Kouijzer, S.; Michels, J. J.; van den Berg, M.; Gevaerts, V. S.; Turbiez, M.; Wienk, M. M.; Janssen, R. A. J. *Journal of the American Chemical Society* **2013**, *135*, 12057.

(147) Nilsson, S.; Bernasik, A.; Budkowski, A.; Moons, E. *Macromolecules* **2007**, *40*, 8291.

(148) Ruiz, R.; Choudhary, D.; Nickel, B.; Toccoli, T.; Chang, K.-C.; Mayer, A. C.; Clancy, P.; Blakely, J. M.; Headrick, R. L.; Iannotta, S.; Malliaras, G. G. *Chem. Mater.* **2004**, *16*, 4497.

(149) Nguyen, L. H.; Hoppe, H.; Erb, T.; Günes, S.; Gobsch, G.; Sariciftci, N. S. *Advanced Functional Materials* **2007**, *17*, 1071.

(150) Cherdhirankorn, T.; Harmandaris, V.; Juhari, A.; Voudouris, P.; Fytas, G.; Kremer, K.; Koynov, K. *Macromolecules* **2009**, *42*, 4858.

(151) Kunal, K.; Robertson, C. G.; Pawlus, S.; Hahn, S. F.; Sokolov, A. P. *Macromolecules* **2008**, *41*, 7232.

(152) Duda, J. L. *Pure Appl. Chem.* **1985**, *57*, 1681.

(153) Yiu, A. T.; Beaujuge, P. M.; Lee, O. P.; Woo, C. H.; Toney, M. F.; Frechet, J. M. *Journal of the American Chemical Society* **2012**, *134*, 2180.

(154) Li, Z.; Tsang, S.-W.; Du, X.; Scoles, L.; Robertson, G.; Zhang, Y.; Toll, F.; Tao, Y.; Lu, J.; Ding, J. *Advanced Functional Materials* **2011**, *21*, 3331.

(155) Jiang, J.-M.; Lin, H.-K.; Lin, Y.-C.; Chen, H.-C.; Lan, S.-C.; Chang, C.-K.; Wei, K.-H. *Macromolecules* **2014**, *47*, 70.

(156) Tournebize, A.; Rivaton, A.; Peisert, H.; Chassé, T. *The Journal of Physical Chemistry C* **2015**, *119*, 9142.

(157) Li, G.; Zhu, R.; Yang, Y. *Nature Photonics* **2012**, *6*, 153.

(158) Alam, M. A.; Ray, B.; Khan, M. R.; Dongaonkar, S. *Journal of Materials Research* **2013**, *28*, 541.

(159) Mikhnenko, O. V.; Azimi, H.; Scharber, M.; Morana, M.; Blom, P. W. M.; Loi, M. A. *Energy & Environmental Science* **2012**, *5*, 6960.

(160) Gulbinas, V.; Mineviciute, I.; Hertel, D.; Wellander, R.; Yartsev, A.; Sundstrom, V. *The Journal of chemical physics* **2007**, *127*, 144907.

(161) Pivrikas, A.; Neugebauer, H.; Sariciftci, N. S. *Solar Energy* **2011**, *85*, 1226.

(162) Wang, E.; Ma, Z.; Zhang, Z.; Vandewal, K.; Henriksson, P.; Inganas, O.; Zhang, F.; Andersson, M. R. *Journal of the American Chemical Society* **2011**, *133*, 14244.

(163) Guo, X.; Zhou, N.; Lou, S. J.; Hennek, J. W.; Ponce Ortiz, R.; Butler, M. R.; Boudreault, P. L.; Strzalka, J.; Morin, P. O.; Leclerc, M.; Lopez Navarrete, J. T.; Ratner, M. A.; Chen, L. X.; Chang, R. P.; Facchetti, A.; Marks, T. J. *Journal of the American Chemical Society* **2012**, *134*, 18427.

(164) Li, W.; Zhou, Y.; Viktor Andersson, B.; Mattias Andersson, L.; Thomann, Y.; Veit, C.; Tvingstedt, K.; Qin, R.; Bo, Z.; Inganäs, O.; Würfel, U.; Zhang, F. *Organic Electronics* **2011**, *12*, 1544.

(165) Schmidt, K.; Tassone, C. J.; Niskala, J. R.; Yiu, A. T.; Lee, O. P.; Weiss, T. M.; Wang, C.; Fréchet, J. M. J.; Beaujuge, P. M.; Toney, M. F. *Advanced Materials* **2014**, *26*, 300.

(166) De Sio, A.; Madena, T.; Huber, R.; Parisi, J.; Neyshtadt, S.; Deschler, F.; Da Como, E.; Esposito, S.; von Hauff, E. *Solar Energy Materials and Solar Cells* **2011**, *95*, 3536.

(167) Liao, H.-C.; Ho, C.-C.; Chang, C.-Y.; Jao, M.-H.; Darling, S. B.; Su, W.-F. *Materials Today* **2013**, *16*, 326.

(168) Chang, L.; Lademann, H. W. A.; Bonekamp, J.-B.; Meerholz, K.; Moulé, A. J. *Advanced Functional Materials* **2011**, *21*, 1779.

(169) Heo, S. W.; Baek, K. H.; Lee, T. H.; Lee, J. Y.; Moon, D. K. *Organic Electronics* **2013**, *14*, 1629.

(170) Dupuis, A.; Tournebize, A.; Bussière, P.-O.; Rivaton, A.; Gardette, J.-L. *The European Physical Journal - Applied Physics* **2011**, *56*, null.

(171) Lilliu, S.; Agostinelli, T.; Pires, E.; Hampton, M.; Nelson, J.; Macdonald, J. E. *Macromolecules* **2011**, *44*, 2725.

(172) Ma, W.; Yang, C.; Gong, X.; Lee, K.; Heeger, A. J. *Advanced Functional Materials* **2005**, *15*, 1617.

(173) Deschler, F.; De Sio, A.; von Hauff, E.; Kutka, P.; Sauermann, T.; Egelhaaf, H.-J.; Hauch, J.; Da Como, E. *Advanced Functional Materials* **2012**, *22*, 1461.

(174) Liu, H.-W.; Chang, D.-Y.; Chiu, W.-Y.; Rwei, S.-P.; Wang, L. *Journal of Materials Chemistry* **2012**, *22*, 15586.

(175) Mahadevapuram, R. C.; Carr, J. A.; Chen, Y.; Bose, S.; Nalwa, K. S.; Petrich, J. W.; Chaudhary, S. *Synthetic Metals* **2013**, *185-186*, 115.

(176) Gryn'ova, G.; Ingold, K. U.; Coote, M. L. *Journal of the American Chemical Society* **2012**, *134*, 12979.

(177) Sinturel, C.; Lemaire, J.; Gardette, J.-L. *European Polymer Journal* **2000**, *36*, 1431.

(178) Turner, S. T.; Pingel, P.; Steyrleuthner, R.; Crossland, E. J. W.; Ludwigs, S.; Neher, D. *Advanced Functional Materials* **2011**, *21*, 4640.

(179) Zeng, H.; Zhu, X.; Liang, Y.; Guo, X. *Polymers* **2015**, *7*, 333.

(180) Kolacyak, D.; Peisert, H.; Chassé, T. *Applied Physics A* **2008**, *95*, 173.

(181) Turkovic, V.; Engmann, S.; Tsierkezos, N.; Hoppe, H.; Ritter, U.; Gobsch, G. *ACS Appl Mater Interfaces* **2014**, *6*, 18525.

(182) Watts, B.; Belcher, W. J.; Thomsen, L.; Ade, H.; Dastoor, P. C. *Macromolecules* **2009**, *42*, 8392.

(183) Rumer, J. W.; McCulloch, I. *Materials Today* **2015**, *18*, 425.

(184) Griffini, G.; Douglas, J. D.; Piliego, C.; Holcombe, T. W.; Turri, S.; Frechet, J. M.; Mynar, J. L. *Adv Mater* **2011**, *23*, 1660.

(185) Khiev, S.; Derue, L.; Ayenew, G.; Medlej, H.; Brown, R.; Rubatat, L.; Hiorns, R. C.; Wantz, G.; Dagron-Lartigau, C. *Polymer Chemistry* **2013**, *4*, 4145.

(186) Png, R.-Q.; Chia, P.-J.; Tang, J.-C.; Liu, B.; Sivaramakrishnan, S.; Zhou, M.; Khong, S.-H.; Chan, H. S. O.; Burroughes, J. H.; Chua, L.-L.; Friend, R. H.; Ho, P. K. H. *Nature materials* **2010**, *9*, 152.

(187) Oklobia, O.; Shafai, T. S. *Solar Energy Materials and Solar Cells* **2013**, *117*, 1.

(188) Jørgensen, M.; Norrman, K.; Krebs, F. C. *Solar Energy Materials and Solar Cells* **2008**, *92*, 686.

(189) Kawano, K.; Pacios, R.; Poplavskyy, D.; Nelson, J.; Bradley, D. D. C.; Durrant, J. R. *Solar Energy Materials and Solar Cells* **2006**, *90*, 3520.

(190) Xu, Z.; Chen, L.-M.; Chen, M.-H.; Li, G.; Yang, Y. *Applied Physics Letters* **2009**, *95*, 013301.

(191) Aygül, U.; Hintz, H.; Egelhaaf, H.-J.; Distler, A.; Abb, S.; Peisert, H.; Chassé, T. *The Journal of Physical Chemistry C* **2013**, *117*, 4992.

(192) Greczynski, G.; Kugle, T.; Keil, M.; Osikowicz, W.; Fahlman, M.; Salaneck, W. R. *Journal of Electron Spectroscopy and Related Phenomena* **2001**, *121*, 1.

(193) Greczynski, G.; Kugler, T.; Salaneck, W. R. *Thin Solid Films* **1999**, *354*, 129.

(194) Kim, Y. H.; Sachse, C.; Machala, M. L.; May, C.; Müller-Meskamp, L.; Leo, K. *Advanced Functional Materials* **2011**, *21*, 1076.

(195) Hwang, J.; Amy, F.; Kahn, A. *Organic Electronics* **2006**, *7*, 387.

(196) Wong, H. C.; Li, Z.; Tan, C. H.; Zhong, H.; Huang, Z.; Bronstein, H.; McCulloch, I.; Cabral, J. T.; Durrant, J. R. *ACS Nano* **2014**, *8*, 1297.

(197) Knupfer, M.; Peisert, H. *Phys Status Solidi A* **2004**, *201*, 1055.

(198) Braun, S.; Salaneck, W. R.; Fahlman, M. *Advanced Materials* **2009**, *21*, 1450.

(199) Hwang, J.; Wan, A.; Kahn, A. *Materials Science and Engineering: R: Reports* **2009**, *64*, 1.

(200) Oehzelt, M.; Koch, N.; Heimel, G. *Nature communications* **2014**, *5*, 4174.

(201) Bao, Q.; Sandberg, O.; Dagnelund, D.; Sandén, S.; Braun, S.; Aarnio, H.; Liu, X.; Chen, W. M.; Österbacka, R.; Fahlman, M. *Advanced Functional Materials* **2014**, *24*, 6309.

(202) Cho, S.; Kim, K. D.; Heo, J.; Lee, J. Y.; Cha, G.; Seo, B. Y.; Kim, Y. D.; Kim, Y. S.; Choi, S. Y.; Lim, D. C. *Scientific reports* **2014**, *4*, 4306.

(203) Xu, Z.; Chen, L.-M.; Yang, G.; Huang, C.-H.; Hou, J.; Wu, Y.; Li, G.; Hsu, C.-S.; Yang, Y. *Advanced Functional Materials* **2009**, *19*, 1227.

(204) Wolski, K.; Szuwarzyński, M.; Zapotoczny, S. *Chem. Sci.* **2015**, *6*, 1754.

(205) Schulz, P.; Kelly, L. L.; Winget, P.; Li, H.; Kim, H.; Ndione, P. F.; Sigdel, A. K.; Berry, J. J.; Graham, S.; Brédas, J.-L.; Kahn, A.; Monti, O. L. A. *Advanced Functional Materials* **2014**, *24*, 7381.

(206) Schlaf, R.; Murata, H.; Kafafi, Z. H.; Babatope, B. *Journal of Electron Spectroscopy and Related Phenomena* **2001**, *120*, 149.

(207) Heremans, P. L.; de Boer, B.; Hadipour, A.; Foekema, R.; van Woudenbergh, T.; Mandoc, M. M.; Mihailetchi, V. D.; Blom, P. W. M.; Muccini, M.; Hofstraat, H. **2004**, *5464*, 18.

(208) Lange, I.; Reiter, S.; Pätzel, M.; Zykov, A.; Nefedov, A.; Hildebrandt, J.; Hecht, S.; Kowarik, S.; Wöll, C.; Heimel, G.; Neher, D. *Advanced Functional Materials* **2014**, *24*, 7014.

(209) Sharma, A.; Hotchkiss, P. J.; Marder, S. R.; Kippelen, B. *Journal of Applied Physics* **2009**, *105*, 084507.

(210) Zhou, Y.; Li, F.; Barrau, S.; Tian, W.; Inganäs, O.; Zhang, F. *Solar Energy Materials and Solar Cells* **2009**, *93*, 497.

(211) Jo, G.; Na, S.-I.; Oh, S.-H.; Lee, S.; Kim, T.-S.; Wang, G.; Choe, M.; Park, W.; Yoon, J.; Kim, D.-Y.; Kahng, Y. H.; Lee, T. *Applied Physics Letters* **2010**, *97*, 213301.

(212) Mao, H. Y.; Wang, R.; Huang, H.; Wang, Y. Z.; Gao, X. Y.; Bao, S. N.; Wee, A. T. S.; Chen, W. *Journal of Applied Physics* **2010**, *108*, 053706.

(213) Peters, C. H.; Sachs-Quintana, I. T.; Kastrop, J. P.; Beaupré, S.; Leclerc, M.; McGehee, M. D. *Advanced Energy Materials* **2011**, *1*, 491.

(214) Heumueller, T.; Mateker, W. R.; Sachs-Quintana, I. T.; Vandewal, K.; Bartelt, J. A.; Burke, T. M.; Ameri, T.; Brabec, C. J.; McGehee, M. D. *Energy & Environmental Science* **2014**, *7*, 2974.

(215) Beamson, G.; Briggs, D. *The Scienta ESCA300 Database* **1992**.

(216) Zhang, X.; Qin, J.; Xue, Y.; Yu, P.; Zhang, B.; Wang, L.; Liu, R. *Scientific reports* **2014**, *4*, 4596.

(217) Stevens, J. S.; Byard, S. J.; Seaton, C. C.; Sadiq, G.; Davey, R. J.; Schroeder, S. L. *Physical chemistry chemical physics : PCCP* **2014**, *16*, 1150.

(218) Topolniak, I.; Gardette, J.-L.; Therias, S. *Polymer Degradation and Stability* **2015**, *121*, 137.

(219) Gaume, J.; Rivaton, A.; Thérias, S.; Gardette, J.-L. *Polymer Degradation and Stability* **2012**, *97*, 488.

(220) Gaume, J.; Wong-Wah-Chung, P.; Rivaton, A.; Thérias, S.; Gardette, J.-L. *RSC Advances* **2011**, *1*, 1471.

Appendix

A1. Experimental techniques 217

A1.1. Thin film processing 217

A1.2. Degradation conditions 218

A1.3. Spectroscopy, general aspects 219

A1.4. Photoemission spectroscopy 219

A1.5. UV-visible spectroscopy 224

A1.6. Infrared spectroscopy 225

A1.7. Raman spectroscopy 226

A1.8. Atomic Force Microscopy 228

A2. Appendix of Chapter 2 229

A2.1. UV-vis and IR spectra of pristine P1-9 polymer films 229

A2.2. IR spectra of pristine P1-9 polymers and blend films (PX:PC$_{60}$BM, 1:2) 229

A2.3. IR spectra of the P1-9 polymer films during photodegradation 230-232

A2.4. UV-vis spectra of the P1-9 polymers during photodegradation 233

A2.5. UV-vis spectra of P1-6 polymer blends during photodegradation 234

A2.6. Raman spectra of pristine P1-6 polymer and blend films 235

A2.7. Raman spectra of P1 as function of the temperature.. 235

A2.8. UV-vis spectra of P1:PC$_{60}$BM (1:2) in the PC$_{60}$BM absorbance region... 236

A2.9. IR spectra of P1-6 polymer blends before and after light exposure... 236

A3. Appendix of Chapter 3 237

A3.1. IR spectra of CB, ODT and DIO exposed in air and dark at 45-50°C. 237

A3.2. IR spectra of CB, ODT and DIO exposed to light in air and at 45-50°C. 237

A3.3. Evolution of IR modes of ODT, DIO and CB exposed to the dark or light. 238

A3.4. IR spectra of ODT under different types of exposures in air 238

A3.5. IR spectra of T765, T65/P3HT and T765/PC$_{60}$BM under pgotooxidation 239

A4. Appendix of Chapter 4 240

A4.1. AFM images of individual material 240-241

A5. Appendix of Chapter 5 242

A5.1. Summary of the evolution of energetic levels as function of C60 evaporation. 242

A5.2. AFM images and profiles before and after C60 evaporation 242

A5.3. UPS spectra of ITO/PEI and ZnO before and after thermal exposure.. 242

A5.4-5-6. XPS spectra of ITO/PEI/AL and ZnO/AL after thermal or light exposure and after the removal of the active layer.. 244-246

Bibliography 247

A1. Experimental techniques

A1.1. Thin film processing

The thickness and morphology of active layers depend of the thin film fabrication and are directly linked to the device performance. Therefore, the selection of the technique and parameters are important to consider for certain scientific investigations. Additionally, different substrates can be used for performing various analyses and it is important to note that the surface energy and roughness of the substrate can also impact the film formation in particular the vertical composition of the polymer blends. F. C. Krebs recently published a review on the fabrication and processing techniques used in OPV.[1]

In the present work, thin films were prepared at different places and the techniques available were not the same. Thus, different techniques or parameters were used from studies to studies. However, inside each investigation, the same technique, parameters and substrates were used in order to obtain reliable results. The technique and substrate used in each investigation are specified in the *Experimental* part.

The polymer blend solution is deposited on the substrate as shown in **Figure A1.1** (step 1). The solution covers fully the substrate for the spin coating process (left) while the solution is inserted between the blade and the substrate in the case of blade casting (right). A large amount of the solution and materials are wasted during the step 2 for the spin coating. The step 3 is the drying process with the evaporation of the solvent. Once dried, the solid film is formed (step 4).

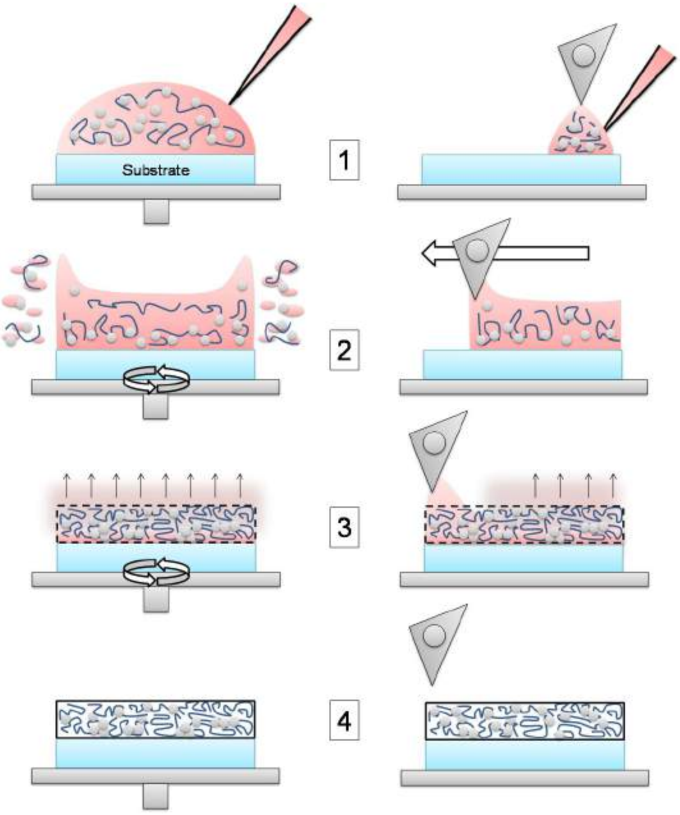

Figure A1.1 - General principles of spin coating and blade casting techniques.

A1.2. Degradation conditions

Organic materials are sensitive to outdoor conditions and therefore it is important to control and report the degradation conditions. The different investigations were carried out at different places or in collaboration with different groups and therefore different setups or degradation conditions were used. In this regard, *"Consensus stability testing protocols for organic photovoltaic materials"* has been published recently and categories different degradation conditions in order to provide standards that the different scientific groups can refer.[2] Please note that in the present work, all the degraded samples and devices were not encapsulated. Depending of the study, various degradation conditions were chosen. (See **Table A1.1**)

Name	**L-0**	**ISOS-L-1**	**T-X**	**ISOS-D-3**
Light source	Simulator	Simulator	None	None
Temperature	Ambient	Ambient	50[a]/100[b]/120/[b]140°C[c]	85°C
Humidity	Ambient	Nitrogen GV	Nitrogen GV	85%
Atmosphere	Air	Nitrogen GV	Nitrogen GV	Air
Involved in	**2.2/3.2/3.3**	**2.4/5.3**	**2.4[a]/3.4[b,c]/5.3[c]**	**4.3**

Table A1.1 - Degradation conditions used in the present manuscript.

The L-0 protocol does not belong to the ISOS protocol but was used in the present work to investigate the stability of the pi-conjugated polymers and blends submitted to light in ambient air, in other words submitted to photooxidative conditions. The humidity was measured and was about 30-40% rH. Xenon lamps were used as light sources and due to the light exposure, the temperature of exposition was about 45°C.

ISOS-L-1 is a laboratory weathering testing protocol and in the present work, samples were irradiated in inert atmosphere (glove box, low humidity and oxygen content) and Xenon lamps were used as light source in the AM1.5 conditions. Due to the light exposure, the temperature of exposition was about 45°C. This degradation protocol was used in Chapter 2 (**2.4**) and Chapter 5 (**5.3**).

ISOS-D-3 is a dark storage and also known as damp heat. The samples were kept in an environmental chamber where the temperature and humidity were fixed to 85°C and 85% rH respectively. This protocol was applied in particular for testing the adhesion properties of the devices in Chapter 4 (**4.3**).

Finally, for testing selectively the thermal resistance of pi-conjugated polymer blends and devices, samples were placed on hot plate in inert atmosphere (glove box) and in the dark at different temperatures, depending of the study. (T-X protocol) Thus, the thermal stability of devices in Chapter 2 (**2.4**) and Chapter 5 (**5.3**) were tested at 50 and 140°C respectively. In Chapter 3 (**3.4**), the polymer blends and devices were exposed to 100, 120 and 140 °C.

A1.3. Spectroscopy, general aspects

Spectroscopy is the study of the interaction between electromagnetic radiation and matter. **Figure A1.2** shows the different radiation/matter interactions depending of the incident radiation wavelength. X-ray and certain UV photons have enough energy to eject electrons from the core levels (X-rays) or the valence region (UV). This process is called photoionization. Photons of the UV-vis region can promote electrons from occupied states to excited states. The absorption of IR photons leads to vibrational transitions. From these various photon/matter interactions, different methods were developed in the past for characterizing materials in order to extract different information concerning the investigated material. (**Table A1.1**)

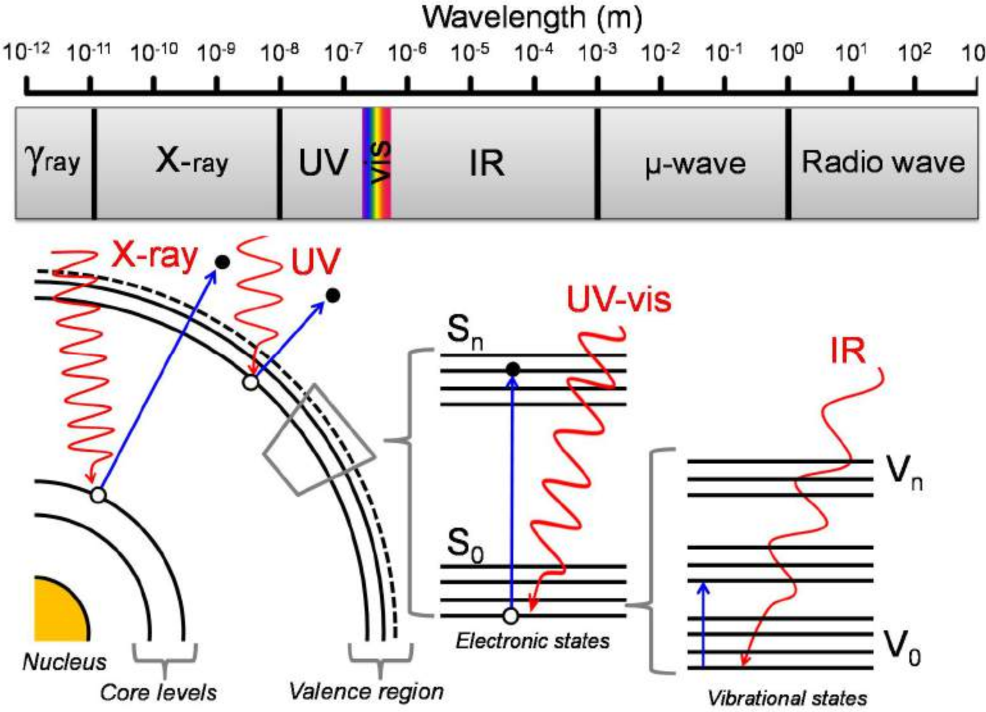

Figure A1.2 - Illustration of the different interactions of electromagnetic radiation with matter.

	Interaction	Information	Conditions	Specificity
XPS	Photoionization	Chemical composition, environment, electronic structure	UHV	Surface sensitive
UPS	Photoionization	Valence bands, work function, electronic structure, energy level alignments	UHV	Surface sensitive
UV-vis	Electronic transitions	Absorbance	Air/controlled atm.	Transmission
IR	Vibrational transitions	Chemical structure	Air/controlled atm.	Transmission
Raman	Vibrational and electronic transitions	Chemical structure	Air/controlled atm.	Bulk of thin film

Table A1.1 – Summary of the spectroscopic techniques involved in the present work.

A1.4. Photoemission spectroscopy (PES: XPS and UPS)

The photoemission spectroscopy (PES) is based on the photoelectric effect where electrons of a material are photo-excited and if their kinetic energy is high enough, electrons can leave the material (in Ultra-High vacuum conditions, UHV) and can be detected. Therefore, PES provides information related to the occupied states only. X-ray and UV photoemission spectroscopy (XPS and UPS) used different photon energies: UV (10-100 eV) and X-ray (100 eV and above). Due to the short inelastic free mean path of the electrons in solids, XPS and UPS are surface sensitive techniques[3] (2-10 angstroms and few tens of angstroms or UPS and XPS respectively). A description of a PES experiment is given in **Figure A1.3**.

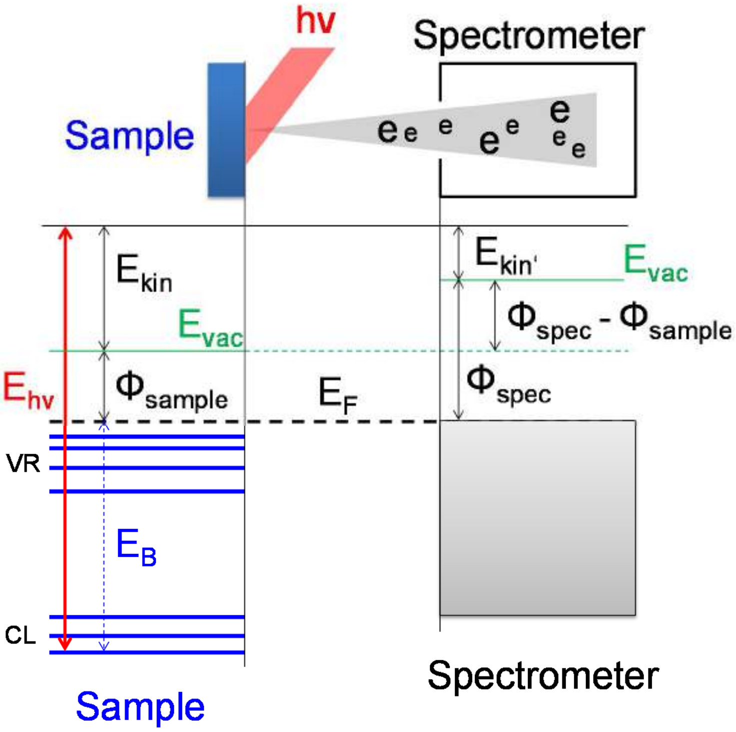

$$E_{kin'} = E_{kin} - (\Phi_{spec} - \Phi_{sample}) \quad (1)$$
$$E_B = E_{hv} - \Phi_{sample} - E_{kin} \quad (2)$$

Figure A1.3 – Energy level diagram for a sample in a PES experiment. When exposed to the beam (E_{hv}), electrons are photo-excited, emitted beyond the vacuum level (E_{vac}) with their kinetic energies (E_{kin}). The measured kinetic energies ($E_{kin'}$) take into account the work function of the spectrometer. The electron binding energy (EB) of a certain energy level is defined relative to the Fermi level (E_F) and can be determine with the equation 2. The work function (Φ) is the energy difference between the Fermi and vacuum level (E_{VAC}) and depends of the investigated sample and the spectrometer.

XPS enables the study of qualitative and even semi-quantitative analysis of chemical composition in the near surface of a sample in UHV conditions. **Figure A1.4** shows the XPS survey and the extracted chemical composition of the p-conjugated polymer poly[4,4′-bis(2-

ethylhexyl)dithieno[3,2-b:2′,3′-d]silole)-2,6-diyl-alt -[2,5-bis(3-tetradecylthiophen-2-yl)thiazole[5,4-d]thiazole)-1,8-diyl] (PCDTSTzTz). The main core levels of each element (C1s, S2p, N1s and Si2p for the carbon, sulfur, nitrogen and silicon atoms respectively) are displayed and their relative areas can be used with their respective sensitivity factors to determine the chemical composition of the investigated material.

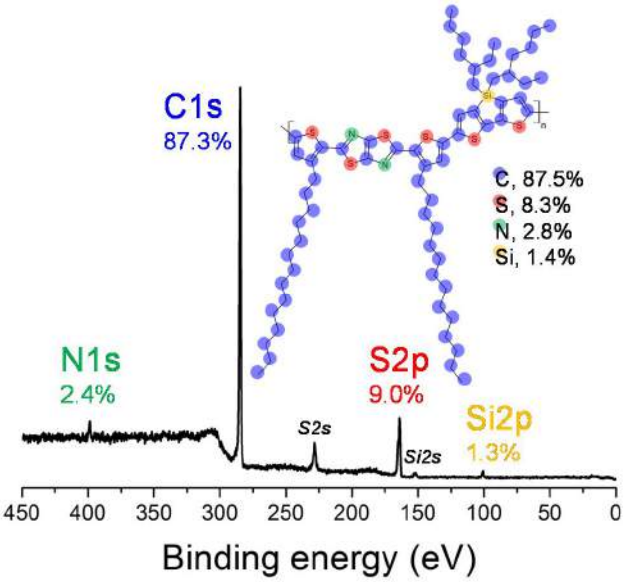

Figure A1.4 – XPS survey spectrum of the pi-conjugated polymer PCDTSTzTz. The theoretical chemical composition of the polymer is extracted from the expected chemical structure. The area of the main core levels (C1s, S2p, N1s and Si2p) of each element and their respective sensitivity factors can be used to estimate the atomic composition.

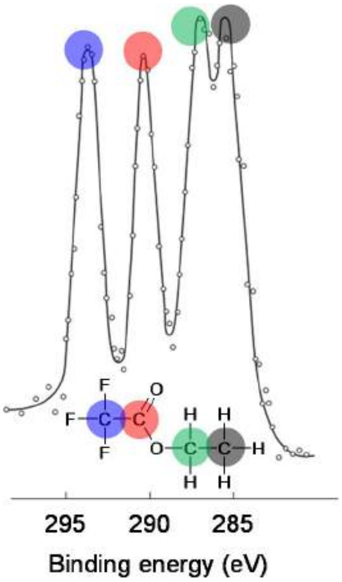

Figure A1.5 – The XPS C1s spectrum of ethyl trifluoroacetate showing the chemical shifts. Adapted from N.V. Alov.[4]

Beside the atomic composition, XPS can also provide information regarding the chemical environment. Indeed, the change in binding energy for a same type of atom (chemical shift) suggests that the neighboring of the atoms is chemically different. This is due to the fact that the neighboring chemical bounds influence locally the electrostatic potential which influences the electron kinetic energy. **Figure A1.5** is adapted from N.V. Alov[4] and illustrates this phenomenon. In this case, the electronegativity of the different neighboring atoms influences drastically the binding energy of the carbon atoms. A shift of the core levels of organic materials can be shifted when exposed to light and oxygen. A short exposure can induce a p-doping (thermally reversible) translated by a shift of the core levels.[5] A longer exposure induces the photooxidation of the material (irreversible, oxygen bounds) and the enrichment in oxygen content in the solid influence the measured kinetic energy of the core levels.

Finally, XPS can be also used to estimate the thickness of thin films. In the present work, we applied the equations in **Figure A1.6** when C60 molecules were deposited on the top of various substrates or to evaluate the layer thickness of PEI and residual organic compounds (Chapter 5, **5.3** and **5.4**). The method can be applied only when the signal of the substrate is still visible. In order to estimate the layer thickness, we need to know the electron free mean path (λ) in the investigated organic material. This latter can be estimated from the formula (3) extracted from the work of M.P. Seah and W.A. Dench.[3] Then, the free mean path is adapted by the formula (2) for being instead in the formula (1). The chemical composition (X) and senility factors (σ) are known and the intensities (I) of organic material and substrates are taken from the XPS spectrum. In the present work, $cos\theta$ is equal to 1.

$$d = \lambda . cos\theta . ln(1 + \frac{I_l . \sigma_S . X_S}{I_S . \sigma_l . X_l}) \qquad (1)$$

$$\lambda = \frac{\lambda_{ORG}}{\rho . 10^{-3}} \qquad (2)$$

$$\lambda_{ORG} = \frac{49}{E^2} + 0.11\sqrt{E} \qquad (3)$$

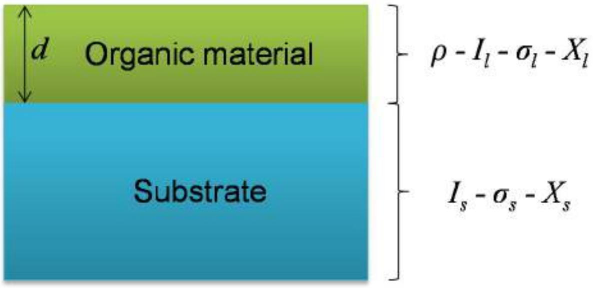

Figure A1.6 – Thickness estimation from the formula 1-3. d denotes the thickness of the organic layer (l), I is the signal intensity, σ is the sensitivity factor, X is the chemical composition, ρ is the density of the organic material and E is the kinetic energy of the considered signal.

The **Figure A1.3** is also valid for UPS except that the analyzed electrons are from the valence region (VR) and have low kinetic energies. When the kinetic energy is not high enough to reach the spectrometer ($E_{kin} < \Phi_{spec}$-Φ_{sample}), an additional bias to overcome this potential barrier is applied. UPS is a powerful tool to investigate the electronic structure of materials but also the energy level alignments at interfaces. **Figure A1.7** shows the most important electronic levels in the case of a conductive substrate/organic interface and illustrates how the energy levels are extracted from UPS spectra. The ZnO/C60 was chosen as example. Two parts of UPS spectra can be discussed separately: the first one is the valence band (VB) region where the valence band of a metal or valence orbitals such as HOMO are directly visible. The second part is the secondary electron cut-off (SECO) where the vacuum level (E_{vac}) and work function (WF) can be extracted considering the energy of the incident light. Several models were established in order to explain the experimental results concerning the energy level alignments. (Refer to Chapter 5, 5.1.1). Also, for deeper information on the PES and ELA in organic electronics, refer to these recent reviews. [6-10]

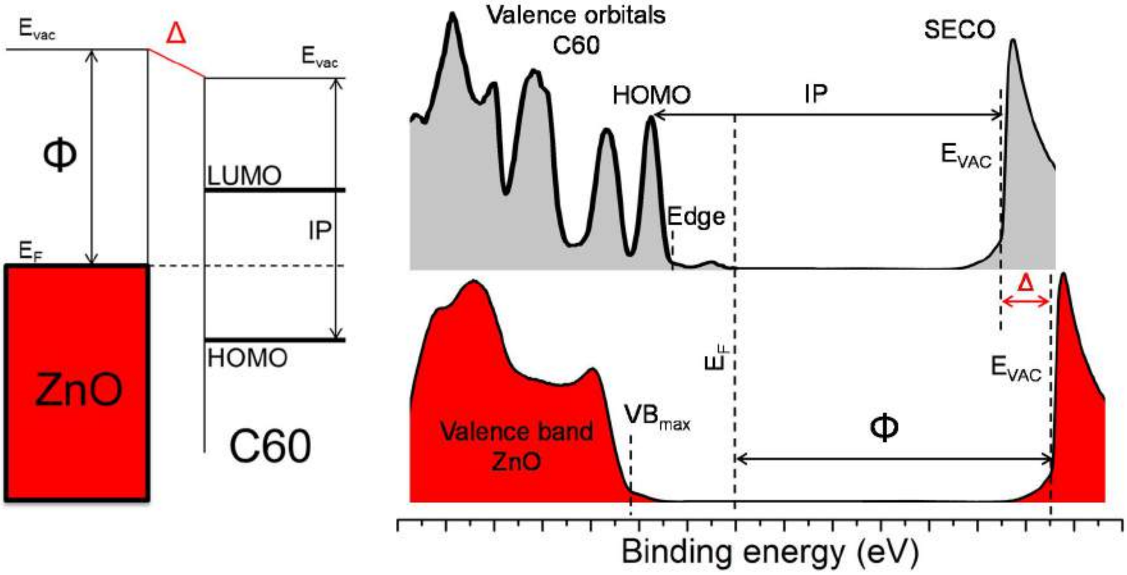

Figure A1.7 - Energy levels at ZnO/C60 interfaces. Schematic energy-level diagram (left) with the ZnO work function (ϕ), Fermi level (E_F), vacuum level (E_{vac}) and ionization potential (IP) and HOMO of C60. Valence photoemission spectrum of ZnO and C60 deposited on ZnO (right) with Secondary Electron Cut-Off (SECO) and Valence Band (VB) sides. In this case, the vacuum levels do not align and an interface dipole (Δ) is observed.

Finally, **Figure A1.8** shows the experimental PES setup. The sample is mounted on a sample holder using tantalum strips and the conductivity is checked before the insertion in the analyze chamber. The XPS source (Al Kα) passes by the quartz crystal of the monochromator before reaching the sample. The use of a monochromatic source allows a better resolution and the removal of satellites. For the UPS source, we need first to generate a plasma (He: 10-5 mbar, filament: 1A and anode: 150V) in order to use the He II transition (21.2 eV). Depending of the source XPS or UPS, different parameters of the detector are selected (pass energy, slits, lens mode …).The regular calibration (using gold or silver samples) is important as the anodes, filaments, alignment of the sources evolve with the time. In-situ preparation is possible and in the present work, the evaporation of C60 was performed in UHV on various substrates. Before exposing the sample to the evaporator, the C60 rate of evaporation depends on the applied current and is controlled by the microbalance. When, the desired rate of evaporation is obtained, the substrate is exposed to the evaporator. The C60 thickness is at the end estimated from the XPS spectra (**Figure A1.6**).

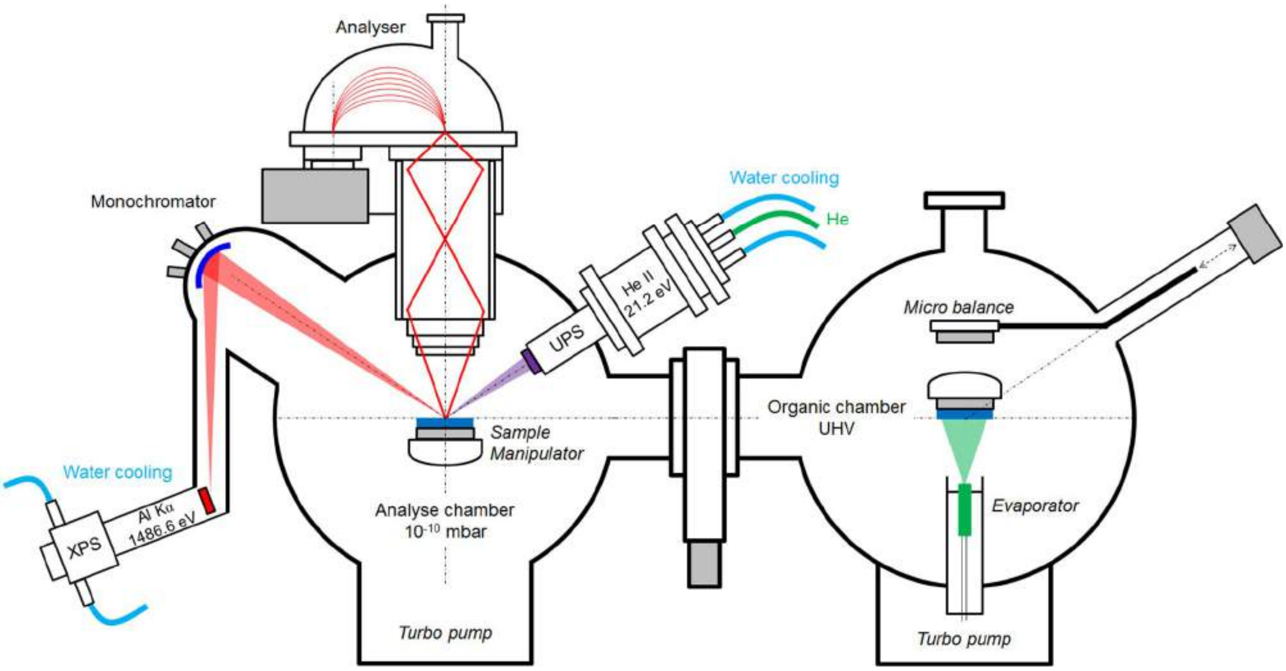

Figure A1.8 - Experimental setup.

A1.5. UV-visible spectroscopy

The absorption of UV and visible photons by a material causes electronic transitions from the ground state to excited states. Depending of the molecular orbitals of the considered molecule or macromolecule, different electronic transitions can take place. (**Figure A1.9**)

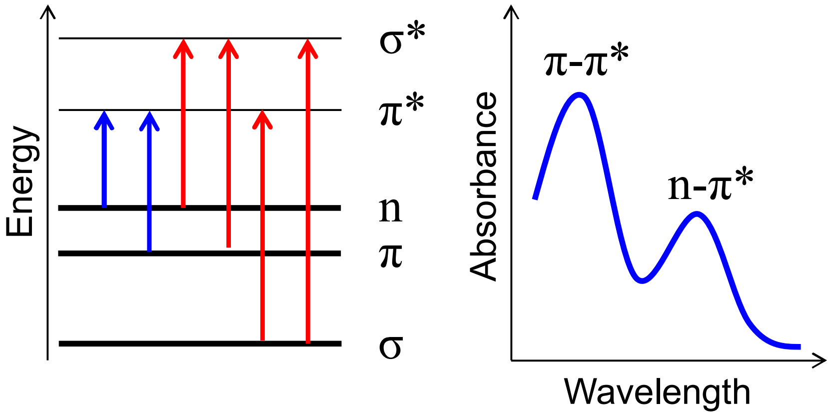

Figure A1.9 – The different electronic transitions according to the different types of orbitals.

In the case of pi-conjugated polymers, the energy of the π-π* transition is lowered by the conjugated system thus shifting the transition to higher wavelength. (See Chapter 1, 1.2.2) Additionally, the shape of the UV-vis spectrum of a pi-conjugated polymer is significantly influenced by the polymer chain self-assembly. Thus, clear differences can be observed depending of the pi-conjugated polymer state (thin film or in solution), the solvent used for the thin film preparation and post treatment such as thermal annealing. **Figure A1.10** is extracted from Hoffmann et al.[11] and shows the evolution of the UV-vis spectra of a conjugated oligomer in solution as function of the temperature.

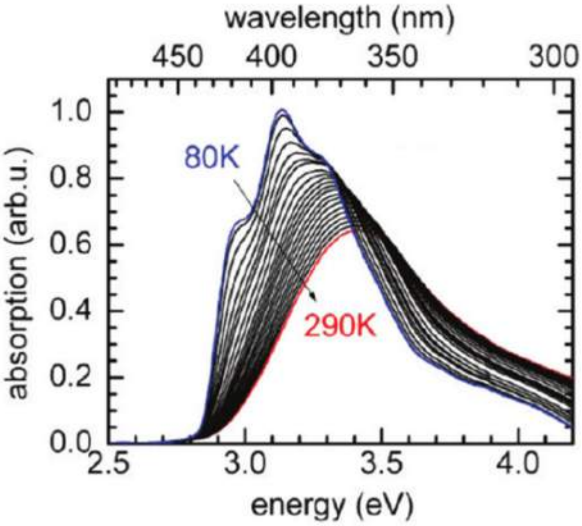

Figure A1.10 – UV-visible spectra of the 2,5-diheptyl-p-divinylbenzene oligomer in methyltetrahydrofuoran solution as function of the temperature. Extracted from Hoffmann et al.[11]

A1.6. Infrared spectroscopy (IR)

The technique exploits the fact that molecules and macromolecules absorb certain frequencies which induce molecular vibrations. If we consider a diatomic molecule, the stretching vibration of a bound behaves like an anharmonic oscillator. (**Figure A1.11**) The wavenumber of a vibrational mode can be calculated via the formula in **Figure A1.11** derived from the Hook's law. The frequency at which a given vibration occurs is determined by the strengths of the bonds involved and the mass of the component atoms. The vibrational modes are categorized in different groups (**Figure A1.11**). In IR, a mode is active only if there is a change in the dipole moment.

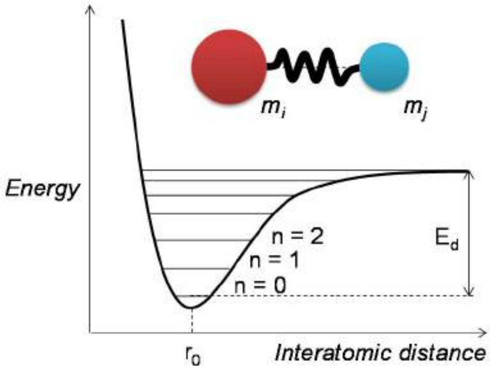

$$\bar{\nu} = \frac{1}{2\pi c}\sqrt{\frac{f(m_i + m_j)}{m_i . m_j}}$$

Figure A1.11 – On the top, the potential curve of an anharmonic oscillator with the formula derived from the Hook's law. The vibrational frequency (ν) can be calculated with f, the force constant, c, the velocity of light and m_i and m_j the masses of the atoms.

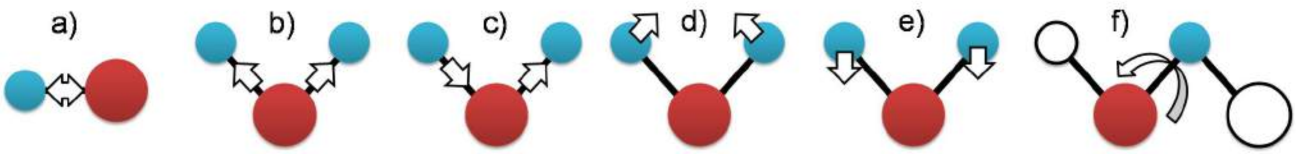

Figure A1.12 – The different vibrational modes: bound stretching a) symmetric stretching b) asymmetric stretching c) bending d), wagging e) and torsion f).

In the present work, we used the Nicolet 760-FTIR spectrophotometer in transmission mode and the optical layout of the setup is shown in **Figure A1.12**.

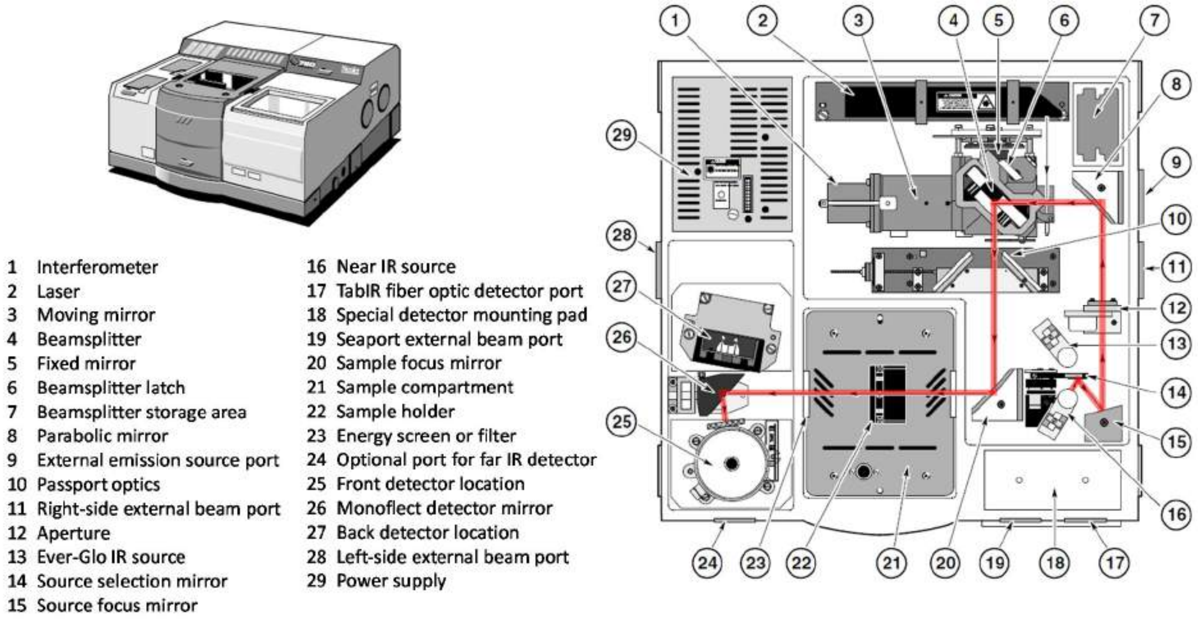

Figure A1.12 -The optical layout of the Nicolet 760-FTIR spectrophotometer. Extracted from: “Magna-IR User’s Guide” system 560 and 760 from the Nicolet Instrument Corporation.

A1.7. Raman spectroscopy

Raman spectroscopy provides information about molecular vibrations that can be used for sample identification and quantitation. The difference with IR spectroscopy is that Raman spectroscopy exploits the scattering process when a material is exposed to a monochromatic light. **Figure A1.13** summarizes the different electronic states and associated transitions occurring in IR and Raman experiments. In IR, only the vibrational states are involved and the molecules absorb certain frequencies related to their different vibrational modes. Concerning Raman, the exposure to the laser involves different interactions. Most of the incident light produces elastic scattering (**Figure A1.13**: Rayleigh b)) while a very small amount of light is shifted in energy producing inelastic scattering (**Figure A1.13**: Stokes c) or anti-Stokes d)) Therefore, in order to achieve adequate Raman signal, the elastic scattering has to be filtered out and the power of the incident light has to be relatively high. When the incident light from the laser allows electronic transitions, the fluorescence emission can be superposed to the Raman signal.

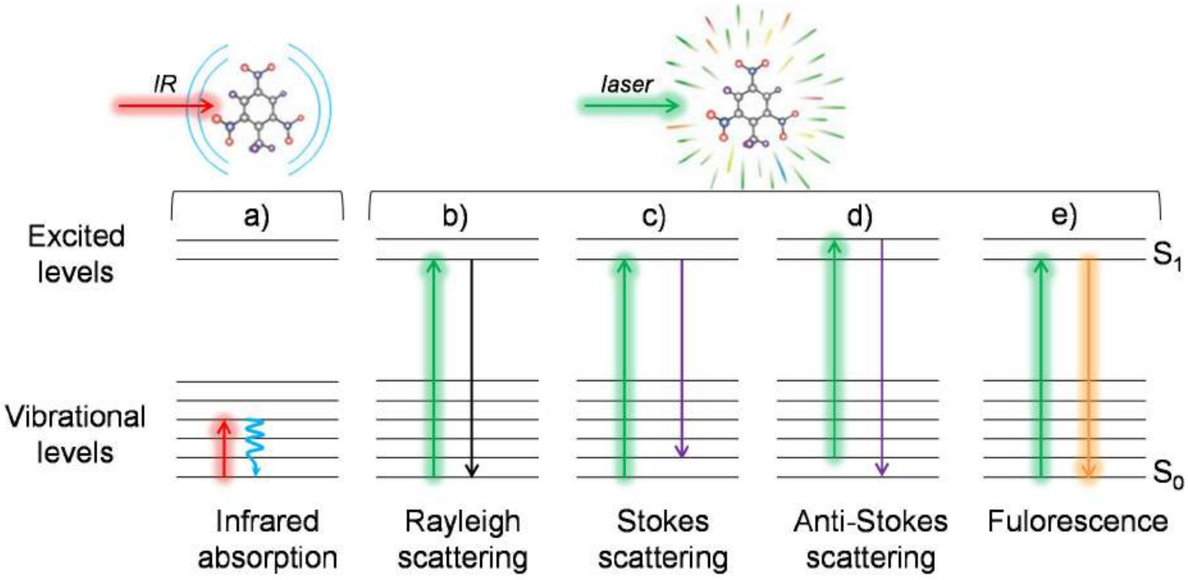

Figure A1.13 – Energy level diagram showing the different transitions involved in IR and Raman experiments.

In the present work, Raman spectroscopy was used in order to investigate structural transitions of pi-conjugated polymers. The underlying idea of the method is that almost every phase transition affects intramolecular vibrations through their self-energies by taking into account the interaction of specific modes with the electronic structure. The electronic structure is affected by intra- and intermolecular interactions, which depend on the phase of the material (solid, liquid, glass…) Thus, change in the vibrational modes as a function of the temperature can provide an indirect probe for structural phase transitions.[12]

In the present work, a home-made chamber was designed in order to perform Raman experiments along heating and cooling steps. (**Figure A1.14**) As the organic materials are sensitive to the laser exposure in air[13], the Raman experiments were performed under inert atmosphere. The nitrogen flux, ramp of heating and cooling were optimized in order to collect Raman signal with reasonable resolution without damaging the investigated pi-conjugated polymers.

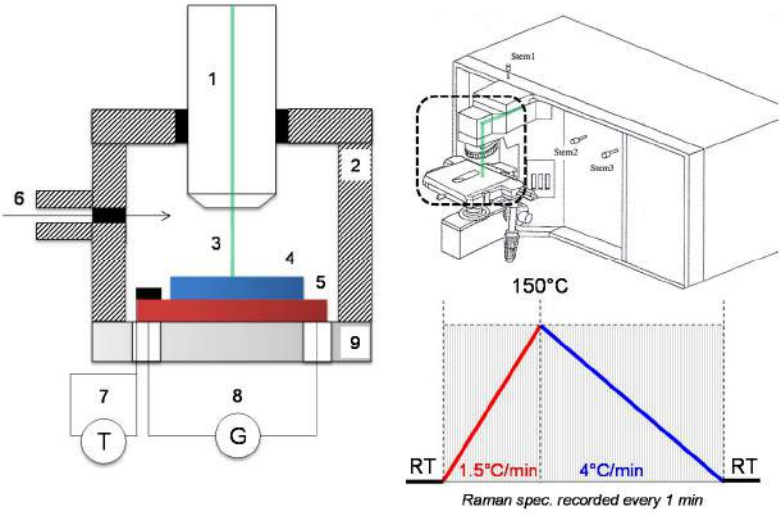

Figure A.14 – Experimental setup.

A1.8. Atomic force microscopy (AFM)

AFM belongs to the scanning probe microscopy family and is a technique used for probing the surface topography of a sample. The technique is based on the interaction between a tip and the surface of the investigated sample. (**Figure A1.15**) The contact mode means that the tip is in direct physical contact with the surface. The tapping mode operates by scanning a tip attached to the end of an oscillating cantilever across the sample surface. The tip is not in direct contact but is interacting with the surface via Van der Waals or electrostatic forces. The feedback loop (**Figure 1.16)** maintains a constant oscillation amplitude by maintaining a constant RMS of the oscillation signal acquired by the photodetector.

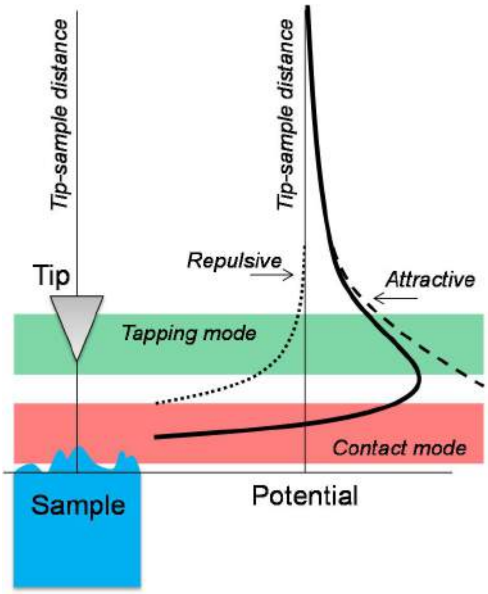

Figure A1.15 – The Lennard-Jones potential curve applied for explaining the interaction between the tip and the sample surface.

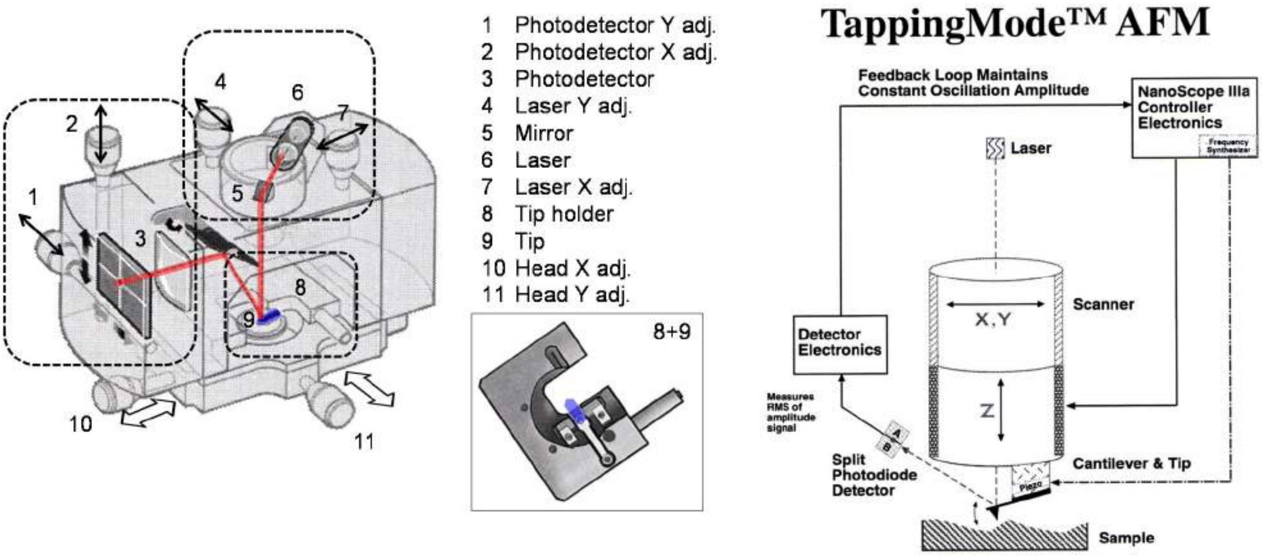

Figure A1.16 - Illustration of the head of the AFM (left) and the general description of the Tapping mode AFM (right). Extracted from the MultiMode Scanning Probe Microscope Instruction Manual (digital Instrument).

A2. Appendix of Chapter 2

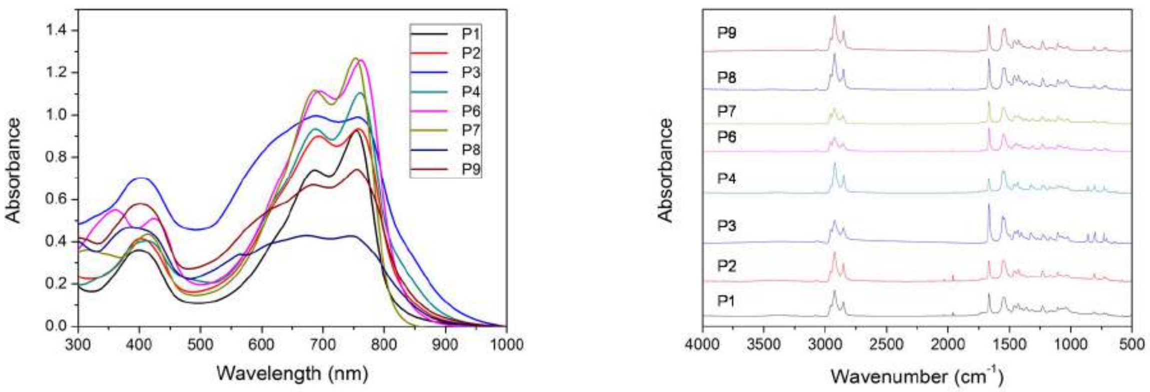

Figure A2.1 - UV-vis (left) and IR (right) spectra of the pristine P1-9 polymer films.

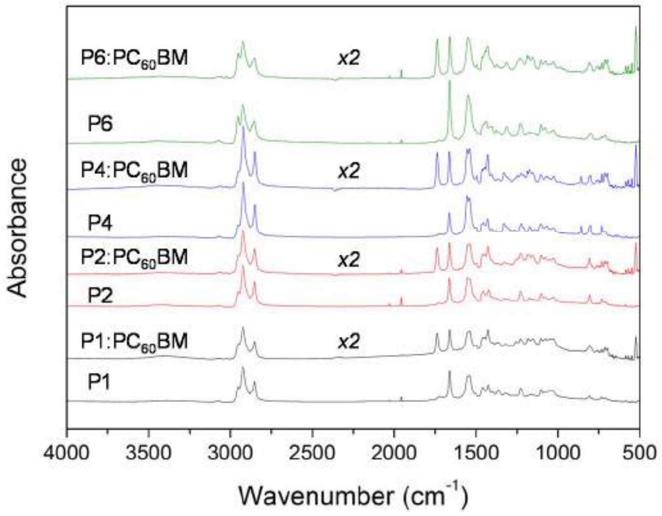

Figure A2.2 - IR spectra of pristine P1-9 polymers, neat and blend films (PX:PC$_{60}$BM, 1:2).

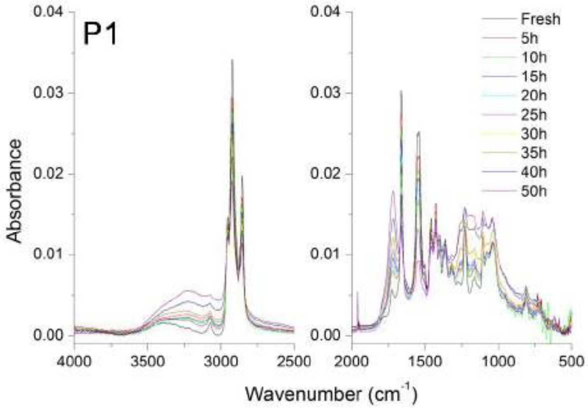
P1
Absorbance
0.04
0.03
0.02
0.01
0.00
4000
3500
3000
2500
2000
1500
1000
500
Wavenumber (cm^{-1})
Fresh
5h
10h
15h
20h
25h
30h
35h
40h
50h

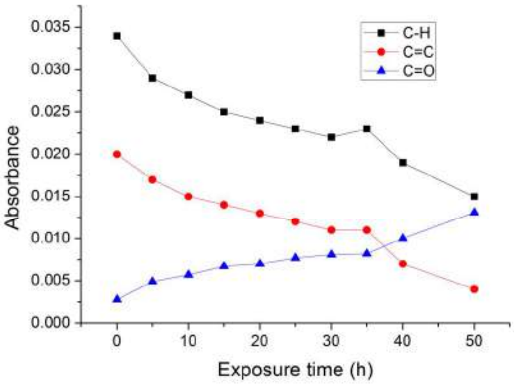
C-H
C=C
C=O
Absorbance
0.035
0.030
0.025
0.020
0.015
0.010
0.005
0.000
0
10
20
30
40
50
Exposure time (h)

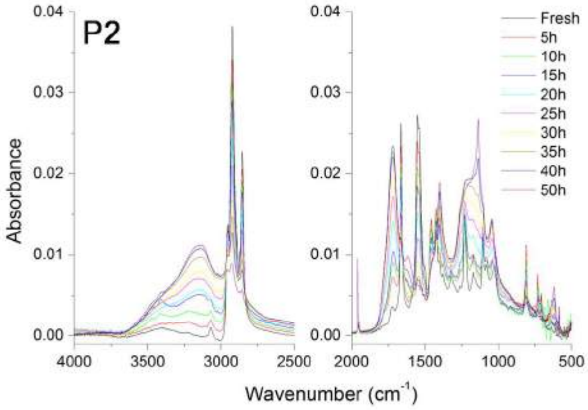
P2
Absorbance
0.04
0.03
0.02
0.01
0.00
4000
3500
3000
2500
2000
1500
1000
500
Wavenumber (cm^{-1})
Fresh
5h
10h
15h
20h
25h
30h
35h
40h
50h

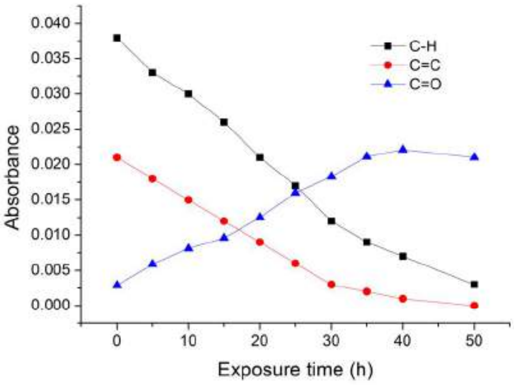
C-H
C=C
C=O
Absorbance
0.040
0.035
0.030
0.025
0.020
0.015
0.010
0.005
0.000
0
10
20
30
40
50
Exposure time (h)

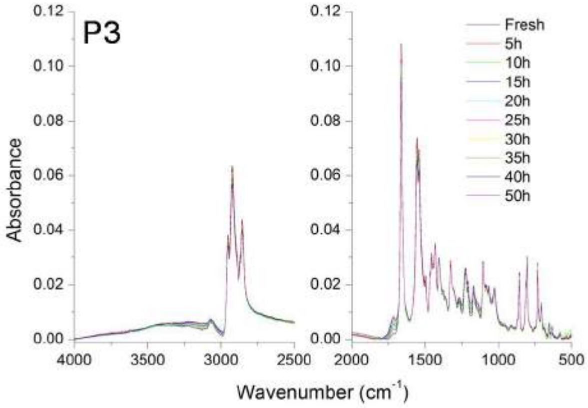
P3
Absorbance
0.12
0.10
0.08
0.06
0.04
0.02
0.00
4000
3500
3000
2500
2000
1500
1000
500
Wavenumber (cm^{-1})
Fresh
5h
10h
15h
20h
25h
30h
35h
40h
50h

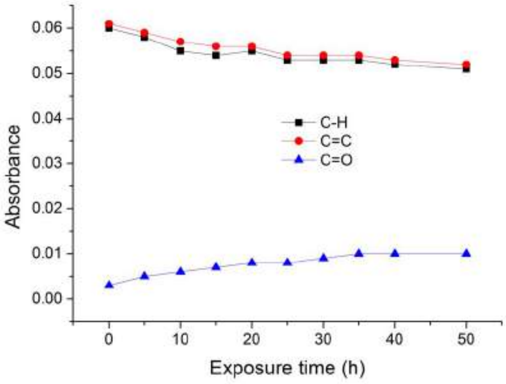
C-H
C=C
C=O
Absorbance
0.06
0.05
0.04
0.03
0.02
0.01
0.00
0
10
20
30
40
50
Exposure time (h)

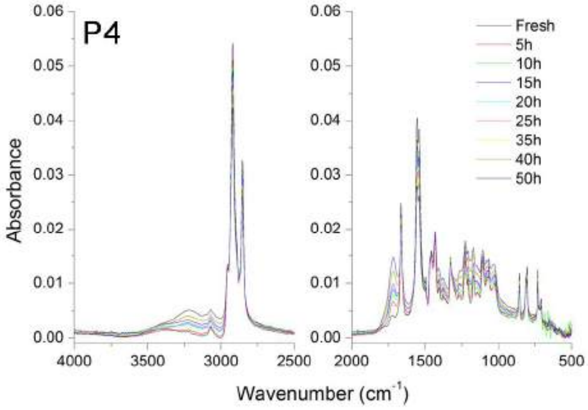
P4
Absorbance
0.00
0.01
0.02
0.03
0.04
0.05
0.06
4000
3500
3000
2500
2000
1500
1000
500
Wavenumber (cm^{-1})
Fresh
5h
10h
15h
20h
25h
35h
40h
50h

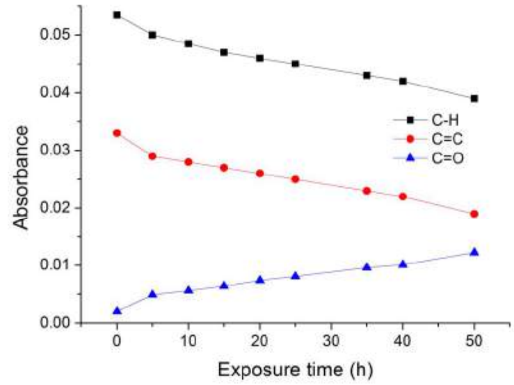
Absorbance
0.00
0.01
0.02
0.03
0.04
0.05
0
10
20
30
40
50
Exposure time (h)
C-H
C=C
C=O

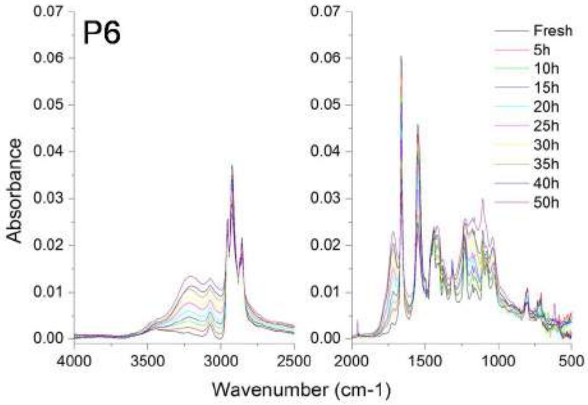
P6
Absorbance
0.00
0.01
0.02
0.03
0.04
0.05
0.06
0.07
4000
3500
3000
2500
2000
1500
1000
500
Wavenumber (cm-1)
Fresh
5h
10h
15h
20h
25h
30h
35h
40h
50h

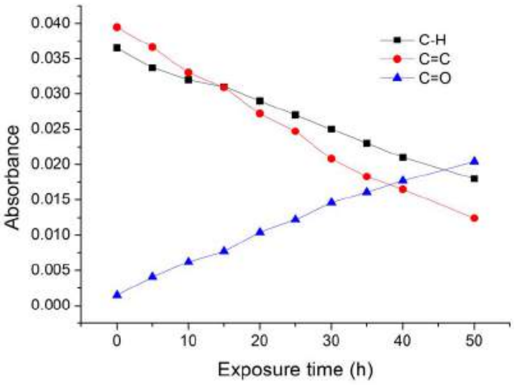
Absorbance
0.000
0.005
0.010
0.015
0.020
0.025
0.030
0.035
0.040
0
10
20
30
40
50
Exposure time (h)
C-H
C=C
C=O

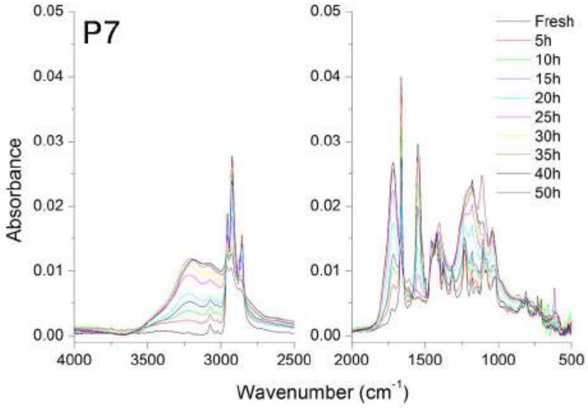
P7
Absorbance
0.00
0.01
0.02
0.03
0.04
0.05
4000
3500
3000
2500
2000
1500
1000
500
Wavenumber (cm^{-1})
Fresh
5h
10h
15h
20h
25h
30h
35h
40h
50h

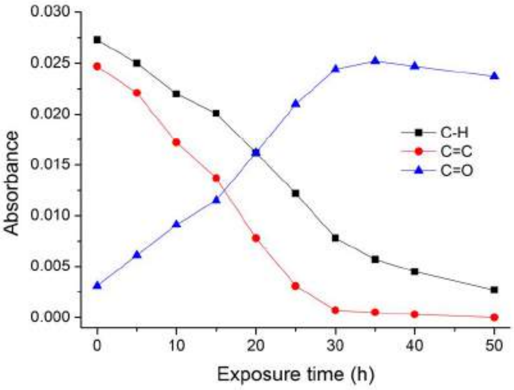
Absorbance
0.000
0.005
0.010
0.015
0.020
0.025
0.030
0
10
20
30
40
50
Exposure time (h)
C-H
C=C
C=O

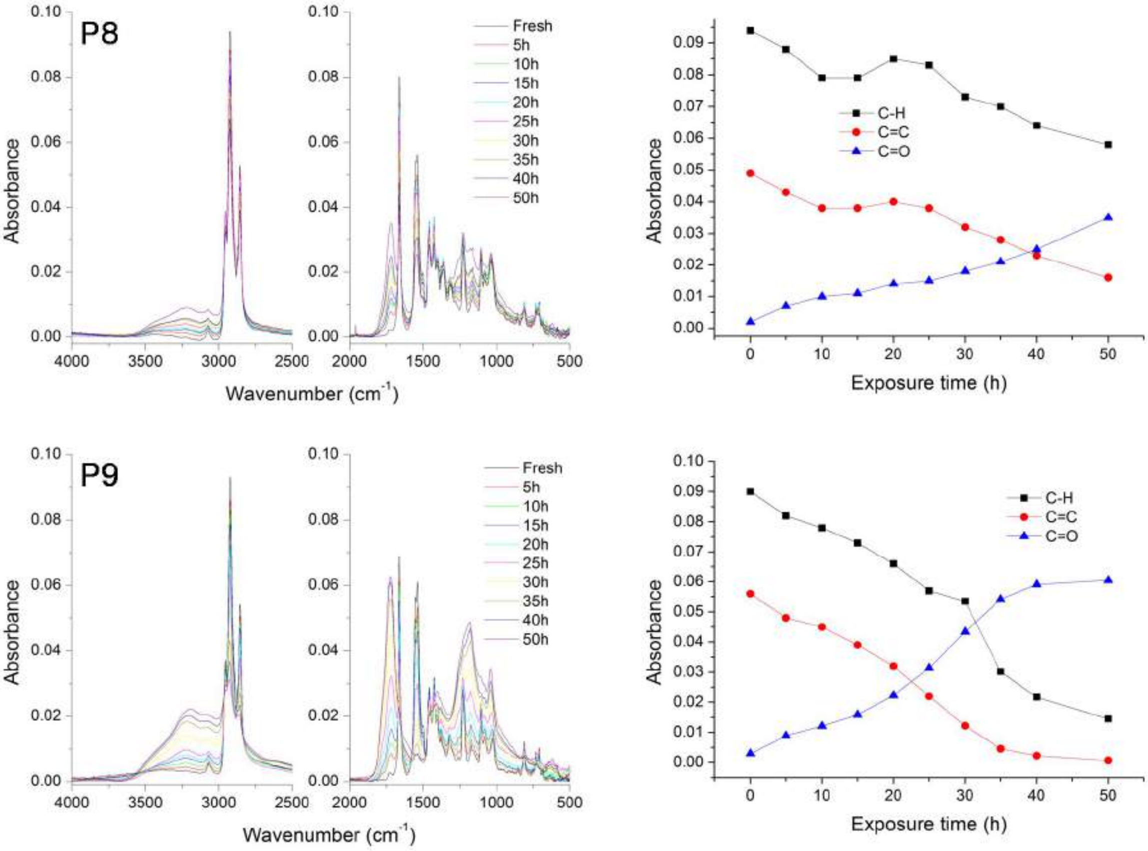

Figure A2.3 - Evolution of the IR spectra of the P1-9 polymer films during photodegradation (left) and kinetics of degradation of specific bands: C-H (2924 cm^{-1}), C=C (1540 cm^{-1}) and C=O (1717 cm^{-1}) (right).

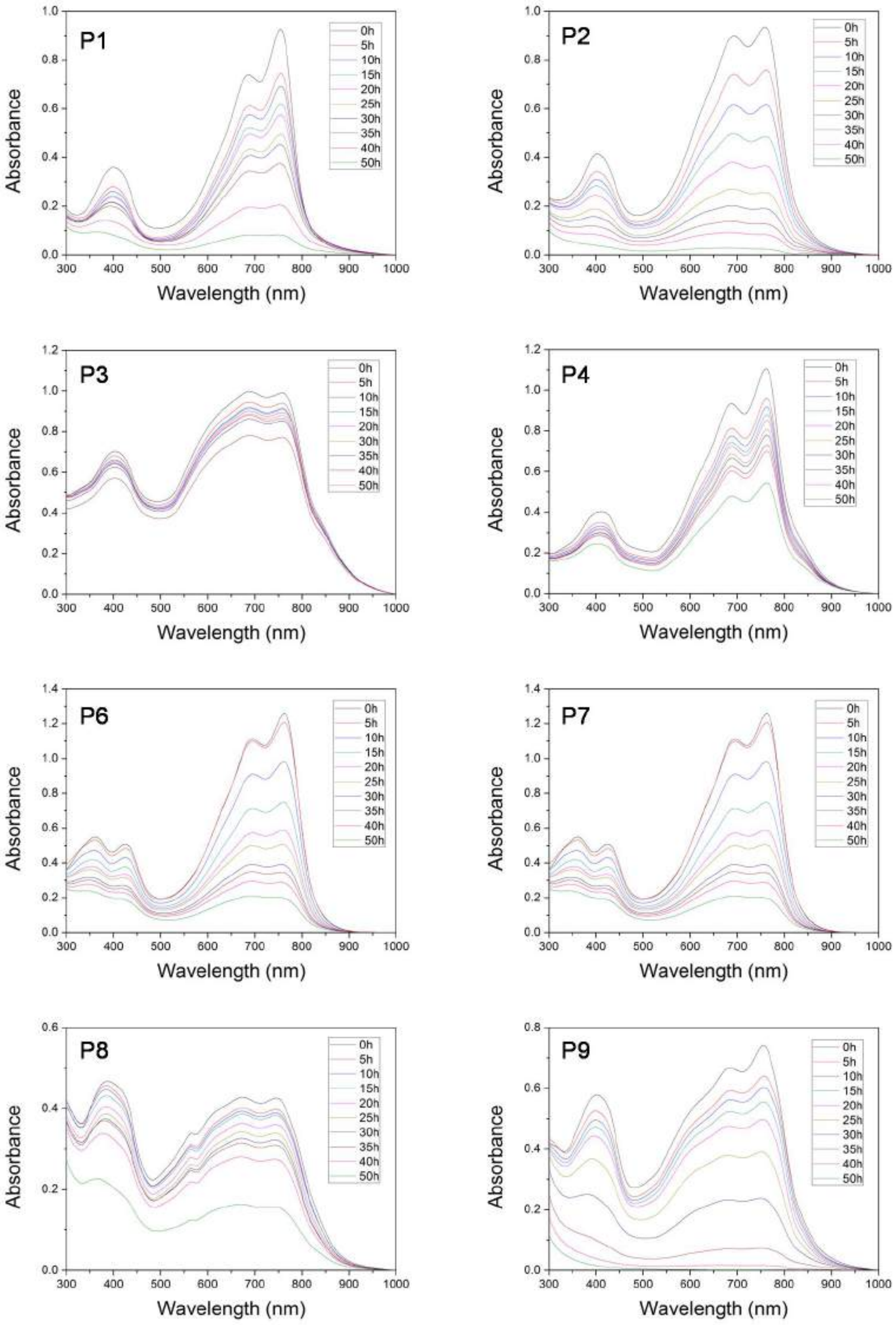

Figure A2.4 - Evolution of the UV-vis spectra of the P1-9 polymers during photodegradation.

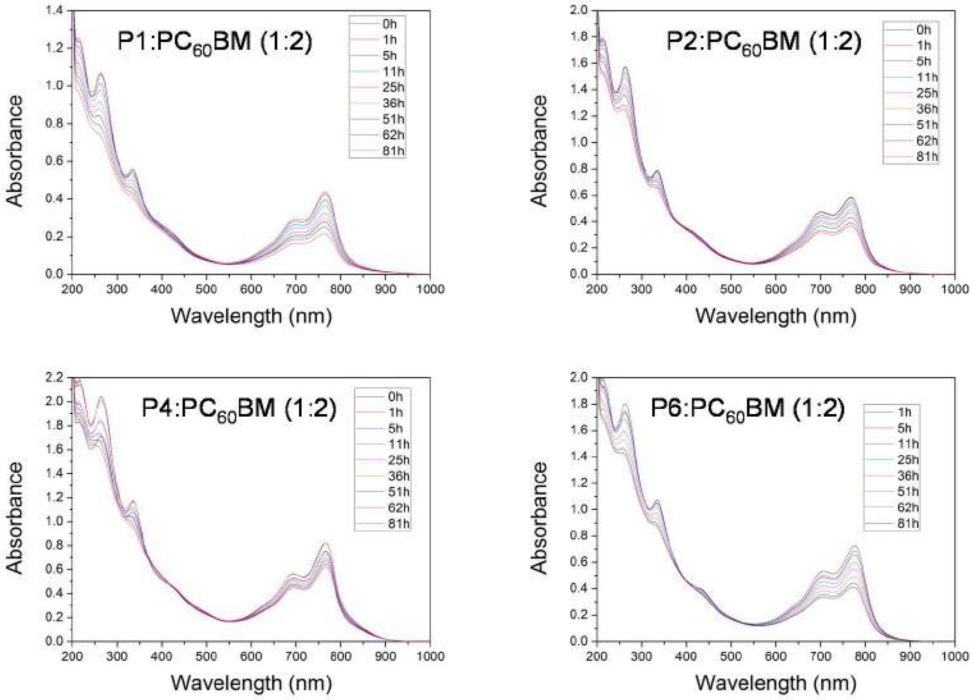

Figure A2.5 - Evolution of the UV-vis spectra of P1-2-4-6 polymer blends during photodegradation.

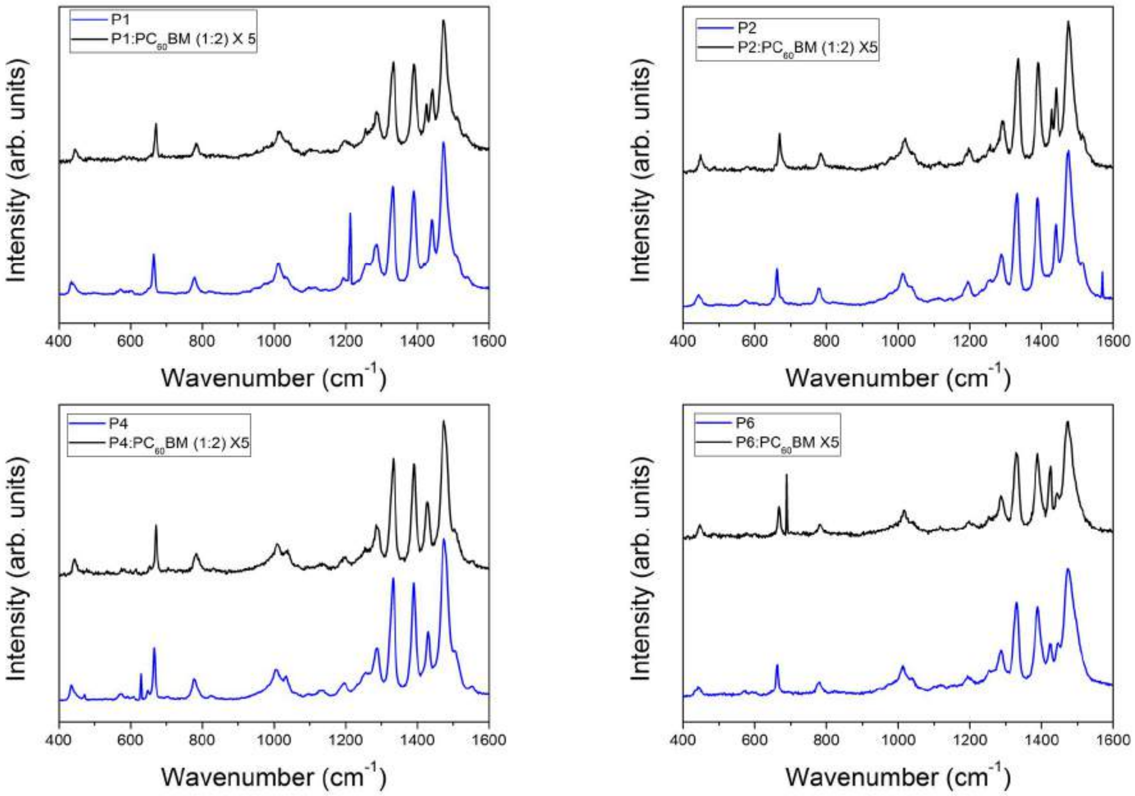

Figure A2.6 – Raman spectra of pristine P1, P2, P4 and P6 polymer and blend films.

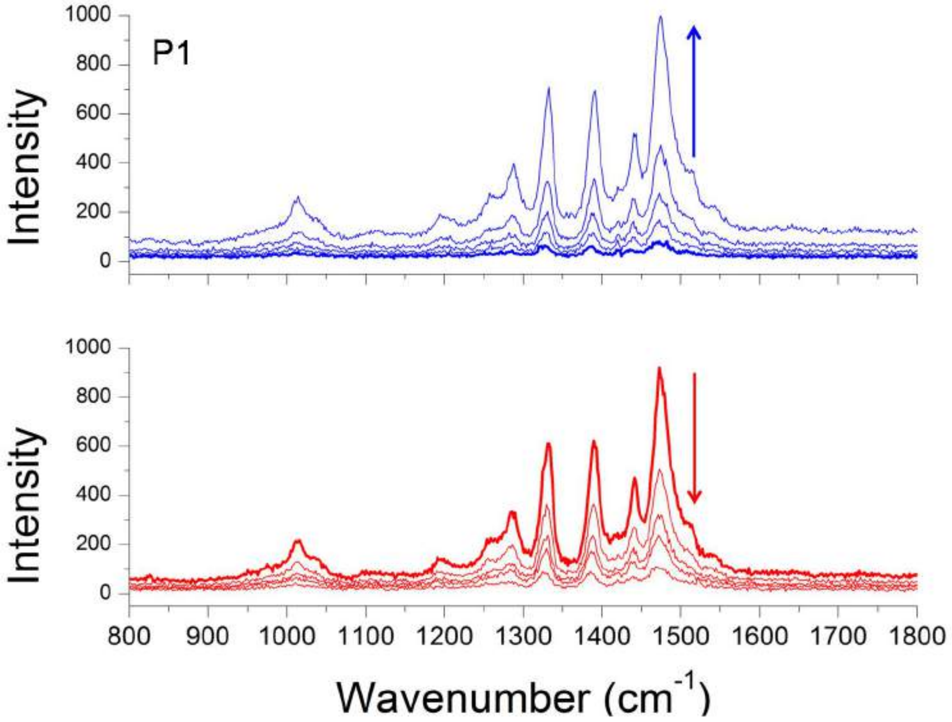

Figure A2.7 – Evolution of the Raman spectra of P1 as function of the temperature (heating in red and cooling in blue).

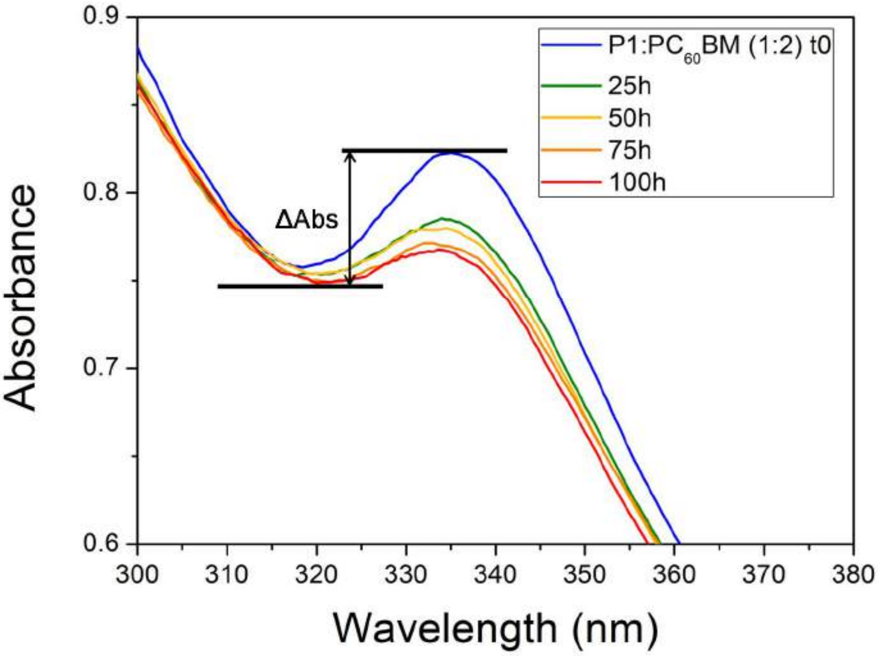

Figure A2.8 – Zoom in the UV-vis spectra of pristine and exposed to light P1:$PC_{60}BM$ (1:2) in the $PC_{60}BM$ absorbance region.

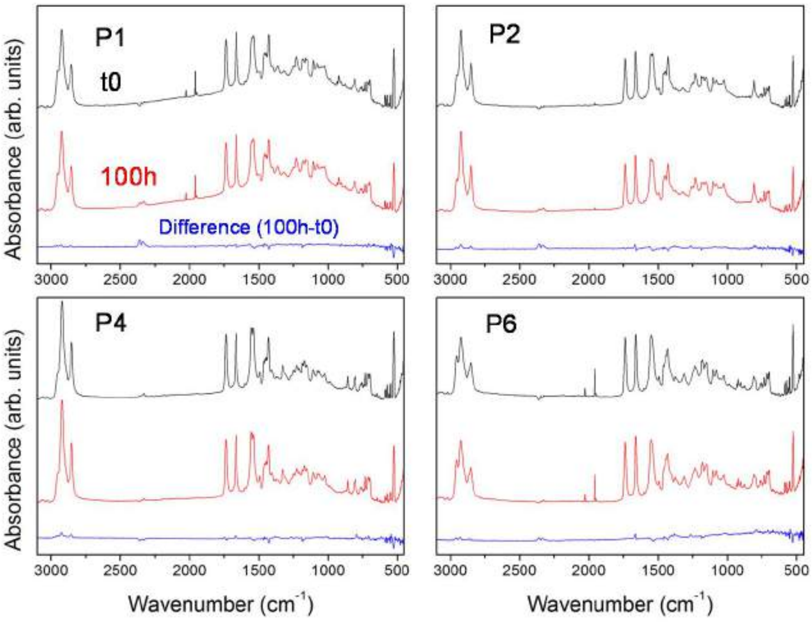

Figure A2.9 – IR spectra of P1, P2, P4 and P4 blends before and after light exposure.

A3. Appendix of Chapter 3

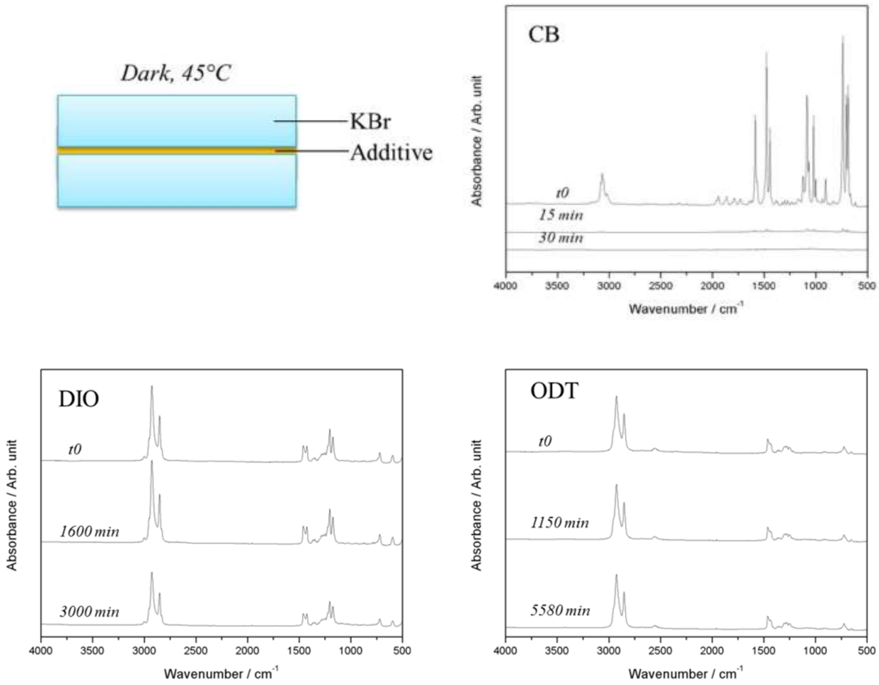

Figure A3.1 - Evolution of the IR spectra of CB, ODT and DIO exposed in air and dark at 45-50°C.

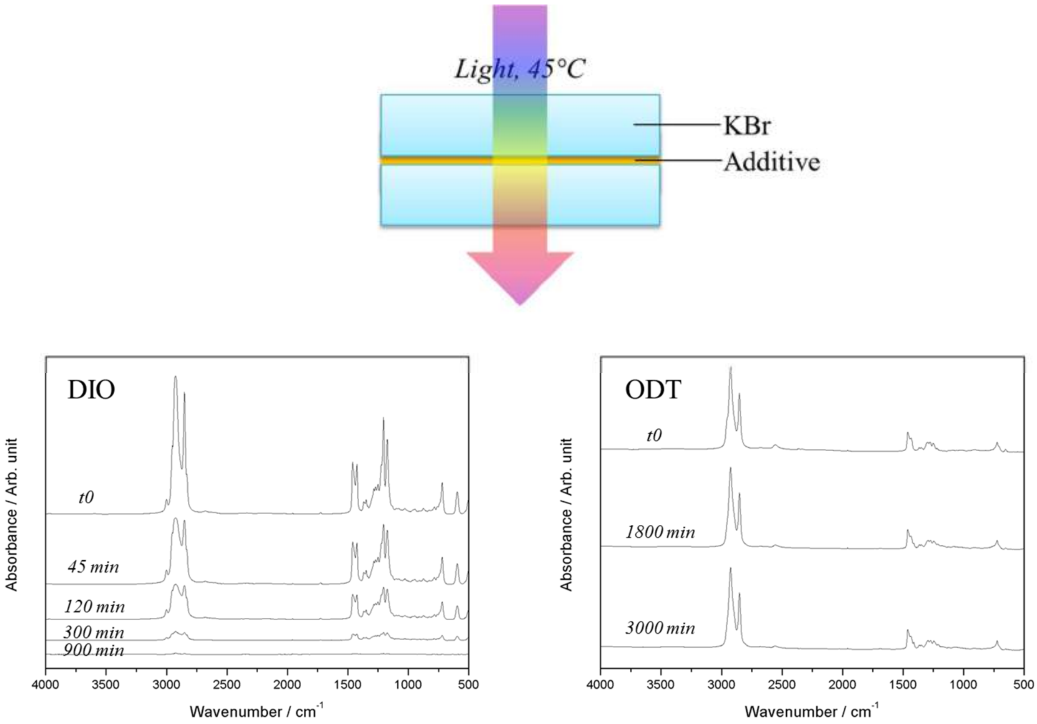

Figure A3.2 - Evolution of the IR spectra of CB, ODT and DIO exposed in air under the light (Xe lamp, 750W/m²) and at 45-50°C.

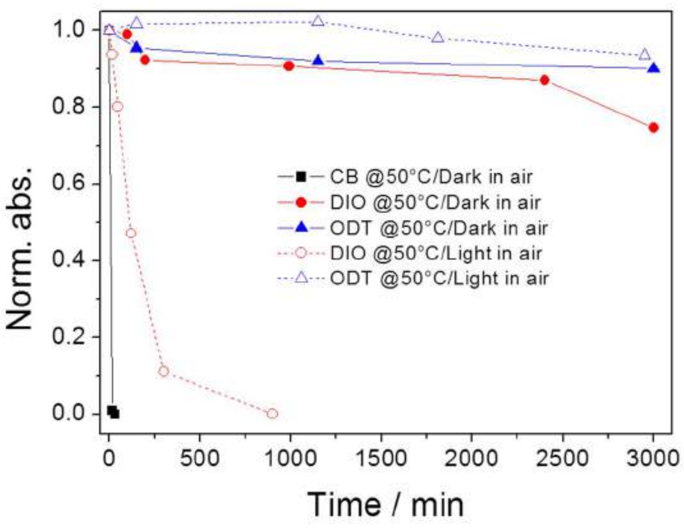

Figure A3.3 - Evolution of the 1463 cm^{-1} vibrational mode (CH$_2$ scissoring) for ODT and DIO and the 1584 cm^{-1} mode (C=C-C aromatic ring stretching) for CB exposed to the dark at 45°C or light at 45°C.

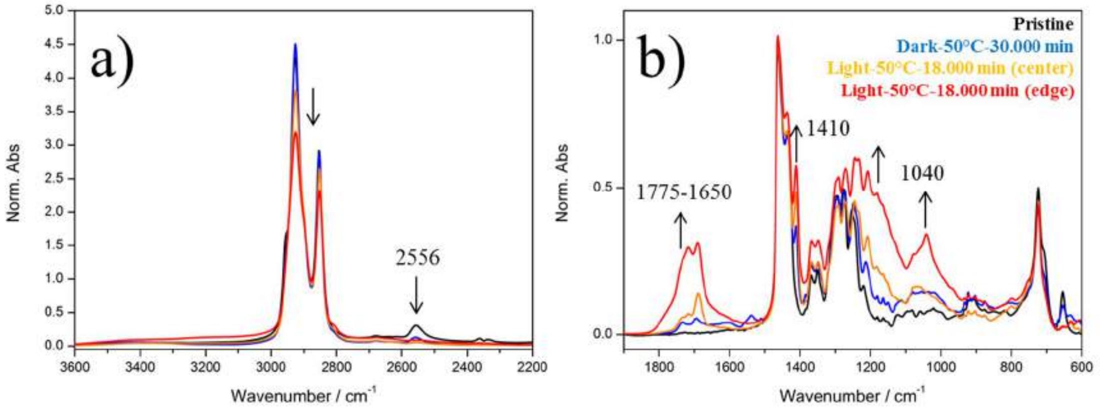

Figure A3.4 - Evolution of the IR spectra in the region 3600-2200 cm^{-1} (a) and 1900-600 cm^{-1} (b) of ODT under different types of exposures in air. The spectra were normalized at 1464 cm^{-1} (CH$_2$ scissoring vibration).

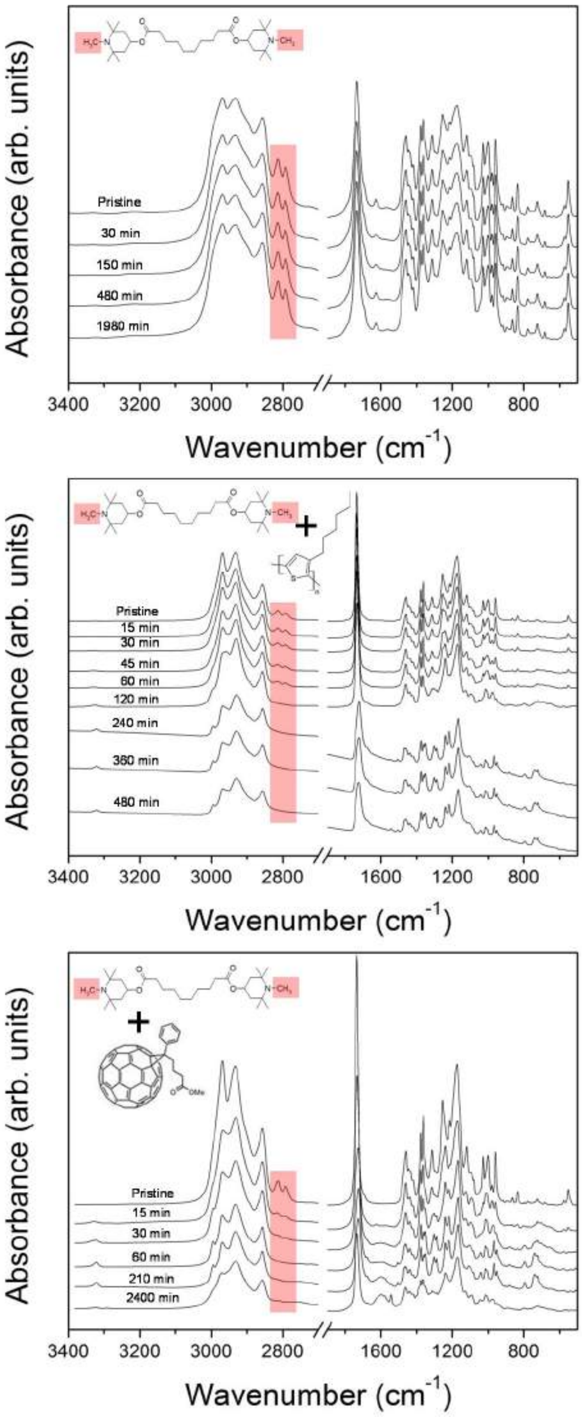

Figure A3.5 – IR spectra of thin films exposed to photooxidation: T765 (top), T765/P3HT (middle) and T765/PC$_{60}$BM (bottom).

A4. Appendix of Chapter 4

ITO

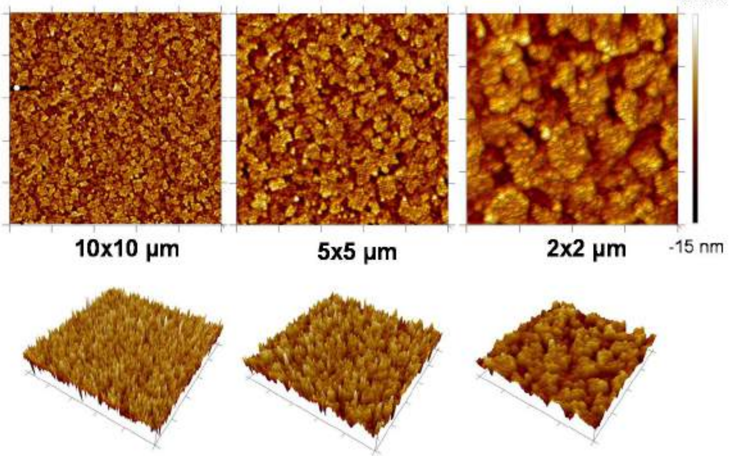

ZnO

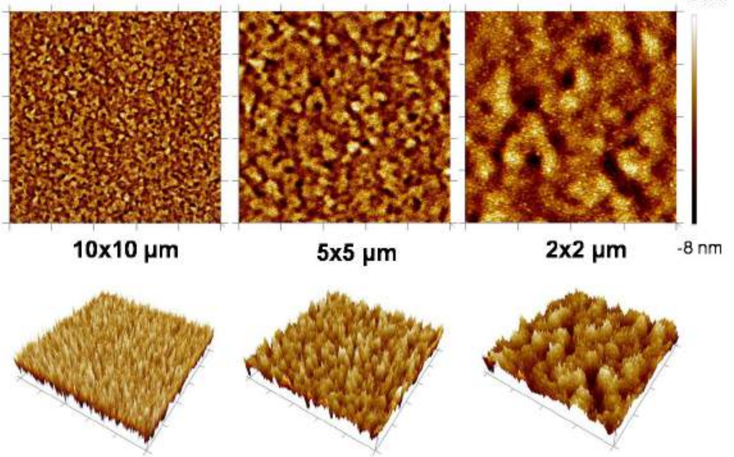

P3HT:PC$_{60}$BM (1:1)

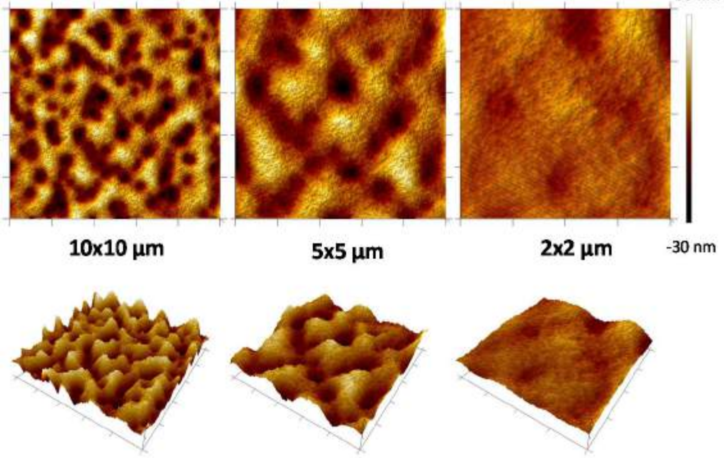

Si-PCPDTBT:PC$_{60}$BM (1:2)

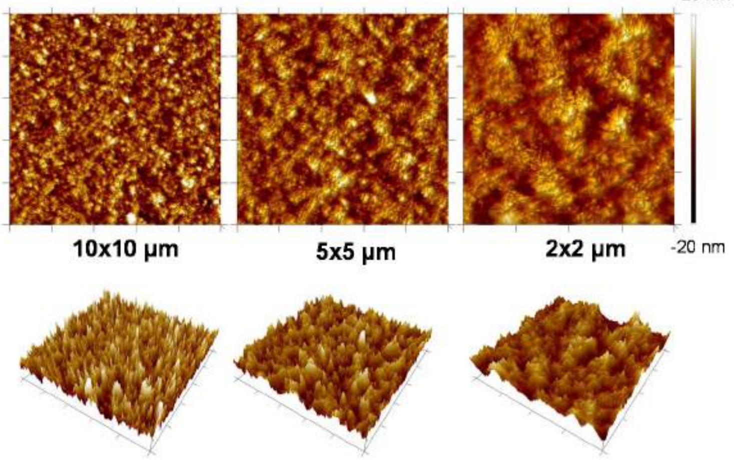

EP10:PC$_{60}$BM (1:2)

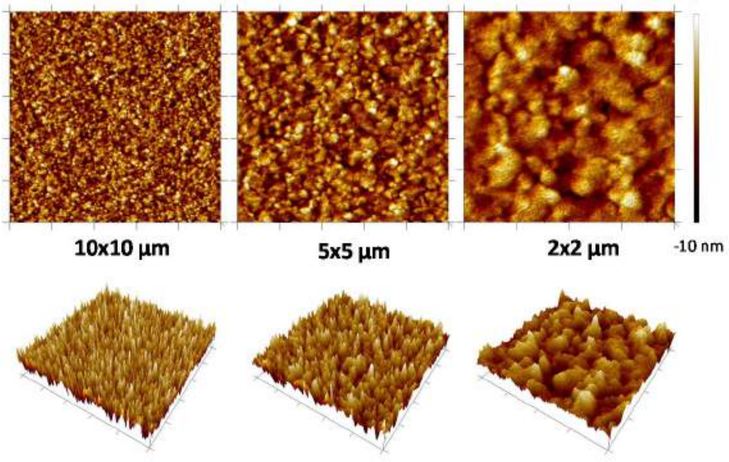

Ag

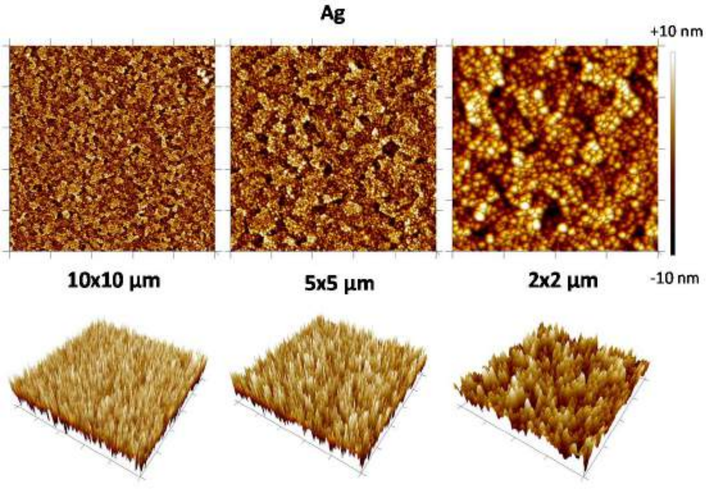

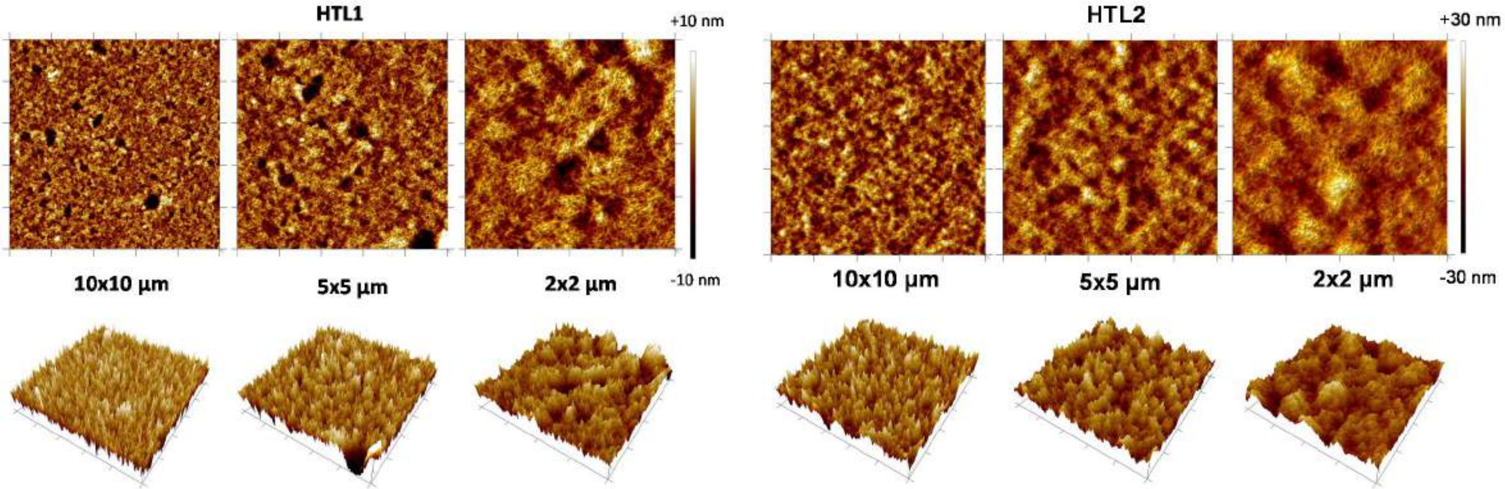

Figure A4.1 – AFM images of all individual material of the investigated inverted device structure.

A5. Appendix of Chapter 5

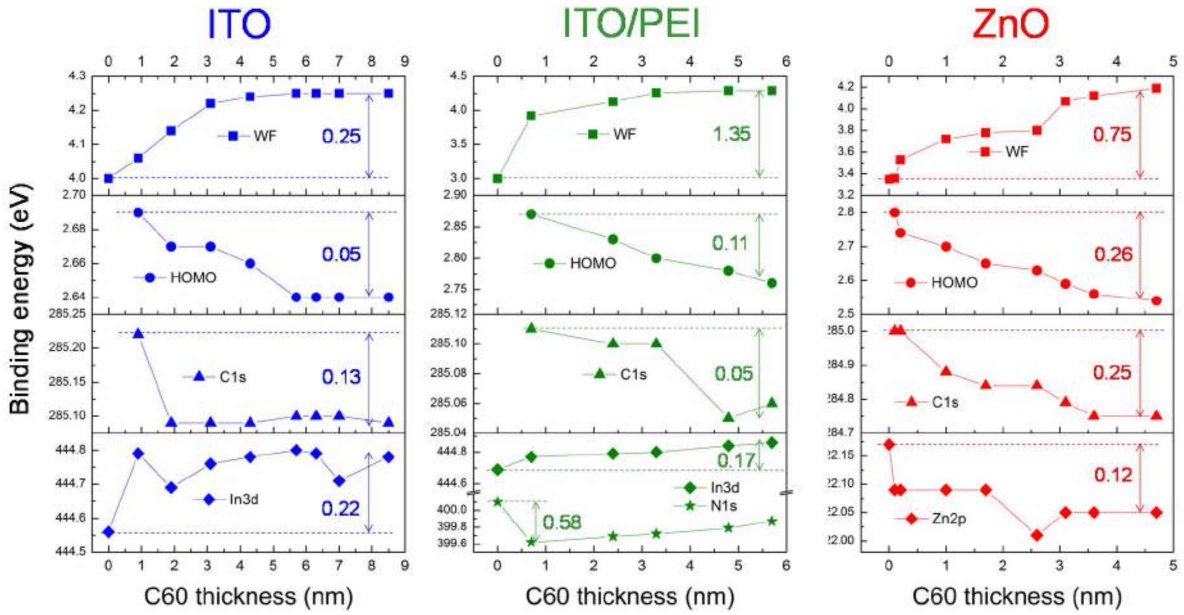

Figure A5.1 – Summary of the evolution of energetic levels as function of C60 evaporation.

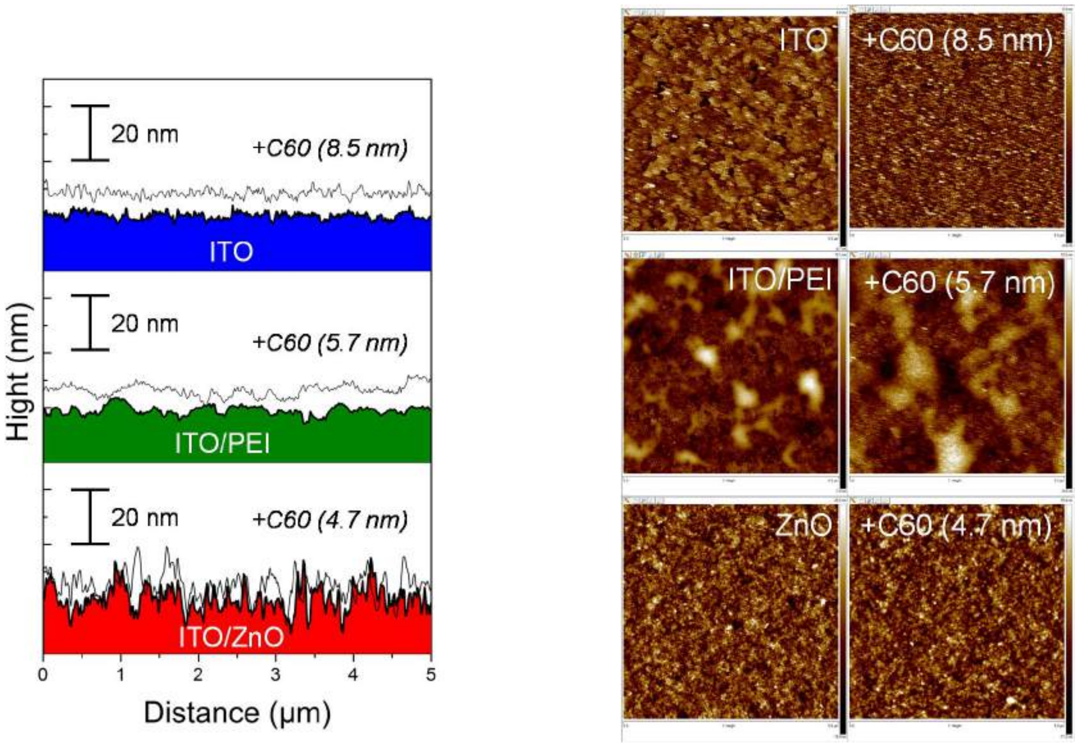

Figure A5.2 – AFM images and profiles before and after C60 evaporation.

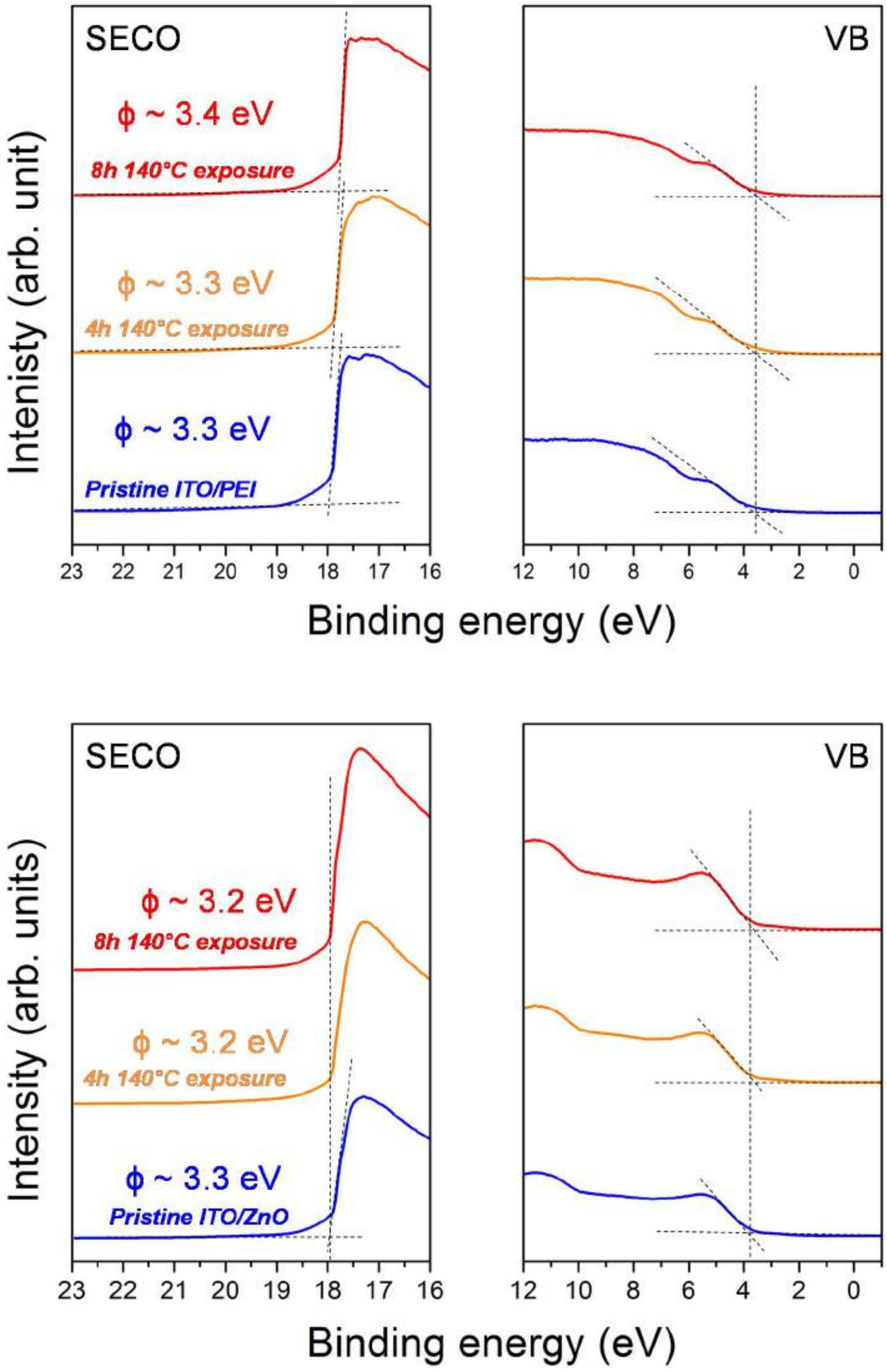

Figure A5.3 – UPS spectra of ITO/PEI (top) and ZnO (bottom) before and after thermal exposure.

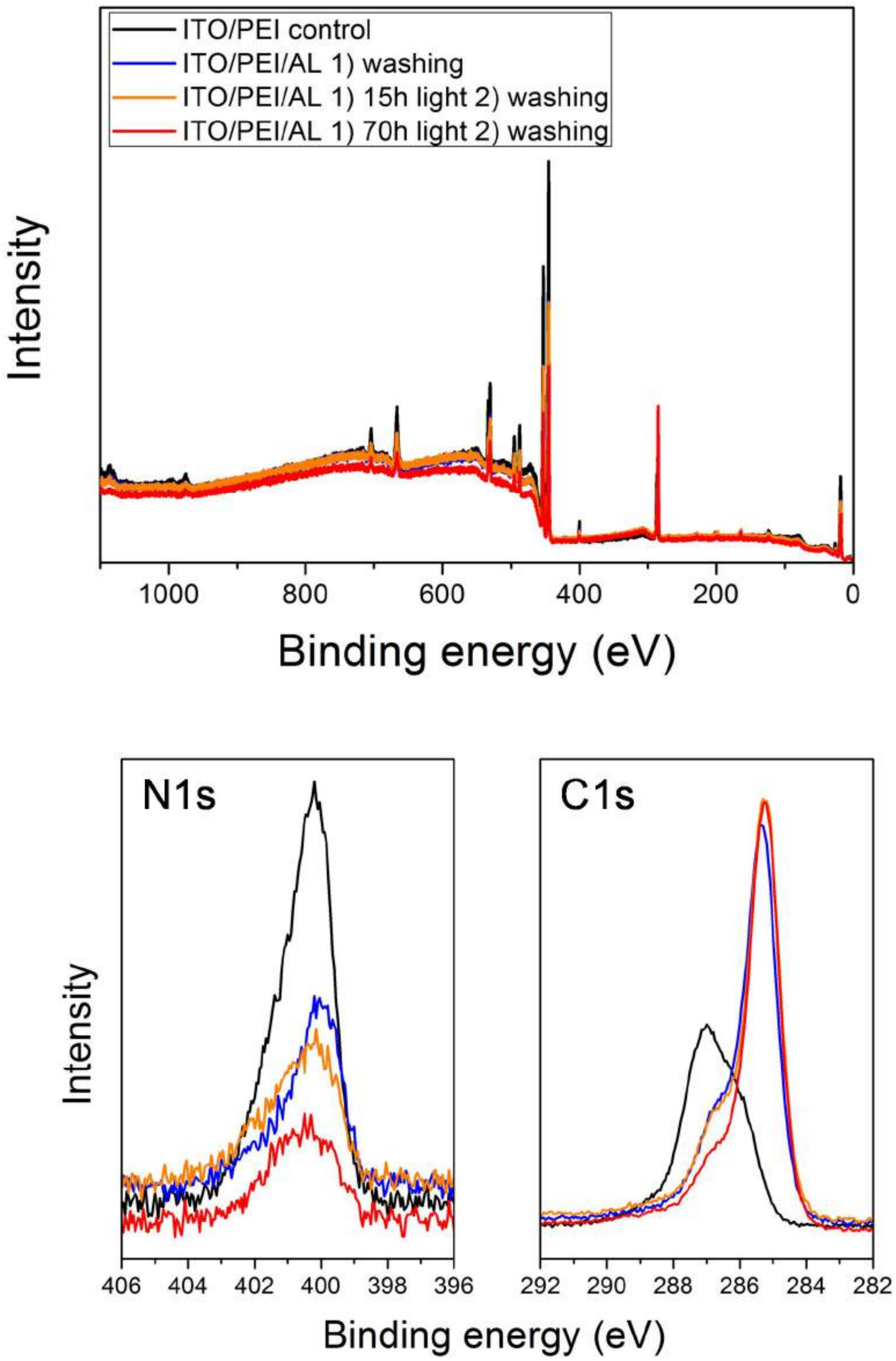

Figure A5.4 – XPS survey (top), N1s and C1s signals (bottom) of ITO/PEI/AL before and after light exposure and after the removal of the active layer.

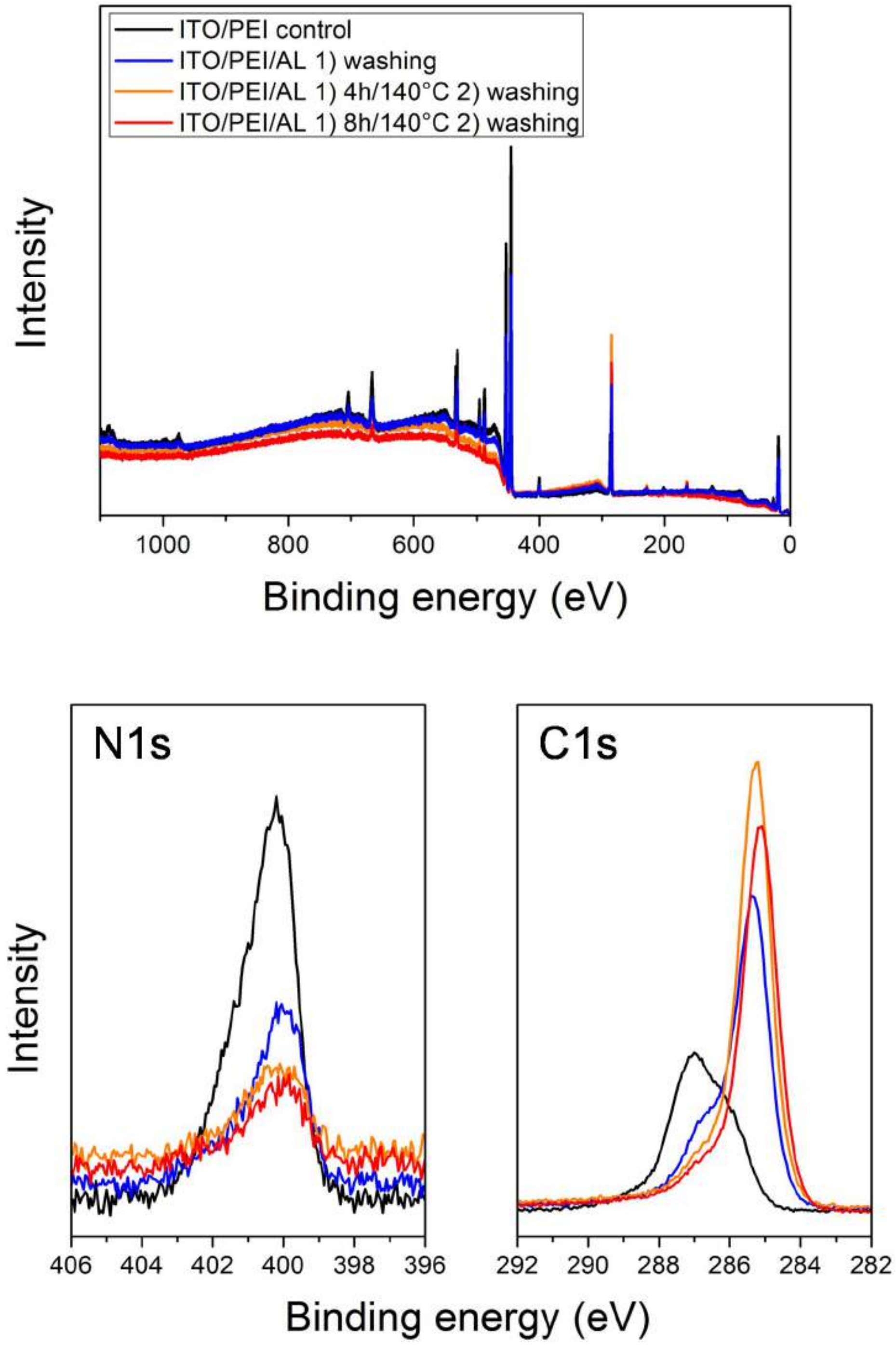

Figure A5.5 – XPS survey (top), N1s and C1s signals (bottom) of ITO/PEI/AL before and after thermal exposure and after the removal of the active layer.

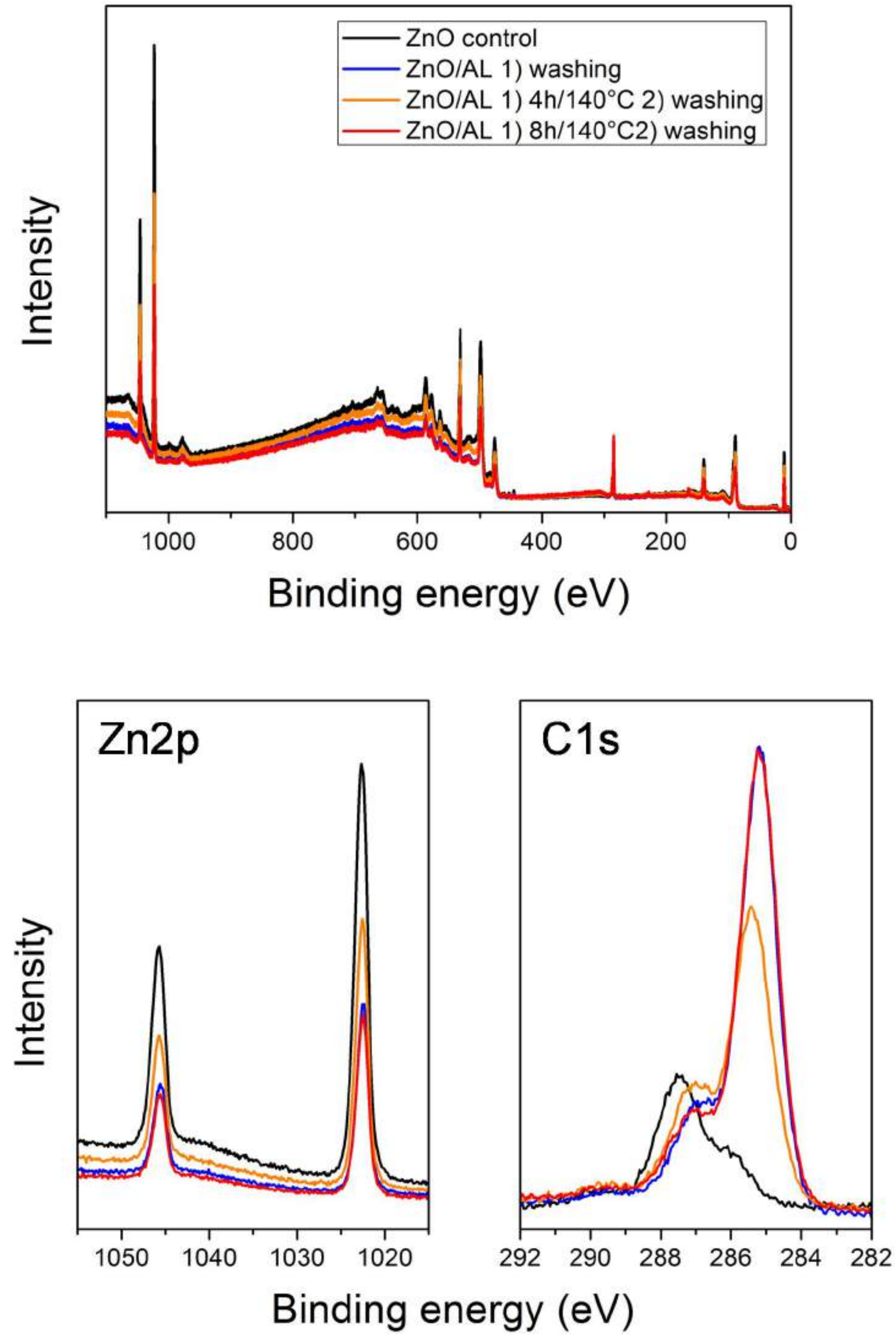

Figure A5.6 – XPS survey (top), Zn2p and C1s signals (bottom) of ITO/ZnO/AL before and after thermal exposure and after the removal of the active layer.

Bibliography

(1) Krebs, F. C. *Solar Energy Materials and Solar Cells* **2009**, *93*, 394.

(2) Reese, M. O.; Gevorgyan, S. A.; Jørgensen, M.; Bundgaard, E.; Kurtz, S. R.; Ginley, D. S.; Olson, D. C.; Lloyd, M. T.; Morvillo, P.; Katz, E. A.; Elschner, A.; Haillant, O.; Currier, T. R.; Shrotriya, V.; Hermenau, M.; Riede, M.; R. Kirov, K.; Trimmel, G.; Rath, T.; Inganäs, O.; Zhang, F.; Andersson, M.; Tvingstedt, K.; Lira-Cantu, M.; Laird, D.; McGuiness, C.; Gowrisanker, S.; Pannone, M.; Xiao, M.; Hauch, J.; Steim, R.; DeLongchamp, D. M.; Rösch, R.; Hoppe, H.; Espinosa, N.; Urbina, A.; Yaman-Uzunoglu, G.; Bonekamp, J.-B.; van Breemen, A. J. J. M.; Girotto, C.; Voroshazi, E.; Krebs, F. C. *Solar Energy Materials and Solar Cells* **2011**, *95*, 1253.

(3) Seah, M. P.; Dench, W. A. *SURFACE AND INTERFACE ANALYSIS* **1979**, *1*, 1.

(4) Alov, N. V. *Journal of Analytical Chemistry* **2005**, *60*, 297.

(5) Hintz, H.; Peisert, H.; Egelhaaf, H. J.; Chassé, T. *The Journal of Physical Chemistry C* **2011**, *115*, 13373.

(6) Braun, S.; Salaneck, W. R.; Fahlman, M. *Advanced Materials* **2009**, *21*, 1450.

(7) KAHN, A.; KOCH, N.; GAO, W. *Journal of Polymer Science: Part B: Polymer Physics* **2003**, *41*, 2529.

(8) Koch, N. *physica status solidi (RRL) - Rapid Research Letters* **2012**, *6*, 277.

(9) Ishii, H.; Sugiyama, K.; Ito, E.; Seki, K. *Advanced Materials* **1999**, *11*, 605.

(10) Hwang, J.; Wan, A.; Kahn, A. *Materials Science and Engineering: R: Reports* **2009**, *64*, 1.

(11) Hoffmann, S. T.; Bässler, H.; Köhler, A. *J. Phys. Chem. B* **2010**, *114*, 17037.

(12) Liem, H.; Cabanillas-Gonzalez, J.; Etchegoin, P.; Bradley, D. D. C. *Journal of Physics: Condensed Matter* **2004**, *16*, 721.

(13) Wang, X.; Egelhaaf, H.-J.; Mack, H.-G.; Azimi, H.; Brabec, C. J.; Meixner, A. J.; Zhang, D. *Advanced Energy Materials* **2014**, *4*, n/a.